Motion Cueing Fidelity in Rotorcraft Flight Simulation
A New Perspective using Modal Analysis

Miletović, Ivan

DOI
10.4233/uuid:4fdea178-a5b1-4620-987e-b1f2f9c23d32

Publication date
2020

Document Version
Final published version

Citation (APA)
Miletović, I. (2020). *Motion Cueing Fidelity in Rotorcraft Flight Simulation: A New Perspective using Modal Analysis*. [Dissertation (TU Delft), Delft University of Technology]. Delft University of Technology, Faculteit Luchtvaart- en Ruimtevaarttechniek. https://doi.org/10.4233/uuid:4fdea178-a5b1-4620-987e-b1f2f9c23d32

MOTION CUEING FIDELITY IN ROTORCRAFT FLIGHT SIMULATION

A NEW PERSPECTIVE USING MODAL ANALYSIS

MOTION CUEING FIDELITY IN ROTORCRAFT FLIGHT SIMULATION

A NEW PERSPECTIVE USING MODAL ANALYSIS

Proefschrift

ter verkrijging van de graad van doctor
aan de Technische Universiteit Delft,
op gezag van de Rector Magnificus prof. dr. ir. T. H. J. J. van der Hagen,
voorzitter van het College voor Promoties,
in het openbaar te verdedigen op maandag 3 februari 2020 om 15:00 uur

door

Ivan MILETOVIĆ

ingenieur luchtvaart en ruimtevaart,
Technische Universiteit Delft, Nederland,
geboren te Sarajevo, Joegoslavië.

Dit proefschrift is goedgekeurd door de

promotor: Prof. dr. ir. M. Mulder
promotor: Dr. M.D. Pavel

Samenstelling promotiecommissie:

Rector Magnificus,	voorzitter
Prof. dr. ir. M. Mulder,	Technische Universiteit Delft, promotor
Dr. M.D. Pavel,	Technische Universiteit Delft, promotor
Onafhankelijke leden:	
Prof. dr. ir. D.A. Abbink	Technische Universiteit Delft
Prof. dr. H.H. Bülthoff	Max Planck Institute for Biological Cybernetics, Germany
Dr. ir. R. de Breuker	Technische Universiteit Delft
Dr. M.D. White	University of Liverpool, United Kingdom
Overig lid:	
Dr. ir. M. Wentink	Desdemona B.V.

Ir. O. Stroosma, dr. ir. D. M. Pool, dr. ir. M. M. van Paassen en dr. ir. M. Wentink hebben in belangrijke mate aan de totstandkoming van het proefschrift bijgedragen.

TUDelft

DESDEMONA
motion simulation for your proficiency

Keywords: helicopter dynamics, flight simulation, simulation fidelity, motion cueing

Printed by: Ipskamp Printing

Front & back: I. Miletović; AH-64 photo by U.S. Navy (public domain) and Desdemona photo by Desdemona B.V. (used with permission)

ISBN 978-94-6384-103-0

“The legacy of heroes is the memory of a great name
and the inheritance of a great example”

Benjamin Disraeli

Dedicated to my father,

Mladenko Miletović
✱1963 - †1993

CONTENTS

SUMMARY

Flight simulators, or Flight Simulation Training Devices (FSTDs), offer great benefits in terms of safety and cost associated with pilot training and certification. To warrant uniform certification standards and to prevent adverse pilot training, (sub)system *fidelity* requirements are imposed by the Federal Aviation Authority (FAA) and European Aviation Safety Agency (EASA). While comprehensive, a notable example of an area in which these requirements are somewhat limited, are those pertaining to the *Motion Cueing System (MCS)* of *full-flight* flight simulators. The MCS comprises *hardware*, typically a set of actuators to enable physical motion of the platform, and *software*, often termed the Motion Cueing Algorithm (MCA), to process the simulated vehicle motion to prevent violation of (physical) simulator constraints. Naturally, the MCA introduces a significant mismatch between the *actual* (i.e., in-flight) and *simulated* vehicle motion perceived by the pilot. Furthermore, this mismatch often comes on top of inaccuracies in the *mathematical model* used to compute the simulated vehicle motion. Because of this complex interaction, the formulation of *quantitative* requirements pertaining to the allowed mismatch between real vehicle and simulator motion has proven cumbersome. To date, certification of flight simulator motion is therefore based predominantly on subjective evaluation by experienced pilots. To address this problem, the aim of this dissertation is to develop a *unifying tool* to quantify *motion cueing fidelity* in helicopter flight simulation and to evaluate its suitability in *realistic* applications.

Before developing a *new* tool, however, existing methods to measure motion cueing fidelity are studied first. A distinction is made between *qualitative* and *quantitative* methods, respectively. Qualitative methods are characterized by their reliance on *direct* human operator judgement when subjected to the simulated environment. In contrast, quantitative methods rely on physical measurements or models to assess motion cueing fidelity. Many methods in both categories are reviewed, from which only a few are selected for evaluation in this thesis. In terms of *qualitative* methods, the thesis focuses on the concept of *rating scales* for the subjective evaluation of simulation fidelity. The *quantitative* method investigated is that of the Objective Motion Cueing Test (OMCT) proposed in the domain of fixed-wing aircraft simulation. The main findings from these two studies are summarized in the next two paragraphs.

Because subjective evaluations made by qualified pilots remain the primary means for the certification of flight simulators, a study is conducted to assess the effectiveness of two prominent subjective metrics, namely the Simulator Fidelity Rating (SFR) and Motion Fidelity Rating (MFR) scales, as indicators of flight simulation fidelity. Of particular interest is the ability of operational pilots to use these metrics to distinguish between the effects of changes in the flight model and/or changes in the MCA. The obtained results have exposed several interesting findings. For example, there is some evidence that changes in SFR and MFR ratings are inconsistent between the experimental conditions evaluated. Also, while the participating pilots seemed able to recognize a large degradation in *both* helicopter

dynamics and motion, degrading either *one* of these characteristics yielded less conclusive results. Finally, a strong relation between the adopted task strategy and awarded ratings is identified, where a less aggressive task strategy is found to result in more favourable ratings. It is concluded that many caveats exist in the application of subjective metrics for the assessment of flight simulation fidelity. Nonetheless, to maximize the utility of subjective metrics, it seems beneficial to limit modifications to a *single* simulator component when conducting these types of studies. Also, close attention must be paid to task performance specifications in relation to the applied pilot strategy as well as flight model and simulator centred limitations. These findings are valuable for later contributions of this thesis, where subjective metrics are used extensively to evaluate the relative merit of different motion cueing strategies.

In terms of existing *quantitative* methods, the utility of the *original* OMCT as defined for fixed-wing aircraft applications is “extended” towards application in the rotary-wing aircraft domain. Both computer-based (“paper pilot”) and pilot-in-the-loop simulations are performed to obtain time traces of human-perceived quantities (i.e., specific forces and angular rates) during typical helicopter manoeuvering flight. Frequence domain spectra of these time traces are then computed and used to define an alternative set of OMCT input signals, in which all MCS degrees-of-freedom are driven *simultaneously*. Subsequent OMCT analyses performed using these alternative signals reveal interactions in the motion cueing signals that are not captured in the original OMCT. In particular, a strong coupling is found between the translational (surge) and rotational (pitch) degrees-of-freedom. It is important to emphasize, however, that the obtained results are specific to a single combination of vehicle and task. That is, a change in either requires a redefinition of the frequency domain data and, hence, might result in substantially different tailored OMCT results. Furthermore, processing of the vehicle- and task-specific frequency domain data is a relatively tedious process sensitive to signal processing particularities and, more importantly, inter-pilot variability. While certainly insightful, the “extended” OMCT developed for modeling the interaction between the vehicle and MCS dynamics is therefore not pursued further in this thesis. Instead, a method is sought to *explicitly* capture the dynamics of *both* the vehicle *and* the MCA.

The first step towards this *new* methodology is the development of a model to describe the six rigid-body degrees-of-freedom dynamics of rotorcraft. This model, named Delft Rotorcraft Simulation (Draftsim), is aimed primarily at efficient (real-time) flight simulation as well as common offline analyses (e.g., trim and linearization). In this process, a variety of existing tools and methods are explored, with particular emphasis on those pertaining to Handling Qualities (HQs) as documented in the Aeronautical Design Standard 33E (ADS-33E). First, Draftsim is verified by a trim and dynamic stability analysis of the Bo-105 helicopter, after which the model is applied to the AH-64 helicopter in a HQs evaluation conducted on the Desdemona simulator. Both these studies are concluded with satisfactory results, indicative of a satisfactory proof-of-match with an existing model of similar fidelity and, in case of the AH-64, a good degree of realism (in terms of HQs) according to expert judgement. More importantly, however, these analyses signify the predictive value of rudimentary quantitative tools in the domain of helicopter flight dynamics. This inspires the development of a new utility, aimed at quantitative analysis of *motion cueing fidelity*.

This new utility is based on the novel concept of Eigenmode distortion (EMD). In EMD, the generally non-linear dynamics of the MCA are *linearized* and subsequently *coupled* algebraically (in state-space form) to an existing and unaltered model of *linear* helicopter dynamics. It is shown that this formulation of the coupled vehicle and MCA dynamics can be studied in terms of the vehicle's dynamic *modes* and, within each mode, also in terms of *human-perceived* quantities (i.e., specific forces and angular rates). In addition, the Mode Participation Factor (MPF) is introduced as a tool to measure the contribution of each mode in a (measured) vehicle response. To exemplify the new method, a case study is also conducted, which shows that EMD is capable of revealing several intricate interactions between the vehicle and MCA dynamics that, up to present, could not be captured using existing tools such as OMCT. A notable example are the inherently coupled pitch-surge dynamics of helicopters, which are found to be strongly affected by the MCA dynamics, a result that is also in accordance with the results predicted by the "extended" OMCT method. EMD, in conjuction with MPFs, is therefore believed to be a powerful model-based framwork for the quantitative analysis of motion cueing fidelity suitable for a wide variety of vehicle types and tasks.

Finally, this thesis also demonstrates the practical utility of the EMD methodology using several *pilot-in-the-loop* experiments conducted on both the SIMONA Research Simulator (SRS) at TU Delft as well as the Desorientation Demonstrator Amst (Desdemona) simulator in Soesterberg, the Netherlands. In these experiments, EMD is used as a *guiding* methodology for the selection of different motion cueing configurations applied to two different helicopter types, the AH-64 and Bo-105, in three typical helicopter Mission Task Elements (MTEs): the *precision hover*, *lateral reposition* and the *depart/abort*. These experiments yield valuable knowledge on the relative merit of motion cues aimed at preserving the various vehicle modes. Specifically, it seems motion cues in the rotational (i.e., roll and pitch) subsidence modes are more valued than motion cues aimed at representing the classic longer-term modes (e.g., phugoid and Dutch roll). For tasks that are more dynamic, involving rapid and large changes in the vehicle attitude, the overall experiment results suggest that the opposite is true. In the Desdemona simulator, a possible explanation for this could be the combination of physical motion cues with immersive Virtual Reality (VR) visuals. This could lead pilots to "reweight" the importance of visual and vestibular cues. Other advanced considerations, such as the incorporation of extended (rotor) dynamics or stability augmentation in EMD, are also addressed. Together, these applications highlight the generality and versatility of the new EMD methodology in motion cueing fidelity assessment applied to helicopter flight simulation.

Reflecting back on the main goal of this dissertation, it can be concluded that a novel and *unifying* tool, the so-called EMD method, has been delivered to *quantify* motion cueing fidelity *from the perspective of the simulated vehicle dynamics*. The method is unifying because, unlike existing tools, it explicitly models the *coupled* dynamics of *both* the vehicle *and* the MCA. Also, the method itself is *task-agnostic*, i.e., it does not require knowledge that pertains to the execution of the task. Nonetheless, many future improvements and extensions to EMD can be suggested. First, an EMD analysis and experimental application to tasks that involves helicopter motion in six degrees-of-freedom would be of interest. This requires the complete formulation of the EMD method as outlined in this thesis. Second, despite the fact that MPFs bridge the gap between the somewhat abstract *modal* domain and the time domain, assigning a relative *importance* to individual modes for EMD-based motion cueing fidelity analyses remains troublesome. Thus, formally exploiting task-specific MPFs as, e.g., weighing factors in EMD-based optimization schemes, could yield improved motion cueing strategies for specific tasks. Third, applications to other helicopter configurations (e.g., tandem-, tilt-rotor, etc.), fixed-wing aircraft and other vehicles of interst in moving-base flight simulation are strongly encouraged. Finally, but certainly not less interesting, is the exension of EMD with models of human operator perception and control behaviour.

SAMENVATTING

De inzet van vliegsimulatoren voor de opleiding en certificering van piloten biedt grote voordelen in termen van kosten en veiligheid. Om uniforme standaarden op het gebied van certificering te kunnen garanderen en om negatieve training van piloten te voorkomen, zijn er formele en gedetailleerde specificaties die betrekking hebben op de benodigde waarheidsgetrouwheid (ofwel *fidelity*) van ieder subsysteem in een vliegsimulator. Deze eisen worden opgesteld en gehandhaafd door de Federal Aviation Authority (FAA) en European Aviation Safety Agency (EASA). Het bewegingssysteem (ofwel het *Motion Cueing System (MCS)*) van een *full-flight simulator* is echter een notoire voorbeeld van een systeem waarin de specificaties tot op heden wat tekort schieten. Het MCS omvat namelijk zowel de *hardware*, meestal een combinatie van actuatoren om de simulator fysiek te kunnen bewegen, als de *software* (ofwel het *Motion Cueing Algorithm (MCA)*). Het MCA manipuleert de gesimuleerde voertuigbewegingen om zo te voorkomen dat fysieke beperkingen van het bewegingsplatform worden overschreden. Dit levert echter ook gesimuleerde bewegingen op die beduidend kunnen afwijken van de werkelijkheid. Bovendien komt deze *mismatch* bovenop reeds bestaande onnauwkeurigheden in het wiskundige model dat wordt gebruikt om de beweging van het voertuig te berekenen. Door deze complexe interactie tussen de verschillende systemen die de uiteindelijke beweging van de simulator bepalen, is het opstellen van *kwantitatieve* specificaties met betrekking tot de toegestane afwijking tussen gesimuleerde beweging en de werkelijkheid in de praktijk lastig gebleken. Tot op heden is de certificering van vliegsimulatoren daarom voornamelijk gebaseerd op *subjectieve* beoordelingen door ervaren piloten. Het doel van dit proefschrift is om een *verenigde methode* te ontwikkelen die in staat is om de waarheidsgetrouwheid van de gesimuleerde beweging (ofwel *motion cueing fidelity*) van helikopters te *kwantificeren*, en om diens geschiktheid te evalueren voor realistische toepassingen.

Voordat een *nieuwe* methode wordt ontwikkeld, is er onderzocht welke bestaande methoden er bestaan voor het meten van de motion cueing fidelity. Hier is een onderscheid gemaakt tussen *kwalitatieve* en *kwantitatieve* methoden. Kwalitatieve methoden worden gekenmerkt door hun afhankelijkheid van de *directe* feedback van mensen die worden blootgesteld aan de gesimuleerde omgeving. Kwantitatieve methoden maken daarentegen gebruik van fysieke metingen en modellen om de motion cueing fidelity te bepalen. Vele methoden in beide categorieën zijn hierbij in beschouwing genomen, waarbij slechts enkele in dit proefschrift zijn geselecteerd voor een uitgebreidere analyse. Met betrekking tot *kwalitatieve* methoden is gekeken naar beoordelingsschalen (ofwel *rating scales*) ten behoeve van de subjectieve evaluatie van de waarheidsgetrouwheid van simulaties. De onderzochte *kwantitatieve* methode is dat van de Objective Motion Cueing Test (OMCT), welke recent is geïntroduceerd in het domein van de vliegtuigsimulatie. De belangrijkste resultaten van deze twee studies zijn samengevat in de volgende twee paragrafen.

Omdat subjectieve metrieken nog altijd de voornaamste manier zijn om vliegsimulatoren te certificeren, wordt een experiment uitgevoerd om de effectiviteit van de meest prominente beoordelingsschalen te bepalen. Het gaat dan om de Simulator Fidelity Rating (SFR) en MFR schalen en diens doeltreffendheid om de waarheidsgetrouwheid van gesimuleerde vliegomgevingen te meten. Hierbij staat de de mogelijkheid van operationele helikoptervliegers om, door middel van deze schalen, veranderingen in het wiskundig vliegmodel dan wel het MCA van elkaar te onderscheiden centraal. De resultaten van deze evaluatie leverden enkele interessante bevindingen op. Zo is er bijvoorbeeld bewijs dat veranderingen in SFR en MFR ratings inconsistent zijn tussen de geëvalueerde experimentele condities. Hoewel vliegers in staat leken om negatieve veranderingen in *zowel* het viegmodel als het MCA als dusdanig te herkennen, bleken veranderingen in *één* van deze twee componenten minder sluitende resultaten op te leveren. Tot slot werd een sterke relatie blootgelegd tussen de taakstrategie die werd toegepast en de hierbij behorende ratings, waarbij een minder agressieve strategie vaker resulteerde in betere ratings. Er zijn aldus vele kanttekeningen te plaatsen bij de toepassing van subjectieve metrieken ter beoordeling van de waarheidsgetrouwheid van gesimuleerde vliegomgevingen. Desalniettemin, om het nut van subjectieve metrieken zoveel mogelijk te vergroten, is het gunstig om veranderingen tijdens evaluaties zoveel mogelijk te beperken tot een enkel subsysteem van de simulator. Daarnaast is het belangrijk om goed te letten op taakprestatie-eisen in relatie tot de toegepaste taakstrategie van piloten als ook limitaties in het vliegmodel en andere simulator(sub)systemen. Deze bevindingen zijn nuttig voor latere bijdragen in dit proefschrift, waar subjectieve metrieken uitgebreid zullen worden toegepast om verschillende *motion cueing* strategieën ten opzichte van elkaar te beoordelen.

Op het gebied van *kwantitatieve* methoden, is de mogelijkheid onderzocht om de OMCT uit het vliegtuigdomein “uit te breiden” naar het helikopterdomein. Zowel computergebaseerde (“paper pilot”) als *pilot-in-the-loop* simulaties zijn uitgevoerd om signalen van door de mens waargenomen grootheden (d.w.z., *specifieke krachten* en *hoeksnelheden*) tijdens typische helikoptermanoeuvres te verkrijgen. Vervolgens zijn spectra in het frequentiedomein berekend op basis van deze tijdsdomeinsignalen en gebruikt om een alternatieve set van OMCT input signalen te definiëren, waarbij alle graden van vrijheid van het MCS *tegelijkertijd* worden aangedreven. Daaropvolgende OMCT analyses op basis van deze alternatieve signalen hebben een aantal interacties in de bewegingssignalen blootgelegd die niet kunnen worden verkregen met de oorsponkelijke OMCT. Zo viel in het bijzonder een sterke interactie op tussen de translationele (*surge*) en rotationele (*pitch*) graden van vrijheid in de simulator. Het is hierbij echter belangrijk om te benadrukken dat de verkregen resultaten specifiek zijn gebonden aan een enkele combinatie van voertuig en taak. D.w.z., een verandering van één van beide heeft tot gevolg dat alle frequentiedomein data moeten worden herzien en dat vandaar ook substantieel andere OMCT resultaten kunnen worden verkregen. Daarbij is het verwerken van voertuig- en taakspecifieke frequentiedomein data een relatief uitvoerig proces dat gevoelig is voor bepaalde bijzonderheden op het gebied van signaalverwerking en, belangrijker nog, variatie tussen piloten. Hoewel de “uitgebreide” OMCT zeker inzichtvol is gebleken, is deze daarom niet verder onderzocht in dit proefschrift. In plaats daarvan is er gezocht naar een beschrijving die *zowel* de voertuig- *als* de MCA-dynamika *expliciet* omvat.

De eerste stap richting de ontwikkeling van deze *nieuwe* methode is de ontwikkeling van een wikundig model om de beweging van een helikopter in zes graden van vrijheid te beschrijven. Dit model, Delft Rotorcraft Simulation (Draftsim), is primair gericht op het uitvoeren van efficiënte (d.w.z. real-time) vliegsimulaties en veelvoorkomende "offline" analyses (bijv. trim en linearisatie). In dit proces zijn verscheidene hulpmiddelen en methoden gebruikt, met een bijzondere nadruk op hetgeen dat betrekking heeft op *Handling Qualities (HQs)*), zoals gedocumenteerd in de Aeronautical Design Standard 33E (ADS-33E). Om het ontwikkelde model te verifiëren zijn eerst trim en dynamische stabiliteitsanalyses toegepast op de Bo-105 helikopter, waarna het model is gebruikt voor een HQs evaluatie van de AH-64 helikopter op de Desorientation Demonstrator Amst (Desdemona) simulator in Soesterberg. In geval van de Bo-105 werd een toereikende "proof-of-match" gevonden in vergelijking met een gelijkwaardig bestaand model, en in geval van de AH-64 een goede mate van realiteit (in termen van HQs) volgens het deskundige oordeel van testvliegers. Bovendien onderschrijven deze analyses de voorspellende kracht van rudimentaire kwantitatieve hulpmiddelen op het gebied van helikoptervliegdynamika. Dit ligt ten grondslag aan de ontwikkeling van een nieuwe methode, die gericht is op de kwantitatieve analyse van de motion cueing fidelity.

Deze methode is gebaseerd op het nieuwe concept van Eigenmode distortion (EMD). In EMD wordt de over het algemeen niet-lineaire dynamika van het MCA gelineariseerd en vervolgens algebraïsch gekoppeld aan een bestaand en ongewijzigd *lineair* model van de helikopterdynamika. Met behulp van deze formulering is het mogelijk om de gekoppelde voertuig- en MCA-dynamika te bestuderen in termen van de zogeheten dynamische voertuig *modi*, en binnen elke individuele mode, ook in termen van door de mens waargenomen grootheden (d.w.z., specifieke krachten en hoeksnelheden). Daarbij is ook de Mode Participation Factor (MPF) geïntroduceerd als hulpmiddel om de bijdrage te meten van iedere mode in een (gemeten) voertuigresponsie. Om de nieuwe methode te illustreren is vervolgens een case studie uitgevoerd. Hieruit bleek dat EMD in staat is om ingewikkelde dynamische interacties tussen voertuigdynamika en het MCA bloot te leggen, welke tot op heden niet konden worden gevangen door bestaande methoden zoals OMCT. Een noemenswaardig voorbeeld hiervan zijn de inherent gekoppelde *pitch-surge* dynamika van helikopters, die sterk worden beïnvloed door de aanwezigheid van het MCA. Deze bevinding is overigens in overeenstemming met resultaten uit de voorgaande 'uitgebreide" OMCT methode. EMD, tezamen met MPFs, vormen hiermee een sterk model-gebaseerd raamwerk voor de kwantitatieve analyse van de motion cueing fidelity, dat bovendien toepasbaar is op een breed scala aan voertuigtypen en taken.

Tot slot heeft dit proefschrift de praktische toepasbaarheid van de nieuwe EMD methode getoetst door middel van een aantal *pilot-in-the-loop* experimenten op de SIMONA Research Simulator (SRS) van de TU Delft en de Desdemona simulator in Soesterberg. In deze experimenten is EMD gebruikt als sturend hulpmiddel voor de selectie van verschillende configuraties van het MCA, toegepast op twee verschillende helikoptertypen, de AH-64 en Bo-105, en drie Mission Task Elements (MTEs): de *precision hover*, *lateral reposition* en de *depart abort*. Deze experimenten hebben waardevolle resultaten opgeleverd over het relatieve belang van bewegingsstimuli die gericht zijn op het weergeven van de verschillende voertuigmodi. In het bijzonder lijken bewegingsstimuli in de rotationele voertuigmodi (d.w.z., de *roll* en *pitch subsidence*) beter gewaardeerd te worden dan bewegingsstimuli die gericht zijn op het weergeven van de klassieke langere-termijn modi (d.w.z., de *phugoide* en de *Dutch roll*). Het tegenovergestelde lijkt echter waar voor dynamischere taken, die gekarakteriseerd worden door snelle en grote verandering in de houding van het voertuig. Een mogelijke uitleg hiervoor in het geval van het experiment op de Desdemona simulator kan worden gevonden in de combinatie van fysieke bewegingsstimuli en een immersief, op Virtual Reality (VR) gebaseerd, visueel systeem. Dit kan mensen er namelijk toe bewegen om het belang van visuele dan wel vestibulaire stimuli te "herwegen". Andere geavanceerdere aspecten, zoals de integratie van hogere orde (rotor)dynamika of stabiliteitsaugmentatie binnen EMD zijn tevens in dit proefschrift opgenomen. Tezamen illustreren deze toepassingen de algemeenheid en veelzijdigheid van de nieuwe EMD methode voor de beoordeling van de motion cueing fidelity toegepast of helikoptervliegsimulatie.

Om terug te komen op het oorspronkelijke doel van dit proefschrift, kan worden geconcludeerd dat er inderdaad een *verenigde* methode is geleverd, namelijk EMD, dat in staat om de motion cueing fidelity te *kwantificeren vanuit het perspectief van de gesimuleerde voertuigdynamika*. De methode is verenigd te noemen, omdat deze in tegenstelling tot bestaande methoden *expliciet* de gekoppelde voertuig- en MCA-dynamika modelleert. Daarnaast is de EMD methode op zichzelf *taak-agnostisch*, d.w.z. dat er voor diens toepassing geen kennis benodigd is die betrekking heeft op de uitvoering van een specifieke taak in de simulator. Desalniettemin zijn er vele mogelijke verbeteringen en uitbreidingen van de EMD methode te bedenken. Ten eerste zou een op EMD gebaseerde analyse en experimentele toepassing voor een taak met beweging in alle zes graden van vrijheid interessant zijn. Hiervoor is de volledige wiskundige formulering van de EMD methode benodigd zoals in dit proefschrift uiteengezet is. Ten tweede kunnen de in dit proefschrift geïntroduceerde MPFs beter worden benut om de kloof tussen het enigszins abstracte *modale* domein en het tijdsdomein te overbuggen. Door bijvoorbeeld op basis van de MPFs een relatieve weegfactor toe te kennen aan de individuele voertuigmodi, kunnen potentieel betere motion cueing strategieën worden verkregen voor specifieke taken. Ten derde worden ook toepassingen op andere helikoptertypen (bijv., tandem- of tilt-rotors), vliegtuigen en andere voertuigen die reeds worden gesimuleerd op bewegende platformen aangemoedigd. Tot slot, maar zeker niet minder interessant, is de uitbreiding van EMD met wiskundige modellen van de menselijke perceptie en stuurgedrag.

NOMENCLATURE

Acronyms

AEE	Allowable Error Envelope
AFCS	Automatic Flight Control System
AHM	Aperiodic Heave Motion
APF	Adaptive Pitch Filter
APM	Aperiodic Pitch Motion
ARM	Aperiodic Roll Motion
CAWA	Coordinated Adaptive Washout Algorithm
CGI	Computer Generated Imaging
CHR	Cooper-Harper HQ Rating
CLS	Control Loading System
CPF	Coordinating Pitch Filter
CWA	Classical Washout Algorithm
DA	Depart/abort
dof	degree-of-freedom
DPF	Direct Pitch Filter
APF	Dutch Roll Motion
Draftsim	Delft Rotorcraft Simulation
Desdemona	Desorientation Demonstrator Amst
DUT	Delft University of Technology
EASA	European Aviation Safety Agency
EMD	Eigenmode distortion
FAA	Federal Aviation Authority
FFS	Full Flight Simulator
FFT	Fast Fourier Transform
FNPT	Flight and Navigation Procedures Trainer
FRF	Frequency Response Function
FSTD	Flight Simulation Training Device
FTD	Flight Training Device
FTR	Force Trim Release
HDU	Helmet Display Unit
HQR	Handling Qualities Rating
HQs	Handling Qualities
HS	Heave subsidence
HT	Hover turn
ICAO	International Civil Aviation Authority
LM^2	Lateral Manoeuvring Motion
LR	Lateral reposition
MCAB	Manual Control Adaptation Boundaries
MCA	Motion Cueing Algorithm
MCS	Motion Cueing System
MFD	Multi-Function Display
MFR	Motion Fidelity Rating
MPC	Model Predictive Control
MPF	Mode Participation Factor

MTE	Mission Task Element
MUAD	Maximum Unnoticeable Added Dynamics
NM	No Motion
NWA	Nonlinear Washout Algorithm
OMCT	Objective Motion Cueing Test
OMCT	Objective Motion Cueing Test
OWA	Optimal Washout Algorithm
PHM	Phugoid Motion
PH	Phugoid or precision hover
PMI	Perceived Motion Incongruence
POS	Project Objective Statement
PS	Pitch subsidence
RMS	Root-Mean-Square
RNLAF	Royal Netherlands Airforce
RPC	Rotorcraft-Pilot Coupling
SAS	Stability Augmentation System
SCAS	Stability and Control Augmentation System
SFR	Simulator Fidelity Rating
SRS	SIMONA Research Simulator
SRS	SIMONA Research Simulator
SWA	Spherical Washout Algorithm
TRC	Translational Rate Command
VMS	Vertical Motion Simulator
VM	Vertical manoeuvre
VR	Virtual Reality
VSI	Vertical Speed Indicator
ZIR	Zero Input Response
ZSR	Zero State Response

Symbols

α	Angle of attack
α_d	Rotor disk angle of attack
$\bar{\square}$	Vector or non-dimensional quantity
$\bar{f}$	Specific force vector
$\bar{G}$	Gravitational acceleration vector
$\bar{g}$	Gravitational acceleration vector
$\bar{u}^{\square}$	Input vector
$\bar{w}_{\square}^{\square}$	Right eigenvector
$\bar{x}^{\square}$	State vector
$\bar{y}^{\square}$	Output vector
β	Blade flap angle and angle of sideslip
δ	Perturbation operator and blade profile drag coefficient
δ_0	Collective deflection
δ_s	Longitudinal cyclic deflection
ϵ	Hub stiffness parameter
γ	Rotor Lock number
γ_s	Built-in rotor shaft tilt
Λ	Diagonal matrix of eigenvalues
λ	Eigenvalue
μ, U_T	(Non-dimensional) velocity tangential to rotor shaft plane
μ_z, U_P	(Non-dimensional) Velocity perpendicular to rotor shaft plane
Ω	Rotor angular velocity
$\omega_{\square}$	Break frequency of filter in subscripted CWA channel
$\Omega_{\times}$	Skew-symmetric rotation operator

ϕ	Vehicle roll angle or
ψ	Vehicle heading angle or blade azimuth
ψ_w	Heading of relative wind w.r.t. rotor
ψ_{mx}	Cyclic phase mixing angle
σ	Rotor solidity
$\square^c$	Quantity in coupled system
$\square^m$	Quantity in motion system
$\square^p$	Quantity in perception state augmented vehicle system
$\square^s$	Quantity inherent to simulator
$\square^{hp}$	Quantity inherent to high-pass filter
$\square^{lp}$	Quantity inherent to low-pass filter
$\square^{x,y,z}$	Quantity along longitudinal, lateral or vertical axis
$\square_e$	Quantity pertaining to equilibrium state
$\square_I$	Inertial frame
$\square_R$	Vehicle body frame
$\square_{1_c}$	Longitudinal disc tilt and lateral cyclic
$\square_{1_s}$	Lateral disc tilt and longitudinal cyclic
$\square_\beta$	Quantities defined in the blade fixed frame
$\square_{\text{cf}}$	Centrifugal force
$\square_{\text{cg}}$	Quantity in vehicle c.g.
$\square_{\text{fs}}$	Quantity pertaining to fuselage
$\square_{\text{ht}}$	Quantity pertaining to horizonal tailplane
$\square_{\text{tr}}$	Quantity pertaining to tail rotor
$\square_{\text{vt}}$	Quantity pertaining to vertical tailplane
$\square_b$	Quantities defined in the vehicle body frame
$\square_h$	Quantities defined in the hub frame
$\square_s$	Quantities defined in the shaft frame
$\square_w$	Quantities defined in relative wind frame
θ	Vehicle pitch or blade pitch angle
θ_0	Blade collective pitch
ζ	Damping ratio of CWA filters
$\{E\}_\square$	Reference frame notation
A	Linearized system matrix
A	System matrix
a	Linear blade lift curve slope
A, B, C	Blade moments of inertia
$a_\square$	Acceleration in subscripted axis
B	Input matrix
B	Linearized input matrix
C	Output matrix
c	Blade chord
$C_\square$	Force or moment coefficient
c_d	Blade local drag coefficient
c_l	Blade local lift coefficient
D	Blade drag
$d\square,\delta\square$	Perturbed quantity
e	Equivalent blade root eccentricity
F	Generic force
$f_\square$	Specific force in subscripted axis
g	Gravitational acceleration

H	Rotor H-force
h_{mr}	Main rotor height above c.g.
$I_{xx}, I_{yy}, I_{zz}, I_{xz}$	Vehicle moments of inertia
K	Correction factor for non-uniform inflow
$K_{\square}$	Gains in the CWA
L	Blade lift
L, M, N	Non-dimensional moment derivatives
M	Generic moment
M_a	Aerodynamic moment about flapping hinge
m_b	Blade mass
p, q, r	Vehicle roll, pitch and yaw angular rates
q	Pitch rate
R	Rotor radius
S	Rotor S-force
T	Rotor thrust force
T_{ab}	Transformation matrix from arbitrary frame b to arbitrary frame a
u	Longitudinal velocity in body frame
u_0	Collective input
u_s	Longitudinal cyclic input
v_0, λ_0	Rotor (non-dimensional) uniform induced velocity
V_∞	Rotor effective airspeed
v_i, λ_i	Rotor (non-dimensional) induced velocity
W	Matrix of right eigenvectors
w	Vertical velocity in body frame
$w_{\square}^{\square}$	Right eigenvector coefficient
x	Non-dimensional distance along blade
X, Y, Z	Non-dimensional force derivatives
x, y, z	Longitudinal, lateral and vertical axes of reference frame
$\square$	Generic symbol placeholder

1

INTRODUCTION

The main objective of this thesis is to advance motion cueing fidelity evaluation in helicopter flight simulation. This requires a comprehensive understanding of problem domains closely related to this objective. Therefore, a literature study was conducted on the state-of-the-art in helicopter dynamics modelling, motion cueing systems and flight simulation fidelity assessment. Based on this study, research opportunities were identified and a research framework was formulated.

The chapter is structured as follows. First, Section 1.1 presents background information regarding the motivation for the research project as well as the stakeholders involved. The literature study is included in Section 1.2. Finally, Section 1.3 presents the proposed research framework and the thesis outline.

1.1. MOTIVATION AND STAKEHOLDERS

Helicopters are used for many applications that require capabilities beyond those offered by regular (fixed-wing) aircraft. Typical examples include medical emergency services, military and law enforcement, offshore oil and gas, as well as transportation in urban environments. The growing usage of helicopters across these sectors, combined with a rising demand from emerging economies around the world, is forecasted to culminate in a growth rate of the global commercial helicopter market of approximately 3.5% during the period 2017-2027 [Anonymous, 2017]. At the same time, key demands in terms of safety and cost effectiveness push Full Flight Simulators (FFSs) (see, e.g., Figure 1.1) to occupy increasingly important roles in helicopter pilot training and certification.

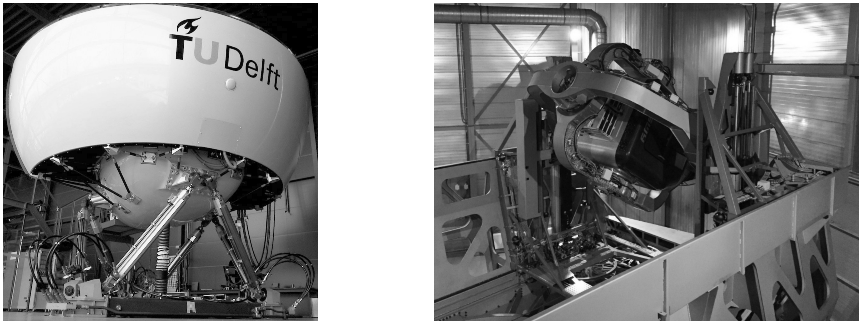

Figure 1.1: Motion platforms studied in present thesis: the SRS (left) and Desdemona (right, courtesy of Desdemona B.V.).

Pilots rely on in-flight cues (e.g., from instruments, outside visuals, haptics, physical motion, etc.) for manual control of their aircraft [Hosman and Stassen, 1998]. FFSs aim to reproduce these cues as accurately as possible by the use of many interacting systems. These include image generators for the out-of-the-window view, detailed cockpit replicas with functional instruments, a flight dynamics model to compute the aircraft's response to pilot control inputs and atmospheric disturbances and robotic mechanisms to reproduce physical motion. For *training* simulators, the required accuracy, or *fidelity*, of each simulator subsystem is regulated. These regulations are formulated by the Federal Aviation Authority (FAA) in the United States [FAA, 2016, App. C] and the European Aviation Safety Agency (EASA) in Europe [EASA, 2012b]. A notable omission from these regulations, however, are comprehensive *quantitative* standards regarding the necessary fidelity of synthetic *motion cues* in relation to those experienced in real flight.

Motion cues in FFSs are provided by the Motion Cueing System (MCS), which simulates a limited portion of the vehicle's physical motion and prevents the simulator from exceeding its mechanical constraints. To this end, the MCS includes a Motion Cueing Algorithm (MCA) to *filter* the vehicle's motion as computed by a *flight dynamics model*. While there is an on-going debate in the flight simulation community regarding the use and necessity of MCSs for pilot training [Burki-Cohen et al., 2000; de Winter et al., 2012], the general consensus seems to be that motion cues contribute to immersion in and acceptance of simulated flight environments [de Winter et al., 2012; Gundry, 1976]. The formulation of quantitative motion fidelity standards and research into improved MCSs therefore remain subjects of great interest in the aeronautical research community. The present thesis aims to contribute to these problem domains in relation to helicopter flight simulation and is the result of a collaboration between TU Delft and Desdemona B.V.

The interest of TU Delft in the research project stems from its recent involvement in the GARTEUR HC/AG-21 action group [GARTEUR HC/AG 21, 2015]. The purpose of this specific action group was to facilitate collaboration between academic institutions and commercial corporations on the topic of rotorcraft simulation fidelity. The section of Control & Simulation has a number of state-of-the-art facilities, including the SIMONA Research Simulator (SRS) [Stroosma et al., 2003] (see Figure 1.1).

Desdemona B.V. is a commercial corporation that operates the Desorientation Demonstrator Amst (Desdemona) simulator, [de Graaf et al., 2002], located in Soesterberg, the Netherlands. Desdemona was manufactured by the Austrian company AMST Systemtechnik GmbH and is a unique moving-base simulator with a large workspace. The simulator is used for a broad range of research and training applications [Desdemona B.V., 2019], including military flight and driving simulation, civil aviation and naval simulation. In the area of (military) helicopter flight simulation, the types of training offered by Desdemona B.V. include landing in degraded visual conditions and flying over treacherous terrains such as mountains. Of main interest to Desdemona B.V. is to determine the appropriate degree of "dynamic detail" required in the various simulator cueing systems, with particular emphasis on the flight dynamics model and the MCS.

The remainder of this chapter is structured as follows. First, a literature study is presented in Section 1.2, based on which a research framework is formulated in Section 1.3. Readers familiar with topics in the areas of helicopter flight dynamics modelling and (motion) simulation may prefer to proceed directly to Section 1.3.

1.2. LITERATURE STUDY

Before formulating the research framework, a literature study was conducted that focused on the state-of-the-art in *helicopter dynamics modelling*, *motion cueing systems and algorithms* as well as *flight simulation fidelity*. These studies are summarized here.

1.2.1. HELICOPTER DYNAMICS MODELLING

An indispensable component in any FFS is the flight dynamics model, which computes the vehicle motion and drives other simulator components (e.g., the outside visuals, instruments and the motion system). The central vehicle of interest in the present work is the helicopter, therefore an in-depth survey on helicopter flight dynamics modelling was performed.

Helicopter flight dynamics is a fundamental subject on which a vast and dedicated body of literature is available, e.g., [Bramwell et al., 2001; Padfield, 2007]. It is evident that helicopter dynamics are complex and can be studied at several levels of physical detail. By far the component that exhibits the most complexity is the main rotor, which provides both the vehicle's lifting and propulsive capability. An overview of the different degrees-of-freedom associated with helicopter modelling, together with common applications, was compiled by Pavel [2001] and is shown in Table 1.1. Modelling complexity is governed by the interaction of two main components in any main rotor model: the *blade dynamics* and the *inflow (aero)dynamics*.

Table 1.1: Different helicopter degrees-of-freedom and known applications [Pavel, 2001].

Model Complexity	6 dof →	8 dof	9 dof	10 dof	12 dof	16 dof
Basic aircraft						
Low frequency maneuver — articulated	■					
Low frequency maneuver — hingeless	◩	◩	◩			
High frequency maneuver — articulated		◩	◩			
High frequency maneuver — hingeless		■	◩	◩		
Helicopter+SCAS system						
Fuselage feedback — articulated	◩	◩				
Fuselage feedback — hingeless	◩	■	◩			
Fuselage / Rotor feedback articulated and hingeless			◩	◩	◩	◩
Full HHQ Basic aircraft						
Within Envelope	◩			◩		◩
At the Boundary				◩		■
Specific HHQ	◩			◩		◩

Legend ■ model used in most of the cases
◩ model used in some cases

Blade dynamics In its most simple form, the rotor blades are generally modelled as rigid and blade motion as *quasi-steady*. The latter entails that the blade's forces, moments and aerodynamics undergo *instantaneous* changes in comparison to the (vehicle) body dynamics. Thus, only the six body degrees-of-freedom are included in the dynamic model. While this is a gross simplification to reality, from Table 1.1 it appears sufficient to capture the main dynamic characteristics of helicopters with articulated rotor systems, constrained to moderately aggressive manoeuvering flight well within the operational flight envelope [Padfield, 2007; Pavel, 2001]. A common first extension to the quasi-steady formulation of blade dynamics is the inclusion of *flapping dynamics*. It has been recognized by Curtiss [1986] that, in particular for helicopters with *hingeless* rotor systems, a so-called *body-flap coupling* is seen to appear. This phenomenon couples the low-frequency (*regressing*) dynamic flap mode of the rotor system to a relatively high-frequency dynamic body mode (*roll subsidence*) producing a new oscillatory mode as a result. For this reason, models concerning (piloted) flight simulation of helicopters with hingeless rotors typically include blade flapping dynamics. However, from Table 1.1 it is also evident that higher dof models tend to be applied more often for applications involving high-frequency manoeuvring flight, extending up to the boundaries of the operational flight envelope. It is indeed known that higher-order blade dynamics, including blade flapping and lagging dynamics, occupy a significant role in the design and validation of high-gain flight control systems commonly applied in helicopters [Chen et al., 1988].

Inflow dynamics A second important aspect pertaining to modelling of helicopter dynamics is the consideration of *inflow* dynamics, which are known to have a strong impact on stability and control characteristics of helicopters [Carpenter and Fridovich, 1953; Chen, 1986; Gaonkar and Peters, 1985; Ormistron, 1976]. It has been shown that natural frequencies associated with inflow dynamics are of the same order of magnitude as those associated with blade flapping dynamics [Curtiss, 1986]. Thus, it is generally accepted that dynamic inflow should be incorporated in applications where flapping dynamics are considered important as well. Over the years, many different models have therefore been formulated to improve understanding of the complex induced flow field surrounding the main rotor [Chen, 1989]. Of these models, the one that has evidently withstood the test of time is the dynamic inflow model developed by Pitt and Peters [Peters and HaQuang, 1988; Pitt and Peters, 1981]. This nonlinear model of the induced velocity field surrounding the main rotor is *phenomenological* at its core, yet still includes sufficient dynamic detail for many practical applications in real-time flight simulation and flight control design [Peters, 2009]. Nonetheless, aeroelastic models aimed at capturing ever higher frequencies associated with main rotor (aero)dynamics are under active development for applications in, e.g., Rotorcraft-Pilot Coupling (RPC) [Pavel et al., 2013a; Serafini et al., 2014] and real-time flight simulation [Bludau et al., 2017; Gori et al., 2015].

1.2.2. MOTION CUEING SYSTEMS AND ALGORITHMS

MCSs are used for the simulation of physical motion cues in FFSs. This section presents an overview of the motion platforms considered in this thesis and reviews the most commonly applied Motion Cueing Algorithms described in the literature.

Motion platforms Human self-motion perception is governed by a number of different sensory *modalities* [Previc and Ercoline, 2004]. These include the *visual* (i.e., brain/visual cortex), the *proprioceptive* (i.e., limb displacement), the *somatosensory* (i.e., skin pressure), the *auditory* (i.e., ears) and, finally, the *vestibular* system, which is sensitive to *specific force* and changes in *angular rate*. Physiological research suggests that the visual and vestibular system are the most dominant [Benson, 1990; Henn et al., 1980].

While visual stimuli can be accurately reproduced in modern simulators and have much improved over the years with advancements in Computer Generated Imaging (CGI) technology, physical motion cues are substantially more problematic [Cyrus, 1977]. To enable the simulation of physical motion cues in FSTDs, *motion platforms* are used. These platforms are available in many forms, but are always constrained in both the *magnitude* and the *duration* of motion cues that can be reproduced before mechanical constraints are exceeded. In the present thesis, two distinct motion platforms are considered, namely the SIMONA Research Simulator at TU Delft and the Desorientation Demonstrator Amst in Soesterberg, the Netherlands. Both platforms bases are depicted in Figure 1.1.

The SRS has a conventional Stewart platform motion base [Stewart, 1965], which comprises a static base that is connected to a movable platform using six linear (hydraulic or electric) actuators. The synergistic extension of these six actuators enables motion in six degree-of-freedom. The main advantages of the Stewart platform is its compact configuration and its ability to accurately reproduce high-frequency acceleration profiles. Due to its compact size, however, its workspace is limited and therefore reproducing sustained, low-frequency, accelerations is significantly impaired.

Desdemona has a more exotic configuration. Here, a cabin is suspended in a three dof gimbal with 360 degrees range of rotation around all axes. The gimballed cabin, in turn, is mounted on a short vertical track to provide a translational degree of freedom. A second translational degree of freedom is provided by a longer, horizontal track. Finally, the horizontal track is connected to a large central pivot with a range of 360 degrees, yielding a total of six degrees-of-freeom of motion. This innovative configuration has a considerably larger workspace than conventional Stewart platform motion bases, as well as the ability to reproduce sustained and large magnitude accelerations.

Motion cueing algorithms To ensure that the motion platform does not exceed its motion limitations, but still provides some sensation of the vehicle motion to pilots, use is made of a Motion Cueing Algorithm (MCA). This algorithm transforms the translational and rotational accelerations calculated from a vehicle dynamics model according to a predefined set of rules. Perhaps the best known and most widely applied MCA is the Classical Washout Algorithm (CWA) [Conrad et al., 1973; Reid and Nahon, 1985, 1986].

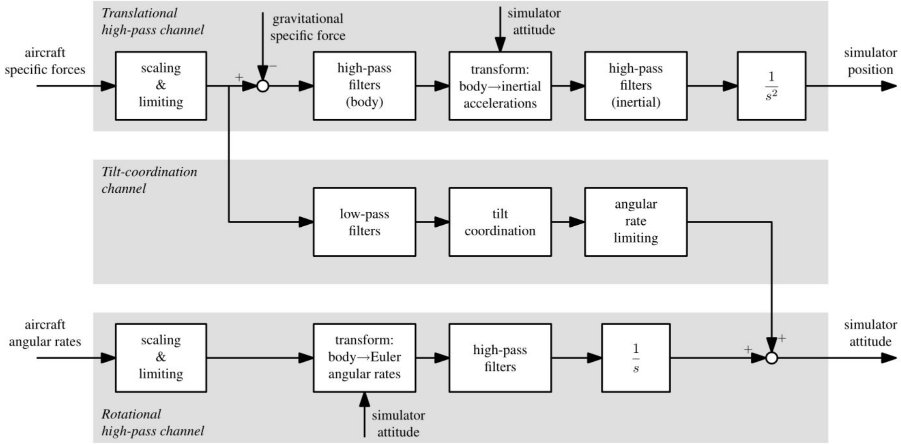

Figure 1.2: The Classical Washout Algorithm developed by Reid and Nahon [1985] (adapted from Pool [2012]).

The CWA, illustrated in Figure 1.2 was developed primarily for conventional Stewart platform motion bases. In order to constrain the motion platform to its motion space, the CWA applies both *scaling* and *filtering*. Here, the magnitude of calculated vehicle accelerations (actually, *specific forces*) is scaled down and low-frequency motion components are filtered out using high-pass filters. These filters also ensure that the platform returns to a neutral point at a rate below the human motion perception threshold. To compensate for the attenuation of low-frequency (sustained) motion components, the CWA also allows for the application of *tilt coordination*. Tilt coordination applies a rotation of the motion platform such that a component of the gravitational force is "aligned" with the vehicle specific force to be reproduced.

The response of the CWA can be controlled separately for each dof of the motion platform using *gains* and *filter break frequencies*. In practice, these parameters are adjusted, or *tuned*, by motion cueing experts on the basis of representative piloted simulator evaluations. The main advantages of the CWA are its relative simplicity, the rather intuitive interpretation of its parameters and the vast amount of experience gathered over the years.

Possible "extensions" to the CWA have also been proposed in the literature [Wu and Cardullo, 1997]. One of such algorithms is the Coordinated Adaptive Washout Algorithm (CAWA), which adaptively updates the CWA parameters to minimize acceleration errors subject to simulator workspace limitations [Parrish et al., 1975]. Other methods, categorized under the Optimal Washout Algorithms (OWAs), include a model of the human vestibular system to minimize perception errors between aircraft and simulator accelerations in the selection of MCA parameters [Reid and Nahon, 1985, 1986; Sivan et al., 1982; Telban and Cardullo, 2005; Wu, 1997]. Piloted simulator evaluations and comparisons of these extended MCAs relative to each other and the CWA have been performed [Telban et al., 2005]. These studies have yielded results, in terms of pilot performance, workload and rating, mildly in favor of the more advanced algorithms. However, a large variability in the subjective pilot ratings gathered was also noted. Reid and Nahon [1986] furthermore concluded that while the CAWA and OWA do seem to offer several key advantages as compared to the CWA, their higher complexity results in more parameters and thus also a less transparant and more involved tuning process. An enhancement to the CWA, namely the Lateral Manoeuvring Motion (LM^2) algorithm, was also proposed by van Biervliet [2008] to more accurately cue the lateral (sway) specific forces at the expense of roll motion cues.

Another recent and promising approach to motion cueing involves the adoption of a Model Predictive Control (MPC)-based strategy for car driving simulation [Augusto and Loureiro, 2009; Baseggio et al., 2011; Beghi et al., 2012; Dagdelen et al., 2004; Venrooij et al., 2015]. The core of this method also comprises a model of the human vestibular system. In the MPC-based approach, however, this model is used to minimize errors between human-perceived motion over a pre-specified prediction horizon and a (known or assumed) reference trajectory. Tuning of the algorithm is accomplished by a proper selection of the prediction horizon and *weighing factors* that act on the individual error terms, MCA inputs and input variations. In addition, the method allows for the implicit incorporation of tilt coordination and motion platform constraints. Beghi et al. [2012] further claim that tuning of the MPC-based MCA is more intuitive than existing methods, as the weighing factors allow for a direct trade-off between workspace exploitation and perceived motion accuracy. Currently, however, MPC-based MCAs have been evaluated primarily using offline computer simulations, which also rely on the availability of future reference trajectories [Augusto and Loureiro, 2009; Dagdelen et al., 2004]. Several studies have also demonstrated the performance of MPC-based MCAs for situations in which a future reference is not available as well as the feasibility of real-time execution [Baseggio et al., 2011; Beghi et al., 2012]. More recently, the merits of an MPC-based MCA were evaluated for application in driving simulation, where it was concluded that "*there exists a potential to further improve the quality of the motion simulation with optimization-based* *methods, deserving future research*" [Cleij et al., 2017a]. However, all studies to date are limited to passive experiments without an active human-in-the-loop element.

The MCAs previously discussed are solutions designed and applied for conventional (Stewart platform based) motion platforms. To exploit the unique capabilities of advanced configurations like the Desdemona simulator, specialized cueing algorithms can also be applied. This was recognized by Wentink et al. [2005], who devised the innovative Spherical Washout Algorithm (SWA) to drive Desdemona. He realized that the motion trajectory of Desdemona is best described using polar coordinates, as opposed to a conventional *Cartesian* reference system in which the CWA operates. The SWA therefore simulates translational vehicle motion by employing arbitrary radials as well as the central and cabin-fixed yaw axes of the simulator. This substantially extends the feasible workspace of the simulator and allows for the cueing of *sustained* accelerations of up to three times the gravitational acceleration [de Graaf et al., 2002]. The downside of the SWA, however, are the centripetal accelerations and *Coriolis effect*-related rotational cues that result from employing circular motion trajectories for simulating rectilinear motion [Bles, 1999].

1.2.3. FLIGHT SIMULATION FIDELITY

Figure 1.3 compares the manual control loop in the real aircraft directly to the situation in a flight simulator. Of central interest in this thesis are the *aircraft dynamics model* and the *Motion Cueing System*, because these elements determine the *motion cueing fidelity* from the perspective of the pilot. The figure demonstrates that *fidelity* in the context of (flight) simulation can be approached from multiple different perspectives.

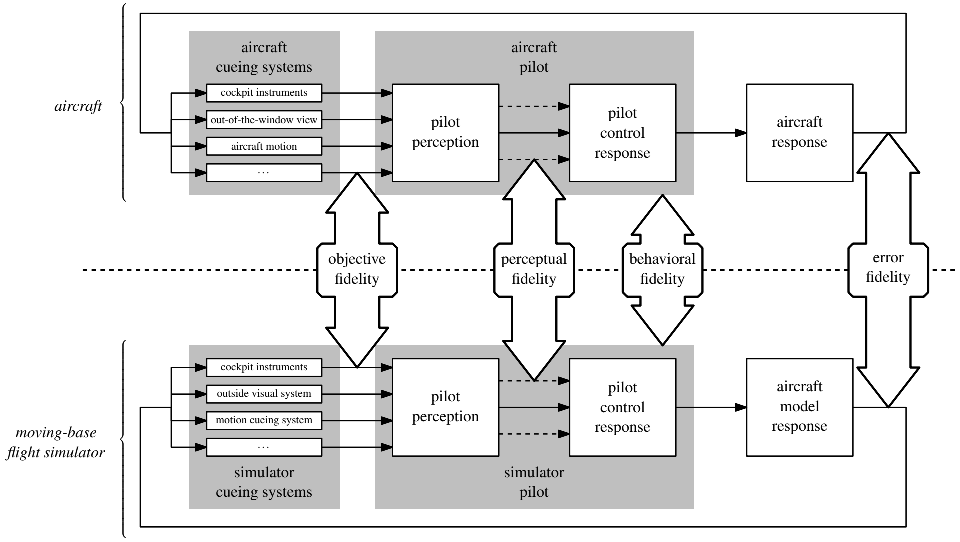

Figure 1.3: Different perspectives on flight simulator fidelity [Pool, 2012].

The extent to which the individual cueing systems of the simulator (e.g., flight dynamics model, visual system, motion system, cockpit layout, etc.) are able to replicate the cues to which human operators are exposed during real flight, is defined as *objective* fidelity. *Error fidelity*, on the other hand, refers to the extent to which equal or similar *task performance* is attainable in the simulator as compared to actual flight [Ashkenas, 1986].

A more human-centered definition of fidelity is *perceptual* fidelity [Rehmann et al., 1995]. Here, the ability of the simulator to match the low-level psychological and physiological processes that occur within the pilot is of primary interest. From the perspective of *training*, it similarly can be argued that the ultimate goal of a flight simulator is to induce human operator control behaviour that is representative of actual flight. This corresponds to the definition of *behavioural* fidelity [Heffley et al., 1981].

An overview of prominent literature according to the adopted definition of simulation fidelity is shown in Table 1.2. The literature is also categorised according to the emphasis on either the flight dynamics model or the MCS or both, when the distinction is not explicit. Many studies combine elements of both perceptual and error fidelity. Therefore, literature in these two categories have been merged in Table 1.2.

Objective fidelity In the current regulatory standards, requirements on simulator cueing systems are stipulated in CFR-Part 60 [FAA, 2016, App. C] and CS-FSTD (H) [EASA, 2012b]. These requirements pertain to the level of detail and accuracy necessary in the replicated cockpit environment and the relevant vehicle subsystems to attain a given fidelity level. A distinction is made between FFSs, Flight Training Devices (FTDs) and Flight and Navigation Procedures Trainers (FNPTs). In the area of FFSs, four levels of simulation fidelity are distinguished: A, B, C and D. Level D is the highest qualification, in principle allowing for zero flight time training (ZFTT) of pilots [EASA, 2012a].

In relation to the fidelity of helicopter dynamics models, developments over the years have culminated in many improvements to rotor (aero)dynamics modelling that are also suitable for (real-time) simulation (see Section 1.2.1). However, determining the *necessary* fidelity of such models in a training simulator is non-trivial [Pavel, 2001]. A sensible approach might be to opt for the most mathematically detailed and tractable models available. However, contemporary FSTDs are naturally limited in reproducing the *synthetic world* perceived by pilots. Thus, adding more detail to the flight dynamics model may not be effective at increasing the *overall* simulation fidelity, if such dynamics cannot be reproduced by other simulator cueing systems. Hence, the statement: "*it is not sufficient to blindly extend a simulation model; one has to identify the right modes to be included in the right situations in order to obtain a good prediction of helicopter behaviour*" by Pavel [2001] applies here. This has also come to light recently when regulatory standards prescribing *error tolerances* with respect to data obtained from in-flight tests were reviewed.

A comprehensive analysis of these criteria in relation to simulation (model) fidelity was performed by Pavel et al. [2013b]. Here, it was shown that due to the nonlinear dynamics and inter-axis coupling inherent in helicopters, compliance with the regulatory standards is not always synonymous with a similarity in vehicle *handling qualities*. To overcome these difficulties, the model is often "tuned", where a distinction is made between *physical* and *artificial* tuning. In physical tuning, the structure and parameters of the model are modified on the basis of physical insights gained from, e.g., flight tests performed in the real aircraft

Table 1.2: Overview of literature according to definition of simulation fidelity and emphasis on aircraft dynamics model, motion or both.

	Objective fidelity	*Perceptual and/or error fidelity*	*Behavioural fidelity*
Model	Section 1.2.1 (this thesis); Pavel [2001]; Pavel et al. [2013b];	Cooper and Harper [1969]; ADS-33E [Anonymous, 2000]; Wood and Hodgkinson [1980]; Tischler [1995]; Mitchell et al. [2006]; Penn [2013]	Damveld [2009]; Yilmaz [2018]; Lu [2018]
Motion	Section 1.2.2 (this thesis); Hosman and Advani [2016]; ICAO 9625 [Anonymous, 2009, II-Att F-1]; Stroosma et al. [2013]; Seehof et al. [2014]; Zaal et al. [2014, 2015b]; Jones [2017a,b]	Sinacori [1977]; Mitchell et al. [1992]; Schroeder [1999]; Schroeder and Grant [2010]; [Gouverneur et al., 2003]; van der Steen [1998]; Grant and Lee [2007]; Valente Pais [2013]; Wentink et al. [2009]; dos Santos Buinhas et al. [2013]; Correia Grácio et al. [2013]; Groen et al. [2001]; Feenstra et al. [2009]; Ellerbroek et al. [2008]; Wiskemann et al. [2014]; Manso et al. [2016]; Reardon and Beard [2015]; Hodge et al. [2015b]; Cleij et al. [2017a,b]	Stapleford et al. [1969]; Levison [1981]; Zaal [2011]; Nieuwenhuizen [2012]; Pool [2012]; Pool et al. [2016]; Zaal and Mobertz [2017]; Zaal and Pool [2014]
Both	CS-FSTD (H) [EASA, 2012b]; CFR-Part 60 [FAA, 2016, App. C]	Padfield et al. [1994]; Li [2016]; Beard et al. [2012, 2013]; Perfect et al. [2014, 2013]	Heffley et al. [1981]; Wiener [1961]; McRuer [1980]; McRuer et al. [1965]; McRuer and Jex [1967]; van der Vaart [1992]; Hosman [1996]; Hess and Malsbury [1991]; Hess and Marchesi [2009]; Steurs et al. [2004]; Mulder et al. [2018]; Padfield [2011]; Padfield and White [2005]

or improved knowledge of fundamental principles. In artificial tuning, modifications to the model are made based on expert judgment. The latter is problematic, however, because the resulting modifications to the model often cannot be justified from a physical perspective [Pavel et al., 2013b].

In relation to MCS fidelity, Section 1.2.1 has reviewed many MCAs aimed at *improving* motion cues in the simulator. However, the regulatory standards only specify robotic constraints and required response times of the MCS, in addition to requirements on the replication of various types of special effects, such as vibrations and buffets. In fact, EASA [2012b] states that these requirements are limited to basic system capability and fail to quantify to what extent the motion cues experienced by pilots in the simulator must represent those experienced in real flight. To date, prescribed practice consequently stipulates that "*until there is an objective procedure for determination of the motion cues necessary [...], motion systems should continue to be tuned subjectively*" [EASA, 2012b, p. 75].

A significant contribution towards a more quantitative approach was initiated over a decade ago by Advani and Hosman [2006a,b]. This approach is based on the measurement of the *linear* frequency response of the integrated MCS. The MCS comprises the MCA, the motion platform hardware in conjunction with all its associated control laws. It therefore provides insight into the amplitude and phase mismatch induced by the complete MCS as a function of motion frequency. After application of the method at independent institutions and subsequent refinement [Advani et al., 2007], the International Civil Aviation Authority (ICAO) adopted the test in its manual of criteria for the qualification of FSTDs in 2009 [Anonymous, 2009, II-Att F-1] as the OMCT. Currently, a preliminary set of criteria based on "industry best practice" is available [Hosman and Advani, 2016], although the validation and refinement of these criteria is an on-going process and is performed in close cooperation with partners from both academia and industry [Jones, 2017a,b; Seehof et al., 2014; Stroosma et al., 2013; Zaal et al., 2014, 2015b].

Perceptual and/or error fidelity It may seem somewhat peculiar to combine two perspectives on simulation fidelity that appear quite distinct. However, many studies use aspects of both error and perceptual fidelity to support research findings. Typically, error fidelity metrics are *quantitative* (e.g., task performance and pilot control inputs), whereas perceptual fidelity metrics are more often *qualitative* (e.g., pilot opinion). Error fidelity metrics are thus often used *in support of* perceptual fidelity metrics.

Useful tools to assess task performance in the context of error fidelity include phase-plane plots and Hooke portraits, which depict a given spatial variable with respect to its first and second order time derivative, respectively. To quantify pilot control strategy, useful metrics are the Root-Mean-Square (RMS) and maximum velocity of the applied control inputs. Such criteria have been used, e.g., in studies to compare pilot strategy in simulation and real flight [Heffley et al., 1981] or as aids in formulating requirements for helicopter flight simulators Schroeder [1999]. Recent studies by Ellerbroek et al. [2008] and Wiskemann et al. [2014] performed similar experiments, where a combination of phase-plane plots, Hooke portraits and pilot control input characteristics were used along with subjective metrics in assessments on the effect of different motion cues. Perfect et al. [2013] proposed an alternative metric that is based on pilot control input characteristics, *control attack*, which is a unified measure of both the speed and magnitude of pilot control inputs.

In the context of perceptual fidelity, pilot/human operator opinion is typically relied upon. However, it is always strived to use a *structured approach* to gather subjective metrics. Perhaps the most famous example of such a subjective metric in the aeronautical domain is the Cooper-Harper Handling Qualities Rating (HQR) scale [Cooper and Harper, 1969], also adopted in the Aeronautical Design Standard (ADS-33E) [Anonymous, 2000] and used in the certification of military rotorcraft. While not directly developed for simulation fidelity assessment, the Cooper-Harper HQ Rating (CHR) scale has been applied, e.g., to assess the effects of simulator motion system properties and time delays on perceived flying qualities Mitchell et al. [1992] or as part of studies on helicopter flight simulator system optimization Beard et al. [2012, 2013]; Reardon and Beard [2015].

Recently, alternative subjective metrics specific to simulation fidelity assessment have been proposed. One example is the SFR scale [Perfect et al., 2014; Timson, 2013], which aims to measure the relative difference in adopted control strategy between real and simulated flight in relation to the task performance attained. The SFR scale was later applied independently by Beard et al. [2013] and Reardon et al. [2014] and appeared consistent to the authors. Another example is the MFR scale [Hodge et al., 2011], which measures *motion cueing* fidelity as the degree to which physical motion cues contribute to an improved task performance in the simulator. The MFR scale was also applied in studies aimed at investigating the performance of two different MCAs for application to a small motion-base flight simulator [Hodge et al., 2015a,b].

Over the years, there have been many attempts to use perceptual fidelity metrics combined with error fidelity metrics, in attempts to formulate re-usable and more *quantitative* criteria on simulation fidelity. A notable example aimed at simulation *model* fidelity is based on the concept of Maximum Unnoticeable Added Dynamics (MUAD) [Tischler, 1995; Wood and Hodgkinson, 1980], where "envelopes" are defined in the frequency domain that correspond to changes in controlled vehicle dynamics, but that are *unnoticeable* by pilots. Later, the concept of MUAD was applied by Mitchell et al. [2006] in relation to a study on pilot sensitivity to variations in vehicle dynamics when performing high-workload manual control tasks. This resulted in the introduction of Allowable Error Envelopes (AEEs), which specify the allowed level of mismatch in the model as a function of frequency and are defined with respect to some baseline aircraft dynamics.

More recent studies on the application of AEE for helicopter model validation in flight simulation were performed by Penn [2013] and Li [2016]. In these studies, several piloted experiments in both fixed- and motion-base flight simulators were conducted in an attempt to establish suitable boundaries for model validity. Efforts have also focused on formulating *motion cueing fidelity* criteria [Schroeder, 1999; Sinacori, 1977]. In these studies, pilot-in-the-loop experiments were performed to define regions of acceptable *gain* and *phase distortion* imposed by the MCS (at a nominal frequency of 1 rad/s). These criteria later resulted in the formulation of several engineering *rules of thumb* [Schroeder and Grant, 2010] to aid in tuning of MCAs and were also extended to include workspace limitations [Gouverneur et al., 2003].

Another notable approach aimed at evaluating perceptual fidelity on a more fundamental level originates from work performed by van der Steen [1998, 2000] and later by Grant and Lee [2007] and Valente Pais [2013]. This work culminated in the so-called *perception coherence zones*, which depict allowable regions of mismatch between perceived visual and motion stimuli in simulated environments. Later, this work was extended by investigating the effects of motion frequency [Wentink et al., 2009], modeling and prediction of coherence zones [dos Santos Buinhas et al., 2013] as well as on the identification of an "optimal" region [Correia Grácio et al., 2013] within coherence zones. A particularly interesting finding in the latter study is that subjects seem to prefer significantly lower than one-to-one amplitude inertial stimuli in the simulator, a result consistent with findings from earlier studies (e.g., [Feenstra et al., 2009; Groen et al., 2001]). Recently, another promising extension to coherence zones by Cleij et al. [2017a,b] was proposed that relies on the notion of Perceived Motion Incongruence (PMI). In contrast to coherence zones, PMI is a *continuous* measure of the mismatch between inertial and visual motion cues. Nonetheless, applications remain mostly limited to a single dof and situations *without* an active human controller in the loop.

Behavioural fidelity Approaching simulation fidelity from a behavioural perspective implies striving for similarity in pilot control *behaviour* beteen the simulator and real flight in a given task and environment [Heffley et al., 1981]. Note that, in contrast to pilot control inputs often used in the context of error fidelity, behaviour is not generally measurable as it depends on many processes that occur (possibly subconciously) *within* the human. This is the subject of the field of *manual control cybernetics*, pioneered by Wiener [1961].

Over the years, many attempts to describe and predict human behaviour in manual control tasks by using control theoretic models have been documented. In aeronautics, the best known example is perhaps the crossover model proposed by McRuer et al. [1965]. The crossover model stipulates that humans adapt their control behaviour in such a way that the *combined* pilot-vehicle system exhibits adequate closed-loop system characteristics in the vicinity of the *crossover frequency*. The crossover frequency, in turn, is selected such to minimize tracking error and determines the *bandwidth* of the pilot-vehicle system. This later led to the development of the precision model to describe the equalization dynamics adopted by humans [McRuer, 1980; McRuer and Jex, 1967]. These models were also extended and applied by Stapleford et al. [1969] and Levison [1981] in studies on the effect of motion cues in manual tracking tasks conducted in a moving-base flight simulator.

More recently, research was initiated to apply the cybernetic approach in the evaluation of simulation fidelity [Steurs et al., 2004]. These efforts culminated in a *multimodal pilot model* that *explicitly* separates the contributions of the different human sensory modalities to the adopted control behaviour [Pool, 2012; Zaal, 2011]. Over the last decade, the multimodal pilot model has been applied extensively in a vast variety of studies to explain manual control behaviour in (combined) tracking and disturbance rejection tasks. Notable and recent examples are Zaal and Mobertz [2017]; Zaal and Pool [2014] and Pool et al. [2016], who studies the transfer of manual control skills between conditions with different motion cues by identifying parameter changes in the multimodal pilot model. A similar approach was adopted by Damveld [2009] and Yilmaz [2018], who studied aircraft and rotorcraft HQs, respectively, using cybernetic models, as well as Lu [2018], who proposed the Manual Control Adaptation Boundaries (MCAB) as a more objective alternative to MUAD envelopes. A comprehensive and detailed review of many other studies is available in [Mulder et al., 2018].

Other authors also contributed models to describe manual control behaviour for simulation fidelity assessment. This includes the well-known *structural model* proposed by

Hess [1990, 1997]. The structural model is based on the same fundamental principles behind McRuer's crossover model, but was developed from a more analytical, rather than experimental, point of view. It is valid for a class of more realistic (e.g., pursuit rather than compensatory tracking) tasks and explicitly models the effects of the human central nervous system, vestibular system and neuromuscular system as well as motion cues on manual control behaviour. It has been applied in several studies on simulation fidelity [Hess and Malsbury, 1991; Hess et al., 1993; Hess and Marchesi, 2009; Timson, 2013].

Difficulties in the application of the structural model, however, stem from the fact that the model parameters must be selected *a-priori* and are difficult to validate using experimental data. Another notable example is the *adaptive pilot model* proposed by Padfield and White [2005]. This model relates the concept of the τ-coupling guidance strategy [Padfield, 2011; Padfield et al., 2003] to changes in parameters of a simple pilot model proposed by [Heffley, 1982]. A comprehensive review of several prominent pilot models was performed by Grant and Schroeder [2010], who conclude that all models can predict pilot behaviour in *well-defined* tasks with reasonable accuracy. However, their application to lesser known problem domains is significantly impaired by the fact that these models rely on prescribed rules in the selection of their parameters. Currently, behavioural pilot models are either profoundly difficult to validate or are mostly limited to simplified tracking and disturbance rejection tasks. Hence, the application of such models for simulation fidelity assessment involving a much broader range of applications requires a more thorough understanding of human perception and adaptive control behaviour (see, e.g., [Mulder et al., 2018; Young, 1969]).

1.3. RESEARCH FRAMEWORK

This section presents the research framework which forms the foundation of this dissertation. First, the state-of-the-art, objective and scope of the project are presented. Subsequently, the research questions are formulated and, finally, the outline of the thesis is given.

1.3.1. STATE-OF-THE-ART, OBJECTIVE AND SCOPE

State-of-the-art The objective of this thesis cannot be formulated in full without consideration of the state-of-the-art of motion cueing fidelity in helicopter flight simulation. From Section 1.2.3, it has become evident that many different approaches to address this problem have been proposed over the years. Perhaps the most significant conclusion that can be drawn from this survey is the lack of generally accepted *quantitative* means to measure simulation fidelity. Indeed, in the rotorcraft domain, existing regulatory standards still require *subjective assessment* by qualified pilots as their most important means of compliance.

There have been many efforts over the years to introduce more quantitative means of fidelity evaluation in this process. The introduction of the Objective Motion Cueing Test (OMCT) in the fixed-wing aircraft domain is a particularly important and promising example. This is because the OMCT has already been adopted in the ICAO Manual of Criteria for fixed-wing aircraft [Anonymous, 2009, II-Att F-1]. However, it was designed for fixed-wing aircraft and therefore may not be directly applicable to rotorcraft. Moreover, it considers the Motion Cueing System (MCS) in isolation and overlooks aircraft- and/or pilot-specific factors. Another promising development, namely that of Maximum Unnoticeable Added Dynamics (MUAD) or Allowable Error Envelopes (AEEs), addresses the problem of aircraft *model* fidelity, but does not explicitly account for the influence of the other simulator cueing systems (e.g., motion). In fact, it appears from Table 1.2 that no efforts have been undertaken yet to study the *combined* effect of the aircraft model and the MCS from the perspective of *objective* fidelity.

The more scientifically rigorous approaches to simulation fidelity are perhaps found in the application of *perceptual* and *behavioural* models of the human controller. The most advanced of these models can account explicitly for the effects of characteristics in *both* the aircraft model *and* the MCS on the perception and action of the human controller. Unfortunately, these models are valid only in strongly simplified tasks involving *tracking* and/or *disturbance rejection* in a limited number of degrees-of-freedom. Similar reservations apply to concepts like the *perception coherence zones* between visual and inertial motion stimuli. While promising, these also have not yet been formalized and have only been validated in conditions where the human controller is *passive*.

In conclusion, it seems *subjective* assessment is to remain the “gold standard” in simulation fidelity assessment for the foreseeable future, possibly supported by structured approaches involving, e.g., the use of the Simulator Fidelity Rating (SFR) and Motion Fidelity Rating (MFR) scales. Until perceptual and behaviour pilot models have matured, quantitative tools such as the OMCT or MUAD/AEEs can play a vital role in formulating accessible and verifiable best practices. Although, for the latter, perhaps a prospective *unifying* tool that captures the combined effect of *both* the flight dynamics model *and* the MCS is more suitable.

Objective Based on the established state-of-the-art and in cooperation with the stakeholders involved in this dissertation, the following objective was formulated:

> *Develop a **unifying tool** to quantify **motion cueing fidelity** in helicopter flight simulation and evaluate its suitability in **realistic** applications.*

A *unifying tool* signifies a methodology that captures both the influence of the flight dynamics model as well as the MCS on motion cueing fidelity. Moreover, the prospective tool should be applicable to real-word (training) scenarios, or common elements thereof, performed in moving-base flight simulators.

Scope From the objective, it is clear that this dissertation approaches motion cueing fidelity from a *quantitative* perspective, aiming to capture the combined effect of the flight dynamics model describing helicopter dynamics and the MCS. This means that the influence of the (many) other simulator cueing systems will not be considered explicitly in this thesis, i.e., they will be used “as is”. The simulators available are the SIMONA Research Simulator (SRS) and the Desorientation Demonstrator Amst (Desdemona), shown in Figure 1.1.

The thesis is concerned with capturing the main dynamic response characteristics of helicopters in *basic manoeuvering flight*. Therefore, in light of the literature reviewed (see Section 1.2.1), it appears sufficient to *initially* limit the level of physical detail inherent in the used helicopter models to the six *rigid-body degrees-of-freedom*, and to consider rotor system dynamics as *quasi-steady*. This is believed to be sufficiently representative for the elementary manoeuvers considered in this thesis. Extensions to this basic model will also be studied briefly in relation to motion cueing fidelity. For the sake of wide applicability, only conventional helicopters, with one main and one tail rotor are considered.

The specific helicopter *types* considered are such to, on the one hand, enable *verification* of the flight dynamics model(s) used and, on the other hand, be able to *evaluate* the prospective tool to be developed in experiments with qualified pilots in realistic manoeuvers. The Messerschmitt-Bölkow-Blohm Bo-105 helicopter is therefore selected because of the accessibility of verification data, while the Boeing AH-64 Apache helicopter is used for the availability of pilots, though limited in quantity, via Desdemona B.V. and the Royal Netherlands Airforce (RNLAF). The choice for the AH-64 also greatly benefits Desdemona B.V. as a stakeholder in this dissertation.

With regard to the MCS, the analysis is limited to the consideration of the Motion Cueing Algorithm (MCA) only. This is because, in modern motion platforms, the effect of motion cueing hardware is negligible in relation to the effect of the MCA [Stroosma et al., 2013]. The analysis is furthermore constrained to the Classical Washout Algorithm (CWA), because it is widely used in industry. While there are many more advanced MCAs (see Section 1.2.2), these provide no substantial advantages to warrant their increased complexity in the domain of helicopter flight simulation.

Finally, in order to allow for the evaluation of the prospective tool in realistic applications, *subjective* metrics are primarily relied upon. These include structured approaches involving, e.g., the Simulator Fidelity Rating (SFR) or Motion Fidelity Rating (MFR) scales. In support of these subjective metrics, use will also be made of more quantitative *error fidelity* metrics, such as task performance. The tasks used in the evaluation are based on the Mission Task Elements (MTEs) documented in ADS-33E [Anonymous, 2000], as they come with clearly defined performance specifications and are likely familiar to pilots.

1.3.2. RESEARCH QUESTIONS

Using the information presented up to this point, the following research questions can be formulated:

① **How to model the interaction between the helicopter dynamics and the MCS?**

This question is about the development of a methodology to describe the interaction between the dynamics of the simulated aircraft and the inherent limitations imposed by the MCS. In order for this methodology to be as general as possible, it is strived for the method to be independent of the specific task or aircraft simulated. To gain insights in how such a method should be applied, a thorough understanding of helicopter and MCS dynamics is required. A substantial portion of this thesis is therefore dedicated to developing this knowledge.

② **What aspects of helicopter dynamics can the MCS feasibly reproduce?**

After having established a means to study the combined effect of the simulated helicopter and MCS dynamics, the next step is to develop knowledge regarding the capabilities of MCSs to feasibly reproduce the helicopter dynamics in the simulator. Insights may furthermore be gained regarding favourable MCA configurations. Thereafter, the flight dynamics model can be extended with more advanced rotor system dynamics. This will lead to an initial understanding of enhanced model fidelity in relation to the capabilities of the MCSs.

③ **What aspects of helicopter dynamics reproduced by the MCS are most valued by pilots?**

At this point, a number of generic guidelines or hypotheses should be available regarding possible variations of parameters in the MCA in relation to aspects of the helicopter dynamics to be simulated. The next step is to validate these guidelines or hypotheses by conducting pilot-in-the-loop experiments in both the SRS and Desdemona for a selected number of realistic flight tasks. A combination of quantitative and qualitative (i.e., subjective) metrics can be employed to evaluate motion cueing fidelity from the perspective of the pilot.

1.3.3. THESIS OUTLINE

Based on the three research questions, a thesis outline can be constructed. This outline is illustrated in Figure 1.4 and shows the contribution of each chapter to the formulated research questions as well as the relation between individual chapters.

In Chapter 2, *subjective* assessment of simulation fidelity in helicopter flight simulation is addressed through a pilot-in-the-loop experiment conducted on the Desdemona simulator. Of specific interest is the sensitivity of SFR and MFR scale ratings when *both* the aircraft model and the MCA are modified. The knowledge gained in this chapter contributes to Research Question ③ and is used in Chapter 6.

Chapter 3 studies the utility of the OMCT for application in the rotorcraft domain. It includes a sensitivity analysis of the test in its current form and proposes helicopter-specific modifications based on both simulated as well as experimental data gathered from a pilot-in-the-loop experiment on the SRS. This chapter contributes to Research Question ① and motivates the existence of Chapter 5.

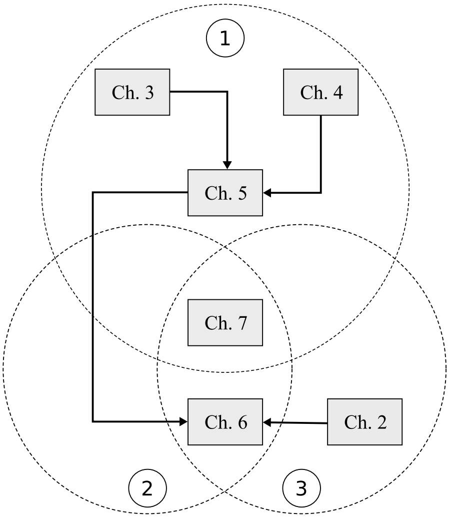

Figure 1.4: Relation between thesis chapters and research questions.

In 4, knowledge on helicopter flight dynamics is refined using a newly developed model named Draftsim. Draftsim is a six-dof nonlinear helicopter model developed specifically for real-time, pilot-in-the-loop, simulation. It is used to conduct an in-depth study on helicopter flight dynamics from a number of different perspectives. This chapter exemplifies the *modal domain* as a novel perspective to study the characteristics of *linear* helicopter dynamics. It thereby strongly relates to Research Question ① and forms the foundation of the contents in Chapter 5.

Chapter 5 presents a new perspective on the motion cueing fidelity problem in helicopter flight simulation by analytically coupling the *linearized* helicopter and MCA dynamics. The application of modal analysis to this coupled system leads to a novel method, named Eigenmode distortion (EMD), capable of quantifying the MCA-induced *distortion* of the vehicle dynamics as perceived by the human controller. It thereby contributes to Research Question ① and is the basis for Chapter 6.

In Chapter 6, the EMD method is evaluated on its utility in the assessment of motion cueing fidelity. To this end, a number of representative pilot-in-the-loop experiments are conducted on both the SRS and Desdemona simulators. The chapter thereby aims to answer Research Questions ② and ③.

Finally, Chapter 7 concludes the dissertation. The main findings are summarized and answers to the three research questions are formulated. It also reflects on the extent to which the *objective* of the dissertation has been attained and presents several opportunities for future research involving Eigenmode distortion.

2

THE USE OF PILOT RATINGS IN HELICOPTER FLIGHT SIMULATION

Many components in a modern full-flight flight simulator interact to produce a realistic flight environment to pilots. Often these interactions, and especially their effect on simulation fidelity from the perspective of the human operator, are poorly understood. As a result, experienced evaluation pilots remain extensively involved in both the development of as well as the acceptance of the flight simulator as a whole. However, the ability of pilots to distinguish between the effects of simultaneous *changes introduced in* different *simulator components during this process remains largely unknown.*

This chapter investigates the effectiveness of state-of-the-art subjective evaluation tools proposed for flight simulation fidelity assessment, when both the Motion Cueing Algorithm and *mathematical vehicle model are varied. The chapter is structured as follows. First, background information on the most prominent subjective fidelity assessment tools is provided in Section 2.1. Then, the design of an experiment performed on the Desorientation Demonstrator Amst (Desdemona) simulator aimed at evaluating the effectiveness of these tools is presented in Section 2.2. The results from this experiment are documented and discussed in Sections 2.3 and 2.4, respectively. The chapter is concluded in Section 2.5.*

The contents of this chapter have been published in: *Miletović, I. et al, The Use of Pilot Ratings in Rotorcraft Flight Simulation Fidelity Assessment, Proceedings of the AHS 73d Annual Forum, Fort Worth (TX), 2017.*

2.1. SUBJECTIVE FIDELITY ASSESSMENT

While there have been studies into objective motion tuning and evaluation methodologies, e.g., [Jones, 2016; Reardon et al., 2014], the general consensus seems to be that subjectively tuned motion is often preferred by pilots. In addition to subjective tuning of the MCA, artificial or *engineering* tuning of the flight model is often also required to match its response to flight test data as demanded by regulations [Pavel et al., 2013b]. In case of rotorcraft, it was shown that this process can produce handling qualities of the flight model that differ significantly from those of the reference aircraft [Pavel et al., 2013b]. With both the mathematical vehicle model and the MCA subject to tuning and having an influence on simulation fidelity, it is of interest to study the relationship between these two components. Their interaction can lead to deficiencies present in either to influence the perceived fidelity of the other [Reardon et al., 2014]. It is therefore important to investigate the sensitivity and effectiveness of state-of-the-art subjective fidelity assessment tools in the presence of such complex interactions.

To support the process of subjective simulation fidelity assessment and enhancement, many *rating scales* have been proposed in the literature over the years. A prominent example is the well-known Cooper-Harper HQ Rating (CHR) scale [Cooper and Harper, 1969]. Drawing from experience in aircraft handling qualities, the application of HQRs for simulation fidelity assessment are actively applied and researched. For example,Mitchell et al. [1992] first applied the well-known Cooper-Harper scale to assess the effects of simulator motion system properties and time delays on perceived rotorcraft flying qualities. Later, HQRs were also used for the assessment of helicopter flight simulation fidelity, e.g., [Schroeder, 1999]. However, it is important to emphasize that the Cooper-Harper HQR scale was not originally intended to be applied for evaluation of flight simulation fidelity. This is because assessing the fidelity of flight simulators is fundamentally different from assessing the performance and HQs of real aircraft. The purpose of flight simulators is to reproduce, as accurately as required and physically possible, the flying characteristics of the modelled aircraft, *including* any specific deficiencies in HQs. That is, while the Cooper-Harper HQR scale provides an *absolute* measure of aircraft HQs, a measure *relative* to the baseline aircraft is actually desired. Simply matching Cooper-Harper HQRs between actual and simulated flight therefore cannot guarantee that simulation fidelity is satisfactory. After all, two different aircraft with similar HQs may still possess distinct dynamic characteristics and may therefore require vastly different control strategies from pilots [Perfect et al., 2014].

To address these issues, the Simulator Fidelity Rating (SFR) scale [Perfect et al., 2014; Timson, 2013] was developed more recently. The SFR scale aims to capture the *relative* difference in adopted control strategy between actual and simulated flight to achieve a prescribed level of desired or adequate task performance (see Figure 2.1). The SFR scale was applied independently by Beard et al. [2013]; Reardon et al. [2014] and although only based on evaluations collected from experiments performed by a relatively small number of test pilots, the scale appeared consistent. Though it can be argued that the SFR scale is an improvement over the CHR scale for flight simulator fidelity assessment, it does lack its well-established level of maturity as well as its level of familiarity and acceptance within the aeronautical community. Also, it lacks a specification of accompanying objective task performance criteria, but instead relies on attained task performance *relative* to the baseline aircraft. Moreover, it remains questionable to what extent pilots are able to recognize and

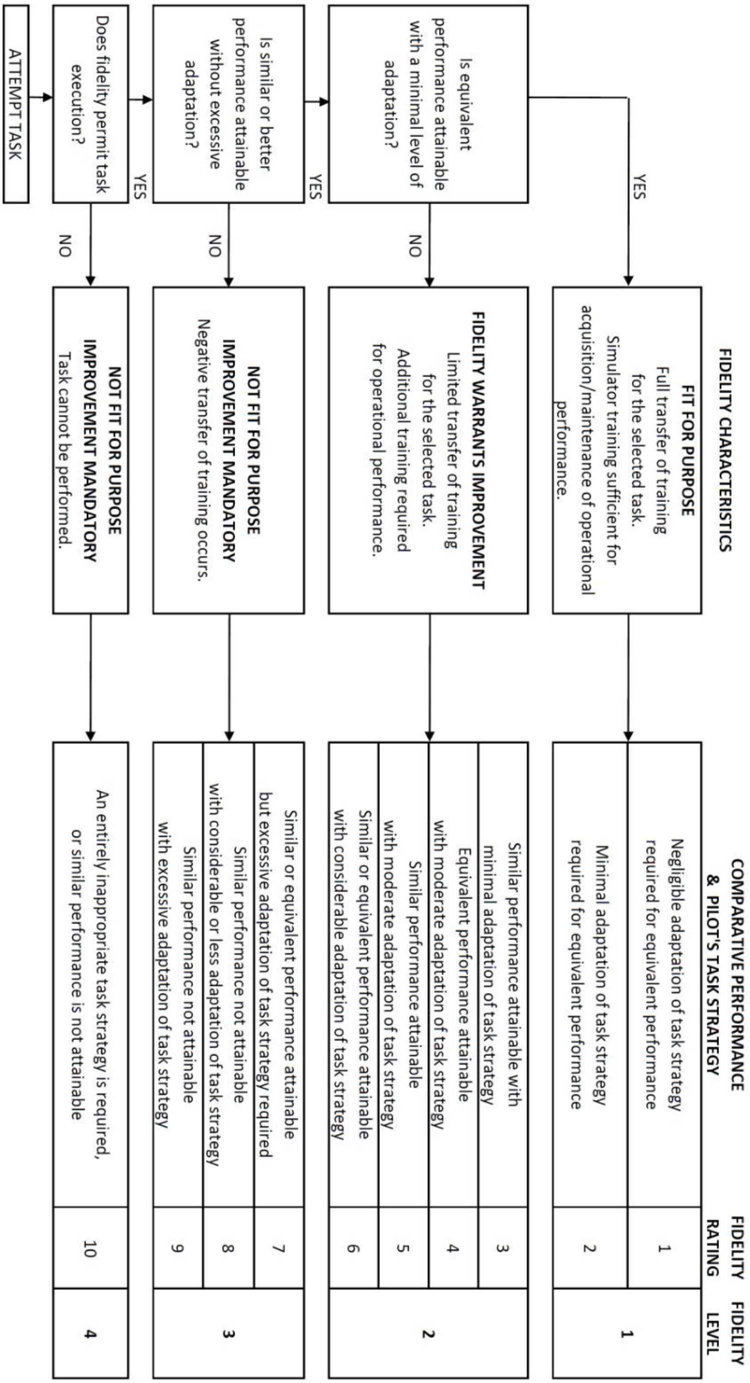

Figure 2.1: SFR scale [Perfect et al., 2014].

quantify required adaptions in their control strategy with respect to an established baseline vehicle. Recommended means to enhance the applicability of the SFR scale in capturing simulator fidelity include minimizing the timespan between experiment trials in the actual aircraft and in the simulator as well as using highly experienced pilots for the specific type of aircraft simulated [Perfect et al., 2014].

A rating scale that is closely related to the SFR scale is the MFR scale [Hodge et al., 2015a], shown in Figure 2.2. It was proposed as an alternative to the more crude MFR scale developed and applied by Sinacori [1977] and Schroeder [1999]. It bears more resemblance to the CHR and SFR scales. Like the SFR scale, the MFR scale asks pilots to quantify fidelity, in this case *specifically* motion fidelity, with respect to the actual aircraft. Pilots are furthermore expected to express to what extent the available motion cues contribute towards attaining the specified task performance and can highlight specific deficiencies using the letter abbreviations as shown in the lower part of Figure 2.2. The MFR scale was successfully applied in conjunction with the CHR scale to quantify pilot opinion in recent studies [Hodge et al., 2015a,b]. In these studies, the performance of two different MCAs for application to a small motion-base flight simulator in a low-speed helicopter flying task were investigated. Two test pilots provided MFR scale ratings that appeared to be in good agreement.

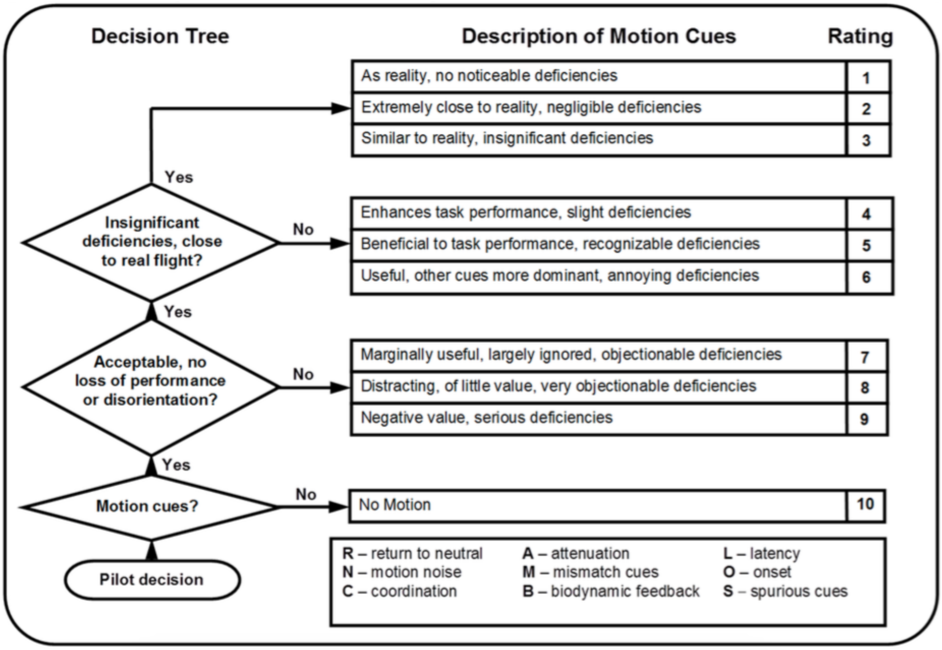

Figure 2.2: MFR scale [Hodge et al., 2015a].

As stated in the first paragraph of this section, however, the question remains to what extent regular operational pilots are able to differentiate between the influence on perceived fidelity of core components of the simulated environment based on such rating scales. For one, while the SFR and MFR scales were developed primarily for application with expert pilots, a sufficiently large sample size of such pilots may not always be available for simulation fidelity assessment studies. Also, while recent studies have shown that various crucial elements in the simulated flight environment have significant effects on task performance, control activity and perceived fidelity in terms of awarded fidelity ratings (e.g, [Hodge et al., 2015a; Nieuwenhuizen et al., 2009; Reardon et al., 2014; Wiskemann et al., 2014]), a poorly addressed issue is the ability of pilots to distinguish between the relative contributions of each of these elements. For example, Reardon et al. [2014] provides some anecdotal evidence that pilots may confuse deficiencies in motion cues with degraded rotorcraft HQs. Figure 2.3 depicts this problem from the point of the pilot. In this figure, the pilot is assumed to perform an arbitrary manual control task in a simulator. It becomes evident that the *equivalent system* perceived by the pilot is the aggregate of the helicopter model *and* the MCA. After all, motion cues from the helicopter model cannot be directly represented by the simulator due to physical constraints. Hence, pilots must rely on the *actual motion feedback* provided by the simulator.

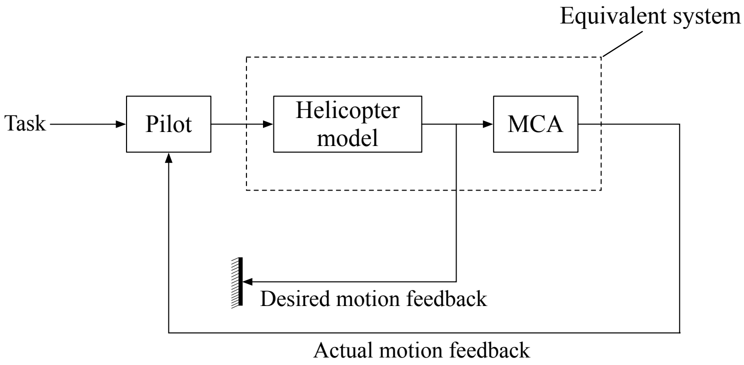

Figure 2.3: Schematic of a manual control task in a motion simulator.

In subjective tuning and assessment of simulator motion and/or the flight model, situations could therefore arise where perceived issues in either of the two components is addressed in the other and vice-versa. This, in turn, could cause actual deficiencies in one subsystem to be masked, or worse, aggravated by the changes inadvertently applied in another subsystem. To investigate this issue, a pilot-in-the-loop experiment on the Desorientation Demonstrator Amst (Desdemona) simulator in Soesterberg, The Netherlands, was performed. The next section discusses the experiment design.

2.2. RATING SCALE EVALUATION EXPERIMENT

The primary purpose of the experiment proposed in this chapter is the assessment of two subjective fidelity assessment tools, namely the SFR and MFR scales, as suitable indicators of simulation fidelity. To this end, two core components of the simulated environment are varied in the proposed experiment, namely the *rotorcraft model* and *Motion Cueing Algorithm (MCA)*.

To gain more insight in the use of rating scales to assess flight simulation fidelity assessment in the presence of varying combinations of rotorcraft dynamics and motion, an experiment with a design as outlined in Table 2.1 was conducted. In the experiment, operational helicopter pilots were asked to perform a task in a simulated flight environment with physical motion. The task, the simulator platform and the pilot population were kept constant throughout the experiment.

Table 2.1: Independent, dependent and controlled experimental variables.

Independent variables	*Dependent measures*	*Controlled variables*
Rotorcraft dynamics	Pilot rating	Simulator platform
MCA configuration	Task performance	Flight task
Rating scale		Pilot population

Three different experimental variables were varied in the experiment: the rotorcraft dynamics (i.e., the flight model), the MCA configuration and, finally, the rating scale used. This design differs from that of previous experiments, where the *type* of rating scale(s) used is most commonly kept constant. In the proposed experiment, the rating scale used is also varied in a *within-subjects* fashion. The following sections elaborate on the experiment design details.

2.2.1. CONTROLLED VARIABLES

Apparatus The experiment was conducted on the Desdemona simulator (see Figure 2.4) located in Soesterberg, the Netherlands [de Graaf et al., 2002]. The simulator comprises a cabin that is suspended in a three dof gimbal with a continuous range of motion around all axes. The gimballed cabin, in turn, is mounted on a short vertical track to provide a translational degree of freedom, 1.5 meters in length. A second translational degree of freedom is provided by a longer horizontal track, 8 meters in length. Finally the horizontal track is connected to a large central pivot in order to provide an additional centrifugal dof with a continuous range of motion. This yields a total of six dof of motion. This innovative configuration has a considerably larger workspace than conventional Stewart platform motion bases and can reproduce sustained and large magnitude accelerations of up to three times the gravitational acceleration in centrifuge mode.

Pilot population The four pilots that participated in the experiment were operational AH–64 Apache pilots from the RNLAF and the US Army who had received prior training in the Desdemona simulator. None of the participating pilots had any prior experience with flight testing or the use of rating scales in an experimental setting. One of the participating pilots is an AH–64 flight instructor in the RNLAF.

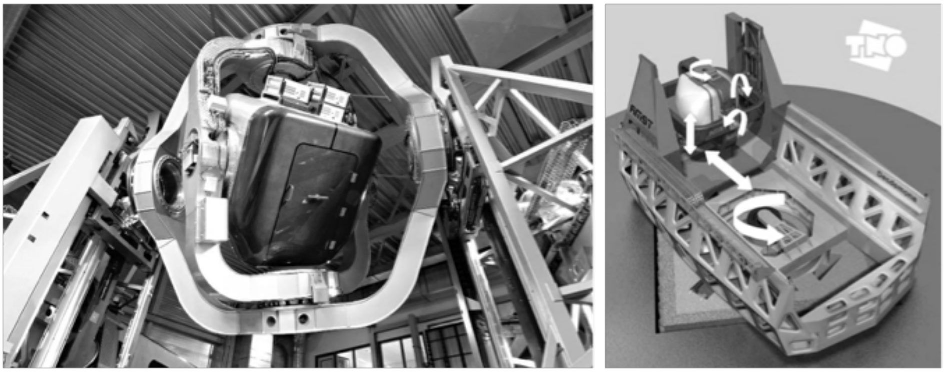

Figure 2.4: The Desdemona simulator at TNO/Desdemona B.V. in Soesterberg, The Netherlands [de Graaf et al., 2002].

Flight task The flight task considered in this experiment is a lateral reposition maneuver over a distance of 400 ft, with corresponding task performance specifications as stipulated in ADS–33E [Anonymous, 2000]:

> "Start in a stabilized hover at 35 ft wheel height (or no greater than 35 ft external load height) with the longitudinal axis of the rotorcraft oriented 90 degrees to a reference line marked on the ground. Initiate a lateral acceleration to approximately 35 knots groundspeed followed by a deceleration to laterally reposition the rotorcraft in a stabilized hover 400 ft down the course within a specified time [*18s desired, 22s adequate*]. The acceleration and deceleration phases shall be accomplished as single smooth maneuvers. The rotorcraft must be brought to within ±10 ft of the endpoint during the deceleration, terminating in a stable hover within this band. Overshooting is permitted during the deceleration, but will show up as a time penalty when the pilot moves back within ±10 ft of the endpoint. The maneuver is complete when a stabilized hover is achieved."

The selected task is also similar to those used in recent studies [Hodge et al., 2015b; Nieuwenhuizen et al., 2009; Wiskemann et al., 2014]. In the current work, however, the lateral reposition was preferred over the more aggressive sidestep maneuver. This is because it was expected that the participating pilots would have more exposure to basic maneuvers performed with moderate levels of agility. Moreover, it was anticipated that a maneuver with a less demanding level of agility would be more suitable in combination with the *linear* rotorcraft model used. Figure 2.5 shows an impression of the task setup in the visual environment of Desdemona.

Figure 2.5: Overview of lateral reposition task in Desdemona.

2.2.2. INDEPENDENT VARIABLES

Rotorcraft dynamics In the current experiment, a simplified lateral position control task is performed. For the controlled dynamics, the altitude, pitch and heading were fixed, so the only dofs controlled by pilots were roll and, consequently, sway. The roll-sway dynamics of rotorcraft in this case can be approximated by a linear function of roll damping and control power [Nieuwenhuizen et al., 2009; Padfield, 2007]:

$$\begin{aligned} \ddot{\phi} &= L_p\, p + L_\delta\, \delta \\ \ddot{y} &= g\, \phi + Y_v\, v \end{aligned} \tag{2.1}$$

The roll damping L_p is a measure of the tendency of the rotorcraft to counteract a rolling moment, while the control power L_δ determines the instantaneous angular acceleration for a given lateral cyclic input. The smaller the absolute value of L_p and the larger L_δ, the more agile the rotorcraft's roll response for a given control input. Consequently, these parameters fully characterize the roll dynamics and their direct manipulation can therefore be used to artificially degrade HQs. A similar model was also used in recent experiments, e.g., [Hodge et al., 2015b; Nieuwenhuizen et al., 2009; Wiskemann et al., 2014]. In contrast to these previous experiments, however, the effect of lateral drag (through Y_v) is included here. This was done after preliminary evaluations with pilots, in which it became apparent that the task could otherwise not be completed with adequate performance.

The primary reason for selecting this simple model is that its fidelity is considered sufficient for the purposes of the current experiment, where only *relative* changes in the fidelity of the overall simulated flight is of lesser importance in this case, as long as it is representative for both environment are of interest. The *absolute* fidelity of the baseline model the task and the pilot population of interest. The stability derivatives L_p and Y_v that appear in Equation (2.1) were chosen such to represent the AH–64 and originate from flight test data as documented in Hossein Mansur [1995]. The values for these parameters are -1.828 s^{-1} and -0.2788 s^{-1}, respectively. The control power L_δ was also determined from preliminary pilot evaluations and was assigned a value of 1.5 s^{-2}. Rotorcraft dynamics were varied by diminishing the roll subsidence L_p, thereby enabling greater agility in roll at the cost of degraded handling qualities. Two conditions were selected, one with the original value for L_p (-1.828 s^{-1}) and one in which the magnitude of L_p was reduced by half to a value of –0.914 s^{-1}.

MCA configuration The motion system kinematics of the Desdemona simulator allow for various potential motion cueing strategies in support of the lateral reposition maneuvre considered in the current experiment [Wentink et al., 2005]. However, it was chosen to simplify the motion cueing strategy applied significantly by only presenting motion in roll. The reason for this is twofold. First, for the purpose of the current experiment, it is sufficient to offer two conditions of motion that, *objectively*, are significantly different in terms of their fidelity level. By presenting a motion condition with relatively good fidelity roll motion and one in which the roll motion fidelity is significantly degraded, this premise is already satisfied. Even though the simulator allows for both motion conditions to be extended with sway, this would introduce complexities that are deemed unnecessary for the objective of the current experiment. Moreover, recent research has demonstrated a strong tendency for roll to dominate perceived fidelity in lateral helicopter maneuvering [Hodge et al., 2015a; Wiskemann et al., 2014]. This is true especially for large phase distortions induced in the roll channel.

For the current experiment, two motion conditions similar to those evaluated in [Wiskemann et al., 2014] will be considered. The roll angle, for both cases, will therefore be filtered using a washout filter of second-order:

$$H_\phi(s) = K_\phi \frac{s^2}{s^2 + 2\,\zeta\,\omega_\phi + \omega_\phi^2} \tag{2.2}$$

The two MCA configurations used differ mainly in the amount of phase distortion incurred by the washout filter. The break-frequency ω_ϕ of the baseline configuration was chosen such to incur a phase lead of 30 degrees ($\omega_\phi = 0.36$ rad/s) at 1 rad/s, while the break-frequency for the second configuration was increased such to incur 60 degrees ($\omega_\phi = 0.67$ rad/s) of phase lead. This is similar to the conditions investigated in [Wiskemann et al., 2014]. The scaling gain K_ϕ of both filters was chosen sub-unity, with a value of 0.6 for the baseline configuration and a value of 0.9 for the degraded configuration. The higher gain for the degraded configuration was chosen such to compensate for the larger attenuation at lower frequencies.

Finally, note that the degraded configuration, with a stronger washout effect (i.e., larger phase lead at 1 rad/s), also has an advantage over the baseline configuration used. Namely, the gravity-induced false specific force cues, due to cabin roll in the absence of lateral cabin motion (i.e., sway), are *lower* in the degraded configuration. However, as stated in the previous paragraphs, it is assumed that the degree of phase distortion in roll dominates the perceived motion fidelity.

2.2.3. DEPENDENT MEASURES

As mentioned in Section 2.2.2, the type of rating scale used is treated as an independent experimental variable. This means that any variation in the type of rating scale used constitutes a separate experimental condition. The foreseen advantage of treating the rating scale as such is that this prevents pilots from consciously, or subconsciously, striving for consistency in awarded ratings from the two scales for each presented combination of rotorcraft dynamics and MCA configuration. In this experiment, two rating scales were used: the SFR scale (see Figure 2.1) and the MFR scale (see Figure 2.2). The ratings awarded by the participating pilots using these scales constitute the primary dependent measure collected during the experiment. Given that task performance, here in the form of maneuver execution time, is also a determining factor in both of the rating scales used, measured task performance was also recorded as a dependent measure.

2.2.4. EXECUTION

With two configurations of rotorcraft dynamics, two MCA configurations and two rating scales, the total number of experimental conditions equals eight. The eight conditions were distributed over the four pilots according to a Latin square design (see Table 2.2). In the table, the conditions are designated by a letter ('b' for baseline or 'd' for degraded) signifying the rotorcraft dynamics, followed by a number (30 or 60) signifying the motion filter used and, finally, another letter ('s' for SFR or 'm' for MFR) signifying the rating scale used.

Table 2.2: Division of experimental conditions over the four subjects.

Pilot	Conditions							
1	b30s	d60m	d30s	d30m	b30m	d60s	b60s	b60m
2	b60m	b60s	d60m	b30s	d30s	b30m	d30m	d60s
3	d60s	d30m	b60s	b60m	d60m	d30s	b30s	b30m
4	d30m	d30s	b30m	b60s	d60s	b60m	d60m	b30s

Prior to the start of the experiment, the pilots were briefed and were given the opportunity to familiarize themselves with the rotorcraft dynamics and task. In the briefing, pilots were introduced to the two rating scales used in the experiment as follows:

> "For the SFR scale, the possible ratings pertain to the attained task performance and the control strategy that was applied. The less these differ from the attainable performance and control strategy in the actual aircraft, the better (that is, *lower*) should be the awarded rating. For the MFR scale the same applies, however, here the possible ratings pertain to the extent to which motion has contributed to attaining the specified performance requirements. The MFR scale also includes indicators that allow you to communicate several specific motion cueing deficiencies you may have perceived. You are encouraged to make use of these indicators, although it is not explicitly required from you in the experiment."

In addition to the briefing, the pilots were also given the opportunity to familiarize themselves with the specific terminology used in the rating scales prior to the start of the experiment. Other than these minor guidelines, pilots were granted the freedom to interpret the rating scales in any way they deemed appropriate. With regard to task execution, pilots were instructed to perform the maneuver in one fluent motion and to strive for optimal task performance in every trial.

During familiarization, pilots were allowed to perform trial runs of the task only with the *baseline* configuration. This was done so as to minimize the risk that pilots would learn about the specific changes to be introduced in the simulated environment prior to the actual experiment (e.g., by means of "probing"). This could inadvertently influence the awarded pilot ratings. The trial runs were repeated until the subject attained at least adequate task performance, for at least two or three times, and the subject felt confident that adequate performance could be maintained.

In the actual experiment, pilots were given the opportunity to repeat the maneuver three consecutive times for each experimental condition before being asked to award a rating according to the specified rating scale. This was done so as to limit within-subject variability. The pilots were told which rating scale to use *after* completion of the task. In case of doubt, inability, or other extraordinary discrepancies noticed during the first three runs, pilots were allowed to repeat the maneuver more often. On average, pilots required four repetitions of the task before a rating could be formulated. Task performance (i.e., maneuver execution time) was measured manually using a stopwatch. Any further comments provided by pilots during the experiment were recorded.

2.2.5. HYPOTHESES

The current experiment was performed so that a better judgment can be formed regarding the use of subjective fidelity metrics as part of flight simulation fidelity assessment studies. Specifically, the central premise that was tested is the ability of pilots to distinguish degradation of motion fidelity from degradation of rotorcraft HQs. Therefore, it is of interest to establish the extent to which SFR and MFR ratings vary with different combinations of rotorcraft dynamics and the MCA. Ideally, pilots are able to distinguish between the influence of both subsystems based on ratings awarded from the SFR and MFR scales. Therefore, the following hypotheses can be formulated:

1. **SFR and MFR ratings will degrade as *both* motion cueing fidelity and rotorcraft HQs are degraded from the baseline condition.** Degraded motion cueing fidelity and rotorcraft HQs are assumed to have a degrading effect on perceived fidelity when compared to the baseline condition. SFR scale ratings are expected to diminish as a result of increased pilot workload, following a degradation of task performance and an expected adaptation of the task strategy. MFR ratings will diminish because the degraded motion cues are expected to no longer contribute to enhanced task performance.

2. **Degraded rotorcraft HQs combined with baseline motion cueing fidelity will *only* result in improved MFR ratings as compared to a condition with *both* degraded rotorcraft HQs and motion cueing fidelity.** Degrading only rotorcraft HQs, while not degrading motion cueing fidelity, is expected to result in a degradation of SFR scale ratings. Degraded rotorcraft HQs are expected to result in a significant control strategy adaptation when compared to the baseline condition. The baseline MCA configuration may still contribute to enhanced task performance. In this case, motion may still help the pilot to generate sufficient lead [Wiskemann et al., 2014]. Hence, this hypothesis effectively stipulates that the MFR scale is not sensitive to changes

in rotorcraft model fidelity and therefore enables pilots to reliably express problems with motion cueing fidelity.

3. **Degraded motion cueing fidelity combined with baseline rotorcraft dynamics will *only* result in improved SFR ratings as compared to a condition with *both* degraded rotorcraft HQs and motion cueing fidelity.** Similar to the condition with both degraded rotorcraft HQs and motion, degrading only motion cueing fidelity is expected to result in diminished MFR scale ratings. In both conditions, motion is not expected to contribute to enhanced task performance.

   In this condition, it is hypothesized that pilots will attempt to actively ignore motion cues and rely mostly on the available visual cues to optimize task performance. This strategy results in a larger effective time delay of the pilot and therefore in a lower task performance and/or adaptation of the task strategy. Consequently, SFR scale ratings are also expected to diminish but, since motion is the dominant deficiency in this condition, not as strongly as for the condition with both degraded motion cueing fidelity *and* degraded rotorcraft HQs.

2.3. EXPERIMENT RESULTS

As explained in the previous section, the primary dependent measures of the experiment are pilot ratings and task performance. To aid in the assessment of the latter, manoeuvre phase portraits showing the vehicle lateral velocity as a function of distance travelled are used. The manoeuvre phase portraits provide valuable insight of the applied task strategy and are therefore presented and discussed first in Section 2.3.1. Pilot ratings and task performance measures in the form of manoeuvre completion times are subsequently covered in Section 2.3.2. Finally, a brief discussion of the pilot comments given in support of the awarded pilot ratings is given in Section 2.3.3.

2.3.1. MANEUVER PHASE PORTRAITS

The primary experiment results collected are pilot ratings and measured task performance. However, during the experiment, pilot control inputs and rotorcraft states were recorded as well. Based on the latter, so-called phase portraits [Wiskemann et al., 2014] of the task executed by the pilots were constructed. Phase portraits depict the rotorcraft speed as a function of travelled distance and provide an indication of the amount of variability in applied task strategy between subjects and experimental conditions. Figure 2.6 shows such phase portraits for the trial numbers associated with the *best* attained task performances per subject and condition. The trial numbers and the associated task performances are selected as a reference because they are assumed to be the most dominant criterium upon which pilots base the awarded ratings for a given condition. The vertical lines shown in the figure designate the target region.

Several observations can be made from Figure 2.6. It can be seen that most subjects adopted notably different task strategies across the experimental conditions presented. Subject 4 seemed to adopt the least aggressive strategy of all participants, while the phase portraits of this subject also show the least variation over experimental conditions. Conversely, the other subjects appear to adopt a more aggressive strategy and also exhibit more variation in the resulting phase portraits. More variability in the task trajectories between experimental conditions and subjects also means that excitation levels of the rotorcraft dynamics and, consequently, motion will strongly vary between subjects and conditions. These differences can have a strong effect on awarded pilot ratings. In the following sections, the experimental results in terms of pilot ratings and task performance are presented. In addition, a detailed review of the most important pilot comments will be given.

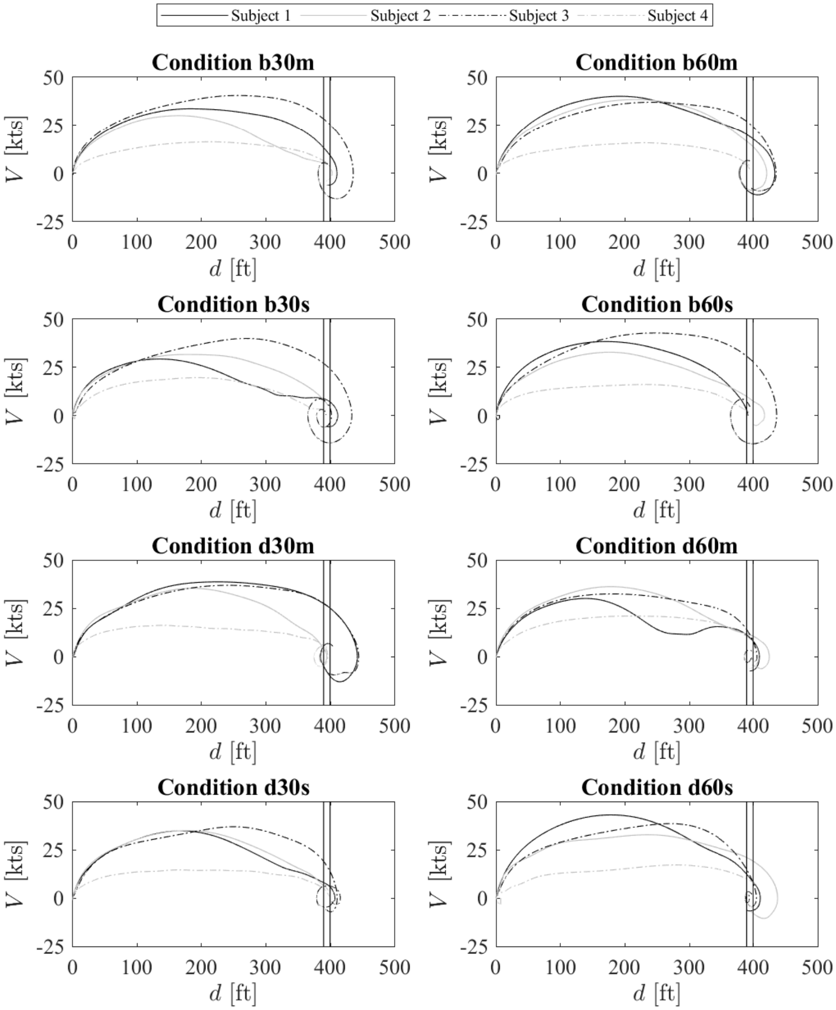

Figure 2.6: Phase portraits for each experimental condition and subject.

2.3.2. Ratings and task performance

The awarded pilot ratings, together with the corresponding task performances attained, are shown in Figure 2.7 and Figure 2.8 for the SFR and MFR scales, respectively. Note that, as explained previously, only *best* attained task performances are considered. Both individual results for each subject as well as the overall trends (using the *median* ratings) and spread calculated from the results corresponding to the first three subjects are shown. The results corresponding to Subject 4 were not taken into account in the overall trends and spread of the results because of the strongly differing task strategy applied by this subject. Several interesting remarks about the results can be made.

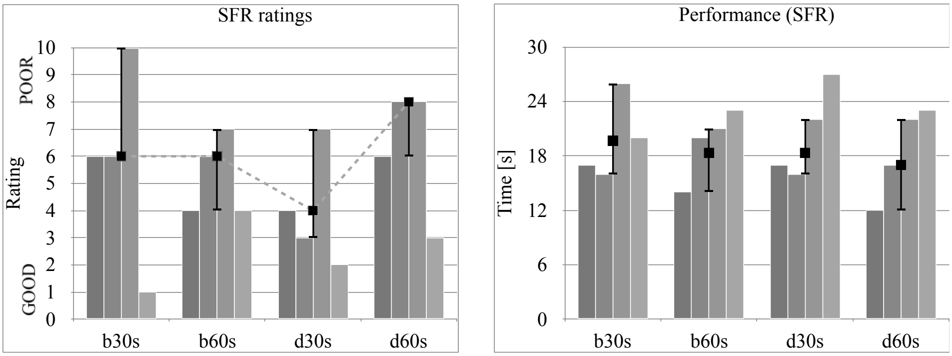

Figure 2.7: SFR ratings (left) and corresponding task performances (right).

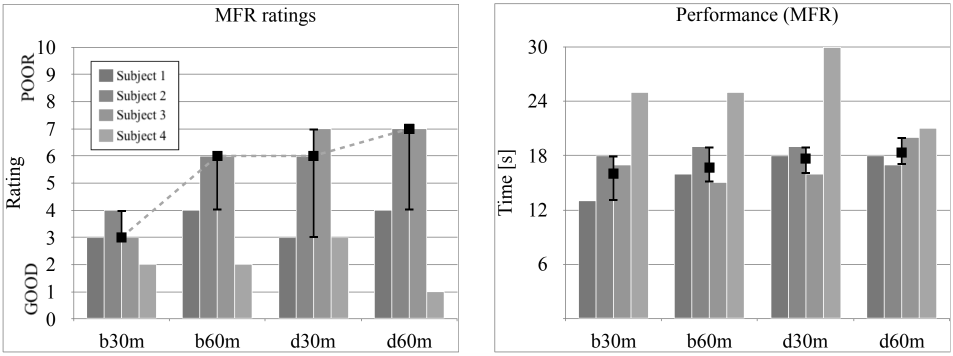

Figure 2.8: MFR ratings (left) and corresponding task performances (right).

First, it can be seen that the overall SFR and MFR ratings awarded for the condition with baseline dynamics and with a motion filter that incurred the least amount of phase distortion (b30) are very different. The same is true for the condition with *only* degraded rotorcraft dynamics (d30). Also, while subjects evidently disliked the condition with *both* degraded dynamics and motion most (d60), degrading *either* dynamics (b→d) or motion (30→60) produced less consistent results. Subjects favoured the condition with only degraded dynamics according to the SFR scale, while according to the MFR scale, the baseline condition (b30) is preferred. This shows the apparent difficulty in separating the influence of rotorcraft dynamics and MCA configuration on perceived motion fidelity.

Another interesting observation can be made regarding the relation between awarded ratings and adopted task strategy. Figure 2.6 showed that Subject 4 adopted a relatively low-gain task strategy as compared to the other subjects. At the same time, however, the ratings awarded by this subject are in general more favourable for each experimental condition than those awarded by the other three subjects. This observation signifies that variability in the adopted task strategy, in terms of the excitation level of rotorcraft dynamics and motion, may indeed lead to large differences in perceived simulation fidelity.

In terms of the stipulated hypotheses, the following concluding remarks about the overall results can be made:

1. For the case of the SFR scale ratings, the baseline condition (b30s) was the second-worst rated, where degrading either motion (b60s) or rotorcraft dynamics (d30s) resulted in a better rating. Only both degraded motion and degraded handling qualities (d60s) result in a worse rating when compared to baseline. For the MFR scale ratings, the baseline was the best rated condition. Degrading either motion (b60m) or handling qualities (d30m) resulted in worst ratings, while degrading both motion and handling qualities (d60m) resulted in the worst rating. As such, the first hypothesis can be confirmed, in that both SFR and MFR ratings degrade when both motion and handling qualities are degraded.

2. The results indicate that the condition with only degraded rotorcraft dynamics received both improved SFR and MFR ratings, the improvement in the SFR ratings appearing stronger than the improvement in MFR ratings. Thus, subjects actually *preferred* the condition with degraded rotorcraft dynamics and therefore the second hypothesis must be rejected.

3. As compared to a condition with both degraded motion fidelity and rotorcraft dynamics, a slight improvement in both SFR and MFR ratings was observed for the condition with only degraded motion. In addition, it can be seen that both SFR and MFR ratings improved by approximately the same degree. A stronger degradation of MFR ratings as compared to SFR ratings could not be observed and therefore the third hypothesis is also rejected.

In summary, it seems pilots are indeed sensitive to changes in rotorcraft dynamics and changes in the configuration of the MCA. However, attempts to separate the contributions of rotorcraft HQs and MCA configuration on perceived fidelity, using the SFR and MFR scales, proved unsuccessful.

2.3.3. PILOT COMMENTS

During the experiment, the pilots were encouraged to support their awarded ratings with comments. An extensive report of the individual pilot comments can be found in Appendix D. Here, the main findings are summarized.

The overall trends observed from the comments are that subjects seem to adequately perceive and communicate the deficiencies pertaining to rotorcraft dynamics (e.g., lateral damping, high inertia, sluggish, etc.) and motion (e.g., lag, latency, overshoot, etc.). At the same time, however, it is also observed that the subjects sometimes pointed out deficiencies in motion, while in fact only rotorcraft dynamics were modified. This is in agreement with the trends found in the awarded SFR and MFR ratings. Nonetheless, some pilot comments also seem to contradict the awarded ratings at times. For example, one subject noted that no change in task strategy was perceived when transitioning between two conditions, but awarded different SFR ratings for the two conditions nonetheless. Similarly, another subject assigned ratings to conditions that suggest no particular deficiencies were perceived, while the subject's comments suggest otherwise.

2.4. Discussion

The results presented in preceding sections give rise to several interesting observations. From inspection of phase portraits (see Figure 2.6), it seems that the subjects' task strategy varies strongly across the different experimental conditions presented. In particular, the aggressiveness and agility with which the task is completed is a measure of the observed variety in the corresponding maneuver phase portraits. The more mild the task strategy of the subject, the lesser the observed variety in the phase portraits.

Based on the awarded pilot ratings, it appears that the subjects are able to discern strong degradations in the simulated environment. In particular, conditions with *both* degraded rotorcraft dynamics *and* motion were rated worst overall with both rating scales used, as hypothesized. On the other hand, conditions in which only one of the two simulation characteristics was degraded produced inconclusive results. It seems pilots preferred the condition with only degraded rotorcraft dynamics in terms of the SFR scale, while preferring the baseline condition in terms of the MFR scale. The former result, however, can be explained based on pilot comments. These indicate that pilots generally perceived the lateral drag of the rotorcraft to be too strong. The more agile characteristics of the rotorcraft in the condition with only degraded dynamics is thought to somewhat alleviate the sluggish characteristics of the rotorcraft in the baseline condition. The fact that the condition with degraded dynamics is rated worse than baseline in terms of the MFR scale shows the difficulty in separating the influence of rotorcraft dynamics and MCA settings when assessing motion fidelity. An explanation for this difficulty can be sought in the apparently ambiguous interpretation of what constitutes "good" motion cues. On the one hand, motion cues help the pilot to recognize deficiencies in rotorcraft HQs, thereby serving as a "window" to actual flight. Therefore, poor motion cues could also mask deficiencies in rotorcraft HQs. On the other hand, even poor motion cues in the presence of deficiencies in rotorcraft HQs could provide valuable feedback to the pilot and may therefore be perceived as beneficial to task performance.

The collected pilot comments also contribute to a better understanding of the subjects' perception of the deficiencies introduced in the simulated environment. In general, the participating pilots were able to provide valuable feedback regarding the specific deficiencies introduced in the simulated environment. However, these deficiencies in some conditions were attributed to the wrong component (e.g., simulator motion instead of rotorcraft dynamic model). Also, several conditions with inconsistencies between comments and ratings were identified. In the current experiment, pilots were deliberately unchallenged in formulating their ratings and comments regarding the fidelity of the simulated environment.

In future experiments, one could consider challenging pilot ratings and comments in case inconsistencies are observed, thereby allowing a potentially more balanced opinion to be formulated. This should be undertaken with caution, however, in such a way as to not introduce observer bias in the results.

In the awarded pilot ratings, a strong between-subjects variation was also observed. For example, the baseline condition was both the best and the worst appreciated condition when inspecting the ratings on a per-subject basis. Also, one subject who adopted a relatively mild task strategy awarded significantly more favourable ratings than the remaining subjects who adopted a more aggressive task strategy. This shows that possibly a relation between the rotorcraft dynamics on the one hand and task performance specifications on the other hand exists. Task performance criteria that force pilots to adopt a more aggressive task strategy, thereby “pushing” the rotorcraft model up to and beyond its region of validity are likely to result in generally poor fidelity ratings. To obtain meaningful results, it is therefore crucial to take this intricate relationship into account in the design of future experiments for simulation fidelity assessment studies. This could mean that equivalent ADS–33E task performance criteria have to be defined for simulator-based experiments, taking into account rotorcraft model and simulator centred limitations (e.g., visual and motion). On the other hand, once such criteria are defined, it is important to enforce them during experiments by motivating subjects to adopt a more aggressive, or less aggressive strategy, based on their attained task performance.

Even though pilots were given the opportunity to repeat the maneuver multiple times in each experimental condition, no repeated trials of the experimental conditions were performed. This means that it was not possible to evaluate within-subject consistency in the awarded ratings per condition. Naturally, it is also of interest to repeat the experiment outlined in the current work with a larger number of pilots and, possibly, for more comprehensive configurations of the rotorcraft dynamics and MCA.

2.5. CONCLUSION

Subjective evaluations made by qualified pilots remain the primary means for the certification of flight simulators. The aim of the study documented in this chapter was to assess the effectiveness of two prominent subjective metrics, the Simulator Fidelity Rating (SFR) and Motion Fidelity Rating (MFR) scales, as indicators of flight simulation fidelity. Of particular interest was the ability of operational pilots to use these metrics to distinguish between the effects of changes in the flight model and/or the Motion Cueing Algorithm (MCA).

The obtained results have exposed several interesting findings. For example, there is some evidence that changes in SFR and MFR ratings are inconsistent between the experimental conditions evaluated. Also, while the participating pilots seemed able to recognize a large degradation in *both* rotorcraft dynamics and motion, degrading either *one* of these characteristics yielded less conclusive results. Finally, a strong relation between the adopted task strategy and awarded ratings was identified, where a less aggressive task strategy was found to result in more favourable ratings.

In conclusion, many caveats exist in the application of subjective metrics for the assessment of flight simulation fidelity were exposed. Nonetheless, to maximize the utility of subjective metrics, it seems beneficial to limit modifications to a single simulator component when conducting fidelity assessment studies. Also, close attention must be paid to task performance specifications in relation to the applied pilot strategy as well as flight model and simulator centred limitations. These findings are valuable for later chapters of the thesis, where subjective metrics will be used extensively to evaluate the relative merit of different motion cueing strategies.

3

TAILORING THE OBJECTIVE MOTION CUEING TEST TO ROTORCRAFT

In Chapter 2, several difficulties related to subjective pilot evaluation of motion cueing fidelity were exposed. Over the years, there have therefore been many efforts towards developing tools for more objective assessment, many of which have been reviewed in Chapter 1. The most promising of such tools is perhaps the OMCT, proposed by Advani and Hosman [2006b]. OMCT is currently adopted in the ICAO manual of criteria for civil FSTDs [Anonymous, 2009] and must therefore be performed by manufacturers of fixed-wing flight simulators for compliance.

This chapter aims to investigate the extent to which OMCT is applicable to rotorcraft *motion simulation, and to extend it where necessary. To this end, first a brief technical background regarding the OMCT is given in Section 3.1. In Section 3.2 a sensitivity analysis is performed to evaluate the effect of the inherent OMCT assumptions on the test outcomes. In Section 3.3 a methodology is proposed and applied to* tailor *the test to helicopter flight simulation. The resulting frequency spectra, based on computer simulations of prescribed tasks, are validated using data obtained from pilot-in-the-loop experiments on the SRS in Section 3.4. Sections 3.5 and 3.6 summarize the main results and conclusions.*

The contents of this chapter have been adapted from: *Dalmeijer, W. et al, Extending the Objective Motion Cueing Test to Measure Rotorcraft Simulator Motion Characteristics, Proceedings of the AHS 73d Annual Forum, Fort Worth (TX), 2017.*

3.1. TECHNICAL BACKGROUND

As discussed in Chapter 2, the integrated performance of a Motion Cueing System (MCS) is still primarily evaluated using subjective pilot assessment, according to ICAO guidelines in [Anonymous, 2009]. The Objective Motion Cueing Test (OMCT), proposed by Advani and Hosman [2006b], is a promising development towards a more objective basis for certification of synthetic motion.

Like the earlier criteria proposed by Sinacori [1977] and later refined by Schroeder [1999], the OMCT aims to quantify the amplitude and phase distortion imposed by the MCS in the frequency domain. However, whereas the Sinacori-Schroeder criteria only consider the frequency response of the MCS at 1 rad/s [1], OMCT aims to capture the frequency response over a much broader range of frequencies.

This is accomplished by exciting the MCS using a set of sinusoidal signals with prescribed amplitudes and frequencies. Each of the six simulator dofs is excited independently, resulting in six *direct* frequency responses (e.g., pitch channel input to pitch channel output). To study typical inter-axes couplings and associated *false cues*, four extra tests are included. Table 3.1 summarizes the prescribed set of input signals in the OMCT as a function of the (longitudinal) simulator dofs driven.

Table 3.1: Longitudinal OMCT test numbers [Advani and Hosman, 2006b].

Input axis	Output axis		
	Pitch	Surge	Heave
Pitch	1	2	-
Surge	7	6	-
Heave	-	-	10

OMCT in itself is a test that yields a set of frequency responses that characterize the linear dynamic response of MCSs and, thus, does not prescribe standards for certification. For lack of better standards, certification of resulting OMCT frequency responses is currently based on industry averages [Anonymous, 2009; Hosman and Advani, 2013, 2016]. Alternative standards have been proposed over the years. For example, Advani et al. [2007] proposed a criterion based on aircraft natural mode frequencies and bandwidth. In addition, Zaal et al. [2017] focused on the development of frequency-domain criteria based on pilot-vehicle task performance. Neither, however, has been adopted to date.

Other than a lack of definite objective standards, researchers tasked with implementation and execution of OMCT have identified a number of additional challenges. For example, Stroosma et al. [2013] conclude that due to (mostly) individually driven simulator dofs and assumed linearity of the input signal spectra, OMCT may yield an incomplete representation of the motion characteristics. For example, both yaw and pitch in fixed-wing aircraft are typically accompanied by significant lateral and vertical specific forces, respectively. Presently, such couplings are not captured in the OMCT.

Seehof et al. [2014] furthermore state that the OMCT prescribes a simplified set of input signal amplitudes. For example, during take-off, the aircraft accelerations in surge might be substantially higher than 1 m/s^2, the amplitude prescribed for the specific force input signals in the OMCT. Because of non-linearities in contemporary motion filters, this may yield different results. Finally, Seehof et al. [2014] note that the training purpose of the simulation may vary to a large extent. An important example is the difference between fixed-

---

[1] The frequency of 1 rad/s was selected because it is associated with a pilot's manual control bandwidth.

and rotary-wing aircraft simulation, where both vehicle dynamics and training scenarios vary substantially. Thus, the OMCT may not necessarily yield representative results when applied to helicopter flight simulation.

In conclusion, several challenges associated with the application of the OMCT have been identified. In the following section, a few crucial assumptions underlying the OMCT are therefore investigated in more detail.

3.2. SENSITIVITY ANALYSIS

As discussed in Section 3.1, two critical assumptions underlying the OMCT pertain to input signal coupling and MCS linearity. To illustrate the effects of these assumptions, a sensitivity analysis of the OMCT is performed using the CWA [Reid and Nahon, 1985] motion cueing algorithm, constrained to the longitudinal (dofs, i.e., pitch, heave and surge) as shown in Figure 3.1. Note that a more detailed analysis of the CWA is postponed until Chapter 5 of this thesis. This chapter only includes a brief description necessary to introduce the sensitivity analysis of interest.

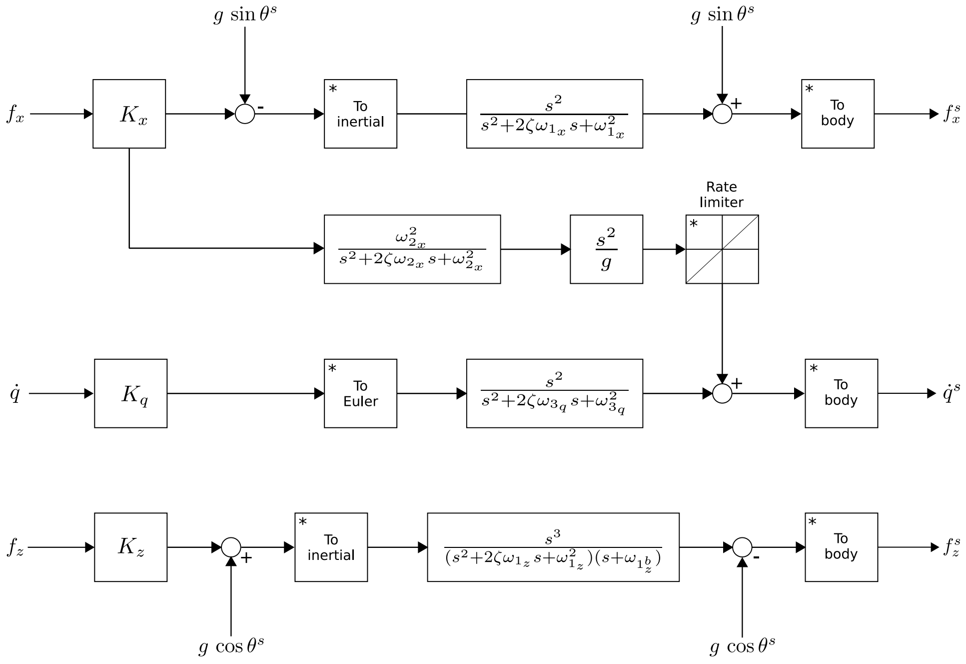

K_x	ω_{1_x}	ω_{2_x}	K_q	ω_{3_q}	K_z	ω_{1_z}	$\omega_{1_z^b}$	ζ
0.7	1.0	2.0	0.7	0.8	0.5	2.5	0.2	1.0

Figure 3.1: Schematic representation and baseline settings of the CWA for the longitudinal simulator degrees-of-freedom.

From Figure 3.1, it is evident that the surge and heave specific forces, as well as the pitch *acceleration* from the mathematical vehicle model, are the inputs signals to the CWA.

Note that the input of pitch *acceleration* to the CWA corresponds to a situation in the SRS and differs from the conventional input of pitch *rate* as described in [Reid and Nahon, 1985]. It can be seen that three channels are present in the figure: two translational channels for surge and heave, respectively, and a single rotational channel for pitch. Furthermore, sustained specific forces in surge are emulated by means of an additional *tilt coordination* channel. Elements marked with an asterisk ("$*$") denote *non-linear* operations and include transformations between simulator body and inertial frames as well as the rate limiter present in the tilt-coordination channel. For the analysis presented in this section, the parameters of the CWA were set to the values also listed in Figure 3.1 and taken from Stroosma et al. [2013], unless specifically stated otherwise.

3.2.1. COUPLING BETWEEN SIMULATOR DOFS

The simultaneous excitation of different simulator dofs affects the output of the MCS because of the inherent coupling between surge and pitch in the CWA depticted in Figure 3.1. Due to inherent axes transformations, this interaction works both ways, i.e., from a surge input to a pitch output and vice-versa.

Surge input to pitch output When the CWA is driven by a sustained specific force in the longitudinal direction, the MCS will simulate the pilot perceived cues through a low-pass filter using the concept of tilt-coordination. Here, a component of the gravitational acceleration is generated by rotating the motion platform. This interaction is captured by the OMCT in two separate tests. First, in Test 7 (see Table 3.1) the surge axis is driven and the output on the pitch axis is measured. This results in a Frequency Response Function (FRF) from surge to pitch. Figure 3.2 shows the resulting gain, $|H_7|$, and phase, $\angle H_7$ for different values of the low-pass filter break frequency in surge (ω_{2_x}).

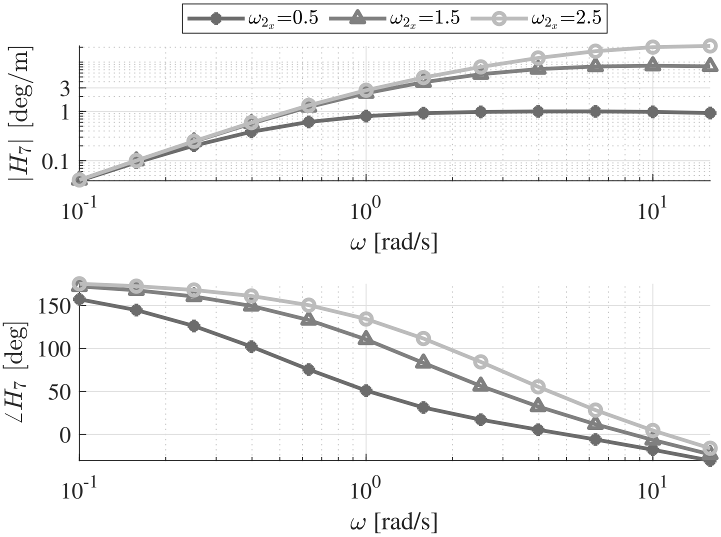

Figure 3.2: Pitch FRF for a surge input, Test 7 of the OMCT.

It should be noted that the simulator pitch angle was taken as output for this test, as was done in Hosman and Advani [2016], as opposed to the simulator pitch acceleration, as was done, e.g., in earlier versions of OMCT and by Stroosma et al. [2013]. Since Test 7 essentially estimates a FRF of the low-pass filter in the tilt-coordination channel, such a representation can be more intuitively related to the MCA.

A typical purpose of this test would be to determine a suitable value for the low-pass filter break frequency found in the tilt coordination channel. A trade-off in the value for this setting exists, because elimination of false pitch cues due to surge is not possible if tilt-coordination is enabled (i.e., ω_{2_x} is non-zero). As can be seen from Figure 3.2, a larger break frequency will result in a pitch response of larger magnitude as a result of a surge input. Note that the units of this particular FRF are deg/m, because the output of the tilt coordination channel is taken as $\dot{q}$, specified in units of deg/s^2 and the inputs, surge specific force, are taken as units of m/s^2. Establishing a suitable trade-off between different settings of ω_{2_x} based on the results in this figure, however, is not straightforward. This is because, in OMCT, magnitudes are by definition defined as frequency-dependent ratios between input (here, surge specific force) and output (here, pitch acceleration). Hence, while it is clear that with increasing break frequency the magnitude of the pitch output increases as a result of a (sustained) surge input, the *absolute* magnitude of the pitch motion cues *perceived* by a pilot in the simulator cannot be feasibly reconstructed from the representation in Figure 3.2. OMCT results therefore cannot be compared directly to absolute values of vestibular thresholds (e.g., [Heerspink et al., 2005]).

Moreover, the motion cues perceived by pilots do not only depend on the characteristics of the MCS, but also on characteristics of the input signals from the mathematical aircraft model. This is clear from the following relation:

$$Y_7(j\omega) = H_7(j\omega) \cdot U_7(j\omega), \tag{3.1}$$

which signifies that the frequency spectrum of the output signal (i.e., pitch) depends on the frequency spectrum of the input signal (i.e., surge). An inverse Fourier transformation applied on $Y_7(j\omega)$ then yields an approximation of the time-domain signal actually perceived by the pilot. In OMCT, the spectrum of $U_7(j\omega)$ is prescribed as a sum of individual sinusoids with equal amplitude and phase. In reality, however, the input signal spectrum strongly depends on the task performed and even the applied pilot strategy.

To obtain a more complete picture of the pitch motion characteristics of the CWA, Test 7 is combined with a direct pitch FRF, Test 1 (see Table 3.1). Test 1 estimates the pitch output of the MCS as a result of a pitch input. However, OMCT assumes *uncoordinated*[2] longitudinal motion for fixed-wing aircraft. As a result, a matching surge signal is supplied to the MCS in conjunction to the pitch input signal: $f_x = g\ \sin(\theta)$. Thus, in this case, the OMCT explicitly imposes a coupled response in both pitch and surge. The resulting FRFs are shown in Figure 3.3 for the case of *uncoordinated* motion and for the case of *coordinated* motion, i.e., where the input to the surge filter is $f_x = 0$.

The FRF prescribed by OMCT is indicated in the figure by the line with circular markers labelled $f_x = g\ \sin(\theta)$. An additional line is shown, corresponding to a situation in which f_x

---

[2] In uncoordinated motion, rotational acceleration is not accompanied by translational acceleration and, hence, a component of gravity is perceived as specific force.

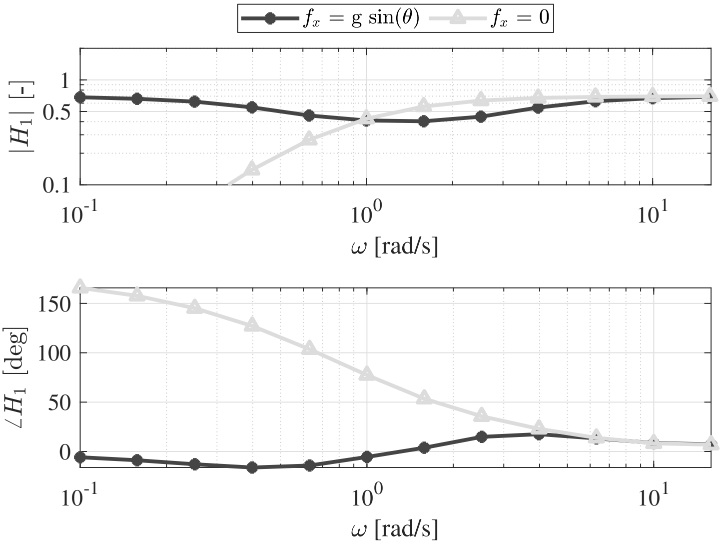

Figure 3.3: Pitch FRF computed with an input on pitch and surge axes, test 1 of the OMCT

equals zero. This situation is more representative of helicopter flight, where it is commonly assumed that motion is *coordinated* [Hodge et al., 2015a; Wiskemann et al., 2014].

From Figure 3.3 it is evident that the choice of whether or not rotational and translational motion are coordinated, significantly affects the pitch motion characteristics predicted by the OMCT. This is true especially at low frequencies where, in the absence of an uncoordinatory surge input, the magnitude of the simulator pitch is strongly reduced as a consequence of the lack of pitch due to tilt coordination. In addition, the phase lead at lower frequencies is seen to strongly increase. This is because, in the *coordinated* case (and therefore *zero* input to the tilt-coordination channel), *only* the high-pass pitch filter of second order induces a phase lead in pitch of 180 degrees at low frequencies. For the *uncoordinated* case, where $f_x = g\ \sin(\theta)$, this induced phase lead is compensated for by the low-pass filter (of equal order) in the tilt-coordination channel.

Pitch input to surge output A second important interaction in the CWA emerges when the simulator is driven in pitch and the output in surge is inspected. The primary contribution of pitch in the simulated specific force in surge is the longitudinal component of the gravitational acceleration. Because the translational motion space is limited in synergistic motion platforms, *false cues* in specific force for *coordinated* aircraft motion cannot be avoided [Zaal et al., 2015a]. A secondary contribution stems from the necessity to filter *acceleration* (as opposed to specific force) in the simulator *inertial* frame to enable effective return-to-neutral. In Figure 3.1, this is accomplished by subtracting $g\ \sin\theta$ from f_x, where θ is the *simulator* pitch angle. The specific force in the simulator is computed by adding the same term again *after* the high-pass filter. However, because of the presence of the high-pass filter, the two operations are not fully complementary. Thus, the transformation from vehicle specific force to simulator acceleration and, finally, to simulator specific force also induces false motion cues.

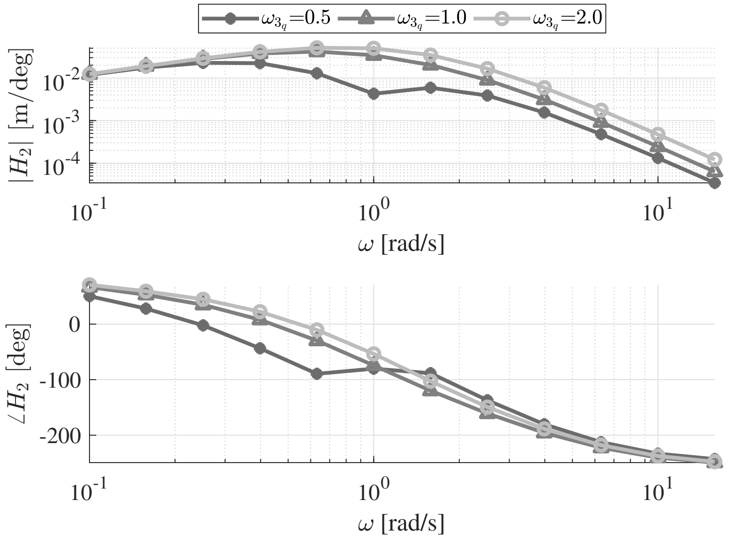

Figure 3.4: Surge FRFs due to pitch input, Test 2 of the OMCT.

This interaction in the CWA is captured using Test 2 of the OMCT. In this test, as is the case for Test 1, the CWA is driven not only by a pure input in aircraft pitch, but also by an accompanying input in surge of the form $f_x = g\ \sin(\theta)$ to ensure *uncoordinated* motion. Also, the prescribed *output* of Test 2 is not the specific force in surge, but the surge acceleration a_x. Figure 3.4 shows the simulator surge FRF for different values of the high-pass filter break frequency in the pitch channel (ω_{3_q}).

A typical purpose of this result would be to assess the "severity" of false surge motion cues due to simulator pitch. As can be seen from Figure 3.4, a higher break frequency will typically result in stronger cross couplings from pitch to surge at higher frequencies. Again, however, the results obtained for this test are difficult to interpret. This is true for the same reasons as already stipulated for the case of Test 1 in Figure 3.2. Here, however, additional complexity is introduced in judging the severity of the false surge motion cues cues present, because the output of Test 2 is prescribed as the simulator *acceleration* as opposed to human-perceived specific force. Finally, it is noted that in order to obtain a complete representation of the surge motion characteristic of the CWA, Test 2 should be combined with Test 6 (surge input to surge output) in the OMCT.

3.2.2. LINEARITY

As illustrated in the previous section, the OMCT prescribes a set of individual input signal sinusoids per dof with a constant amplitude and (relative) phase. These signals may not be representative for many tasks performed in a typical flight simulator. This is a potential limitation, because differences in amplitude of the vehicle specific forces and rotations affect the excitation of non-linear operations (e.g., axes transformations and rate limiting) present in the CWA.

The rate-limiter (see Figure 3.1) is present to ensure that rotational rates arising from tilt coordination remain below human perception thresholds. The sensitivity of the OMCT to rate limiting was studied in [Hosman and Advani, 2016]. The effect of this non-linearity is best seen by inspecting the outcome of Test 6 (i.e., surge input to surge output) of the OMCT. Figure 3.5 shows results from this test for constant filter settings but different amplitudes of the input sinusoid.

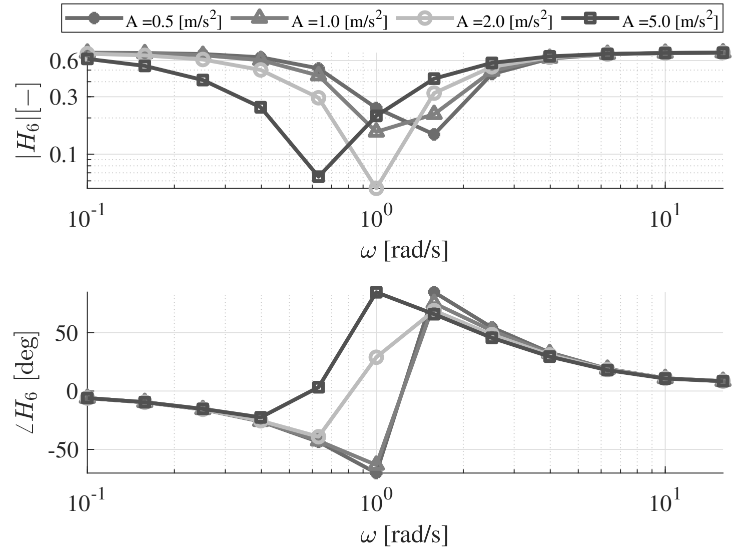

Figure 3.5: Surge FRFs computed using an input signal on the surge axis, $f_x = A\sin(\omega t)$, with different amplitudes, Test 6 of the OMCT.

It can be seen that for the chosen CWA settings (see Figure 3.1), the frequency response amplitude ratio at the Sinacori frequency of 1 rad/s ranges from a value of 0.05 to 0.3 for input amplitudes ranging from 0.5 to 5.0 m/s^2. In practice, this means that for this configuration the estimated gain may vary up to a factor of 6, depending on the prescribed amplitude of the surge input sinusoid in Test 6.

The challenges associated with the OMCT in the rotorcraft domain can thus be summarized essentially into three categories. First, tests aimed at capturing the surge-pitch interaction in the CWA rely on an assumption (i.e., uncoordinated motion) that is not necessarily valid in helicopter flight simulation. Second, the results from cross-coupling tests (i.e., Test 2 and 7) are difficult to interpret and apply. Finally, as MCSs generally do not have fully linear dynamics, there is significant sensitivity to prescribed input signal amplitudes (caused primarily by the rate-limiter present in the tilt coordination channel of the CWA).

3.3. TAILORING THE OMCT TO ROTORCRAFT FLIGHT DYNAMICS

The underlying cause of many of the identified challenges associated with OMCT stems from the fact that, while straightforward, the prescribed tests abstract away many vehicle and pilot specific characteristics, as also recognized by Stroosma et al. [2013]. Thus, it would be beneficial if the prescribed tests could be *tailored* more to a specific combination of a task and vehicle. This section presents a possible approach to achieve this.

To this end, first an off-line simulation environment using a simple three-dof helicopter model and automatic controller ("paper pilot") is developed. This setup is subsequently used to simulate two typical helicopter flight tasks: an acceleration-deceleration and precision hover manoeuvre. Time traces of these simulations are then transformed to the frequency domain using Fourier transformations and used to define a new set of input signals to the CWA. Finally, an alternative OMCT is defined, in which all dofs of the MCS are driven by the new input signals *simultaneously* in a way that is more representative for typical helicopter flight.

3.3.1. OFF-LINE SIMULATION ENVIRONMENT

To generate representative time-domain data required for the tailored OMCT, an offline simulation environment is necessary. This environment encompasses a helicopter model and a means to simulate representative helicopter flight tasks using an automatic controller.

Helicopter model For the (prelimnary) analyses presented in this chapter, the three dof, non-linear, longitudinal helicopter model as described in [Van Holten and Melkert, 2002] is used, with parameters taken from a DRA Research Lynx helicopter as found in [Padfield, 2007]. The main assumptions underlying the used model are:

- A non-eccentric, springless flapping hinge is assumed on the main rotor. This means that no in-plane moments are acting at the rotor hub.
- Aerodynamic drag forces on the main rotor blades are neglected. Hence, there are no in-plane forces and torque. While the latter is an especially gross simplification in general, for a longitudinal three dof model with a fixed yaw axis it is a reasonable assumption. It also implies that engine dynamics are omitted.
- Quasi-steady inflow velocity and flapping dynamics are assumed. This means that both inflow and blade flapping angles are assumed to instantaneously adopt new equilibria as a result of changing flow conditions and pilot control inputs.
- Fuselage drag is estimated by $D = C_D \frac{1}{2}\rho V^2 S$, with $C_D = 0.08[-]$ taken from [Padfield, 2007]. All other aerodynamic forces on the fuselage and other aircraft components are neglected.

The implication of these assumptions is that the only contributions to vehicle motion stem from the main rotor thrust and fuselage drag force. While this is a gross simplification, the simple model is believed to be sufficient to approximate helicopter flight characteristics for the OMCT analysis in this chapter. More information regarding the theoretical background (e.g., equations of motion) be found in both [Dalmeijer, 2016] and [Van Holten and Melkert, 2002].

Task simulation For quantitative analysis of helicopter dynamics, reference trajectories of typical flight tasks are required. The tasks should be realistic and, preferably, standardized so that they can be feasibly reproduced. Furthermore, the tasks should excite the aircraft dynamics in a broad range of the OMCT input signal frequency range. Suitable candidates for such tasks, or MTEs, are described in ADS-33E [Anonymous, 2000], a military design standard for handling qualities requirements. Using these task specifications, an offline simulation environment as shown in Figure 3.6 is developed. This schematic shows both the Lynx model and an automatic (“paper pilot”) controller used to track the prescribed MTE trajectories. In Section 3.4, the results obtained from the offline simulations will be validated with piloted simulator trials. This chapter considers two different MTEs suitable for application to the three-dof aircraft model: the precision hover and take-off/abort manoeuvres from [Anonymous, 2000].

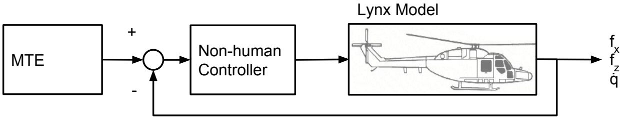

Figure 3.6: Schematic of the off-line simulation environment.

Precision hover To excite the higher frequencies present in the prescribed OMCT spectrum, the precision hover MTE combined with moderate turbulence is also considered. The hover MTE is initiated with a low forward velocity of 6-10 knots. The helicopter is subsequently to be stabilized in hover at a specific location and remain in place for approximately 30 seconds. Figure 3.7 shows the corresponding velocity profile, while Table 3.3 lists the desired and adequate performance criteria for this task.

The turbulence present in the hover task is modelled using the Dryden spectra [Anonymous, 1980; Chalk et al., 1969]. As Dryden spectra are not applicable for $V \approx 0$, the model was configured to generate equivalent turbulence to a fictive “category A” fixed-wing aircraft at an airspeed of 90 knots and an altitude of 500 ft. Futhermore, the turbulence model was configured to perturb the helicopter model only in the longitudinal and vertical directions. More details about the turbulence model applied can also be found in Appendix A.9.2 of this thesis.

Take-off/abort The take-off/abort MTE is initiated in hover at 35 feet wheel height. The helicopter is then accelerated to a speed between 40-50 knots while keeping the altitude constant. Upon reaching this velocity, take-off is aborted and the helicopter is decelerated to hover at a distance of 800 feet from the initial location. Figure 3.8 shows the velocity profile of the take-off/abort manoeuvre. Table 3.3 furthermore lists the accompanying desired and adequate performance criteria. As can be seen from the velocity profile in Figure 3.8, the take-off/abort MTE is a manoeuvre that excites primarily the lower frequency aircraft dynamics.

Table 3.2: Adequate and desired longitudinal performance for the precision hover MTE.

	Adequate	Desired
Time to stabilize [s]	< 8	< 3
Longitudinal position [ft]	±6	±3
Altitude [ft]	±2	±5

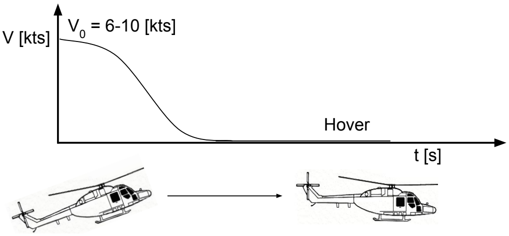

Figure 3.7: Schematic of the precision hover MTE.

Table 3.3: Adequate and desired performance criteria for the take-off/abort MTE.

	Adequate	Desired
Altitude [ft]	< 75	< 50
Time to complete [s]	< 30	< 25

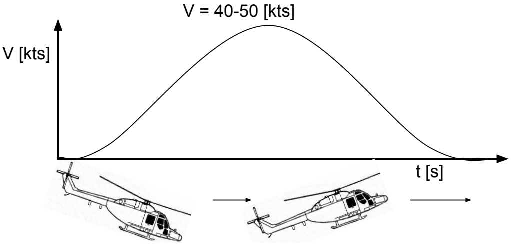

Figure 3.8: Schematic of the take-off/abort MTE.

Automatic controller An automatic controller was devised to guide the helicopter along the prescribed track for both MTEs. The controller comprises two parts: 1) collective control is governed by feedback of the vehicle's altitude such to track a constant height while 2) velocity control is achieved using a nested control structure. An inner loop regulates the aircraft's pitch attitude using longitudinal cyclic control. In turn, an outer loop with velocity feedback is used to track the velocity profiles shown in Figures 3.7 and 3.8. The controller's tracking performance for both MTEs is shown in Figures 3.9 and 3.10. It can be seen from these figures that deviations from the specified velocity and altitude profiles are small, while control inputs remain well within the available blade pitch ranges.

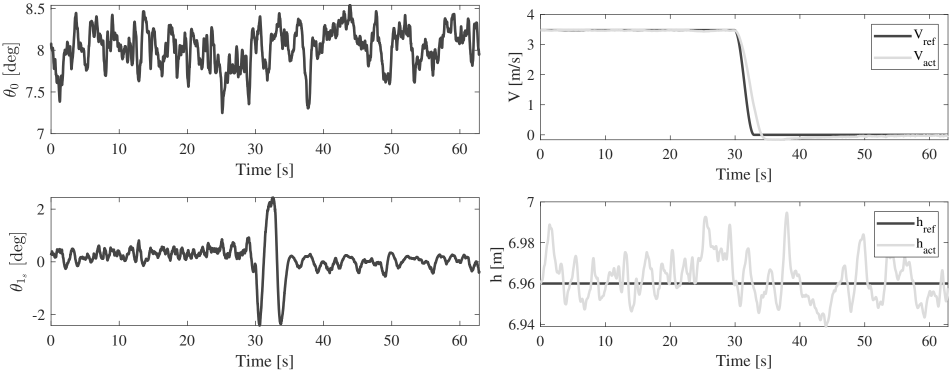

Figure 3.9: Control inputs and tracking performance of automatic controller for hover MTEs.

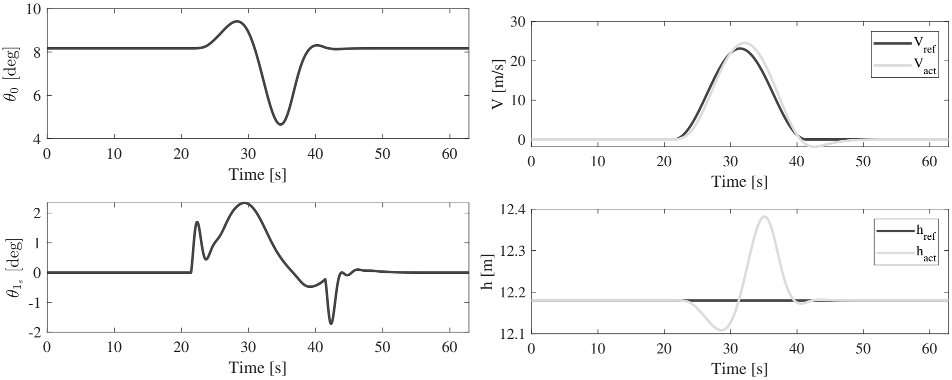

Figure 3.10: Control inputs and tracking performance of automatic controller for take-off/abort MTEs.

3.3.2. TAILORING THE INPUT SIGNAL PROPERTIES

The simulated time traces of pilot-perceived specific forces (f_x and f_z) and pitch acceleration ($\dot{q}$) for both MTEs as shown in Figures 3.9 and 3.10, are used to *tailor* alternative, potentially more representative, OMCT input spectra. The idea behind this approach is that the resulting time-domain responses can be converted to the frequency domain by means of the Fast

Fourier Transform (FFT). This results in two sets (i.e., one for each MTE) of three signal amplitude (related to "power") and phase spectra (i.e., one set of spectra for each human-perceived signal).

Because of the characteristics of the FFT, a value of the amplitude and phase does not necessarily exist at every exact frequency prescribed in the *original* OMCT. Therefore, a model based on univariate splines was constructed to estimate the amplitude and phase *at the OMCT prescribed frequencies*. This enables a set of alternative OMCT input signals to be constructed, a set which contains amplitude and (relative) phase information that are more specific and relevant to the vehicle-task combinations under consideration.

While the resulting amplitude spectra can be used directly, deriving relevant phase information is slightly more involved. This is because the FFT computes the *absolute* phase of the individual sinusoids in the decomposed signal. What is desired, however, are the *relative* phases of these components across the degrees-of-freedom. To illustrate, see Figure 3.3, where, the OMCT pitch FRF as a result of an input signal in the surge axis is examined. When the surge axis is excited by $g\ \sin(\theta)$, i.e., corresponding to *uncoordinated* motion, the predicted pitch motion characteristics differ substantially from those corresponding to *coordinated* motion where the surge axis input is zero. This is true particularly for the amplitude and phase at low frequencies.

One way to obtain *relative* phase information is to select an arbitrary reference degree-of-freedom with respect to which the phases of the remaining degrees-of-freedom are expressed. That is:

$$\angle\tilde{F}_x(\omega) = \angle F_x(\omega) - \angle\dot{Q}(\omega), \qquad \angle\tilde{F}_z(\omega) = \angle F_z(\omega) - \angle\dot{Q}(\omega), \qquad \angle\dot{\tilde{Q}}(\omega) = \angle\dot{Q}(\omega) - \angle\dot{Q}(\omega) = 0 \tag{3.2}$$

where the pitch axis is selected as the reference degree-of-freedom. The resulting spectra for both tasks under consideration are shown in Figure 3.11. The markers in this figures denote values at the prescribed frequencies in the orignal OMCT.

From Figure 3.11, a number of observations can be made. From the amplitude spectrum pitch (see Figure 3.11a), it becomes evident that the take-off/abort MTE dominates the lower frequencies, while the hover MTE is responsible for the frequency content at higher frequencies in excess of 2 rad/s. The take-off/abort MTE furthermore dominates both the surge and heave spectra as can be seen from Figures 3.11b and 3.11c.

It can also be seen that for f_x and f_z, the amplitude spectra at most frequencies are a factor of 50 times smaller than the 1 m/s^2 prescribed in the original OMCT Anonymous [2009]. This indicates that the prescribed OMCT signals are exaggerated in amplitude for applications in helicopter flight simulation. Some apparent "oscillations" in the amplitude spectra are also visible, in particular for $\dot{q}$, which are a result of *spectral leakage* (see, e.g., [Oppenheim and Verghese, 2015]) from the application of the FFT. Note that no particular *windowing* was applied, as it was found to not substantially improve the obtained spectra. Figure 3.11 furthermore shows that a considerable amount of noise is present for frequencies above 2 rad/s. This noise can also be attributed to spectral leakage, but in case of the hover MTE, it is also caused by the presence of atmospheric turbulence.

Finally, Figure 3.11b shows that the relative phase between pitch and surge is approximately 100 degrees at low frequencies and about 180 degrees for $\omega > 0.7$ rad/s. For

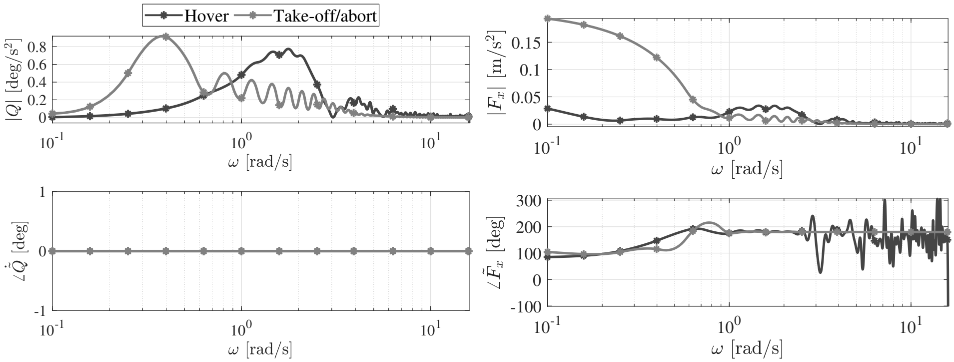

(a) Pitch **(b)** Surge

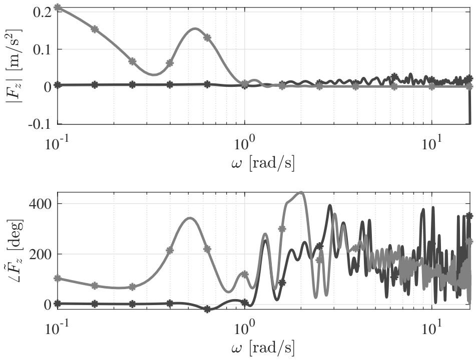

(c) Heave

Figure 3.11: Tailored OMCT input signal spectra based on take-off/abort and precision hover MTEs.

the high-frequencies in the flight envelope, a *positive* pitch acceleration therefore entails a *negative* surge acceleration and vice-versa.

A theoretical justification for this observation is found after some algebraic manipulation of the equations of motion that are used in the three-dof helicopter model. Momentarily neglecting the effects of drag and assuming purely rotational motion, it is possible to write the longitudinal and rotational helicopter equations of motion as (see [Dalmeijer, 2016; Van Holten and Melkert, 2002]):

$$\dot{u} = -g\sin(\theta) + \frac{T}{m}\sin\left(\theta_{1_s} - \beta_{1_c}\right) - qw \tag{3.3}$$

$$\dot{q} = -\frac{Th_R}{I_{yy}}\sin(\theta_{1_s} - \beta_{1_c}) \tag{3.4}$$

$$\dot{\theta} = q \tag{3.5}$$

Here $\dot{u}$ and $\dot{w}$ are the derivatives of the body velocities and $\dot{q}$ is the pitch rotational acceleration. Furthermore, θ is the pitch attitude of the helicopter, θ_{1_s} is the longitudinal cyclic input and β_{1_c} is the longitudinal disc tilt angle. The vehicle-specific parameters are the mass (m), pitch moment of inertia (I_{yy}) and the main rotor vertical distance from the center of gravity (h_R). Recognizing f_x as the sum of forces acting on the vehicle per unit mass in Equation (3.4), i.e.:

$$f_x \equiv \frac{T}{m}\sin\left(\theta_{1_s} - \beta_{1_c}\right),$$

from Equation (3.5) it is apparent that:

$$-\frac{I_{yy}}{h_R}\dot{q} = T\ \sin(\theta_{1_s} - \beta_{1_c}).$$

It then becomes possible to write:

$$f_x = -\frac{I_{yy}}{m\,h_R}\dot{q} \tag{3.6}$$

The presence of the minus sign in this result explains the 180 degrees phase shift between surge and pitch seen in Figure 3.11b at high frequencies. Thus, in summary, the tailored spectra as well as the theory predict *coordinated* vehicle motion at high frequencies, whereas in the original OMCT, *uncoordinated* motion is assumed.

3.3.3. SIMULTANEOUS EXCITATION OF SIMULATOR DOFS

The values in the amplitude spectra from Figure 3.11 at the 12 prescribed OMCT frequencies ranging from 0.1 to 15.8 rad/s are here used as alternatives to the amplitudes in the original OMCT. However, the *relative* phase information available from Figure 3.11 can also be used as described in the following paragraphs.

During pilot-in-the-loop simulation, the vehicle dofs are excited *simultaneously* as a result of pilot control inputs. The CWA channels shown in Figure 3.1 are therefore also excited by individual sinusoids in the pitch, surge and heave axes *simultaneously* in the tailored OMCT. The phases of the individual sine waves on the pitch axis are always fixed at zero. However, the phases of the sine waves on the surge and heave axes vary according to the results in Figure 3.11. Since all axes are excited simultaneously, the cross-tests for the original OMCT become superfluous and hence only three *coupled* tests remain in the tailored OMCT. For consistency with the original OMCT, the coupled tests are numbered 1, 6 and 10 for the pitch, surge and heave channels, respectively (see Table 3.1).

Tailored OMCT results corresponding to the motion filter parameters given in Figure 3.1 are shown in Figure 3.12 for both the precision hover and take-off/abort input spectra. Results from the original OMCT are also included in the figure for reference. Figures 3.12a–3.12c show the estimated FRFs of the pitch, surge and heave channels CWA, respectively.

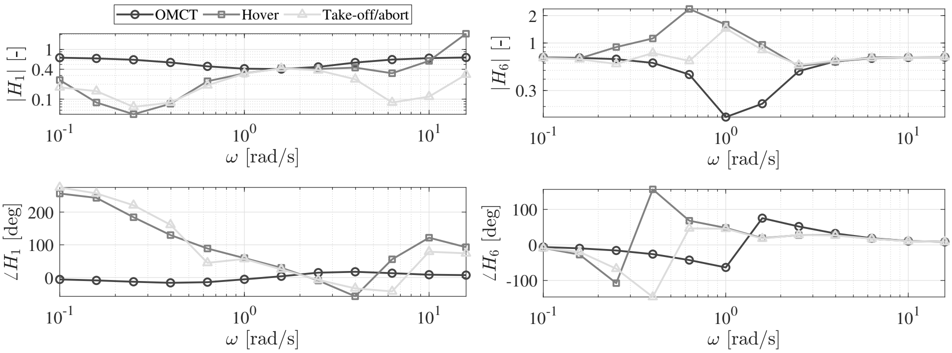

(a) Pitch **(b)** Surge

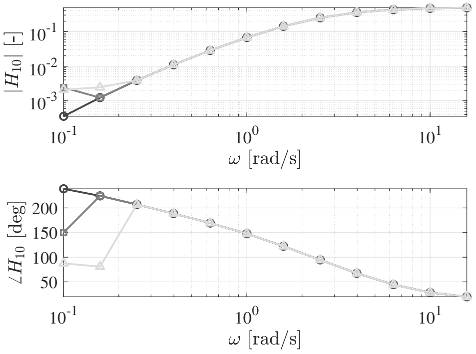

(c) Heave

Figure 3.12: Comparison between the two tailored OMCTs and the original OMCT.

The most interesting result in Figure 3.12a can be seen at low frequencies of the pitch FRF, where the original OMCT predicts favourable motion characteristics, with a gain of close to one and a phase distortion of close to zero degrees. In contrast, both tailored OMCTs based on the precision hover and take-off/abort MTEs show poor motion characteristics with a notably lower gain and a phase lead in excess of 200 degrees. This is an indication that the simulated pitch-surge motion is indeed *coordinated* and more similar to the case of $f_x = 0$ shown in Figure 3.3.

From Figure 3.12b it can be seen that the surge FRF corresponding to the original OMCT predicts a characteristic gap in the gain caused by the imperfectly complementary low- and high-pass filters in the tilt coordination and the surge translational channel, respectively. However, in both tailored OMCTs an opposite trend is seen, where the gain seems to be *magnified*. This effect is due to coordination of the pitch and surge motion. Namely, in real flight, rotation of the vehicle is accompanied by translation. Hence, the component of gravity sensed due to the accumulated pitch angle is (approximately) cancelled by the vehicle's translation acceleration. In the simulator, this translation is strongly limited by the high-pass surge filter present in the CWA. As a result, a *false cue* is seen in the tailored OMCTs which appears because of the simultaneous excitation of the CWA channels.

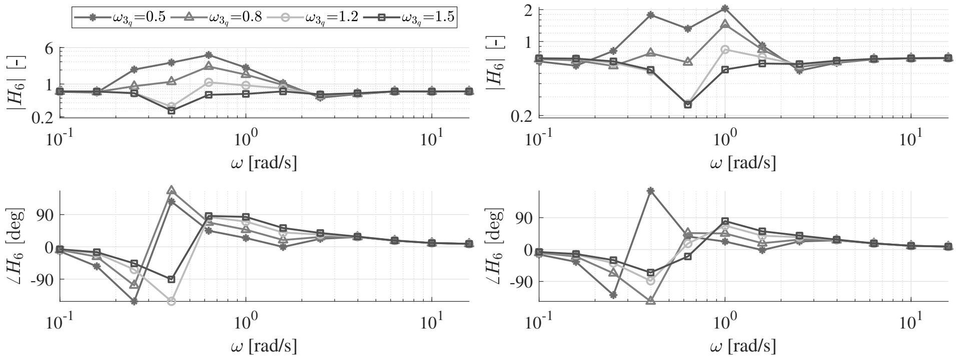

(a) Hover **(b)** Take-off/abort

Figure 3.13: Surge FRF (Test 6) tailored to the hover and take-off/abort MTEs.

A somewhat closer examination of this effect is shown in Figure 3.13, where the high-pass break frequency of the pitch filter was varied and the resulting surge FRF for both MTEs was studied. From this figure, it can be seen that by increasing the break frequency (hence, limiting motion in pitch), the predicted amplification in the surge FRF is reduced and will begin to resemble the original OMCT (for $\omega_{3_q} \approx 1.5$ rad/s.

Finally, Figure 3.12c, shows that there is little difference in the FRFs of the heave channel between the original OMCT and both tailored OMCTs. This is a direct result of the fact that in the CWA the heave channel is largely uncoupled from the other dofs.

In conclusion, from an off-line simulation-based comparison, notable differences between the original and tailored OMCTs were identified, particularly in the pitch and surge axes of the simulator. The remainder of this chapter outlines an experiment that aims to validate the latter result by using time traces from a performed *pilot-in-the-loop* experiment instead of a "paper pilot".

3.4. TAILORED OMCTS FROM PILOTED FLIGHT SIMULATION DATA

In piloted flight simulation, the pilot strategy and, hence, the excitation of the vehicle model may differ substantially when compared to an automatic controller (i.e., the "paper pilot"). Hence, a potential limitation of the analysis in Section 3.3 is that the task-specific amplitude

Figure 3.14: Interior of the SRS, showing the projected visuals, instruments and CLS-driven helicopter controls.

and relative phase spectra may not only be influenced by the vehicle dynamics and task specifications, but also by human perception and control limitations.

Dalmeijer et al. [2017] performed an experiment on the SRS at Delft University of Technology to study the influence of a human pilot on the resulting tailored OMCTs. In addition, the experiment also assessed, by using *subjective* measures, whether the exposed trends in the offline simulation-based OMCTs (particularly those shown in Figure 3.13) resulted in a notable change of pilot strategy.

This section summarizes the main findings from the experiment, with a particular emphasis on the results pertaining to the influence of the human pilot on the tailored OMCTs. First, the experimental setup is discussed, after which the results are outlined.

3.4.1. METHOD

The experiment setup consists of the task specification, the tested MCA settings, the hypotheses, participants and procedure and, finally, the dependent measures. Each will be discussed in the subsequent paragraphs.

Apparatus The SRS is a Stewart platform based flight simulator with six hydraulically driven actuators. The synergistic extension and compression of these actuators provides six degrees-of-freedom of motion. The other relevant cueing systems of the simulator are the visual system, instruments and helicopter controls. An impression of the interior of the SRS showing each of these system is shown in Figure 3.14.

The visual system of the SRS consists of three projectors with a refresh rate of 120 Hz mounted on top of the simulator. Using a set of mirrors, light from the projectors is directed such to produce a collimated 180 degrees (horizontal) and 40 degrees (vertical) field of view image. The generated images are rendered using the open-source OpenSceneGraph software [OpenSceneGraph, 2019].

The instruments available to the pilots constitute a simple extended "basic six" representation rendered using OpenGL on of the Multi-Function Displays (MFDs) in the simulator. From the top left to the bottom right, the torque (inactive), airspeed, artificial horizon, altitude, turn rate/sideslip, compass rose and, finally, vertical speed are shown.

Finally, the helicopter controls are provided by an electically driven Control Loading System (CLS). The cyclic and collective controls were developed by Moog™, whereas the pedals were developed by TU Delft. The grips on the controls are generic and equiped with reprogrammable buttons. Most of these buttons were inactive during the experiment, although one "thumb" button on the cyclic was utilized as the Force Trim Release (FTR).

Task specification In the experiment, the precision hover and take-off/abort MTEs considered in Section 3.3 were executed on the SRS. Tables 3.2 and 3.3 list the accompanying desired and adequate performance criteria from [Anonymous, 2000]. Dedicated visual references for both task were shown on the SRS outside visual display, and are illustrated in Figures 3.15 and 3.16.

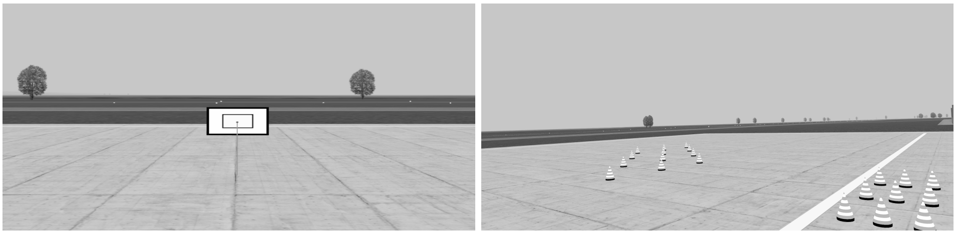

Figure 3.15: Front (left) and diagonal (right) views of the precision hover visual reference as seen from the SRS visual system.

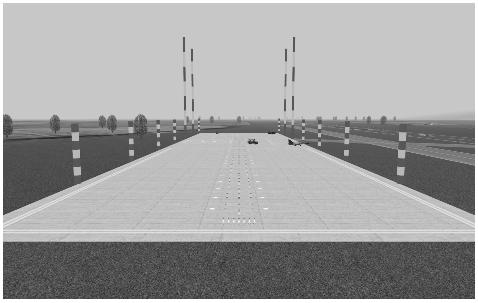

Figure 3.16: View of the take-off/abort visual references as seen from the SRS visual system.

Hypotheses In the off-line simulation results presented in Section 3.3, the most notable difference between the original and tailored OMCTs is the apparent upswing in surge (Test 6) present for frequencies slightly below 1 rad/s. It was found that the severity of this upswing is strongly influenced by the high-pass break frequency of the CWA pitch channel (ω_{3_q}).

The experiment performed by Dalmeijer et al. [2017] proposed two hypotheses related to this finding:

1. The primary purpose of the performed pilot-in-the-loop experiment was to reconstruct the observed trends in the tailored OMCTs with ω_{3_q} as shown in Figure 3.13 for both the precision hover and take-off/abort MTEs. It is expected that the excitation of the vehicle model by a human pilot differs in comparison to a "paper pilot". Most notably, pilot performance is strongly affected by limitations in human perception and actuation [Hosman, 1996].

   Hence, it is hypothesized that tailored OMCTs based on the experimental data will show some differences when compared to the tailored OMCTs obtained from the off-line simulation data. For one, it is expected that the experimental data will show more variability in the tailored OMCTs. The identified upswing in Test 6 is nonetheless hypothesized to also appear from the experimental data and to follow a similar pattern as observed in Figure 3.13. This is because this effect is believed to originate from the *inherently* coordinated pitch-surge dynamics of helicopters.

2. A natural question that arises from the exposed trends in the tailored OMCTs shown in Figure 3.13 is whether pilot strategy is also affected by the, supposedly, degraded fidelity in the surge specific force. Hence, in the experiment, pilots were asked to express perceived changes in their applied control strategy by means of the Simulator Fidelity Rating (SFR) scale [Perfect et al., 2014].

   It was hypothesized that SFR ratings would improve for both the precision hover and take-off/abort MTEs with increasing values for ω_{3_q}, indicating that pilots preferred conditions where the upswing in the surge specific force as a result of pitch is less.

Unfortunately, results pertaining to Hypothesis (2) were found to be inconclusive, with no apparent trend appearing in the gathered SFR ratings [Dalmeijer et al., 2017]. Therefore, the remainder of this chapter is focussed only on results pertaining to Hypothesis (1).

Independent variable: MCA parameters Four different CWA parameter sets were presented to the participating pilots. In order to verify that the observed trends in Figure 3.13 could be reproduced used piloted flight simulation data, the same four cases of ω_{3_q} were selected, namely = 0.5, 0.8, 1.2 and 1.5 rad/s, respectively. The other CWA parameters were kept constant in the experiment and set identically to the values used in the off-line simulations, i.e., as listed in Figure 3.1.

Participants and briefing Three operational helicopter pilots participated in the experiment. Before the experiment, the participants were instructed to strive for attaining the desired task performance. Familiarization was conducted such that the participants experienced each condition once before the actual experiment commenced. During the familiarization, the participants were allowed to practice until an approximately stable performance for each evaluated MTE was attained. Then, the eight (i.e., four for each MTE) different experiment conditions were presented to the participants.

Each condition was flown until three consecutive runs with a similar performance were completed. The order in which experiment conditions were presented to the participants was determined using a partially balanced experiment design as shown in Table 3.5. As can be seen from this table, each subject first performed the precision hover MTE before the take-off/abort MTE.

Table 3.5: Experiment conditions per participant (S1, S2 and S3). ω_{3_q} is expressed in rad/s.

Condition	**Task**	ω_{3_q} **(S1)**	ω_{3_q} **(S2)**	ω_{3_q} **(S3)**
1	Hover	0.5	1.2	0.8
2	Hover	1.2	0.8	1.5
3	Hover	0.8	1.5	1.2
4	Hover	1.5	0.5	0.5
5	Take-off/abort	1.2	1.2	1.5
6	Take-off/abort	0.5	1.5	0.8
7	Take-off/abort	1.5	0.8	0.5
8	Take-off/abort	0.8	0.5	1.2

Dependent measures For Hypothesis 1), the primary dependent measures collected during the experiment are time traces of the vehicle model states as well as the MCA inputs and outputs. These were necessary for the computation of tailored input signal frequency spectra corresponding to the precision hover and take-off/abort MTEs as outlined in Section 3.3.

3.4.2. RESULTS

The following paragraphs present the obtained input signal spectra corresponding to the precision hover and take-off/abort MTEs, as well as the subsequently computed tailored OMCTs. First, tailored input signals and OMCT outcomes are compared to the off-line simulation results presented in Section 3.3, for the condition with CWA settings as given in Table 3.5. Subsequently, the trends in the tailored OMCTs for both MTEs with a different value for ω_{3_q} are examined.

Tailored input signals To compare the tailored OMCT input signals to the ones obtained in the off-line analysis in Section 3.3, time traces of the specific forces and pitch acceleration from the recorded experiment data corresponding to the condition with $\omega_{3_q} = 0.8$ rad/s for *all subjects* were used. These time traces were transformed to the frequency domain using the FFT and, subsequently, *relative* phases were computed from Equation (3.2) as outlined in Section 3.3. Figures 3.17 and 3.18 show the resulting spectra for $\dot{q}$, f_x and f_z for the precision hover and take-off/abort MTEs, respectively. Also shown in these figures are vertical bars at each OMCT frequency, which represent the *standard errors* across individual subjects and runs.

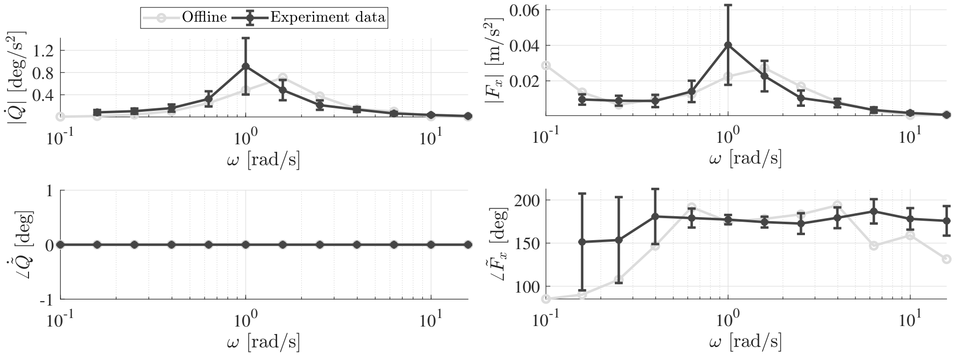

(a) Pitch **(b)** Surge

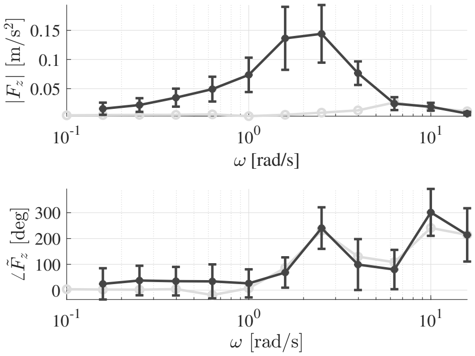

(c) Heave

Figure 3.17: Input signal spectrum for the precision hover MTE obtained from experiment data.

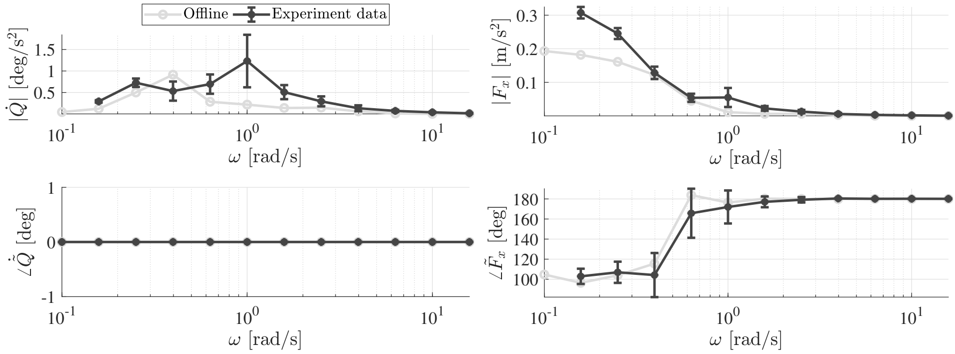

(a) Pitch **(b)** Surge

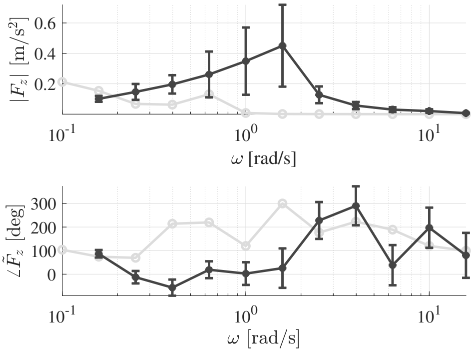

(c) Heave

Figure 3.18: Input signal spectrum for the take-off/abort MTE obtained from experiment data.

From these figures, a number of observations can be made. First, it can be seen that the peak amplitude in both the pitch acceleration spectra (see Figures 3.17a and 3.18a) appears at 1 rad/s. Compared to the offline simulation results (see Figure 3.11), these peak values are larger for the take-off/abort and smaller for the hover MTE, respectively.

Second, in the surge spectrum for the take-off/abort MTE (see Figure 3.18b), the amplitude appears to be larger at low frequencies than predicted in the offline simulation. This is not the case for the hover MTE, although when compared to the offline simulation results, the relative phase of the specific force in this case does appear somewhat flatter over the whole frequency range under consideration. Furthermore, a substantial amount of variability across subjects and runs is present at lower frequencies.

Finally, it can be seen from both heave specific force spectra that the amplitude at frequencies ranging from 0.1 to approximately 8 rad/s is larger than predicted in the offline simulation. This is an indication that pilots are more “active” in the vertical axis than the automatic controller within this frequency range. In [Dalmeijer et al., 2017], this was indeed made evident from time traces of the altitude, where in case of the precision hover and take-off/abort MTEs deviations up to 5 and 20 ft, respectively, were observed.

Tailored OMCTs from experimental data From the spectra in Figures 3.17 and 3.18, the tailored OMCTs corresponding to the precision hover and take-off/abort MTEs were subsequently computed. Figures 3.19 and 3.20 show the individual FRFs in the tailored OMCTs, along with the spread (i.e., standard error) in the experimental data at every individual OMCT prescribed frequency. For reference, the figures also include the corresponding results obtained from the offline simulations in Section 3.3, as well as the corresponding original OMCT results.

From Figure 3.19a pertaining to the precision hover MTE, it is evident that the experimental data follow a similar general trend as predicted in the off-line simulation for Test 1. Furthermore, there is some spread in both the computed amplitude and phase for frequencies below 0.3 and above 2 rad/s. This indicates that pilot control behaviour at those frequencies is affected by the (unstable) longitudinal vehicle dynamics and the presence of turbulence. A similar reasoning also holds for the results corresponding to the take-off/abort MTE in Figure 3.20a. Here, a larger variance at lower frequencies is also present.

Figures 3.19b and 3.20b show the surge FRFs in the tailored OMCTs. From both these graphs, it is clear that the characteristic upswing predicted in the offline simulation is also present and follows a similar trend, as hypothesized. However, more variance in the FRFs appears to be present at lower frequencies (below 1 rad/s), which is true in particular for the FRF pertaining to the hover MTE in Figure 3.19b.

Finally, Figures 3.19c and 3.20c show the heave FRFs for the tailored OMCTs. As also predicted in the offline simulation, and despite large apparent differences in input excitation (see Figures 3.17c and 3.18c), little differences in comparison to to the original OMCT can be discerned. At low frequencies, below approximately 0.3 rad/s, both the offline simulation and experiment data predict a slightly higher amplitude than the original OMCT. For the FRFs corresponding to the take-off/abort MTE, the induced phase lead at low frequencies also appears to be substantially less.

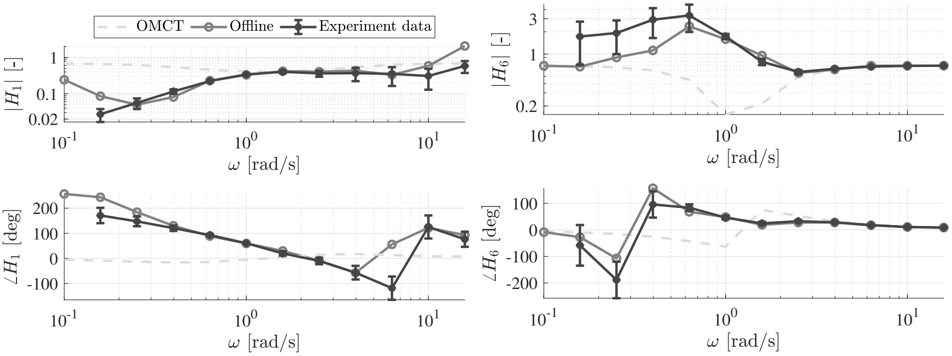

(a) Pitch **(b)** Surge

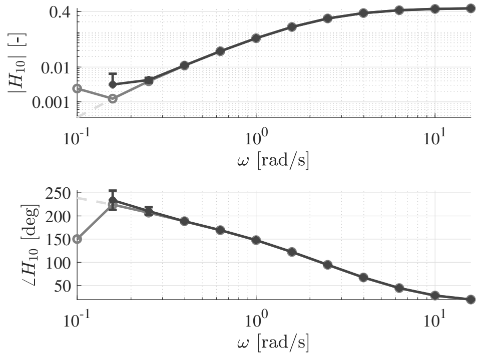

(c) Heave

Figure 3.19: Tailored OMCTs for the hover MTE.

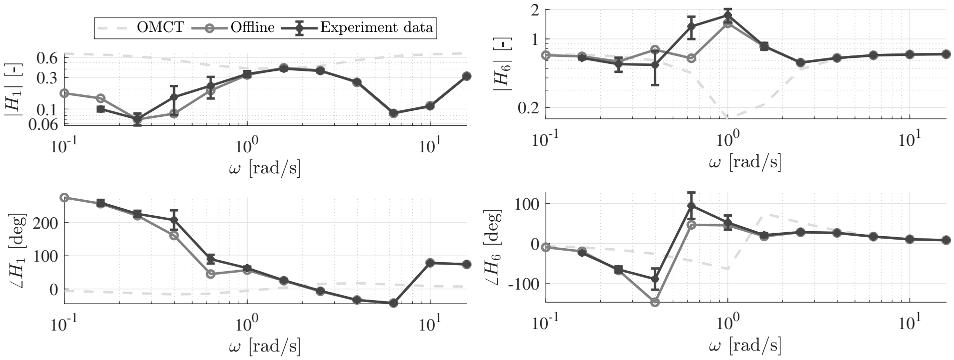

(a) Pitch **(b)** Surge

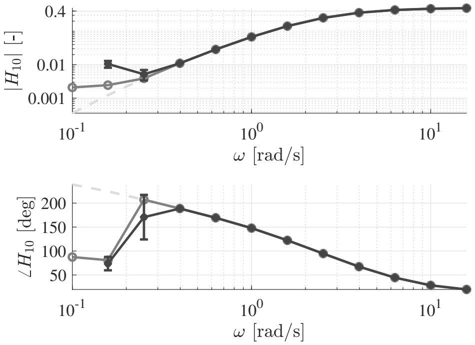

(c) Heave

Figure 3.20: Tailored OMCTs for the take-off and abort MTE.

Sensitivity to break-frequency of high-pass pitch filter Recall from Section 3.4.1 that it was hypothesized that a similar trend with a change in ω_{3_q} in the outcome of Test 6 (surge FRF) of the tailored OMCT would appear as found in Figure 3.13. To examine this effect, time-domain data across all subjects and runs were processed seperately for each experimental condition in Table 3.5.

The corresponding results are shown in Figure 3.21 for both MTEs. It can indeed be be seen that the results are similar to those already obtained in Figure 3.13. Namely, for smaller values of the high-pass pitch filter break frequency, an amplification (or "upswing") in the surge specific force at low to moderate frequencies appears.

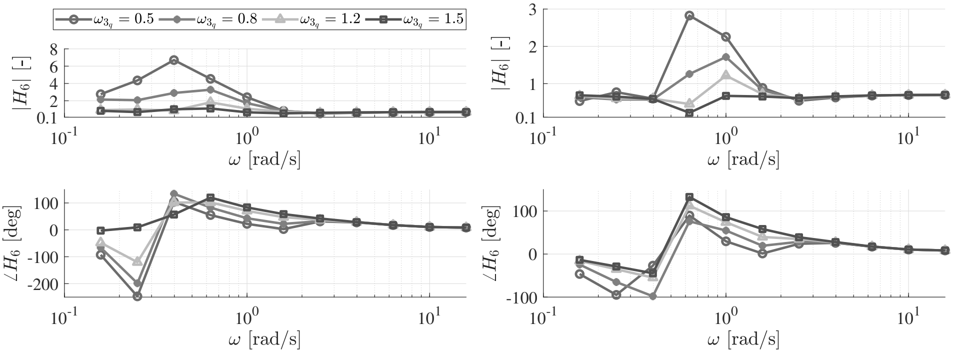

Figure 3.21: FRFs corresponding to Test 6 of the tailored OMCTs, obtained using experimental data from the precision (hover) and take-off/abort (right) MTEs.

3.5. DISCUSSION

This chapter has introduced an alternative to the original Objective Motion Cueing Test (OMCT) proposed by Hosman and Advani [2016]. First, a sensitivity analysis of the effects of the inherent assumptions regarding the OMCT test signals was conducted. These assumptions primarily concern the assumed amplitude as well as the inherent couplings of motion in different degrees-of-freedom. Based on these results, an alternative methodology was devised to define a new, more *tailored*, set of OMCT test signals suitable for helicopter flight simulation. The new test signals are based on the frequency spectra of typical helicopter manoeuvres, obtained from offline simulation of representative tasks using an automatic controller (i.e., "paper pilot") or online piloted simulations. The representative tasks selected are the precision hover and take-off/abort Mission Task Elements (MTEs) described in [Anonymous, 2000].

The new test signals were subsequently used to *simultaneously* (i.e., in a single test) drive the MCA and thereby obtain *tailored* OMCT data for the two MTEs evaluated. This approach has two advantages. First, the new test signals contain not only more realistic information regarding the motion amplitude at different frequencies, but also about the *relative* phase of motion in different degrees-of-freedom. Second, by driving the simulator degrees-of-freedom simultaneously using the new test signals, the inherent couplings governed by the vehicle dynamics are better preserved. These advantages are particularly evident from the strongly differing results obtained for Test 6 (i.e., corresponding to the simulator surge degree-of-freedom). Here, a characteristic amplification (or “upswing”) caused by the inherently coupled pitch-surge dynamics appeared that is not present in the original OMCT data. It was furthermore found that the magnitude of this upswing is most sensitive to changes in the high-pass break frequency of the pitch channel in the CWA.

To validate the results obtained from the offline simulation, a validation experiment on the SIMONA Research Simulator (SRS) was executed. The purpose of this experiment was to evaluate the degree to which the presence of a human controller affects the tailored OMCTs results. In other words, to what extent use can be made of “paper pilots” for this type of analysis. Furthermore, it was of interest to validate the exposed trends in Test 6 of the tailored OMCT with a change in high-pass filter break-frequency in the pitch channel of the CWA. Three pilots were therefore invited to perform the two MTEs on the SRS in motion conditions with a high-pass pitch filter break-frequency from 0.5 to 1.5 rad/s.

The obtained results were found to be largely in line with those obtained from the offline analysis. Most importantly, the characteristic upswing in surge was present in the tailored OMCTs for both MTEs evaluated. However, the tailored OMCTs computed from the experimental data also contained substantial variance, particularly in surge and pitch at frequency below 1 rad/s. Nonetheless, it appears that the tailored OMCTs described in this chapter are able to expose interactions in motion cueing signals that are not fully captured in the present OMCT. Unfortunately however, as mentioned in Section 3.4 and found by Dalmeijer et al. [2017], this apparent difference between the tailored and original OMCTs could not be further corroborated on data from subjective pilot assessment.

3.6. CONCLUSION

Summarizing, this chapter proposed an alternative Objective Motion Cueing Test (OMCT) that is tailored more towards the evaluation of motion cueing fidelity in *helicopter* flight simulation. This new test is computed from frequency domain data derived from typical helicopter flight manoeuvers. The precision hover and take-off/abort Mission Task Element (MTE) were selected as reference tasks. Results from both off-line (“paper pilot”) and on-line piloted flight simulations suggest that the tailored tests are able to expose interactions in motion cueing signals that are not captured in the present OMCT. Nonetheless, it is important to emphasize that the results presented in this chapter are specific to a combination of vehicle and task. A change in either requires a redefinition of the frequency domain data and, hence, might result in substantially different tailored OMCT results. Furthermore, processing of the vehicle- and task-specific frequency domain data is a tedious process sensitive to signal processing particularities and, more importantly, inter-pilot variability. In conclusion, tailored OMCT results are difficult to generalize across differences in vehicle dynamics, tasks and pilots.

To overcome some of these limitations, a more sophisiticated method is desired, one that preferably *decouples* the consideration of motion cueing fidelity from the actual excitation of the vehicle dynamics. In other words, instead of capturing the vehicle dynamics *implicitly* by means of (“paper”) pilot excitation, would it be possible to model the dynamics of *both* the vehicle and the Motion Cueing Algorithm (MCA) and subsequently *couple* these formulations *explicitly*? To this end, the next two chapters of this thesis present a practical and comprehensive methodology, aimed at exposing the intricate three-way interaction between 1) the vehicle dynamics, 2) the task specification and execution and 3) the MCA.

4

EXPLORING HELICOPTER FLIGHT DYNAMICS USING DRAFTSIM

In Chapter 3, substantial differences in the outcomes of the Objective Motion Cueing Test (OMCT) were observed when the input signals to the motion platform were tailored such to implicitly account for the flight dynamics of helicopter. This input-output signal approach, however, was also found to have some limitations. In this thesis, a method is therefore sought that more explicitly incorporates helicopter flight dynamics. Before such an approach can be developed, however, a comprehensive understanding of the existing tools and methods to study helicopter flight dynamics is necessary. This chapter aims to develop that knowledge.

First, Section 4.1 presents an overview of a six (rigid-body) degrees-of-freedom helicopter flight dynamics model is given. In Section 4.2, the model is applied to an example case of the Bo-105 helicopter, where rotorcraft trim and dynamic stability characteristics are examined. Section 4.3 documents a handling qualities evaluation of an independently-developed model of the AH-64 helicopter conducted on the Desdemona simulator.

4.1. OVERVIEW OF DRAFTSIM AND ITS PARAMETERS

Delft Rotorcraft Simulation (Draftsim) is the name of a helicopter flight dynamics model developed as part of this dissertation. It is aimed at predicting helicopter flight characteristics in *low to moderately agressive* manoeuvering flight. Furthermore, it strives to be most suitable for applications where *high performance* (i.e., fast) and *real-time* (i.e., pilot-in-the-loop) execution are desired. The model is implemented directly in the C++ programming language, leveraging the capabilities of the Eigen matrix template library [Jacob and Guennebaud, 2018]. For off-line simulation, a wrapper was developed using Cython [Behnel et al., 2018] and Eigency [Boomsma, 2018]. This extension allows the model to be executed in a user-friendly Python programming environment while still maintaining high performance and avoiding duplicate implementations.

Because Draftsim is aimed at predicting helicopter flight dynamics primarily in basic maneuvering flight, several simplifying assumptions are made throughout the model. These are stipulated in detail in Appendix A, however the most significant assumptions are also listed here:

- The main rotor blades are assumed to be rigid, with all flexibility concentrated at the hub in the form of an eccentric flapping hinge.
- The main rotor blade flapping dynamics are principally assumed to be *quasi-steady*, which means that a blade's flapping response is treated as *instantaneous* due to a change in blade pitch or local flow conditions.
- The main (and tail) rotor blade lead-lag and torsional dynamics are neglected.
- The main and tail rotor angular speeds are assumed to be constant. This is a reasonable assumption for all but the most extraordinary flight conditions (e.g., autorotation).
- Blade aerodynamics are assumed to be *linear* and (dynamic) stall effects are neglected.
- The tail rotor blade flapping dynamics and built-in pitch-flap coupling are neglected. This means that the tail rotor generates an *instantaneous* thrust force in response to a change in tail rotor (collective) blade pitch.
- Terms in the various rotor equations that are $\ll \mu^2$, where μ is the rotor *advance ratio* (defined by $V_\infty \cos\alpha_c/\Omega R$, see Equation (A.33)), are neglected. According to Padfield [2007], this incurs an error of less than 10% in the rotor's flap angle response.

An overview of the model parameters in Draftsim is given in Table 4.1. Detailed background information on the listed parameters can be found in Appendix A. As an example, the value of each parameter for the the Bo-105 helicopter is also included in the table [Kerler et al., 2012; Padfield, 2007; Pavel, 2001; Wan, 2014]. In the following sections, the different classes of parameters are discussed in more detail.

Table 4.1: Example list of model parameters corresponding to the Bo-105 helicopter.

Parameter	Description	Example (Bo-105)	Unit
$a_{0_{mr}}$	Main rotor lift curve slope	6.11	1/rad
$a_{0_{tr}}$	Tail rotor lift curve slope	5.70	1/rad
$a_{0_{ht}}$	Horizontal tail lift curve slope	3.26	1/rad
$a_{0_{vt}}$	Vertical tail lift curve slope	2.70	1/rad
α_{ht_0}	Horizontal tail incidence	4.00	deg
β_{vt_0}	Vertical tail incidence	-4.65	deg
c	Main rotor blade chord length	0.27	m
g_{tr}	Tail rotor gearing ratio	5.25	-
e	Main rotor equivalent blade eccentricity	0.142	-
ψ_{mx}	Cyclic pitch control mixing angle	12.0	deg
I_β	Main rotor blade moment of inertia	231.7	kg m^2
I_{xx}	Roll moment of inertia	1433	kg m^2
I_{xz}	Asymmetric moment of inertia	660	kg m^2
I_{yy}	Pitch moment of inertia	4973	kg m^2
I_{zz}	Yaw moment of inertia	4099	kg m^2
m	Helicopter gross weight	2200	kg
m_b	Main rotor blade mass	27.3	kg
n_b	Number of rotor blades	4	-
R	Main rotor radius	4.91	m
R_{tr}	Tail rotor radius	0.95	m
S_{vt}	Vertical tail surface area	0.81	m^2
S_{ht}	Horizontal tail surface area	0.80	m^2
$\bar{f}s_0$	Fuselage drag frontal area	[1.3,7.0,3.7]	m^2
V_{fs_m}	Fuselage volume for drag pitch moment	8.43	m^3
V_{fs_n}	Fuselage volume for drag yaw moment	19.45	m^3
k_{fs}	Correction factor for fuselage drag	0.83	-
σ_{tr}	Tail rotor solidity	0.12	-
$\bar{x}_{cg}$	Center of gravity coordinates	[0.0,0.0,0.0]	m
$\bar{x}_{mr}$	Main rotor coordinates	[-0.03,0.0,-1.48]	m
$\bar{x}_{tr}$	Tail rotor coordinates	[-6.03,-0.32,-1.72]	m
$\bar{x}_{vt}$	Vertical tail coordinates	[-5.45,0.0,-0.6]	m
$\bar{x}_{ht}$	Horizontal tail coordinates	[-4.59,0.0,-0.6]	m
γ_s	Main rotor shaft tilt (pos. forward)	3.0	deg
θ_{tw}	Main rotor blade tip twist	-6.2	deg
$\theta_{tw_{tr}}$	Tail rotor blade tip twist	0.0	deg
Ω	Main rotor rotational speed	44.4	rad/s

4.1.1. VEHICLE GEOMETRY, INERTIA AND MASS

The vehicle geometry pertains to the relative location of the various helicopter subsystems. These are denoted in Table 4.1 by the $\bar{x}_\square$s in the list of parameters. The location of the vehicle center of gravity (c.g.) is denoted by $\bar{x}_{cg}$. The reference point with respect to which these quantities are specified is arbitrary, but the reference frame convention used is *right-handed* with the x-axis pointing forward (see also Appendix A). In Draftsim, the value for the location of subsystems and the vehicle c.g. is therefore a vector containing three elements. For the most part, these parameters are used to correctly resolve the *resultant* moments with respect to the vehicle c.g. However, the parameters are also used to compute the velocity components perceived at each individual subsystem, which affects quantities like angle of attack and generated (lift or drag) force. An overview of the different reference frames in conjunction with the forces and moments acting on the vehicle is shown in Figure 4.1.

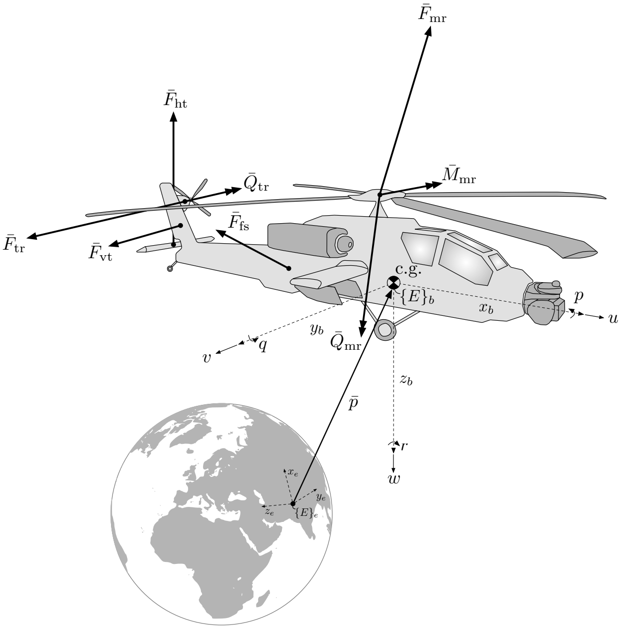

Figure 4.1: Free body diagram of a helicopter in flight, showing the different components, reference frames and forces and moments (vehicle wireframe based on 3D-render by [Sabates, 2016]).

The *total* vehicle mass is denoted by the parameter m, whereas its moments of inertia are denoted by I_{xx}, I_{yy}, I_{zz} and I_{xz}, respectively. The latter assumes that the vehicle is (nearly) symmetric with respect to the *vertical* plane spanned by the body x- and z-axes. These parameters appear directly in the equations of motion and therefore strongly affect the dynamic response of the vehicle.

4.1.2. MAIN ROTOR PARAMETERS

The majority of the parameters in Table 4.1 pertain to the main rotor, as this is the most complex system in the model. Most of these parameters are rather self-explanatory (e.g., number of blades, rotor radius, chord, etc.). Others, however, require additional explanation.

The parameter e is listed as the blade eccentricity, expressed as a fraction of the rotor radius. However, it should be noted that this is the *equivalent* blade eccentricity and *not* the physical offset of the flapping hinge with respect to the hub. The purpose of the equivalent blade eccentricity parameter is to match the *first flap frequency* of the rotor system. The normalized first flap frequency, λ_β, is expressed as a fraction of the rotor angular velocity and its value is typically slightly greater than unity.

Given a value for λ_β, it is possible to derive an approximation for e_{mr}. The parameter ϵ introduced in Appendix A, which can be described as a measure of the *hub stiffness*, is related to the normalized first flap frequency through:

$$\epsilon + 1 = \lambda_\beta^2 \tag{4.1}$$

However, assuming a uniformly distributed mass, it can also be derived that (see Appendix A, Equation (A.69)):

$$\epsilon = \frac{3e}{2(1-e)} \tag{4.2}$$

Thus, a direct relation exists between the equivalent blade eccentricity and the first flap frequency of the rotor system. Due to the prominent role of ϵ in the flapping equation (see Equation (A.16)) and the direct influence of e in the magnitude of the centrifugal moments generated at the rotor hub (see Equation (A.58)), it is a parameter that strongly affects the dynamic response characteristics of the helicopter. Because the specification of e effectively sets the first flap frequency, it also primarily governs the degree of cross-coupling between roll and pitch responses as a result of cyclic control inputs. This cross-coupling can be mitigated to some extent by *cyclic control mixing* (through ψ_{mx}, see Appendix A.2.7).

Another notable parameter pertaining to the main rotor is I_β, which is the flap moment of inertia that appears in the expression for the blade *Lock number* (γ) given by Equation (A.33). The Lock number is a measure of the magnitude of aerodynamic forces acting on the blade in relation to inertial forces. The aerodynamic forces are represented by the air density (ρ), the lift curve slope of the blade airfoil ($a_{0_{mr}}$), the blade chord (c) and radius (R). As can be seen from Equations (A.40) and (A.41) in Appendix A, the Lock number strongly affects the flap response of the blades. Also note that, because the Lock number varies with air density, it changes with flight altitude and, hence, the blade flapping response is also affected by altitude.

4.1.3. TAIL ROTOR PARAMETERS

The tail rotor model in Draftsim is essentially a simplified version of the main rotor. The primary differences with the main rotor are that blade flapping as well as in-plane forces and moments are neglected. This also means that *pitch-flap coupling* typically built-in to tail rotors was not included in the model. In effect, the tail rotor only produces a single thrust force (directed along the body y-axis) and torque (about the body y-axis).

Table 4.1 contains several parameters that pertain to the tail rotor. The parameters that determine the geometry of the tail rotor are the radius (R_{tr}) and *solidity* (σ_{tr}). The solidity was defined in Appendix A.2.2 of Appendix A as:

$$\sigma_{\Box} = \frac{n_{b_{\Box}} c_{\Box}}{R_{\Box} \pi}$$

where □ denotes either the main (mr) or tail (tr) rotor. In effect, the solidity expresses the total blade area relative to the disk area and directly *scales* the force produced by the tail rotor as can be seen from Equation (A.72).

The parameter $a_{0_{tr}}$ is the lift curve slope corresponding to the airfoil used on the tail rotor and directly influences the *effectiveness* of the tail rotor. On the other hand, the tail rotor blade twist ($\theta_{tw_{tr}}$), if set, reduces the effectiveness of the tail rotor. Finally, the parameter g_{tr} is the tail rotor *gearing ratio*, which when multiplied by the main rotor angular velocity (Ω) yields the (constant) angular velocity of the tail rotor.

4.1.4. FUSELAGE PARAMETERS

At higher flight speeds, the fuselage is an important contributor to the total forces and moments acting on the vehicle. As such, the inclusion of its effect in Draftsim is requisite. It has been opted, again for simplicity sake, to implement an empirical model to capture the aerodynamic drag forces and moments generated by the fuselage. This model is from [Marinescu and Anghel, 1992] and is similar to the one implemented by [Pavel, 2001].

The parameters in Table 4.1 that pertain to the fuselage are $\bar{f}s_0$, V_{fs_m} and V_{fs_n} and k_{fs}. The former two parameters determine the magnitude of the drag *forces* along the three body axes. $\bar{f}s_0$ is a vector that contains the *equivalent flat plate* areas as seen from the front, side and bottom, respectively. Often, only the *frontal* equivalent flat plate area is specified. However, by calculating the ratios of the *geometric* areas of the front, side and bottom of the fuselage, it is possible to approximate the other equivalent flat plate areas.

V_{fs_m} and V_{fs_n} are equivalent volumes computed (or approximated) using Equation (A.79). These two parameters govern the pitch and yaw moments generated by the fuselage. The parameter k_{fs} is a correction factor, typically between 0.8 and 1.0, to directly scale the magnitude of the moments. Its value is a function of the ratio of the fuselage length and diameter [Marinescu and Anghel, 1992] (see Figure A.8).

4.1.5. EMPENNAGE PARAMETERS

The empennage for a conventional helicopter consists of a horizontal and vertical tailplane typically mounted aft of the main rotor. In Draftsim, these are modelled as simple *lifting surfaces*. As such, the associated parameters pertain to the aerodynamic characteristics of the surface (i.e., lift coefficients $a_{0_{ht}}$ and $a_{0_{vt}}$) as well as geometrical properties (i.e., surfaces S_{ht} and S_{vt}). Principally, the lift generated by the horizontal and vertical tailplane is therefore proportional to the perceived angle of attack (α_{ht}) and angle of sideslip (β_{vt}), respectively. However, the surface may be mounted such that a force is generated in normal (i.e., straight and level) forward flight. This is accommodated through the built-in incidence angles $\alpha_{0_{ht}}$ and $\beta_{0_{vt}}$.

4.2. TRIM AND DYNAMIC STABILITY ANALYSIS

This section presents the application of the Draftsim model to the Bo-105 helicopter. First, the results of a trim sweep are given to verify trends in the static equilibrium of the vehicles as a function of forward flight speed. Finally, linearization results are presented to study and verify the inherent dynamic characteristics of the modelled helicopters. The Bo-105 analyses are used as the primary means of verification of the Draftsim model. This is because a substantial amount of validation data are available in the open literature.

During these discussions, it will be attempted to clarify discrepancies between Draftsim results and the reference data by "tuning" some of the model parameters. Note that this is meant solely for illustrative purposes and is otherwise beyond the scope of this thesis. Thus, the Bo-105 model parameters listed in Table 4.1 are *not* changed for the analyses in the remainder of this thesis.

4.2.1. MODEL PARAMETERS

The values for the Bo-105 model parameters listed in Table 4.1 were mostly taken from Padfield [2007]. Note that the main rotor equivalent blade eccentricity listed in Table 4.1 was calculated from the specified flapping hinge stiffness (K_β) of 113330 Nm/rad using [Padfield, 2007]:

$$\lambda_\beta^2 = 1 + \frac{K_\beta}{I_\beta \Omega^2} \tag{4.3}$$

and subsequently applying relations Equations (4.1) and (4.2) to obtain a value for e.

The locations of the various vehicle subsystems are specified with respect to the vehicle center of gravity. These were taken from [Wan, 2014]. Also, because a different fuselage drag model is used in Draftsim than the one applied in [Padfield, 2007], the values for parameters pertaining to fuselage drag were approximated from the known geometry of the helicopter. To this end, the equivalent (frontal) flat plate drag area of the fuselage and the correction factor k_{fs} from [Pavel, 2001] were used. The value for single blade mass (m_b) was also taken from [Pavel, 2001]. Finally, the cyclic mixing angle ψ_{mx} is mentioned in [Kerler et al., 2012].

4.2.2. TRIM IN FORWARD FLIGHT

Figures 4.2 and 4.3 show the trim curves corresponding to the Bo-105 helicopter. Also shown in the figures are reference values taken from [Padfield et al., 1996], corresponding to the the Common Baseline Model (CBM) developed as part of GARTEUR Action Group (AG) 06 and documented in the same paper. This model is similar to Draftsim in terms of its fidelity level, in the sense that it is a six dof rigid-body model of helicopter dynamics, where all rotor dynamics are considered *quasi-steady*.

Figure 4.2 shows the control deflections (in degrees). Overall, the match with the reference data is satisfactory. All trends in control positions with increasing airspeed are accurately predicted. It appears, however, that the collective position is consistently higher than that of the (baseline) CBM model. Though the exact parameters of the CBM model were not specified, an alternative collective trim curve corresponding to a higher mean lift curve slope of the main rotor was also provided. This alternative curve significantly improves the match with Draftsim. At higher speeds, from approximately 80 kts, Draftsim predicts higher collective deflections. As expected, this is also reflected in the lateral cyclic stick and pedal positions. For a higher collective position, more pedal deflection (to the left, which generates a force *along* the body y-axis) is required which increases the roll moment, hence also necessitating a larger lateral cyclic deflection (also to the left). In contrast, the longitudinal cyclic stick position matches the reference data remarkably well.

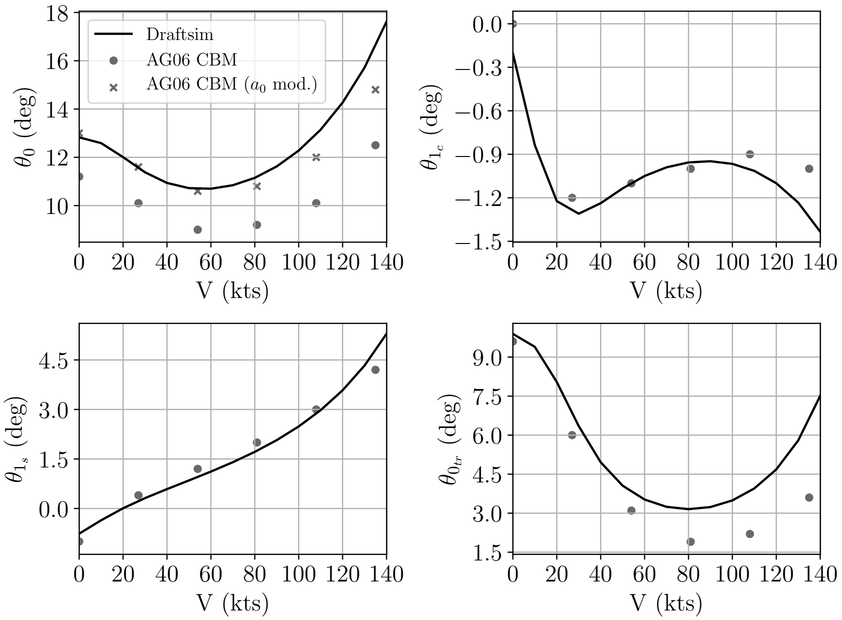

Figure 4.2: Control deflections in trim as a function of forward flight speed for the Bo-105 helicopter.

Figure 4.3 shows the helicopter attitude and disc tilt angles. Here, only reference data for the pitch angle are available from [Padfield et al., 1996]. The pitch angle matches well with the reference data up to speeds of approximately 80 kts, above which the required helicopter pitch angle is overestimated. As expected, the disc coning angle (β_0) follows the trends of the collective control position. The trend of the longitudinal disc tilt angle (β_{1_c}) is positive (i.e., towards the rear) with increasing airspeed. As noted in Padfield [2007], the longitudinal disc tilt compensates for the residual of the sum of (longitudinal) moments acting on the other helicopter components. In Draftsim, the predicted residual moment for the Bo-105 is negative (i.e., pitch forward) and therefore positive disc tilt is required for equilibrium. A similar reasoning applies to the lateral disc tilt. Also note that the disc tilt angles required are in the order of a few degrees only.

The over-approximations of the trim curves predicted by Draftsim at higher speeds are explained by the simplified fuselage drag model currently implemented. For example, the parameters $\bar{f}_0$ and V_{fs_m} are found to have a strong impact on the predicted trends and magnitudes of the trim curves in longitudinal direction. Nulling the effect of V_{fs_m} affects

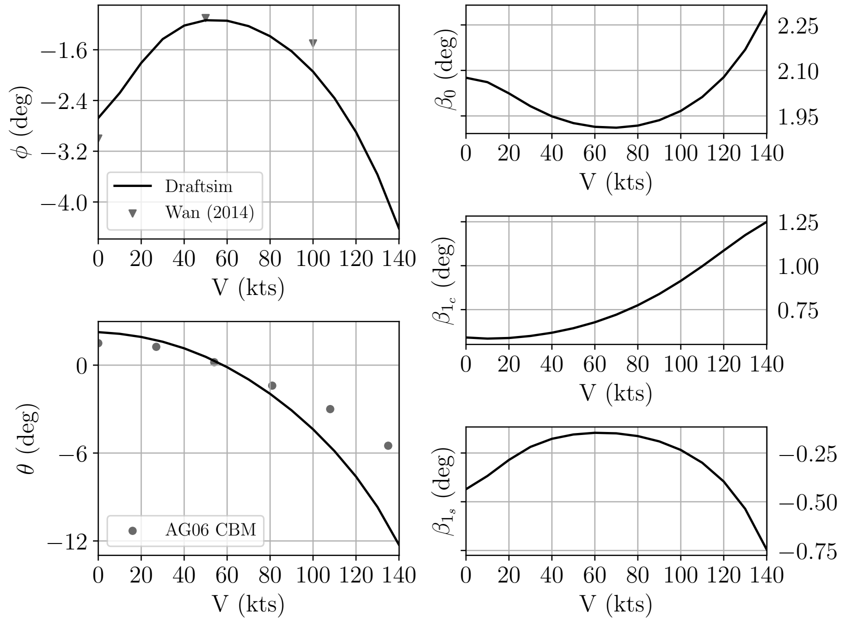

Figure 4.3: Bo-105 helicopter attitude and disc tilt angles in trim as a function of forward flight speed.

the longitudinal cyclic trim position and entails a longitudinal disc tilt in the opposite direction (i.e., forward) with increasing flight speed. Also, reducing the value for fs_0 to 0.8 drastically improves the match of the trim curves at higher forward flight speeds, in particular the helicopter pitch angle.

4.2.3. DYNAMIC STABILITY ANALYSIS

The linearization results are presented in two forms. First, the eigenvalues of the linearized system matrix are inspected to study the dynamic properties of the helicopter. These consist of the frequency and stability of the characteristic vehicle *modes*. Second, the properties of the input matrix are studied to determine the sensitivity of the helicopter to control inputs. To this end, control derivaties are computed and compared to reference data for different forward flight speeds.

Eigenvalue analysis For the Bo-105, the results of the eigenvalue analysis are summarized in Figure 4.4. In the figure, each eigenvalue is labelled according to the name of its corresponding mode and, where applicable, arrows indicate trends with increasing airspeed (from 0 to 140 kts, with steps of 20 kts). The results predicted by Draftsim for the Bo-105 are compared with reference data obtained from Helisim, also shown in the figure. Helisim is a helicopter simulation model developed and described by Padfield [2007] that is of similar fidelity as Draftsim.

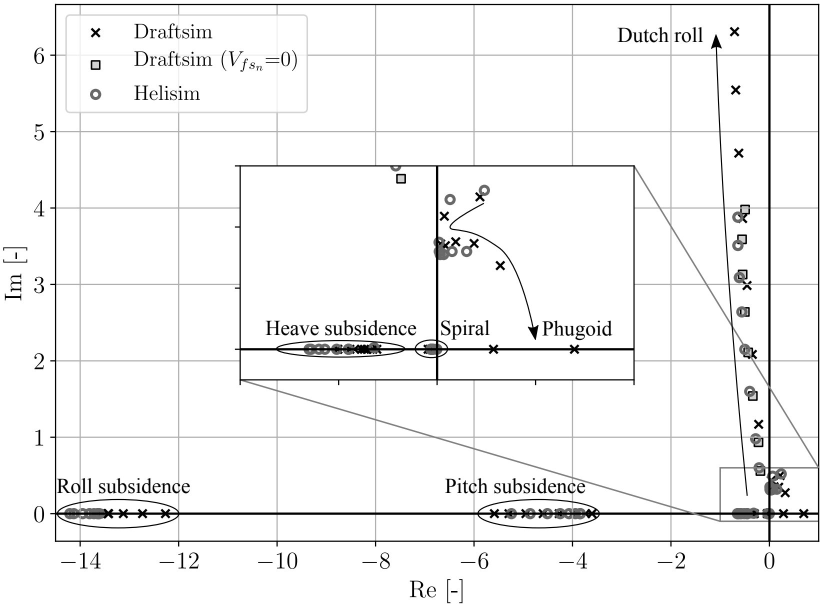

Figure 4.4: Bo-105 eigenvalues compared with reference data from [Padfield, 2007].

It can be seen that the dynamic properties of the Bo-105 are well predicted in comparison to Helisim. Again, the largest offsets with respect to the reference data occur at higher flight speeds, where the fuselage aerodynamics become important. The largest discrepancy is seen in the Dutch roll mode. Whereas the general trend of this mode is well-captured by Draftsim, its frequency at higher speeds is overestimated when compared to Helisim. From the figure, it can be seen that nullifying the effect of V_{fs_n} greatly improves the quality of match of the Dutch roll mode with respect to Helisim, with negligible changes seen in the other vehicle modes. More minor discrepancies are found in the phugoid and roll subsidence modes. The trend of the phugoid mode is over-predicted for higher airspeeds and, at 140 kts, the mode even becomes non-oscillatory. This, again, can be attributed to the simplified fuselage aerodynamic moment in Draftsim. Reducing the value for V_{fs_m} was found to greatly improve the match with the reference data.

Control derivatives Figures 4.5 and 4.6 show the computed control derivatives as a function of forward flight speed in comparison to those predicted by Helisim and documented in Padfield [2007]. Note that the units used for these derivatives differ between the models and, therefore, two separate scales are shown in the figures. In Draftsim, control inputs are regarded as percentages of corresponding blade ranges. The Helisim derivatives, however, are reported using the actual blade angles (in radians). While this makes comparing absolute amplitudes difficult, the main objective here is merely to verify the general trends of the derivatives with airspeed. Also note that the Helisim reference data were obtained by manually reading off figures and may contain slight inaccuracies as a result. Finally, note that Helisim uses a reversed sign convention for the cyclic control inputs as compared to Draftsim. For purposes of comparison, the sign of all Helisim derivatives pertaining to the cyclic controls have therefore been reversed.

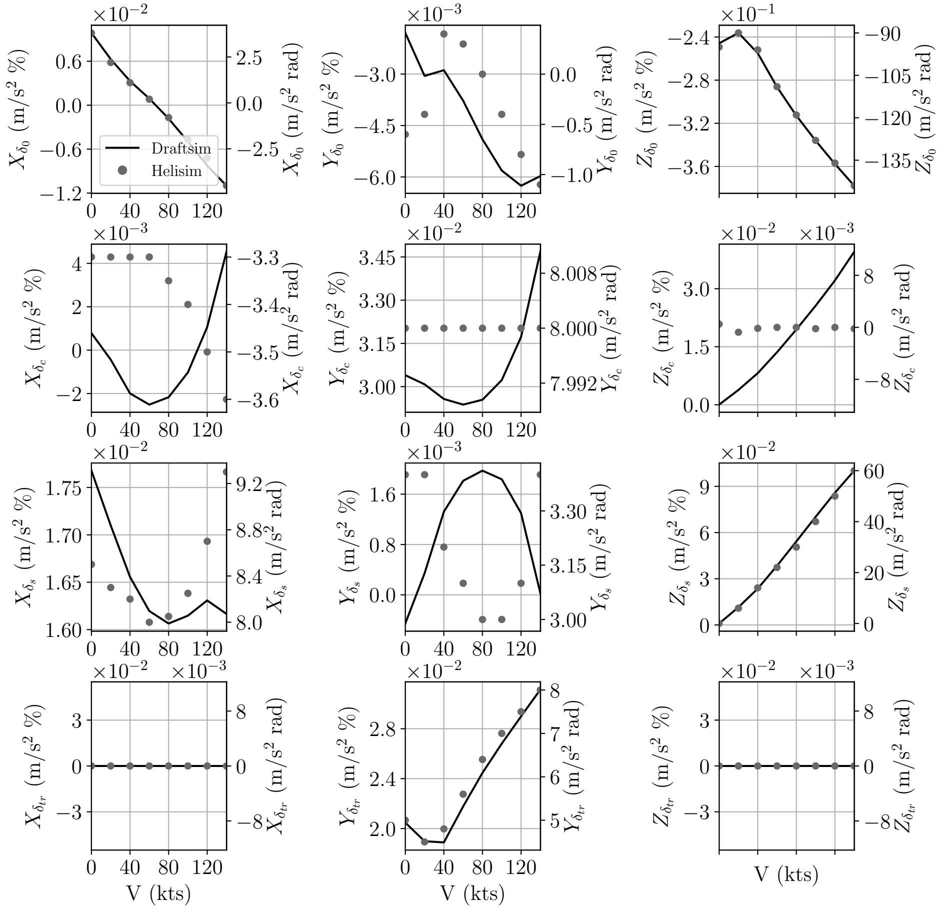

Figure 4.5: Bo-105 force control derivatives as function of forward flight speed compared with reference data.

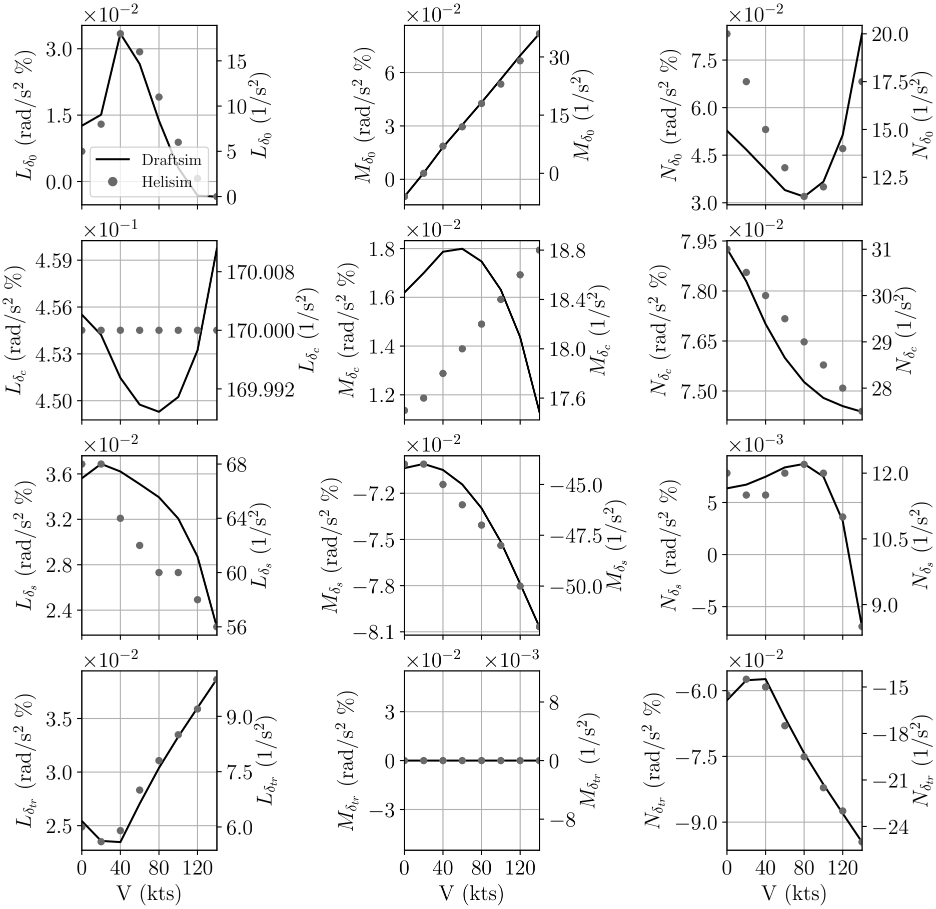

Figure 4.6: Bo-105 moment control derivatives as function of forward flight speed compared with reference data.

From Figure 4.5, mixed results in terms of the quality of match between Draftsim and Helisim derivates can be seen. While trends with increasing airspeed of several derivatives match remarkably well (e.g., X_{δ_0}, Z_{δ_0}, Z_{δ_s} and $Y_{\delta_{tr}}$), others exhibit some discrepancies. Notable examples are X_{u_c} and Y_{δ_s} (i.e., the cross-derivatives), where the predicted trends with airspeed seem reversed with respect to Helisim. For a few derivatives, trends with increasing airspeed are predicted well only for a limited range of airspeeds. For example, the declining trend of X_{δ_s} matches up to approximately 80 knots, but breaks down at higher airspeeds. It was found that this is related primarily to the fuselage aerodynamic parameters selected. For example, the quality of match of X_{δ_s} at speeds above 80 knots could be improved by setting a substantially larger value for V_{fs_m}. Another parameter that was found to affect the values of the force derivatives with respect to δ_c and δ_s is the cyclic phase mixing angle ψ_{mx}. For example, nulling this parameter was found to bring the *sign* of Y_{δ_s} at low speed in agreement with Helisim, but also results in an increased amplitude for *all* cross-derivatives and thus the overall cross-coupling between pitch and roll inherent in the model. It is unclear, however, whether the Helisim data reported by Padfield [2007] includes the effect of cyclic phase mixing through ψ_{mx}.

From Figure 4.6, it can be seen that the match between Draftsim and Helisim is in line with the predictions obtained from the force derivatives. Both in terms of the signs and trends of the derivatives with increasing airspeed. The only notable exceptions are L_{δ_c} and M_{δ_c}. The variation with airspeed predicted by Draftsim in case of the former, however, is negligible for the range of airspeeds under consideration, whereas in case of Helisim it is constant. The discrepancy seen in the trend of M_{δ_c} seems more significant. Up to approximately 60 kts, the predicted trends between the models match, whereas above this speed Draftsim predicts a sharp decline in amplitude in contrast to Helisim. This trend could be reproduced in Draftsim by nulling the effect of ψ_{mx} and substantially reducing the value of the fuselage frontal area.

It can be concluded from this analysis that Draftsim predicts the dynamic characteristics of rotorcraft reasonably well in comparison to a model of similar fidelity. Some differences between Draftsim and Helisim in the control derivatives were exposed, but pertained primarily to cross-derivatives, the magnitude of which is considerably smaller in comparison to the on-axis derivatives. The discrepancies that were observed at higher speeds can be attributed primarily to the fuselage aerodynamics. Also, the possible absence of cyclic phase mixing (through ψ_{mx}) in the Helisim model could explain some of the discrepancies seen in the cross-derivatives.

4.3. HANDLING QUALITIES EVALUATION

From the application of Draftsim to the Bo-105 helicopter in the preceding section, sufficient confidence was gained regarding the accuracy of the model in predicting trim as well as dynamic stability. In this section, Draftsim will therefore be applied to a different helicopter type, the Boeing AH-64 Apache, in a pilot-in-the-loop handling qualities evaluation.

The necessary model parameters for the AH-64 were gathered from a number of sources available in open literature. The reference data for the most part originate from the test program performed by the United States Airforce on the AH-64A in the early 1980's [Anonymous, 2002; Bender et al., 1981, 1984; Hossein Mansur, 1995; Kelley, 1990; Kunz and Jones, 2001; Picasso et al., 1982]. Data against which this model could be verified were

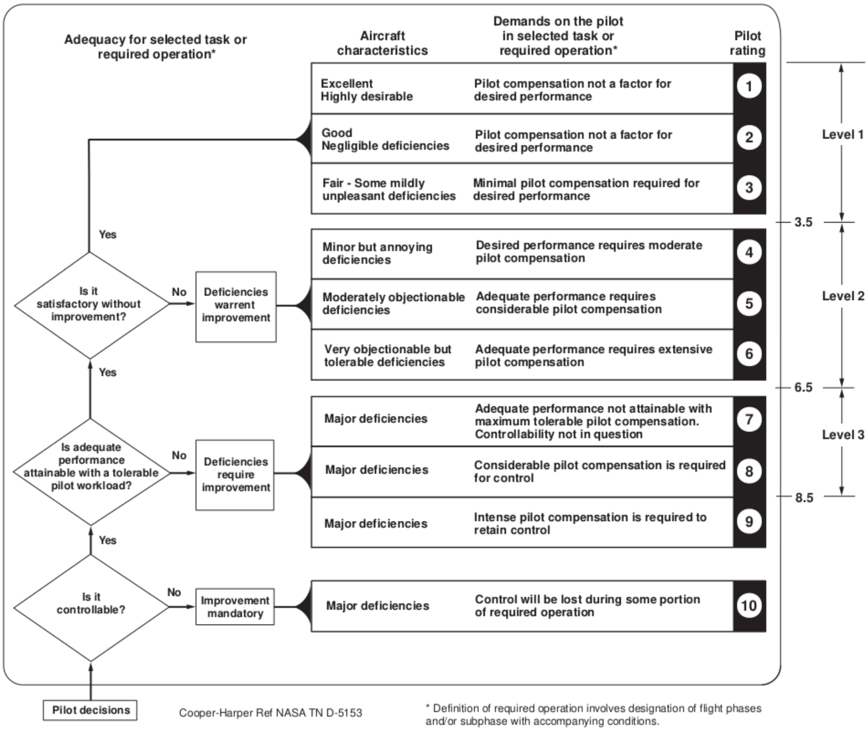

Cooper-Harper Ref NASA TN D-5153

* Definition of required operation involves designation of flight phases and/or subphase with accompanying conditions.

Figure 4.7: The Cooper-Harper HQ Rating (CHR) scale [Cooper and Harper, 1969].

scarcely available. Appendix B presents a comparison of stability and control derivatives (in hover) with reference data that could be found in open literature. Unfortunately, this comparison did not produce satisfactory results. This is undoubtedly the result of uncertainty in the model parameters and some peculiarities in the reference data. The HQs analysis in this section is therefore aimed at establishing the extent to which the model in its current form is *representative* of the actual AH-64 Apache helicopter in *basic manoeuvering flight*. Note that this does not and cannot constitute a formal *validation* of the model fidelity. It *can*, however, uncover whether *any* deficiencies in the model, whichever their origin, are acceptable to the point that similar HQs are obtained in comparison to the actual helicopter.

To support HQs evaluations in the development of rotorcraft, the United States Army has devised an Aeronautical Design Standard [Anonymous, 2000], ADS-33E, specifying requirements on task performance and vehicle HQs. These specifications provide criteria on both *predicted* (or *quantitative*) and *pilot-assigned levels* of HQs. These levels are based on definitions found in the Cooper-Harper HQ Rating (CHR) scale, and are shown in Figure 4.7 [Cooper and Harper, 1969].

Predicted HQs levels are derived from quantitative data gathered from flight tests and/or model-based simulations. Pilot assigned levels, on the other hand, are determined by *test pilots* trained to evaluate the amount of *pilot compensation* required to attain prescribed levels of adequate and/or desired task performance. ADS-33E describes a wide range of manoeuvers , or Mission Task Elements (MTEs), to be evaluated in order to obtain assigned levels of HQs. Because the present thesis focusses on helicopter flight dynamics in basic manoeuvering flight, only criteria and tasks characterized as *low to moderate agility* are selected. Also, because in Section 4.2 it was found that Draftsim is accurate primarily at relatively low speed flight and because this is also the main flight envelope of interest in helicopter applications, only hover and low speed speed flight will be considered. In the following sections, the evaluation of the predicted and pilot-assigned handling qualities, respectively, of the developed AH-64 flight dynamics model are presented.

4.3.1. PREDICTED HANDLING QUALITIES

In ADS-33E, several criteria are formulated that pertain to hover and low speed flight, with low to moderate (L/M) agility. Here, the "All Other MTEs" criteria apply and a distinction is made between small and moderate amplitude attitude changes. For the former, requirements on *bandwidth* and the *mid-term response* are given, whereas in the case of the latter criteria on the *attitude quickness* are specified. All analyses are performed with the Stability and Control Augmentation System (SCAS) *enabled* (see Appendix A.9.1). In case of the bandwidth and mid-term response analyses, both *rate* and *attitude* feedback are active. For the attitude quickness analysis, only *rate* feedback is active, because pilots are assumed to perform larger amplitude attitude changes with FTR enabled[1].

Bandwidth The bandwidth criteria from ADS-33E aim at evaluating the aircraft short-term response characteristics for small amplitude attitude changes. It is a measure of the frequency range over which the pilot can excert active control. The bandwidths have been computed using transfer functions derived from linearized and reduced dof models (see Appendix A.8), containing only the vehicle's *angular rates* and *attitudes*. The resulting bandwidths per axis (in hover) are shown in Figure 4.8 along with the boundaries specified in ADS-33E.

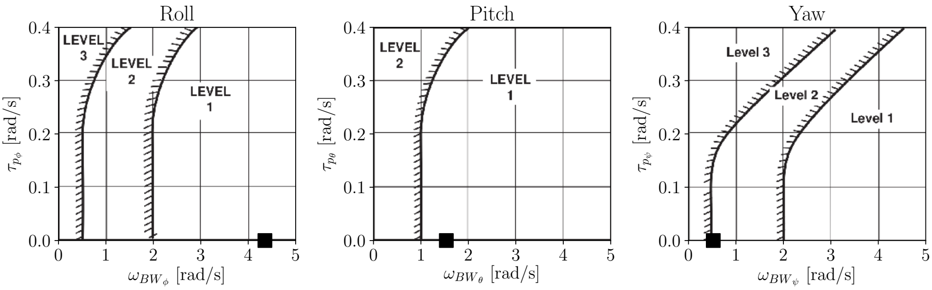

Figure 4.8: Predicted bandwidth per axis in hover, including ADS-33E boundaries [Anonymous, 2000].

---

[1] Note that when pilots engage the Force Trim Release (FTR) on the cyclic grip, typically during more dynamic manoeuvers, the attitude feedback loops are disengaged and the corresponding setpoints are reset. The rate feedback loops, in contrast, are always enabled.

From the figure, it can be seen that the bandwidth in roll is firmly in the Level 1 region, as is the bandwidth in pitch. In yaw, the bandwidth is approximately on the boundary between Level 2 and 3. Also note that in all cases the *phase delay* parameter $\tau_{p_\square}$ is zero (i.e., no phase delay). This is because, in the bandwidth calculation method used, the phase of the transfer functions from the controls to the attitude angles were found to never cross the neutral stability limit of -180°. This, in turn, is explained by the lack of modelled delays in the system (e.g., actuators).

Mid-term response The mid-term response criteria from ADS-33E also pertain to small amplitude attitude changes, but consider the *mid-term* responses. These criteria are specified in terms of limits on damping and frequency of pitch, roll and yaw oscillations. For the AH-64, notable oscillations occur only in pitch (i.e., the phugoid) and yaw (i.e., the Dutch roll). The characteristics of these oscillatory motions can also be obtained from linearized models (see Appendix A.8) and are shown in Figure 4.9, for the cases where the SCAS is both enabled and disabled. HQss boundaries from ADS-33E are also shown in the figure.

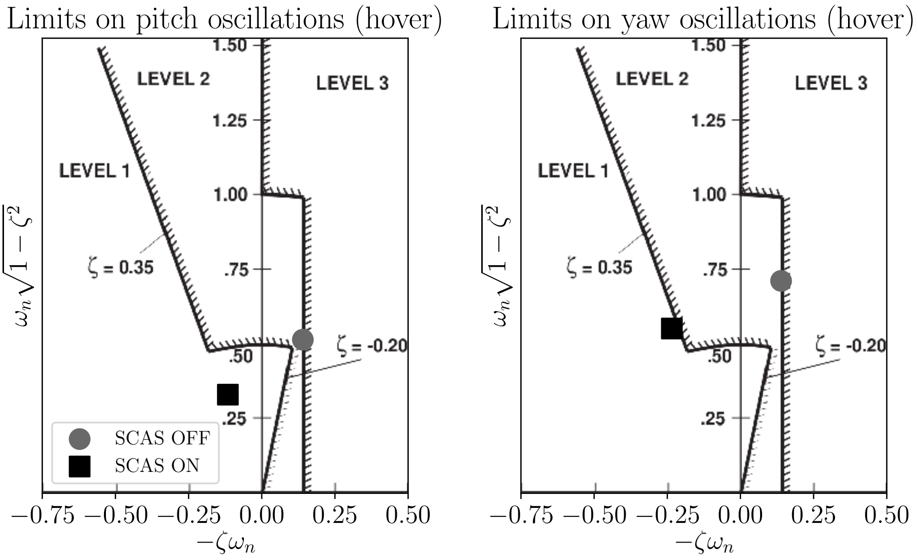

Figure 4.9: Predicted pitch and yaw oscillation characteristics in hover, including ADS-33E boundaries [Anonymous, 2000].

With the SCAS *disabled*, it can be seen that the characteristics of both the pitch and yaw oscillations are on the boundary of Level 2 and 3. With the SCAS enabled, however, both become Level 1. This shows that the SCAS is effective at improving the (mid-term) response characteristics of the model.

Attitude quickness The last metric considered is the *attitude quickness* and captures the characteristics of the aircraft for the case of moderate amplitude attitude changes. Attitude quickness is a measure of the *agility* with which a certain change in attitude can be realized. It is obtained from *isolated* pulse-input responses, with varying pulse durations and fixed control input amplitudes in the pitch, roll and yaw dofs. The pulse durations were chosen as 0.6, 1.2, 1.8, 2.4 and 3.0 seconds, with corresponding (constant) input amplitudes per axis set such that attitude changes within 10 to 60 degrees were obtained for roll and yaw, and 5 to 30 degrees for pitch, respectively. The results, along with the boundaries prescribed by ADS-33E, are shown in Figure 4.10.

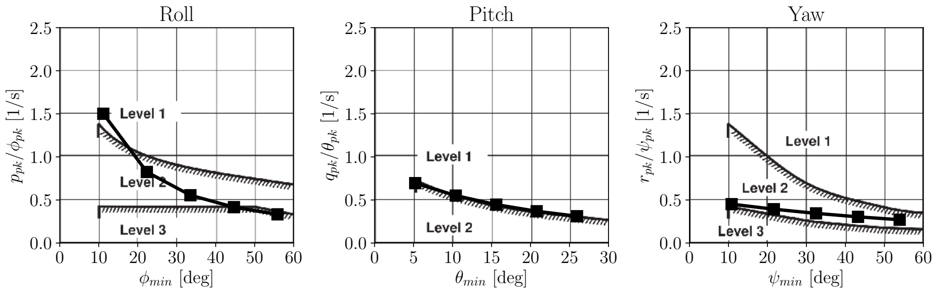

Figure 4.10: Predicted attitude quickness per axis in hover, including ADS-33E boundaries [Anonymous, 2000].

For the roll axis, it can be seen that the quickness for relatively small attitudes between 10 and 20 degrees, attains Level 1 characteristics. Above 20 degrees, however, Level 2 characteristics are attained. The pitch quickness characteristics follow the boundary between Level 1 and Level 2 over the complete range of pitch attitude changes up to approximatelly 30 degrees. Similarly, the yaw quickness can be characterized as Level 2 for the complete range of heading angle changes up to 60 degrees.

4.3.2. PILOT-ASSIGNED HANDLING QUALITIES

The predicted HQs analyses in Section 4.3.1 are validated using a pilot-in-the-loop evaluation of the *assigned* HQs of the model. The following paragraphs present discuss the apparatus, methods and results of this evaluation.

Apparatus The evaluation of pilot-assigned HQs was performed on the Desdemona simulator, shown in Figure 1.1, with *three* AH-64 Apache test pilots from the RNLAF. Whereas the motion platform of the Desdemona simulator was already discussed in Chapter 2 (see Section 2.2.1), the other cueing systems of the simulator, namely the visual system, instrumentation and helicopter controls, received less attention. These are therefore briefly addressed here.

Visual cues were made available to the pilots through the use of a VR headset. The Oculus Rift [Oculus, 2019], with a resolution of 2160 (horizontal) and 1200 (vertical) pixels and a refresh rate of 90 Hz was used. While limited in resolution, this system offers an essentially “unlimited” field of view because the rendered visual scene changes according to both the position and orientation of the pilot’s head. Note that with the advancement of CGI technology, the use of VR in simulated (flight) environments is increasingly common [Lele, 2013]. At Desdemona B.V., the VR-enabled visuals have been developed in conjunction to a traditional projection based system. Preliminary evaluations with AH-64 Apache helicopter pilots indeed suggest that the increased “field-of-view” is strongly appreciated, with most pilot preferring VR over the projected visuals. A minority, however, has indicated an increased susceptibility to simulator sickness. Nonetheless, the VR-enabled environment is considered sufficiently mature for application in this dissertation.

In contrast, no *physical* motion cues were offered, i.e., the Desdemona motion platform was kept stationary. This decision is based on two factors. First, directly before the HQs evaluation, an experiment (see Chapter 6) *with* physical motion cues *and* VR was conducted and, when asked, two of the participating test pilots preferred *no motion*. Second, the presence of motion cues limits the VR-enabled visuals to account *only* for rotation, instead of both rotation and translation, of the pilot’s head.

Instrumentation and relevant symbology was also available in the virtual world. The instruments were projected in the cockpit through somewhat enlarged “virtual” screens, but were also shown as an “overlay” on the rendered visual scene (see Figure 4.11) in replication of the Helmet Display Unit (HDU) available in the actual AH-64 helicopter.

Figure 4.11: Illustration of virtual cockpit instruments and HDU overlay in the VR-enabled visual environment of the Desdemona simulator.

The cyclic, collective and pedal controls used are electically driven Control Loading Systems (CLSs) developed by Brunner [Brunner, 2019]. The grips mounted on the cyclic and collective sticks are functional replica's of the actual AH-64 control grips.

Method Before the evaluation, pilots were briefed on the Mission Task Elements (MTEs) to be evaluated and were given time to review the corresponding task descriptions and performance criteria. Five Mission Task Elements (MTEs) were selected for the evaluation of the flight dynamics model in basic manoeuvering flight: the *precision hover* (PH), *depart-abort* (DA), *hover turn* (HT), *vertical manoeuvre* (VM) and *lateral reposition* (LR). An impression of each MTE as seen in the VR-world is given in Figure 4.12 and brief descriptions are included in the following paragraphs.

The PH is initiated at a ground speed of between 6 and 10 knots and at an altitude of less that 20 feet. The target location at which a stable hover should be attained is located approximately 45 degrees relative to the initial heading of the vehicle. The ground track of the vehicle should be such that the target location is reached in a straight line. At the target location, a stable hover should be attained within a prescribed amount of time and positional accuracy, in terms of altitude, longitudinal and lateral offset as well as heading.

The DA is initiated at an altitude of approximately 35 feet and at a distance of 800 feet from the intended target location. From this position, an acceleration up to a prescribed velocity is to be performed, directly followed by a deceleration such that the vehicle is brought to a stable hover within 20 feet of the target location. Both acceleration and deceleration should be performed smoothly. Overshoot of the target location is not permitted and changes in the vehicle's pitch attitude should be kept below approximately 20 degrees. The performance criteria for the DA pertain to the peak velocity reached, the amount of time allowed and the accuracy, in terms of lateral track deviations, altitude and heading.

The HT is initiated in stabilized hover at an altitude of less than 20 feet. From this condition, a 180 degree turn in both direction should be performed whilst maintaining a prescribed positional accuracy in terms of longitudinal, lateral and vertical drift. In addition, the target heading at the end of the turns should be captured within a prescribed number of degrees and within a prescribed amount of time.

The VM is initiated in a stabilized hover at an altitude of 15 ft, from where a vertical ascent over a distance of 25 ft is performed, followed after 2 seconds by a descent back to the original hover position. The manoeuvre should be performed within a prescribed amount of time and with a presribed positional accuracy in terms of longitudinal and lateral drift, heading as well as under- and overshoots of the prescribed vertical distance.

Finally, the LR is initiated in a stabilized hover at an altitude of 35 feet, with the vehicle's body x-axis orientated perpendicular to a reference track marked on the ground. From this position, a lateral acceleration up to a prescribed speed is to be performed, followed by a deceleration to a stabilized hover at a distance of approximately (± 10 feet) 400 feet from the initial position. Like the DA described in one of the previous paragraphs, the LR should also be performed smoothly, with both under- and overshoots being permitted in this case. Performance standards pertain to the amount of time allowed as well as the positional accuracy in terms of longitudinal track deviations, altitude and heading.

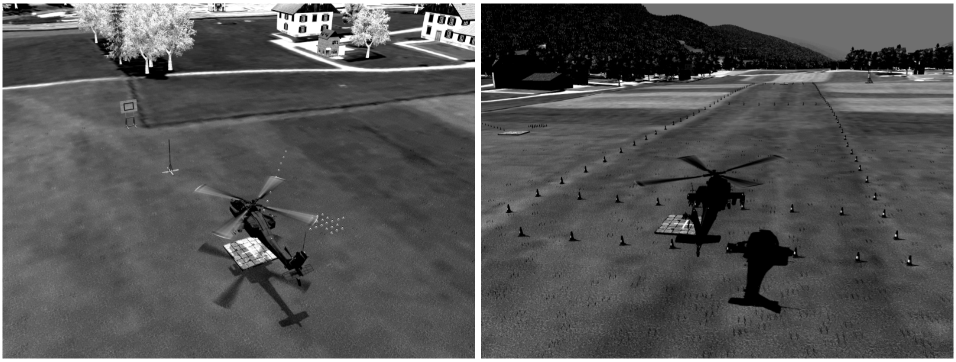

(a) Precision hover

(b) Depart/abort

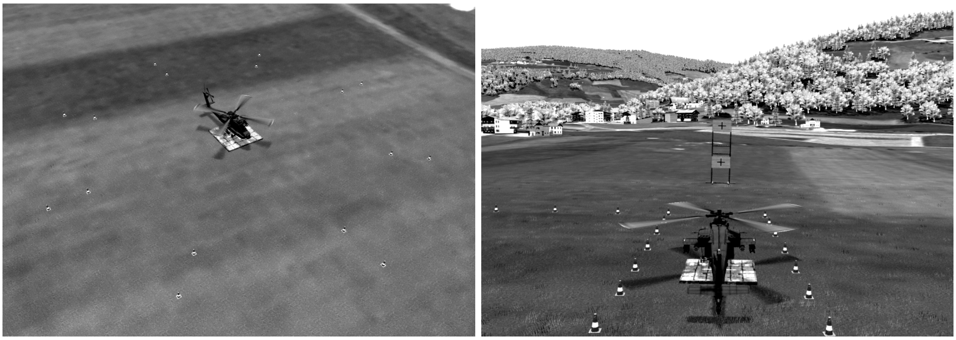

(c) Hover turn

(d) Vertical manoeuver

(e) Lateral reposition

Figure 4.12: Overview of each evaluated Mission Task Element, as seen in the VR-rendered world.

Table 4.2 shows the corresponding performance criteria for each MTE that have been adopted for each of the five MTEs. As indicated in the table, these criteria were somewhat relaxed as compared to the original values specified in ADS-33E [Anonymous, 2000]. This stems from the conclusion of Chapter 2, where it was found that in simulator-based evaluations, limitations in the various cueing systems (including the flight dynamics model) combined with criteria that demand a level of performance beyond the capabilities of these systems are likely to bias pilot ratings. Thus, the ADS-33E criteria were modified in the evaluation with the first participating test pilot, based on the attained performance over several trials for each MTE, and thereafter kept constant and used in all the remaining evaluations.

Table 4.2: Adequate (ADQ) and desired (DES) performance criteria per evaluated MTE in ADS-33E [Anonymous, 2000], criteria that were modified from original specifications are ~~crossed~~.

	ΔV (kts)	Δt (s)		Δx (ft)		Δy (ft)		Δz (ft)		$\Delta\psi$ (deg)	
		DES	ADQ	DES	ADQ	DES	ADQ	DES	ADQ	DES	ADQ
PH	10	~~3~~ 5	~~8~~ 10	3	6	3	6	2	4	5	10
DA	~~50~~ 40	~~25~~ 30	~~30~~ 35	-	-	10	20	15	40	10	15
HT	-	10	15	3	6	3	6	3	6	3	6
VM	-	~~10~~ 14	~~15~~ 16	6	10	6	10	3	6	3	6
LR	~~35~~ 30	~~18~~ 25	~~22~~ 30	10	20	10	20	10	15	10	15

Per evaluated MTE, the test pilots were allowed up to *two* training trials and up to *three* evaluation trials before an Handling Qualities Rating (HQR) was asked. The HQRs are derived from the Cooper-Harper HQ Rating (CHR) scale shown in Figure 4.7. Care was furthermore taken to ensure that each test pilot evaluated the five MTEs in a different order according to a partial Latin square design. In addition to the HQRs, the pilots were asked to comment on any anomalies they might have experienced while evaluating the AH-64 flight dynamics model.

During the evaluations, attained task performance in support of the HQRs was assessed solely based on observations of the vehicle position in the virtual world (relative to reference objects) and instrumentation readings. A stopwatch was used to record the duration of the manoeuvers. Pilot control inputs and simulation model states were also logged in order to be able to clarify potential discrepancies in the results afterwards, but were not used *during* the evaluations to determine the attained task performance. Finally, the evaluations were performed with the SCAS *enabled*, including both the rate damping *and* attitude feedback loops for extra stabilization (see Appendix A.9.1).

Results The results of the evaluation are shown in Table 4.3. This table lists the attained performance level (PRF), the assigned HQR and the accompanying HQs level (LVL) per test pilot. The last column of the table shows the *combined* HQs level for each MTE.

Of all evaluated MTEs, the precision hover (PH) is the only one for which Level 1 HQs were attained and for which all pilots managed to attain the desired performance level. This is consistent with the results of the analysis from Section 4.3.1, where Level 1 HQs were also predicted for tasks involving relatively high-frequency, low-amplitude attitude changes. When asked for noticeable deficiencies in the flight dynamics model, two out of three pilots had no notable comments, with one pilot remarking it is “similar to what one would expect from an Apache”. TP2, who awarded an HQR of 4, noted that some difficulty was experienced in keeping the altitude constant during deceleration to hover. This was attributed to a somewhat light/sensitive collective control feel. Otherwise the model felt “pretty close to the real aircraft”. Regarding potential improvements, two pilots suggested the incorporation of more advanced SCAS modes, such as position and/or heading hold as well as Translational Rate Command (TRC).

Table 4.3: Attained performance (PRF), assigned Handling Qualities Rating (HQR) and corresponding HQs levels (LVL) per MTE and test pilot.

		TP1	**TP2**	**TP3**	
PH	PRF	DES	DES	DES	**LVL 1**
	HQR	3	4	3	
	LVL	1	2	1	
DA	PRF	ADQ	DES	ADQ	**LVL 2**
	HQR	5	4	5	
	LVL	2	2	2	
HT	PRF	ADQ	ADQ	ADQ	**LVL 2**
	HQR	5	5	5	
	LVL	2	2	2	
VM	PRF	DES	DES	ADQ	**LVL 2**
	HQR	4	4	5	
	LVL	2	2	2	
LR	PRF	ADQ	ADQ	ADQ	**LVL 2**
	HQR	5	5	5	
	LVL	2	2	2	

For the depart-abort (DA) MTE, one of the three test pilots (TP2) managed to attain desired performance, with a corresponding HQR of 4. The two other pilots attained adequate performance and both awarded HQRs of 5. Thus, the combined HQs of the model in this MTE can be characterized as Level 2. In this task, two pilots could not identify notable deficiencies in the flight dynamics model as compared to the real aircraft. TP1 noted that the pitch attitude of the model during the manoeuver seemed to match “quite well”. TP2 noted that the “standard” helicopter couplings were “difficult” in this task, with particular emphasis on the pitch, heave and power setting. However, the damping of the model in pitch seemed accurate and control in the yaw axis was also characterized as “representative”. TP3 corraborated that altitude control was most difficult to maintain during the manoeuver and also added that “pitch-up” seemed overdamped, noting it is somewhat more “aggressive” in reality. The difficulty in altitude control identified by the pilots could be attributed to the *non-level terrain* along which the DA MTE was executed. This caused the (“radar”-driven) Vertical Speed Indicator (VSI) on the HDU to exhibit “jumps”, thereby providing misleading cues to the pilots. When asked on suggested improvements, more advanced SCAS modes (e.g., altitude hold) were recommended.

For the hover turn (HT) MTE, it can be seen from Table 4.3 that the three pilots were unanimous in their awarded HQR of 5. The model therefore exhibits Level 2 HQs in this task. The most challenging aspect, as remarked by two pilots, was maintaining position in the horizontal plane. The general consensus was that desired performance, in terms of duration, could be attained at the cost of position accuracy and vice-versa. Regarding the flight dynamics model, two pilots remarked that the pedal input to yaw rate response seemed accurate. TP1 noted that in reality the response is “maybe somewhat more aggressive”. TP2 noted that it was “easier” to maintain a certain yaw rate with the model than in reality. Suggested improvements to the model for a higher HQs level all pertain to incorporating more advanced SCAS modes, in particular position hold.

From Table 4.3, it can be seen that for the vertical manoeuver MTE, two of the three pilots attained desired performance and awarded an HQR of 4, whereas TP3 awarded an HQR of 5. The flight dynamics model therefore has an overall Level 2 HQs level for this MTE. TP1 noted that maintaining altitude accurately was experienced as "difficult", citing a "limited control" of the heave axis. Along the same line of reasoning, TP2 identified "power limitations" as an inhibiting factor, while TP3 also remarked that "quite some altitude adjustments" were necessary. TP2 and TP3 furthermore noted that the collective-to-yaw coupling either "matched well" or was "realistic" as compared to the real aircraft. TP2 remarked that the "onset" and the amount of pedal compensation also matched well with reality. Possible improvements to enhance the HQs level for this MTE also include the incorporation of more advanced SCAS modes, such as heading and/or position hold. No particular suggestions regarding improvements to the flight dynamics model or basic SCAS were given.

The last MTE evaluated was the lateral reposition (LR), where from Table 4.3 it can be seen that an overall HQR rating of 5, corresponding to Level 2 HQs, was awarded. In support of these ratings the pilots remarked that maintaining a constant heading as well as Table 4.3 it can be seen that pilots unanimously awarded an restricting longitudinal drift required substantial pilot compensation. Regarding the flight dynamics model, TP2 furthermore remarked that the pitch axis seemed "slightly less damped" than in the real aircraft. TP3 commented that the response in the roll axis felt "quite realistic" and that the proportion of cross-coupling (i.e., roll-to-pitch) "felt natural". Suggestions for improving the HQs of the flight dynamics model in this MTE are the incorporation of more advanced SCAS modes, in particular heading hold.

Interestingly, for all MTEs involving a moderately aggressive control strategy (i.e., all except PH), the *assigned* HQs levels in Table 4.3 seem to match the *predicted* HQs levels from Section 4.3.1. Moreover, the for the most part Level 2 HQs of the AH-64 are in line with those found in other studies [Harding et al., 2007].

4.4. CONCLUSION

This chapter has described the utility of a generic six degrees-of-freedom helicopter flight dynamics model named Delft Rotorcraft Simulation (Draftsim), aimed primarily at efficient (real-time) flight simulation as well as many common offline analyses (e.g., trim and linearization). In this process, a variety of existing tools and methods were explored, with particular emphasis on those documented in the Aeronautical Design Standard 33E (ADS-33E) [Anonymous, 2000]. First, Draftsim was verified by a trim and dynamic stability analysis of the Bo-105 helicopter, after which the model was applied to the AH-64 helicopter in a handling qualities evaluation conducted on the Desdemona simulator.

The analyses contained in this chapter again signify the strength of quantitative analysis of helicopter flight dynamics. In particular, it is interesting how relatively simple models, assumptions and (reference) data lead to good insights and results. The remainder of this thesis therefore aims to leverage the strength of these types of simplified, model-based analyses and *extend* them to applications in motion cueing fidelity assessment.

5

A NEW PERSPECTIVE ON MOTION CUEING FIDELITY

The previous chapters of this thesis have mainly focused on the separate problem domains of motion cueing fidelity assessment and helicopter flight dynamics using (extensions of) existing tools and methods. In this chapter, the knowledge gained thus far is consolidated to develop a new methodology to address the motion cueing fidelity problem in helicopter flight simulation. This method relies on the application of modal analysis to a linear system that incorporates the coupled helicopter and Motion Cueing Algorithm (MCA) dynamics.

The chapter is structured as follows. First, the significance of modal analysis is highlighted in Section 5.1, which includes a proposition for a system structure to capture the coupled vehicle and MCA dynamics. Then, in Section 5.2, the dynamics of a commonly applied MCA, the Classical Washout Algorithm (CWA), are explained and linearized. Section 5.3 subsequently completes the formulation of the coupled system and presents its sought eigenstructure. Finally, in Section 5.5, a case study and brief sensitivity analysis is included to exemplify the utility of the novel methodology.

5.1. THE SIGNIFICANCE OF MODES

In Chapter 4, the flight dynamics of helicopters was studied using a number of different analyses. Characterizing the vehicular dynamics in terms of *modes* proved particularly useful. Namely, this yielded valuable information about both dynamic stability and (through criteria specified in ADS-33E [Anonymous, 2000]) vehicular handling qualities. Moreover, knowledge of the vehicle modes in combination with the application of partial *state feedback* allowed for the design of an effective Stability and Control Augmentation System (SCAS) for the AH-64 helicopter model.

In the remainder of this section, the significance of modes for linear systems analysis is further addressed. Subsequently, a new perspective on the motion cueing fidelity problem that relies on *modal analysis* is proposed.

5.1.1. SYSTEM RESPONSE IN TERMS OF MODES

The property that makes modes attractive for the analyses of linear dynamic systems, is the fact that they represent the response characteristics of the system along *decoupled coordinates* [Oppenheim and Verghese, 2015]. These coordinates are often collectively termed the *modal coordinates*, the *eigenstructure* or, simply, the *modes* of the system. This section will show how the modes of a generic linear system can be retrieved and how modes are related to the dynamic response characteristics of the system.

Given a *linear*, *non-singular* and *time-invariant* system of the form:

$$\begin{aligned} \dot{\bar{x}} &= A\,\bar{x} + B\,\bar{u} \\ \bar{y} &= C\,\bar{x}, \end{aligned} \tag{5.1}$$

one can define a transformation of the state vector, $\bar{x}$, i.e.:

$$\bar{x} = W\bar{r}, \tag{5.2}$$

such that:

$$\begin{aligned} \dot{\bar{r}} &= W^{-1}AW\bar{r} + W^{-1}B\bar{u} \\ \bar{y} &= CW\bar{r} \end{aligned} \tag{5.3}$$

The system in Equation (5.3) is said to be *similar* to the one in Equation (5.1), in the sense that the dynamic characteristics of the system are unaffected. In fact, the input-output relation from $\bar{u}$ and $\bar{y}$ remains unchanged. This furthermore holds for *any* (non-singular) choice of the transformation matrix W. However, a special choice for W exists, such that [Oppenheim and Verghese, 2015]:

$$W^{-1}AW = \Lambda = \text{diag}(\lambda_1, \lambda_2, \ldots, \lambda_n) = \begin{bmatrix} \lambda_1 & 0 & \cdots & 0 \\ 0 & \lambda_2 & \cdots & 0 \\ \vdots & \vdots & \ddots & \vdots \\ 0 & 0 & \cdots & \lambda_n \end{bmatrix} \tag{5.4}$$

In this case, the matrix A is said to be *diagonalized* and $\lambda_1, \ldots, \lambda_i, \ldots, \lambda_n$ are real- or complex-valued *scalars* known as the *eigenvalues* of the system. In turn, the columns of W, i.e., $\bar{w}_1, \ldots, \bar{w}_i, \ldots \bar{w}_n$, have the property:

$$A\bar{w}_i = \lambda_i \bar{w}_i \quad \text{or} \quad \bar{w}_i^T \cdot \bar{w}_j = 0 \quad \forall \quad i \neq j \tag{5.5}$$

Or, in words, the matrix W is *orthogonal* and its columns are *eigenvectors* of the system. W is also often referred to as the *modal matrix*, which effectively *decouples* the system into its n linearly independent *modal coordinates*. An individual mode of the system, then, can be uniquely specified as:

$$m_i = \{\lambda_i, \bar{w}_i\} \tag{5.6}$$

The type (e.g., stable vs. unstable, oscillatory vs. non-oscillatory, etc.) of the response in a given mode is determined by the *eigenvalue* associated with that mode. In turn, the *eigenvector* associated with a mode defines the *relative contribution* of, and the *relation* between, the individual states of the system in that mode. This property is commonly referred to as the *mode shape*. An example of modes and their corresponding shapes is shown in Figure 5.1, depicting the eigenvalues and the associated eigenvectors of a three degree-of-freedom (dof) longitudinal helicopter model.

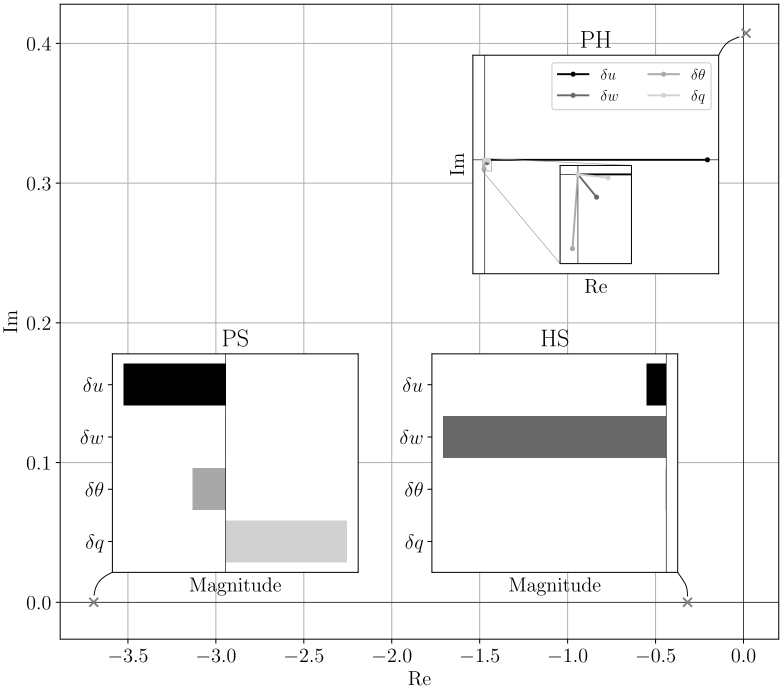

Figure 5.1: Modes in a three degree-of-freedom linear model of the Bo-105 in hover.

For complex eigenvalues, the corresponding eigenvector coefficients are, in general, also complex valued. Hence, each state has a *magnitude and phase* relative to the others. This relation is best visualised in a *complex plane* representation of the eigenvector coefficients. Real eigenvalues are accompanied by real-valued coefficients in the corresponding eigenvectors. In this case, each state has a relative *magnitude* with respect to other states and is either *positively* or *negatively* related to the other states. Thus, the relative relation between real valued coefficients in an eigenvector can be conveniently represented in a *bar plot*. Finally, note that eigenvectors are essentially *dimensionless*, in that they can be arbitrarily scaled and normalized. In this process, however, the *relative* relation between the coefficients in each eigenvector is preserved.

The state response of the system is directly related to the modes through the following equation [Oppenheim and Verghese, 2015]:

$$\bar{x}(t) = \sum_{i=0}^{n} \Big[\underbrace{(\bar{v}_i^T \bar{x}_0) e^{\lambda_i t}}_{\text{ZIR}} + \underbrace{\int_{0}^{t} \bar{v}_i^T B \bar{u}(\tau) e^{\lambda_i (t-\tau)} \, \mathrm{d}\tau}_{\text{ZSR}} \Big] \bar{w}_i \tag{5.7}$$

where the row vectors $\bar{v}_i^T$ are *left eigenvectors* of the system, which in this case are the rows of a matrix V^T obtained from[1]:

$$V^T = W^{-1} \tag{5.8}$$

It can also be seen from Equation (5.7) that the state response is composed of two parts. The Zero Input Response (ZIR) captures the contribution to the response due to a *direct* perturbation of the state itself (i.e., the initial values response). Conversely, the Zero State Response (ZSR) only contributes to the response as a result of external inputs. To obtain a response that is isolated to a single system mode, the ZIR corresponding to $\bar{x}_0 = \bar{w}_i$ can be evaluated[2]. An example corresponding to the modes in Figure 5.1 is shown in Figure 5.2. This figure reveals a number of analogies between the modal domain and the time domain. For example, the responses corresponding to the phugoid mode are unstable and indicate that δu dominates in terms of amplitude and exhibits *lead* with respect to δw and $\delta\theta$ (see dashed lines at first minimum). Furthermore, δu and δq appear to be approximately in phase with one another. In Figure 5.1, these properties of the response can also be deduced from the relative *angle* and *magnitude* between the phugoid eigenvector coefficients in the complex plane. In case of the aperiodic subsidence modes, it can be seen that the further *left* the eigenvalue lies in the complex plane, the *faster* the response. Furthermore, the mode shapes in Figure 5.1 reveal the dominant states (i.e., δq for the pitch and δw for the heave subsidence, respectively) as well as the relative *sign* of the isolated state responses.

---

[1] Note that many combinations of V and W exist such that $V^T AW = \Lambda$ and $\bar{v}_i^T \cdot \bar{w}_j = 0 \, \forall \, i \neq j$ [Oppenheim and Verghese, 2015]. Therefore, in contrast to *eigenvalues*, the left and right *eigenvectors* of a linear system are generally *not unique*. The choice $V^T = W^{-1}$ is convenient because it implies that $\bar{v}_i^T \cdot \bar{w}_j = 1 \, \forall \, i = j$, which in turn implies that Equation (5.7) holds without introducing additional *scaling* as a result of the implicit inner products of $\bar{v}_i^T$ and $\bar{w}_i$.

[2] For periodic modes with complex eigenvectors, the equivalent ZIR is obtained by setting $\bar{x}_0 = 2\mathrm{Re}(\bar{w}_i)$.

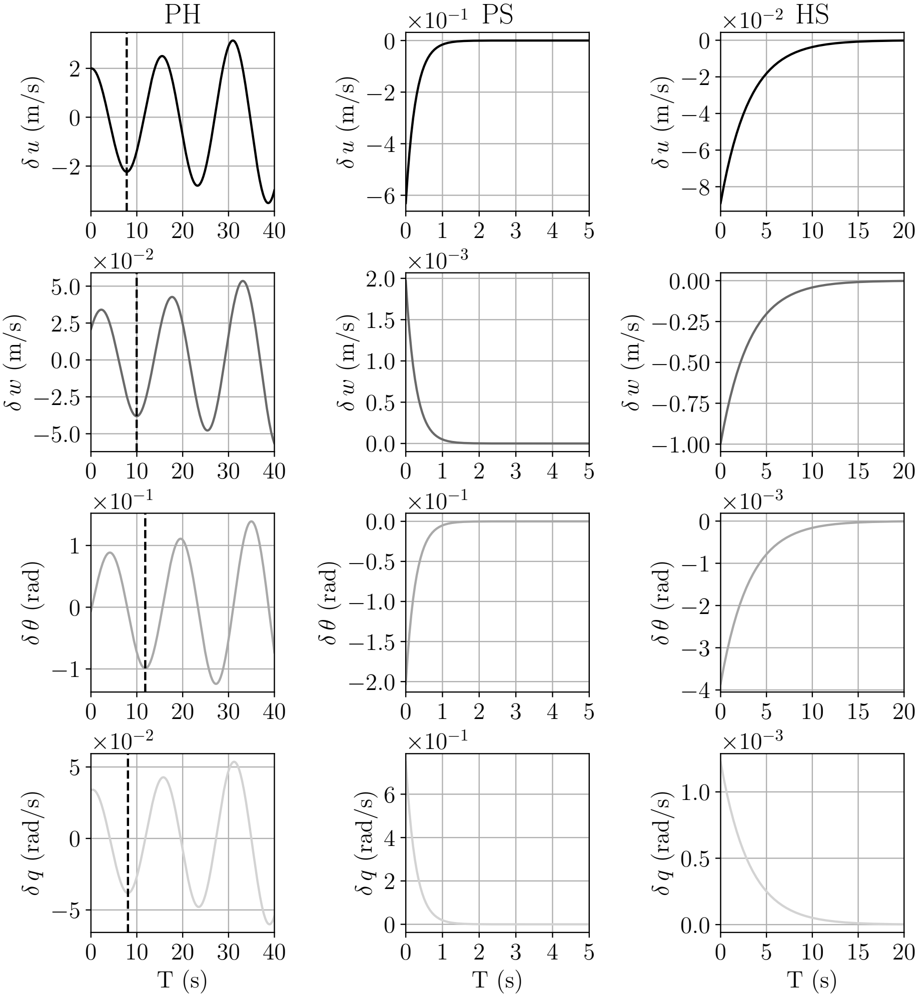

Figure 5.2: State responses of isolated modes in a three degree-of-freedom linear model of the Bo-105 in hover.

Given an arbitrary (initial) state or input, Equation (5.7) also reveals the extent to which the i-th system mode is "triggered" as a result of perturbing the system. This information is present in the terms:

$$\bar{v}_i^T \bar{x}_0 \quad \text{and} \quad \bar{v}_i^T B\bar{u} \tag{5.9}$$

Hence, these terms are often referred to as *mode participation factors* (e.g., [Padfield, 2007]). One can also directly express a (measured) system state in terms of its modal coordinates using (see Equation (5.2)):

$$\bar{r}(t) = W^{-1}\bar{x}(t) \tag{5.10}$$

which constitutes an alternative and more complete measure of the participation of each individual system mode in the state response, as it includes both the contibution of the ZIR and ZSR.

5.1.2. FROM MODE ASSIGNMENT TO DISTORTION

The utility of modes is well understood in the domain of control system design since the late sixties [Wonham, 1967]. Then, it was recognized that closed-loop system eigenvalues could be "assigned" arbitrarily through the utility of *state feedback*, i.e.:

$$\bar{u} = K\bar{x}$$

Later, Moore [1976] showed that state feedback in *multivariable* dynamic systems offers additional freedom beyond eigenvalue placement. Namely, the possibility to specify a *unique* and *favourable* set of corresponding closed-loop *eigenvectors*. This approach later became known as *eigenstructure assignment* [Liu and Patton, 1998]. In the two decades following Moore's publication, eigenstructure assignment gained little traction in favor of frequency-domain methods. At the time, the latter proved more suitable for analyses involving *output* (in contrast to *state*) feedback as well as (noise) sensitivity minimization and robustness. Currently, these issues are well-understood in the domain of eigenstructure assignment [Liu and Patton, 1998] and several applications have been documented in both fixed- (e.g., [Sobel and Shapiro, 1985]) and rotary-wing (e.g., [Low and Garrard, 1993]) aircraft control.

The main contribution of this dissertation is the application of *modal analysis* to the problem of motion cueing fidelity in helicopter flight simulation. This is enabled by developing a comprehensive and explicit *linear* model structure that *couples* typical vehicle and Motion Cueing Algorithm (MCA) dynamics. This prospective model has the following proposed form:

$$\begin{aligned}
\delta\dot{\bar{x}}^c &= \begin{bmatrix} A^p & 0 \\ A^{pm} & A^m \end{bmatrix} \begin{bmatrix} \delta\bar{x}^p \\ \delta\bar{x}^m \end{bmatrix} + \begin{bmatrix} B^p \\ B^m \end{bmatrix} \delta\bar{u}^p = A^c\delta\bar{x}^c + B^c\delta\bar{u}^p \\
\delta\bar{y}^c &= \begin{bmatrix} C^p & 0 \\ C^{pm} & C^m \end{bmatrix} \begin{bmatrix} \delta\bar{x}^p \\ \delta\bar{x}^m \end{bmatrix} + \begin{bmatrix} D^p \\ D^m \end{bmatrix} \delta\bar{u}^p = C^c\delta\bar{x}^c + D^c\delta\bar{u}^p
\end{aligned} \tag{5.11}$$

The state vectors $\delta\bar{x}^p$ and $\delta\bar{x}^m$ that together form the *coupled* system state $\delta\bar{x}^c$ in Equation (5.11) contain states that describe the evolution of the *linearized* vehicle and MCA dynamics, respectively. Here, the δ-notation is used to emphasize the fact that Equation (5.11) describes the *perturbation* dynamics of the coupled system. The matrices A^p and A^m are the respective system matrices corresponding to $\delta\bar{x}^p$ and $\delta\bar{x}^m$. The matrix A^{mp} *couples* the dynamics of both systems, while the coupled system itself is excited solely by the input vector $\delta\bar{u}^p$ through the matrices B^p and B^m (combined in the matrix B^c). The matrices A^p and B^p are determined by the vehicle dynamics only and and may change, e.g., as a function of forward flight speed in case of helicopters. Conversely, A^m changes as a function of parameters in the MCA only, while A^{mp} and B^m depend on *both* vehicle dynamics and MCA parameters. The coupled system output $\bar{y}^c$ contains vehicle *reference* as well as *simulated human-perceived* quantities. The latter are specific forces and angular rates [Hosman and Stassen, 1998] that are a linear combination, determined by the matrices C^c and D^c, of the states in $\bar{x}^p$ and $\bar{x}^m$.

The key advantage of the formulation in Equation (5.11) is that it accommodates *modal analysis* of the *coupled* system, as described in Section 5.1. This is analogous to eigenstructure assignment, in the sense that a mechanism is introduced that strongly affects the dynamic properties of the closed-loop system. In eigenstructure assignment, this mechanism (i.e., state feedback) is introduced purposefully with the aim of *shaping* the dynamic characteristics of the closed-loop system. However, in Equation (5.11), the presence of the MCA dynamics has the *undesired* (yet inevitable) “side-effect” of *distorting* the *actual* vehicle dynamics perceived by a human operator in a motion-base flight simulator. The newly proposed method therefore enables a systematic analysis of this MCA-induced *distortion* of human perceived quantities in terms of the vehicle’s *eigenstructure*.

In the following sections, the necessary elements in Equation (5.11) will be derived, starting with a detailed description and linearization of the Classical Washout Algorithm (CWA). In this process, the *motion state* vector $\bar{x}^m$ is defined and expressions for both A^m as well as C^m are obtained. Subsequently, human-perceived quantities (i.e., specific forces and angular rates) will be expressed in terms of the vehicle dynamics states in $\bar{x}^p$. It will become apparent that these constitute the defition of the A^{pm}, B^m, C^p, C^{pm} and D^m matrices and thus complete the definition of the coupled system in Equation (5.11).

5.2. LINEARIZING THE CLASSICAL WASHOUT ALGORITHM

Figure 5.3 shows a schematic representation of a commonly applied Motion Cueing Algorithm (MCA), namely the Classical Washout Algorithm (CWA) [Reid and Nahon, 1985].

This figure shows that the inputs to the CWA are the vehicle *specific forces* and *angular velocities*, i.e., the quantities perceived by the human vestibular system [Previc and Ercoline, 2004]. In the CWA, three distinct mechanisms are applied to feasibly reproduce these quantities in the simulator. The purpose of Channel 1 is to reproduce high-frequency components of the specific forces. Channel 2 is often referred to as the *tilt coordination* channel, enabling the use of motion platform rotation for reproducing *sustained* (i.e., low-frequency) specific force components. This channel is optional and only active for specific forces acting in the horizontal plane [Reid and Nahon, 1985]. Finally, Channel 3 is responsible for reproducing high-frequency contributions in the angular velocities of the vehicle. In the following sections, the detailed contribution of each channel, as well as the linearization thereof, are outlined.

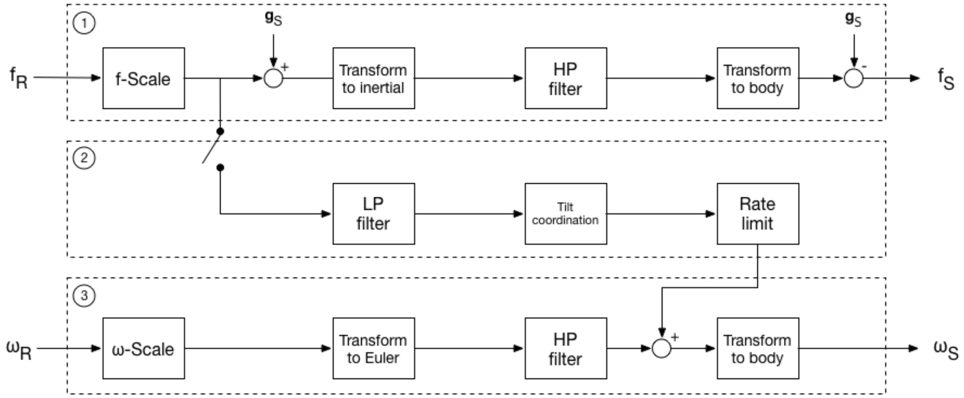

Figure 5.3: A schematic of the Classical Washout Algorithm [Reid and Nahon, 1985].

5.2.1. DESCRIPTION AND LINEARIZATION OF CHANNEL 1

The specific force inputs to Channel 1 are first scaled. It is important to understand that, in the CWA this scaling is performed relative to a situation where the vehicle body frame is aligned with the inertial frame. This is reasonable because aircraft mostly fly horizontally, i.e., the gravitational acceleration in the body frame is always approximately aligned with the inertial z-axis. Thus, the scaling of specific forces can be expressed as [Reid and Nahon, 1985]:

$$K^m(\bar{f}^r + \bar{g}_0^r) - \bar{g}_0^r \tag{5.12}$$

where $\bar{g}_0^r \equiv \begin{bmatrix} 0 & 0 & g \end{bmatrix}^T$ and K^m is a diagonal gain matrix with motion scaling gains in each of the translational motion axes of the simulator:

$$K^m = \text{diag}\left(K_x, K_y, K_z\right) \tag{5.13}$$

To enable effective washout of the simulator motion, high-pass filtering is performed on *acceleration* defined in the *simulator inertial frame*. The output of the scaling block, however, is essentially a scaled specific force defined in the *vehicle body frame*. To convert this quantity to *acceleration* in the simulator inertial frame, the gravitational acceleration expressed in the *simulator body frame* is added first. A transformation to the simulator inertial frame is subsequently carried out before high-pass filtering the resulting signal[3]. The contribution of Channel 1 to the perceived specific force ($\bar{f}^s$) in the simulator is then obtained by transforming the *output* of the high-pass filter back to simulator body frame and *subtracting* $\bar{g}^s$ from the result. It is important to note that, because of the presence of the high-pass filter in this channel, the addition and subsequent subtraction of $\bar{g}^s$ are *not complementary*. As such, *false cues* in specific forces are inherently introduced by filtering in the inertial frame of reference.

---

[3] Note that, without this transformation to the simulator inertial frame before filtering, return-to-neutral would not be attained.

In summary, several distinct elements are present in Channel 1 that determine the degree to which vehicle specific forces are affected by the MCA. These are the scaling, the addition and subtraction of the gravitational acceleration in the simulator body frame, the transformation between reference frames and, finally, the presence of a high-pass filter. In the following paragraphs, the linearisation of each of these elements is outlined.

Scaling Scaling is a purely *linear* operation and is therefore easily incorporated in a linearized model of the CWA. Substitution of a specific force vector defined as:

$$\bar{f}^r = \bar{f}_0^r + \delta \bar{f}^r \tag{5.14}$$

into Equation (5.12) yields the result:

$$K^m \left((\bar{f}_0^r + \delta \bar{f}^r) - \bar{g}_0^r \right) + \bar{g}_0^r \tag{5.15}$$

Here, $\bar{f}_0$ is a *constant* vector that defines the value of the specific force in the state about which the vehicle and CWA are linearized and $\delta \bar{f}^r = \begin{bmatrix} \delta f_x & \delta f_y & \delta f_z \end{bmatrix}^T$. With some algebraic manipulation, Equation (5.15) can then be written as:

$$K^m \bar{f}_0^r + (K^m - I_3)\bar{g}_0^r + K^m \delta \bar{f}^r \tag{5.16}$$

In the linear CWA model, the term containing $\delta \bar{f}$ is of primary interest as it describes the influence of scaling on a perturbation of the specific force. The values of the first two (constant) terms in Equation (5.16) is of no particular interest in describing the *linear* perturbation dynamics of the CWA. Note that this does not mean that the constant reference is not *perceived*, but merely that its value is determined from *past* vehicle dynamics and is of no consequence for the *future* evolution of the system. Hence, the effect of scaling in the CWA can be linearized as:

$$K^m \delta \bar{f} \tag{5.17}$$

where the superscript r was dropped for notational convenience in the remainder of this chapter.

Transformations between reference frames Important non-linearities in Channel 1 are the transformations of the simulator translational accelerations to (or from) the simulator inertial (or body) frame before (or after) high-pass filtering. The general transformation matrix between these two frames can be expressed as (see also Appendix A, Equation (A.2)):

$$T_{bi}^s(\bar{\Phi}^s) = \begin{bmatrix} \cos(\theta^s)\cos(\psi^s) & \cos(\theta^s)\sin(\psi^s) & -\sin(\theta^s) \\ \sin(\phi^s)\sin(\theta^s)\cos(\psi^s) - \cos(\phi^s)\sin(\psi^s) & \sin(\phi^s)\sin(\theta^s)\sin(\psi^s) + \cos(\phi^s)\cos(\psi^s) & \sin(\phi^s)\cos(\theta^s) \\ \cos(\phi^s)\sin(\theta^s)\cos(\psi^s) + \sin(\phi^s)\sin(\psi^s) & \cos(\phi^s)\sin(\theta^s)\sin(\psi^s) - \sin(\phi^s)\cos(\psi^s) & \cos(\phi^s)\cos(\theta^s) \end{bmatrix} \tag{5.18}$$

where ϕ^s, θ^s and ψ^s are the *simulator* pitch, roll and yaw angles, respectively, which are combined and written in vector form: $\bar{\Phi}^s = \begin{bmatrix} \phi^s & \theta^s & \psi^s \end{bmatrix}^T$. Therefore, *before* high-pass filtering, one may write:

$$\bar{a}^i = T_{ib}^s(\bar{\Phi}^s)\,\bar{a}^b, \tag{5.19}$$

where $T_{ib}^{s} = (T_{bi}^{s})^T$ and where $\bar{a}^i$ and $\bar{a}^b$ are the *simulator* translational acceleration vectors expressed in the *simulator* inertial and body frames of reference, respectively. Equation (5.19) can subsequently be linearized by evaluating its Taylor series expansion up to the first-order:

$$T_{ib}^{s}(\bar{\Phi}_0^s + \delta\bar{\Phi}^s)\,\bar{a}^b \approx T_{ib}^{s}(\bar{\Phi}_0^s)\,\bar{a}^b + \left.\frac{\partial\left(T_{ib}^{s}(\bar{\Phi}^s)\bar{a}^b\right)}{\partial\bar{\Phi}^s}\right|_0 \tag{5.20}$$

where $\bar{\Phi}_0^s = \begin{bmatrix}\phi_0^s & \theta_0^s & \psi_0^s\end{bmatrix}^T$ and $\delta\bar{\Phi}^s = \begin{bmatrix}\delta\phi^s & \delta\theta^s & \delta\psi^s\end{bmatrix}^T$. Because it is of interest to linearize the contribution of the tranformation matrix, the vector $\bar{a}^b$ can be assumed *constant* without loss of generality and, hence, can be dropped from both sides of the equation. It can then be shown that Equation (5.20) can be rewritten to [Barfoot et al., 2011]:

$$T_{ib}^{s}(\bar{\Phi}_0^s + \delta\bar{\Phi}^s) \approx \left(I_3 - (L_{ib}^{s}(\bar{\Phi}_0^s)\,\delta\bar{\Phi}^s)_\times\right) T_{ib}^{s}(\bar{\Phi}_0^s) \tag{5.21}$$

where (see also Equation (A.87) in Appendix A):

$$L_{ib}^{s}(\bar{\Phi}^s) = \begin{bmatrix} 1 & \sin(\phi^s)\tan(\theta^s) & \cos(\phi^s)\tan(\theta^s) \\ 0 & \cos(\phi^s) & -\sin(\phi^s) \\ 0 & \frac{\sin(\phi^s)}{\cos(\theta^s)} & \frac{\cos(\phi)}{\cos(\theta)} \end{bmatrix} \tag{5.22}$$

and where the notation $\square_\times$ indicates a skew-symmetric matrix from an arbitrary vector, e.g.:

$$\bar{\epsilon}_\times = \begin{bmatrix} 0 & -\epsilon_3 & \epsilon_2 \\ \epsilon_3 & 0 & -\epsilon_1 \\ -\epsilon_2 & \epsilon_1 & 0 \end{bmatrix} \qquad \text{for} \qquad \bar{\epsilon} = \begin{bmatrix}\epsilon_1 & \epsilon_2 & \epsilon_3\end{bmatrix}^T \tag{5.23}$$

From Equations Equation (5.21) to Equation (5.23), it is apparent that in linearized form, the transformations between reference frames in the CWA generally introduce many inter-axes coupling terms. Fortunately, these can be reduced and simplified substantially. Namely, MCAs like the CWA aim to return the simulator to its *neutral position* at all times. Therefore, it seems reasonable to linearize the CWA dynamics with respect to the neutral position of the motion platform, i.e., $\bar{\Phi}_0^s \approx \bar{0}$. Moreover, deviations from the neutral position are typically constrained because of mechanical limitations inherent in contemporary motion platforms, such that it also appears reasonable to assume small deviations in the simulator attitude from the neutral position. Applying this assumption to Equation (5.21), both T_{ib}^{s} and L_{ib}^{s} become identity matrices. Subsequently perturbing Equation (5.19) yields:

$$\begin{aligned} \bar{a}_e^i + \delta\bar{a}^i &= T_{ib}^{s}(\bar{\Phi}^s + \delta\bar{\Phi}^s)(\bar{a}_e^b + \delta\bar{a}^b) \\ &\approx \left(I_3 - \delta\bar{\Phi}_\times^s\right)\left(\bar{a}_e^b + \delta\bar{a}^b\right) \end{aligned} \tag{5.24}$$

where $\bar{a}_e^i$ and $\bar{a}_e^b$ are the translational accelerations of the vehicle expressed in the simulator inertial and body reference frames, respectively. Assuming the vehicle is linearized with respect to an *equilibrium* state, these quantities are zero and Equation (5.24) can be further simplified to:

$$\delta\bar{a}^i \approx \left(I_3 - \delta\bar{\Phi}^s_\times\right)\delta\bar{a}^b \approx \delta\bar{a}^b \tag{5.25}$$

where the final result is the consequence of the fact that both $\delta\bar{\Phi}^s_\times$ and $\delta\bar{a}^b$ are *small perturbations* from the simulator reference state, such that $\delta\bar{\Phi}^s_\times\,\delta\bar{a}^b \approx 0$. In conclusion, transformations between reference frames in the CWA can be omitted in the linearized model.

Addition and subtraction of gravity It can be seen from Figure 5.3 that the gravitational acceleration vector, expressed in the *simulator body* frame, is both added and subtracted in Channel 1 before and after high-pass filtering, respectively. As explained earlier, this is necessary because specific force, in an *inertial* reference frame, is defined as:

$$\bar{f}^i = \bar{a}^i - \bar{g}^i \tag{5.26}$$

i.e., the vehicle accelerations *not* due to gravity. To obtain the total translational vehicle acceleration (i.e., the quantity on which the high-pass filter in Channel 1 operates) from specific force, gravity must therefore be *added* first. In the CWA, this operation is performed in the *simulator* body frame. To this end, the components of the gravitational acceleration vector in the simulator body frame can be expressed as [Reid and Nahon, 1985]:

$$\bar{g}^s = \begin{bmatrix} g^s_x & g^s_y & g^s_z \end{bmatrix}^T = \begin{bmatrix} -g\sin(\theta^s) \\ g\sin(\phi^s)\cos(\theta^s) \\ g\cos(\phi^s)\cos(\theta^s) \end{bmatrix} \tag{5.27}$$

Perturbing Equation (5.27) and using the insights from the previous paragraph, where it was assumed that $\bar{\Phi}^s_0 \approx \bar{0}$, it possible to write these components in linearized form as:

$$\delta\bar{g}^s = \begin{bmatrix} \delta g^s_x & \delta g^s_y & \delta g^s_z \end{bmatrix}^T = \begin{bmatrix} -g\,\delta\theta^s \\ g\,\delta\phi^s \\ 0 \end{bmatrix} \tag{5.28}$$

Thus, *before* the high-pass filter in Channel 1, using Equations (5.17) and (5.25) it is obtained that:

$$\delta\bar{a}^i = K^m\,\delta\bar{f} + \delta\bar{g}^s = \begin{bmatrix} K_x\,\delta f_x - g\,\delta\theta^s \\ K_y\,\delta f_y + g\,\delta\phi^s \\ K_z\,\delta f_z \end{bmatrix} \tag{5.29}$$

As can be seen from Figure 5.3, *after* high-pass filtering of $\bar{a}^i$, the gravity components defined in Equation (5.28) must be *subtracted* again to obtain the (perturbed) *human-perceived* specific forces in the simulator:

$$\delta\bar{f}^s = \begin{bmatrix} \delta f^s_x & \delta f^s_y & \delta f^s_z \end{bmatrix}^T = \delta\bar{a}^s - \delta\bar{g}^s = \begin{bmatrix} \delta a^s_x + g\,\delta\theta^s \\ \delta a^s_y - g\,\delta\phi^s \\ \delta a^s_z \end{bmatrix} \tag{5.30}$$

where $\delta\bar{a}^s = \begin{bmatrix} \delta a^s_x & \delta a^s_y & \delta a^s_z \end{bmatrix}^T$, i.e., the perturbed *simulator* acceleration.

High pass filtering Arguably the most important element in Channel 1 is the high-pass filter that, in the *linear* model of the CWA, acts upon the perturbed vehicle accelerations expressed in the simulator inertial frame. From Equation (5.29), it becomes clear that these in turn depend on perturbed (and scaled) specific forces and the perturbed simulator attitude. The high-pass filter itself is a *linear* filter of arbitrary order. Most commonly, the CWA contains high-pass filters up to third-order for the translational channels [Reid and Nahon, 1985]. In transfer function form, these can generally be written as:

$$H_{1_\square} = \frac{s^3}{(s^2 + 2\zeta\omega_{n,1_\square}\, s + \omega^2_{n,1_\square})(s + \omega_{b,1_\square})} \tag{5.31}$$

where the number in the subscript signifies the CWA channel (i.e., high-pass specific force), $\square$ denotes the direction (i.e., x, y or z) and where, for $\omega_{b,1_\square} = 0$, the transfer function reduces to second order. Without loss of generality, this thesis assumes that the damping ratio ζ is the same for all low- and high-pass filters in the CWA. To capture the effect of the high-pass filter in the linear model of the CWA, it is necessary to convert the transfer function in Equation (5.31) to the time-domain, i.e., to state-space form. A possible format is the so-called Controllable Canonical Form [Ogata, 2001], such that the system in Equation (5.31) can be written as:

$$\begin{aligned} \dot{\bar{q}}_{1_\square} &= A_{1_\square}\bar{q}_{1_\square} + B_{1_\square}u_{1_\square} \\ y_{1_\square} &= C_{1_\square}\bar{q}_{1_\square} + d_{1_\square}u_{1_\square} \end{aligned} \tag{5.32}$$

where $\bar{q}_{1_\square}$ denotes a vector containing auxilliary state variables, $u_{1_\square}$ is the scalar input to the filter and $y_{1_\square}$ is the scalar output of the filter. For the third-order high-pass filter as given in Equation (5.31), the remaining definitions in Equation (5.32) are:

$$\begin{aligned} A_{1_\square} &= \begin{bmatrix} 0 & 1 & 0 \\ 0 & 0 & 1 \\ -\omega^2_{n,1_\square}\omega_{b,1_\square} & -\omega_{n,1_\square}(2\zeta\omega_{b,1_\square} + \omega_{n_{1,\square}}) & -(2\zeta\omega_{n,1_\square} + \omega_{b,1_\square}) \end{bmatrix}, \quad B_{1_\square} = \begin{bmatrix} 0 \\ 0 \\ 1 \end{bmatrix} \\ C_{1_\square} &= \begin{bmatrix} -\omega^2_{n,1_\square}\omega_{b,1_\square} & -\omega_{n,1_\square}(2\zeta\omega_{b,1_\square} + \omega_{n,1_\square}) & -(2\zeta\omega_{n,1_\square} + \omega_{b,1_\square}) \end{bmatrix}, \quad d_{1_\square} = 1 \end{aligned} \tag{5.33}$$

For second-order high-pass filters, Equation (5.33) can be simplified to:

$$\begin{aligned} A_{1_\square} &= \begin{bmatrix} 0 & 1 \\ -\omega^2_{1_\square} & -2\zeta\omega_{1_\square} \end{bmatrix}, \quad B_{1_\square} = \begin{bmatrix} 0 \\ 1 \end{bmatrix} \\ C_{1_\square} &= \begin{bmatrix} -\omega^2_{1_\square} & -2\zeta\omega_{1_\square} \end{bmatrix}, \quad d_{1_\square} = 1 \end{aligned} \tag{5.34}$$

and where the "*n*" denoting the break-frequencies of the filters was dropped for notational convenience. Subsequently, from Equation (5.29):

$$\begin{aligned} u_{1_x} &= K_x\,\delta f_x - g\,\delta\theta^s, \qquad & y_{1_x} &= \delta a^s_x \\ u_{1_y} &= K_y\,\delta f_y + g\,\delta\phi^s, \qquad & y_{1_y} &= \delta a^s_y \\ u_{1_z} &= K_z\,\delta f_z, \qquad & y_{1_z} &= \delta a^s_z \end{aligned} \tag{5.35}$$

It is evident from the definitions in Equation (5.35) that the dynamics of the perturbed simulator *acceleration* in the surge and sway directions depend not only on the dynamics of the vehicle-driven *specific force*, but also on the *simulator* attitude. Thus, the linear CWA model developed in this chapter includes an *explicit* coupling of both translational and rotational MCA dynamics. In turn, the perturbed simulator attitude appearing in Equation (5.35) is driven by Channels 2 and 3 of the CWA (see Figure 5.3), which will be derived in the following two sections. The *human-perceived* specific forces in the simulator are finally obtained from the outputs of the high-pass filters using Equation (5.30), i.e., after subtracting the perturbed gravity components.

5.2.2. DESCRIPTION AND LINEARIZATION OF CHANNEL 2

As most contemporary motion cueing systems are strongly limited in the degree to which long-term accelerations can be represented, a commonly applied technique to emulate the perception of these motions is to employ a portion of the platform's rotational motion space. To this end, the scaled specific forces from Channel 1 are low-pass filtered before *tilt coordination* is applied. As can be seen from Figure 5.3, tilt coordination converts the scaled and low-pass filtered specific forces to a corresponding simulator attitude and angular velocity. In effect, components of the gravitational acceleration are used for reproducing the sensation of sustained acceleration. Because platform rotation due to tilt coordination is essentially a *false cue*, a rate limiter is added to Channel 2 to ensure that the amplitude of the resulting angular velocity does not exceed human perceptual thresholds [Reid and Nahon, 1985].

Low-pass filtering and tilt coordination The input to Channel 2 are the perturbed and scaled specific forces in surge and sway (i.e., δf_x and δf_y) as obtained from Equation (5.17). These are first *low-pass filtered*. This mechanism can be expressed in transfer function form as:

$$H_{2_\square} = \frac{\omega_{2_\square}^2}{s^2 + 2\zeta\omega_{2_\square}s + \omega_{2_\square}^2} \tag{5.36}$$

where, without loss of generality, a filter of second order is assumed and where □ is a placeholder for the MCA dofs where tilt-coordination is active (i.e., x and y for surge and sway, respectively). In analogy to the high-pass filters in Channel 1, Equation (5.36) can be converted to state-space form:

$$\begin{aligned} \dot{\bar{q}}_{2_\square} &= A_{2_\square}\bar{q}_{2_\square} + B_{2_\square}u_{2_\square} \\ y_{2_\square} &= C_{2_\square}\bar{q}_{2_\square} + d_{2_\square}u_{2_\square} \end{aligned} \tag{5.37}$$

where $\bar{q}_{2_\square}$ denotes a vector containing auxilliary state variables, $u_{2_\square}$ is the scalar input to the filter and $y_{2_\square}$ is the scalar output of the filter. For the second-order low-pass filter as given in Equation (5.36), the remaining definitions in Equation (5.37) are:

$$\begin{aligned} A_{2_\square} &= \begin{bmatrix} 0 & 1 \\ -\omega_{2_\square}^2 & -2\zeta\omega_{2_\square} \end{bmatrix}, & B_{2_\square} &= \begin{bmatrix} 0 \\ \omega_{2_\square}^2 \end{bmatrix} \\ C_{2_\square} &= \begin{bmatrix} 1 & 0 \end{bmatrix}, & d_{2_\square} &= 0 \end{aligned} \tag{5.38}$$

The inputs to the low-pass filters in Channel 2 are the scaled specific forces from Channel 1 (see Equation (5.17)), whereas the outputs are simply their low-pass filtered equivalents:

$$\begin{aligned} u_{2_x} &= K_x\,\delta f_x, & y_{2_x} &= \delta f_x^{tc} \\ u_{2_y} &= K_y\,\delta f_y, & y_{2_y} &= \delta f_y^{tc} \end{aligned} \tag{5.39}$$

The mechanism of tilt coordination is subsequently applied on $\delta f_\square^{tc}$, where it is treated as a desired quantity to be reproduced by a proportional *rotation* of the motion platform. This is enabled by the inability of the human vestibular system to distinguish between pure acceleration and the effects of gravity. Hence, a rotation in an inertio-gravitational field that is not accompanied by corresponding visual stimuli will be perceived by the human as equivalent to a pure translational acceleration [van der Steen, 1998]. In the absence of translational accelerations of the motion platform (which are accounted for in Channel 1 of the CWA), the *non-linear* and *sustained* specific forces to be reproduced in surge and sway can be written as [Reid and Nahon, 1985]:

$$\begin{aligned} f_x^{tc} &= 0 - \left(-g\sin(\theta^{tc})\right) &&= g\sin(\theta^{tc}) \\ f_y^{tc} &= 0 - \left(g\sin(\phi^{tc})\cos(\theta^{tc})\right) &&= -g\sin(\phi^{tc})\cos(\theta^{tc}) \end{aligned} \tag{5.40}$$

Here, ϕ^{tc} and θ^{tc} are the simulator roll and pitch angles *due to tilt coordination only*. Recalling the result from Equation (5.28), the *perturbed* specific forces to be reproduced and the required simulator pitch and roll angles to achieve this are found:

$$\begin{aligned} \delta f_x^{tc} &= g\,\delta\theta^{tc} \quad \text{or} \quad \delta\theta^{tc} = \frac{\delta f_x^{tc}}{g} \\ \delta f_y^{tc} &= -g\,\delta\phi^{tc} \quad \text{or} \quad \delta\phi^{tc} = -\frac{\delta f_y^{tc}}{g} \end{aligned} \tag{5.41}$$

Differentiation of Equation (5.41) yields the end result:

$$\delta\dot{\theta}^{tc} = \frac{\delta\dot{f}_x^{lp}}{g} \qquad \text{and} \qquad \delta\dot{\phi}^{tc} = -\frac{\delta\dot{f}_y^{lp}}{g} \tag{5.42}$$

where $\delta\dot{f}_x^{lp}$ and $\delta\dot{f}_y^{lp}$ are available from the solution of Equation (5.37). Equation (5.42) represents the required perturbation in the angular velocity of the simulator in order to reproduce a proportional perturbation of the *sustained* human-perceived specific force in the simulator.

Rate limiter Depending on the maneuver or task flown in the simulator, the dynamics of the low-pass filtered specific forces in surge and sway (governed by Equation (5.36)) may be such that the required angular velocity of the platform (from Equation (5.42)) exceeds human perceptual thresholds [Heerspink et al., 2005]. This leads to undesirable *false cues*

[Hosman and van der Steen, 1993] and, in practice, a rate limiter on the required angular velocity is therefore added (see Figure 5.3 and [Reid and Nahon, 1985]).

Unfortunately, the rate limiter is a non-linear element that cannot be linearized and included in the proposed *linear* model of the CWA. As a consequence, it is simply *omitted* under the assumption that the scaling and low-pass filter parameters appearing in Equation (5.42) are selected conservatively, that is, they are chosen such that the required angular velocity of the platform remains below human perceptual thresholds. As suggested by Reid and Nahon [1985], this could also be facilitated by introducing additional scaling *directly before* the low-pass filter in Channel 2.

5.2.3. DESCRIPTION AND LINEARIZATION OF CHANNEL 3

Angular velocities, like specific forces, are also perceived by the human operator and should therefore be reproduced in the CWA. To this end, the simulated vehicle angular velocities ($\bar{\omega}$ in Figure 5.3) are first scaled before they are converted to *Euler angle rates*. This step ensures that platform rotations are effectively *washed out* since Euler angles are defined with respect to the inertial reference frame. In the CWA, the transformation to Euler angle rates uses the attitude of the *simulator* and *not* the attitude of the simulated vehicle. High-pass filtered Euler angle rates, in conjunction with the angular velocities commanded in Channel 2, are subsequently reproduced by the MCA. The total angular velocity reproduced, then, constitutes the *Euler angle* rates expressed in the *simulator body frame*. In the next paragraphs, the linearization of the elements that appear in Channel 3 are discussed in more detail.

Scaling Angular velocities from the simulated vehicle are first scaled in Channel 3. This operation is analogous to the one already discussed in Section 5.2.1, in the sense that it can be written and subsequently perturbed as:

$$\text{diag}(K_p, K_q, K_r)\,\bar{\omega} = \text{diag}(K_p, K_q, K_r)\,(\bar{\omega}_0 + \delta\bar{\omega}) \tag{5.43}$$

Here, again, the constant reference vector $\bar{\omega}_0$ can be omitted from the linear CWA model, such that we obtain:

$$\text{diag}(K_p, K_q, K_r)\,\delta\bar{\omega} = \text{diag}(K_p, K_q, K_r)\begin{bmatrix}\delta p & \delta q & \delta r\end{bmatrix}^T \tag{5.44}$$

Transformation to Euler rates In order for the simulator to return to its neutral position, vehicle angular velocities in the CWA must also be filtered in an *inertial* reference frame. Therefore, referring back to Figure 5.3, the first step is to transform the incoming simulated vehicle rates defined in the vehicle's *body* frame to *Euler angle* rates. This is accomplished using Equation (5.22), which can be linearized using the method outlined in Appendix A.8.1. For the Euler roll and pitch angles, it was already found that (see Equations (A.114) and (A.115)):

$$\begin{aligned}
\delta\dot{\phi} &= \delta p + \sin(\phi_0^s)\tan(\theta_0^s)\,\delta q + \cos(\phi_0^s)\tan(\theta_0^s)\,\delta r + \\
&\quad \left(q_e\cos(\phi_0^s) - r_e\sin(\phi_0^s)\right)\tan(\theta_0^s)\,\delta\phi^s + \left(q_e\sin(\phi_0^s) + r_e\cos(\phi_0^s)\right)\sec^2(\theta_0^s)\,\delta\theta^s \\
\delta\dot{\theta} &= -\left(q_e\sin(\phi_0^s) + r_e\cos(\phi_0^s)\right)\,\delta\phi + \cos(\phi_0^s)\,\delta q - \sin(\phi_0^s)\,\delta r
\end{aligned} \tag{5.45}$$

whereas the result for the yaw angle rate can be found similarly:

$$\begin{aligned}\delta\dot{\psi} = {} & \left(q_e \cos\left(\phi_0^s\right) - r_e \sin\left(\phi_0^s\right)\right) \sec\left(\theta_0^s\right) \delta\phi^s + \left(q_e \sin\left(\phi_0^s\right) + r_e \cos\left(\phi_0^s\right)\right) \tan\left(\theta_0^s\right) \delta\theta^s + \\ & \left(\sec\left(\theta_0^s\right) \sin\left(\phi_0^s\right)\right) \delta q + \left(\sec\left(\theta_0^s\right) \cos\left(\phi_0^s\right)\right) \delta r\end{aligned} \tag{5.46}$$

In Section 5.2.1, it was already assumed that the CWA is linearized about its *neutral* position, where $\bar{\Phi}_0^s \approx \bar{0}$. Furthermore, the simulated vehicle is most commonly linearized about an *equilibrium* state with no angular velocity, such that $\bar{\omega}_e \equiv \begin{bmatrix} p_e & q_e & r_e \end{bmatrix}^T = \bar{0}$. If this is not the case, it can be seen from Equations (5.45) and (5.46) that the transformation from body rates to Euler rates induces couplings between (simulator) dofs (e.g., a steady-state yaw rate will also induce a roll rate when perturbing the pitch angle). Otherwise the equations simplify to:

$$\delta\dot{\phi} = \delta p, \qquad \delta\dot{\theta} = \delta q, \qquad \delta\dot{\psi} = \delta r \tag{5.47}$$

Thus, as was found for the transformations between simulator body and inertial accelerations in Channel 1 (see Section 5.2.1), the transformation between Euler angle rates and body rates can also be omitted in Channel 3 of the linearized CWA.

High-pass filtering In Channel 3, high-pass filtering is utilized to "wash out" accrued attitude angles. This operation is analogous to the high-pass filtering of simulator accelerations in Channel 1 of the CWA. For angular rates, a high-pass filter of second order is commonly applied [Reid and Nahon, 1985]:

$$H_{3_\square} = \frac{s^2}{s^2 + 2\zeta\omega_{3_\square} s + \omega_{3_\square}^2} \tag{5.48}$$

where $\square$ is a placeholder for the rotational degrees-of-freedom (i.e., p, q and r for roll, pitch and yaw, respectively). Like Equation (5.31), Equation (5.48) can also be written in state-space form using:

$$\begin{aligned}\dot{\bar{q}}_{3_\square} &= A_{3_\square}\bar{q}_{3_\square} + B_{3_\square}u_{1_\square} \\ y_{3_\square} &= C_{3_\square}\bar{q}_{3_\square} + d_{3_\square}u_{3_\square}\end{aligned} \tag{5.49}$$

where $\bar{q}_{3_\square}$ again denotes a vector containing (two) auxilliary state variables and where, in the case of Channel 3, the constant definitions are:

$$\begin{aligned}A_{3_\square} &= \begin{bmatrix} 0 & 1 \\ -\omega_{3_\square}^2 & -2\zeta\omega_{3_\square} \end{bmatrix}, \quad B_{3_\square} = \begin{bmatrix} 0 \\ 1 \end{bmatrix} \\ C_{3_\square} &= \begin{bmatrix} -\omega_{3_\square}^2 & -2\zeta\omega_{3_\square} \end{bmatrix}, \quad d_{3_\square} = 1\end{aligned} \tag{5.50}$$

Using Equation (5.47), the inputs $u_{3_\square}$ to the high-pass filter in Channel 3 can then be defined as:

$$u_{3_p} = K_p \, \delta p, \qquad u_{3_q} = K_q \, \delta q, \qquad u_{3_r} = K_r \, \delta r \tag{5.51}$$

To obtain the final *simulator* angular rates, the outputs from the high-pass filters in Channel 3 for the roll and pitch dofs (see $y_{3_\square}$) need to be added to the rates from Channel 2 given by Equation (5.42):

$$\delta\dot{\theta}^s = \delta q^s = y_{3_q} + \frac{\delta \dot{f}_x^{lp}}{g} \qquad \text{and} \qquad \delta\dot{\phi}^s = \delta p^s = y_{3_p} - \frac{\delta \dot{f}_y^{lp}}{g} \tag{5.52}$$

Tilt coordination does not affect simulator yaw in the *linearized* CWA, such that $\delta\dot{\psi}^s = \delta r^s = y_{3_r}$.

5.2.4. SYNTHESIS

The description and linearization of the CWA is hereby completed. It was shown that under a number of restrictive yet reasonable assumptions, the dynamics of the CWA in six degrees-of-freedom can be captured in linear form.

The main assumptions on which this process relies are:

- The CWA is linearized about the *neutral* state of the simulator, in which the simulator is assumed to be stationary with an attitude equal to zero. This is a reasonable assumption because the CWA itself ensures that the simulator always returns to this state. Moreover, due to mechanical constraints inherent in most contemporary motion platforms, excursions from the neutral position remain relatively small.
- The vehicle dynamics are linearized with respect to an *equilibrium* state, which means that (sustained) translational and rotational accelerations are assumed zero in the model. To linearize the CWA, it was furthermore assumed that rotational *rates* of the vehicle in equilibrium are also zero.

Figure 5.4 summarizes the final schematic obtained for the *linear* CWA. It can be seen that, even though many operations have been simplified (e.g., transformations between simulator body and inertial quantities), still many inherent inter-axis couplings remain. Most notably, the rotational dynamics of the CWA in roll and pitch affect the simulated specific forces in sway and surge, respectively, through the addition and subtraction of gravitional components. In turn, the roll and pitch dynamics of the simulator are also influenced by the vehicular specific forces through tilt coordination. The vertical specific force and yaw rate channels, however, do appear as uncoupled dofs in the linear CWA model.

Figure 5.4 shows that the linear dynamics of the CWA are fully determined by a selection of scaling gains, $K_\square$, as well as the various filters $H_{1_\square}$, $H_{2_\square}$ and $H_{3_\square}$ given by Equations (5.31), (5.36) and (5.48). The configurable parameters that appear in these equations are the various break frequencies $\omega_{1_\square}$, $\omega_{2_\square}$ and $\omega_{3_\square}$ as well as the common damping ratio ζ. Reflecting back to the coupled model in Equation (5.11), it is evident that to capture the linear CWA dynamics a *motion state* vector, $\bar{x}^m$, can be defined as:

$$\delta\bar{x}^m = \begin{bmatrix} \bar{q}_{1_x}^T & \bar{q}_{1_y}^T & \bar{q}_{1_z}^T & \bar{q}_{2_x}^T & \bar{q}_{2_y}^T & \bar{q}_{3_p}^T & \bar{q}_{3_q}^T & \bar{q}_{3_r}^T & (\bar{\Phi}^s)^T \end{bmatrix}^T \tag{5.53}$$

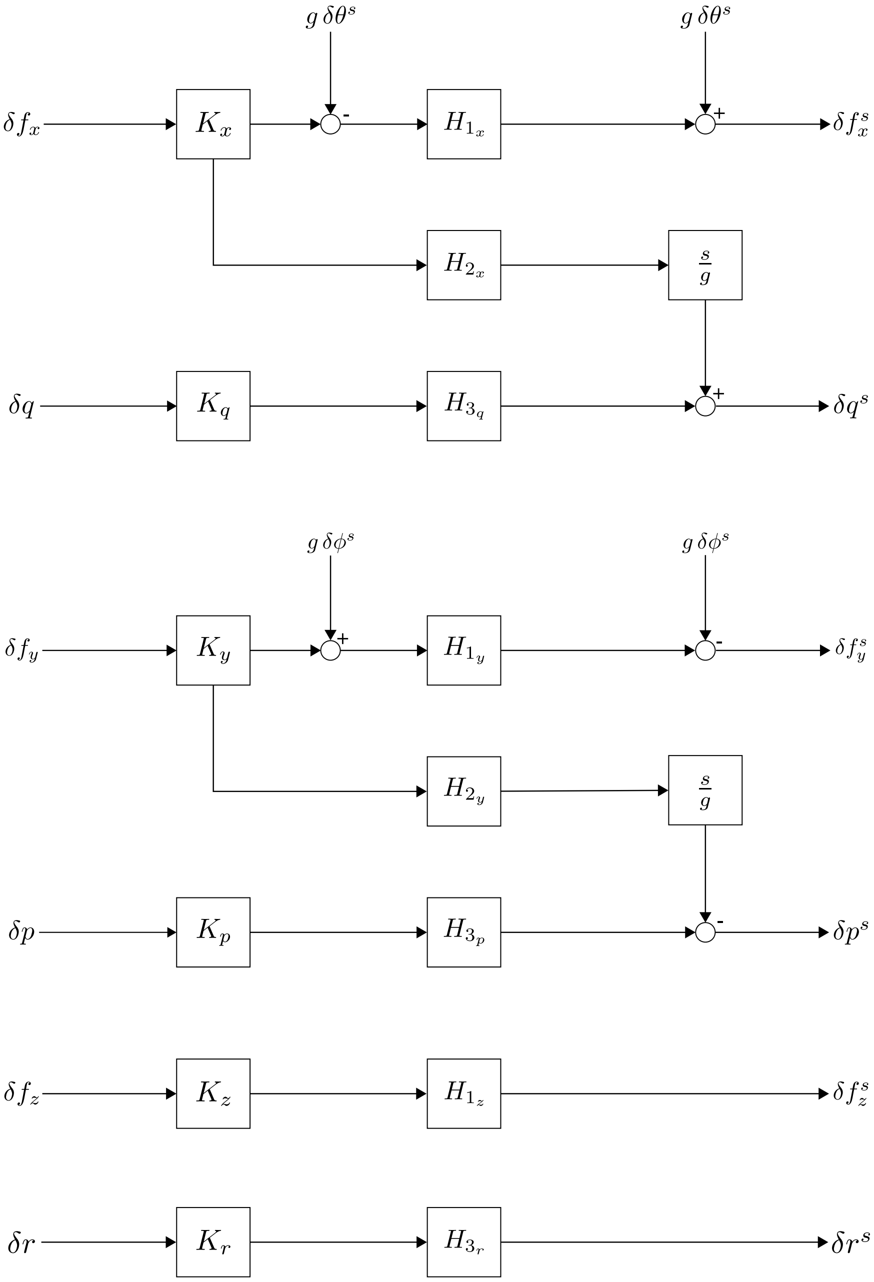

Figure 5.4: A schematic of the linearized Classical Washout Algorithm.

where $\bar{q}_{1_\square}$, $\bar{q}_{2_\square}$ and $\bar{q}_{3_\square}$ are auxilliary state vectors that appear as a result of the conversion of $H_{1_\square}$, $H_{2_\square}$ and $H_{3_\square}$ to state-space form, and $\bar{\Phi}^s$ is a vector that contains the simulator attitude. The outputs of the linear CWA depicted in Figure 5.4 that are of primary interest are the (perturbed) human-perceived specific forces and angular rates. Thus the *motion output* vector can be defined as:

$$\delta\bar{y}^m = \begin{bmatrix}\delta f_x^s & \delta f_y^s & \delta f_z^s & \delta p^s & \delta q^s & \delta r^s\end{bmatrix}^T \tag{5.54}$$

Based on the definitions in Equations (5.53) and (5.54), combined with the results from the CWA linearization in the preceding sections, it is possible to obtain expressions for the matrices A^m, B^m and C^m also appearing in Equation (5.11). These are not listed in this chapter for the sake of brevity, but can be found in Appendix C for reference.

5.3. OBTAINING THE COUPLED SYSTEM EIGENSTRUCTURE

In Section 5.2, the linearization of the Classical Washout Algorithm (CWA) was outlined. From the end result, depicted in Figure 5.4, it is apparent that the inputs to the CWA are the vehicle perturbed *specific forces* and *rotational rates*. In this section, it will be shown how these quantities can be obtained and expressed in terms of the vehicle dynamics states. This constitutes the last step in the derivation of the coupled vehicle-MCA system proposed in Equation (5.11). Subsequently, it will be shown how to obtain and exploit the eigenstructure of the coupled system in order to obtain a measure of the *amount of distortion* in each human-perceived perceived quantity as a result of motion filtering.

5.3.1. HUMAN-PERCEIVED STATES FROM VEHICLE DYNAMICS

In order to couple the linear vehicle and CWA dynamics, expressions for human-perceived quantities (i.e., specific forces and angular rates) in perturbed form are necessary. To this end, the linear vehicle dynamics are defined first:

$$\begin{aligned}\delta\dot{\bar{x}}^p &= A^p\,\delta\bar{x}^p + B^p\,\delta\bar{u}^p\\ \delta\bar{y}^p &= C^p\,\delta\bar{x}^p + D^p\,\delta\bar{u}^p\end{aligned} \tag{5.55}$$

In this formulation, the linear vehicle dynamics are governed by A^p and B^p, which for helicopters has been derived in Appendix A (see Equation (A.117)). Here, the vehicle state and input vectors were also defined as (see Equation (A.118)):

$$\begin{aligned}\delta\bar{x}^p &= \begin{bmatrix}\delta u & \delta v & \delta w & \delta\phi & \delta\theta & \delta p & \delta q & \delta r\end{bmatrix}^T\\ \delta\bar{u}^p &= \begin{bmatrix}\delta\theta_0 & \delta\theta_{1_c} & \delta\theta_{1_s} & \delta\theta_{0_{tr}}\end{bmatrix}^T\end{aligned} \tag{5.56}$$

The desired quanities in the vehicle *output* vector, $\bar{y}^p$, are the perturbed specific forces and rotational rates, i.e.:

$$\delta\bar{y}^p = \begin{bmatrix}\delta f_x & \delta f_y & \delta f_z & \delta p & \delta q & \delta r\end{bmatrix}^T \tag{5.57}$$

Comparing Equation (5.56) and Equation (5.57), it is evident that the perturbed rotational rates are already present in the perturbed state vector. To obtain (linear) expressions for the perturbed specific forces, the vehicle translational equations of motion (see Equation (A.88)) can be used:

$$\dot{\bar{V}} = \bar{f}(\bar{x}^p, \bar{u}^p) + T_{bi}(\psi, \theta, \phi)\,\bar{g} - \bar{\omega} \times \bar{V} \tag{5.58}$$

where $\bar{V} \equiv \begin{bmatrix} u & v & w \end{bmatrix}^T$ and $\bar{f}(\bar{x}^p, \bar{u}^p) \equiv \bar{F}_{\text{cg}}(\bar{x}^p, \bar{u}^p)/m$. Hence, the specific forces appearing in Equation (5.58) are the resultant *non-gravitational forces acting on the vehicle per unit mass*. These quantities were already expressed in linear form in Appendix A.8.1 (see, e.g., Equation (A.100)). The following generic expression for the linearized specific forces can thus be defined:

$$\begin{aligned} \delta f_{\square} = \frac{\delta F_{\text{cg}}^{\square}}{m} = \square_u \delta u + \square_v \delta v + \square_w \delta w + \square_p \delta p + \square_q \delta q + \\ \square_r \delta r + \square_{\theta_0} \delta\theta_0 + \square_{\theta_{1_c}} \delta\theta_{1_c} + \square_{\theta_{1_s}} \delta\theta_{1_s} + \square_{\theta_{0_{tr}}} \delta\theta_{0_{tr}} \end{aligned} \tag{5.59}$$

where □ is a placeholder for the translational vehicle dofs. (i.e., x, y and z). Equation (5.59) expresses the perturbed specific forces as a linear combination of the vehicle states and inputs. Combined with the insight that the vehicle rotational rates appear directly in the state vector, it is possible to specify the C^p and D^p matrices appearing in Equation (5.55). The definitions of these matrices can be found in Appendix C for reference and lead directly to the necessary definitions of A^{pm}, B^m, C^{pm} and D^m appearing in Equation (5.11). These, in turn, are also included in Appendix C and complete the linear model of the coupled vehicle and MCA dynamics.

5.3.2. EXTENDED EIGENVECTORS OF THE COUPLED SYSTEM

In Section 5.1, the significance of *modes* to characterise vehicle dynamics was discussed. The eigenvalues of a linear system were shown to reveal information about stability, frequency and damping of the characteristic vehicle modes. Furthermore, the eigenvector associated with each mode was found to expose the mode shape through the relative magnitude and phase (for complex eigenvalues) between the various states contained in the model. Finally, it was shown that the vehicle response could be described in terms of its modal coordinates, where the *mode participation factor* was introduced as a measure of the contribution of each mode in the vehicle's state response. In this section, the eigenstructure of the coupled system in Equation (5.11) will be used to *quantify* the effect of the MCA dynamics on the *existing* vehicle modes in terms of *human-perceived quantities*.

This information can be obtained by applying a modal coordinate transformation to the coupled system. This operation was outlined in Section 5.1 and has resulted in Equation (5.3). In summary, the state vector could be expressed as (see Equation (5.2)):

$$\bar{x}^c = W^c \bar{r}^c \qquad \text{or} \qquad \bar{r}^c = (W^c)^{-1}\,\bar{x}^c \tag{5.60}$$

where W^c is the *modal matrix* containing the eigenvectors of the coupled system matrix, i.e., A^c in Equation (5.11). Subsequent pre-multiplication of W^c with the coupled system output matrix C^c from Equation (5.11) yields the *extended modal matrix*:

$$C^c W^c = \begin{bmatrix} \bar{w}_{\bar{y}^c}^{\lambda_1} & \bar{w}_{\bar{y}^c}^{\lambda_2} & \cdots & \bar{w}_{\bar{y}^c}^{\lambda_{m-1}} & \bar{w}_{\bar{y}^c}^{\lambda_m} \end{bmatrix} = \begin{bmatrix} w_{f_x}^{\lambda_1} & w_{f_x}^{\lambda_2} & \cdots & w_{f_x}^{\lambda_{m-1}} & w_{f_x}^{\lambda_m} \\ \vdots & \vdots & & \vdots & \vdots \\ w_r^{\lambda_1} & w_r^{\lambda_2} & \cdots & w_r^{\lambda_{m-1}} & w_r^{\lambda_m} \\ w_{f_x^s}^{\lambda_1} & w_{f_x^s}^{\lambda_2} & \cdots & w_{f_x^s}^{\lambda_{m-1}} & w_{f_x^s}^{\lambda_m} \\ \vdots & \vdots & & \vdots & \vdots \\ w_{r^s}^{\lambda_1} & w_{r^s}^{\lambda_2} & \cdots & w_{r^s}^{\lambda_{m-1}} & w_{r^s}^{\lambda_m} \end{bmatrix} \tag{5.61}$$

From Equation (5.61), it can be seen that the matrix C^c scales and combines the right eigenvectors of A^c such that a different set of eigenvectors is obtained, in terms of both the vehicle and CWA-filtered *perception states*. This set of *extended* eigenvectors are a *linear* combination of the original eigenvectors in W^c and, in Equation (5.61), are denoted by $\bar{w}_{\bar{y}^c}^{\lambda_i}$. The superscript λ_i signifies that the eigenvector corresponds to the i-th eigenvalue of the matrix A^c, with $i \in \mathbb{Z} : i \in [1, m]$. Here, m is the number of eigenvalues (i.e., the rank) of matrix A^c. The subscript $\bar{y}^c$ is used to signify the extended eigenvectors pertaining to the system *output* vector $\bar{y}^c$ and distinguishes them from the eigenvectors in W^c pertaining to the coupled system state vector $\bar{x}^c$. Finally, the quantities $w_{\square}^{\lambda_i}$ denote the extended eigenvector coefficients pertaining to both unfiltered and filtered perception states. The dimension of the extended modal matrix is therefore $12 \times m$, where each column is an eigenvector of A^c.

Because of the block triangular structure of the matrix A^c (see Equation (5.11)), the m eigenvalues (and eigenvectors) of A^c consist of the n eigenvalues of A^p as well as the k eigenvalues of A^m [Strang, 2006]. As noted earlier, the *internal* dynamics of the CWA effectively *distort* the dynamics of the human-perceived quantities governed by the vehicle dynamics. To quantify this distortion, it is of interest to *compare* the extended eigenstructures of the *uncoupled* and (CWA-)*coupled* vehicle dynamics. This information is readily contained in the extended modal matrix defined in Equation (5.61). Namely, of the m eigenvectors in the extended modal matrix, only the n eigenvectors corresponding to the n eigenvalues of A^p are of interest. The remaining k eigenvectors in the extended modal matrix correspond to the eigenvalues of A^m, which capture how the individual dynamic elements in the CWA distort the human-perceived vehicle dynamics. Thus, a new extended modal matrix can be constructed from Equation (5.61), which only contains the n eigenvectors corresponding to the eigenvalues of A^p:

$$(C^c W^c)_{*n} = \begin{bmatrix} \bar{w}_{\bar{y}^c}^{\lambda_1} & \bar{w}_{\bar{y}_c}^{\lambda_2} & \cdots & \bar{w}_{\bar{y}^c}^{\lambda_{n-1}} & \bar{w}_{\bar{y}_c}^{\lambda_n} \end{bmatrix} = \begin{bmatrix} w_{f_x}^{\lambda_1} & w_{f_x}^{\lambda_2} & \cdots & w_{f_x}^{\lambda_{n-1}} & w_{f_x}^{\lambda_n} \\ \vdots & \vdots & & \vdots & \vdots \\ w_r^{\lambda_1} & w_r^{\lambda_2} & \cdots & w_r^{\lambda_{n-1}} & w_r^{\lambda_n} \\ w_{f_x^s}^{\lambda_1} & w_{f_x^s}^{\lambda_2} & \cdots & w_{f_x^s}^{\lambda_{n-1}} & w_{f_x^s}^{\lambda_n} \\ \vdots & \vdots & & \vdots & \vdots \\ w_{r^s}^{\lambda_1} & w_{r^s}^{\lambda_2} & \cdots & w_{r^s}^{\lambda_{n-1}} & w_{r^s}^{\lambda_n} \end{bmatrix} \tag{5.62}$$

where the subscript $*n$ signifies the n columns of $C^c W^c$ in Equation (5.61) that correspond to $\lambda_1 \ldots \lambda_n$, i.e., the eigenvalues of A^p. The result in Equation (5.62) is the foundation of the proposed *EMD* methodology, because it allows for the direct comparison of the unfiltered vehicle mode shapes (captured by the coefficients $w_{f_x}^{\lambda_\square}$ through $w_r^{\lambda_\square}$) as well as their CWA-filtered equivalents (captured by the coefficients $w_{f_x^s}^{\lambda_\square}$ through $w_{r^s}^{\lambda_\square}$). Consequently, it becomes possible to *quantify the degree of modal distortion imposed by the MCA dynamics*. In the last section of this chapter, the utility of the new EMD methodology outlined here will be demonstrated using a case study.

5.4. THE EMD METHOD

Given the theoretical foundation of the EMD method, it is now possible to formalize the method in terms of a few concrete steps:

1. Obtain a *linear* model of the vehicle dynamics, containing expressions for the human-perceived quantities (i.e., specific forces and angular rates) either implicitly or explicitly. This model can be derived analytically, as done in this dissertation for helicopters, or can be obtained empirically.

2. Linearize the applicable MCA. Section 5.2 presented a possible approach for the commonly applied CWA. However, a similar approach can also be adapted for other MCAs, as long as its main components can be linearized.

3. Couple the two separate linear models of the vehicle and MCA dynamics using Equation (5.11). As outlined in Section 5.3, this coupled model can then be subjected to a modal coordinate transformation in order to extract information on the MCA-induced modal distortion of human-perceived quantities in terms of the vehicle's dynamic modes.

To illustrate the practical utility of the EMD method, an example application is included in the next section.

5.5. EIGENMODE DISTORTION: A CASE STUDY

This section applies the EMD method to a motion cueing evaluation of the three-dof hover dynamics of the Bo-105 helicopter (see Figure 5.1). First, the *visualization* of the MCA-induced modal distortion obtained from Equation (5.62) will be explained. Subsequently, the effect of changing the break frequency of the high-pass filter in the pitch channel of the CWA is examined.

5.5.1. VISUALIZATION OF MCA-INDUCED MODAL DISTORTION

As explained in Section 5.1.1 and shown in Figure 5.1, three distinct modes can be identified in the three-dof *longitudinal* model of the Bo-105 hover dynamics: the *phugoid* (PH), *pitch subsidence* (PS) and the *heave subsidence* (HS). The phugoid is a *periodic* mode with a natural frequency of 0.4 rad/s and a damping ratio of 0.04. The pitch and heave subsidences are both *aperiodic* modes. The pitch subsidence is a relatively high-frequency mode, with a natural frequency of approximately 3.3 rad/s, whereas the heave subsidence is a low frequency mode with a natural frequency of 0.32 rad/s.

In order to demonstrate the utility of the new EMD methodology, the linear vehicle model is coupled to the CWA dynamics according to Equation (5.11). The linearized model of the CWA in Section 5.2 was derived for the generic six-dof case, but is easily simplified by omitting the *off-axis* CWA channels (i.e., roll, sway and yaw) in Figure 5.4 as well as their corresponding states and outputs from Equations (5.53) and (5.54). In effect, for the three-dof longitudinal case, the *extended eigenvector coefficients* of interest remaining in Equation (5.62) correspond to $\delta f_x^{(s)}$, $\delta f_z^{(s)}$ and $\delta q^{(s)}$. These can be visualized using *modal distortion portraits*, an example of which is depicted in Figure 5.5a. The CWA parameters selected for this example are listed in Figure 3.1 of Chapter 3, with the exception of ζ and $\omega_{b,1_z}$, which were set to values of 0.7071 and 0, respectively.

Figure 5.5a depicts the MCA-induced distortion in each mode of the three-dof model of the Bo-105 helicopter. The distortion of the *aperiodic* pitch and heave subsidences is represented by a set of horizontal bars, showing the magnitude of both the *unfiltered* and *filtered* contributions of the human-perceived quantities. The arrows in the figure indicate the induced modal distortion from the unfiltered to the filtered quantities. In the example shown, *amplification* of δf_x^s with respect to δf_x is seen for both the PS and HS. However, it can also be seen that the contributions of δf_x and δq to the HS are very small in terms of *absolute* amplitude in comparison to δf_z. Similarly, the contribution of δf_z in PS is small in comparison to δf_x and δq. Furthermore, in PS, *attentuation* of δq^s with respect to δq is observed, whereas in HS δf_z^s is also strongly attenuated with respect to δf_z. It is important to note, however, that these observations reveal nothing about the *relative importance* of the human-perceived quantities. This is true in particular when comparing $\delta q^{(s)}$ to $\delta f_x^{(s)}$ and $\delta f_z^{(s)}$, because their units differ (i.e., rad/s versus m/s^2). The corresponding modal time traces are also shown in Figure 5.5b and, as expected, are consistent with the findings from the modal distortion portraits.

The modal distortion of the *periodic* phugoid mode is represented in the complex plane, as also shown in Figure 5.5a. In contrast to aperiodic modes, here the human-perceived quantities are subjected to *arbitrary* distortions in phase ranging from 0° to 180° in either clockwise (*lag*) or counter-clockwise (*lead*) directions[4]. From the figure, it is deduced that δf_x^s in PH is affected most by the MCA, as it shows a phase lag of approximately 135° and is strongly amplified at the same time. The pitch rate, δq^s, is also strongly affected and shows a phase lead in excess of 90° with respect to δq as well as an attenuation of its amplitude. It also appears that δf_z (in hover) has a limited contribution and that δf_z^s is strongly attenuated to the point where its contribution can no longer be discerned in PH. Again, the corresponding modal time traces are also shown in Figure 5.5b.

While the modal distortion portraits reveal the effect of the MCA on the *individual* human-perceived quantities, they also show how the induced distortion affects the relation *between* these quantities. For example, for the PS, δq is seen to "dominate" the response in terms of its *absolute* ampltide when compared to δf_x. However, as a result of the MCA, δf_x^s becomes larger in absolute amplitude than δq^s. A similar result is seen in the relation between $\delta q^{(s)}$ and $\delta f_x^{(s)}$ in PH where, as a result of the MCA, the phase lead of δq^s with respect to δf_x^s is reduced from approximately 180° to only 90°. At the same time, the contribution of δf_x^s with respect to δq^s in PH is found to increase substantially.

---

[4] Note that these directions depend entirely on which of the two complex conjugate eigenvalues of the mode is examined. Here, and in the remainder of this thesis, only eigenvalues with a *positive* complex part are considered.

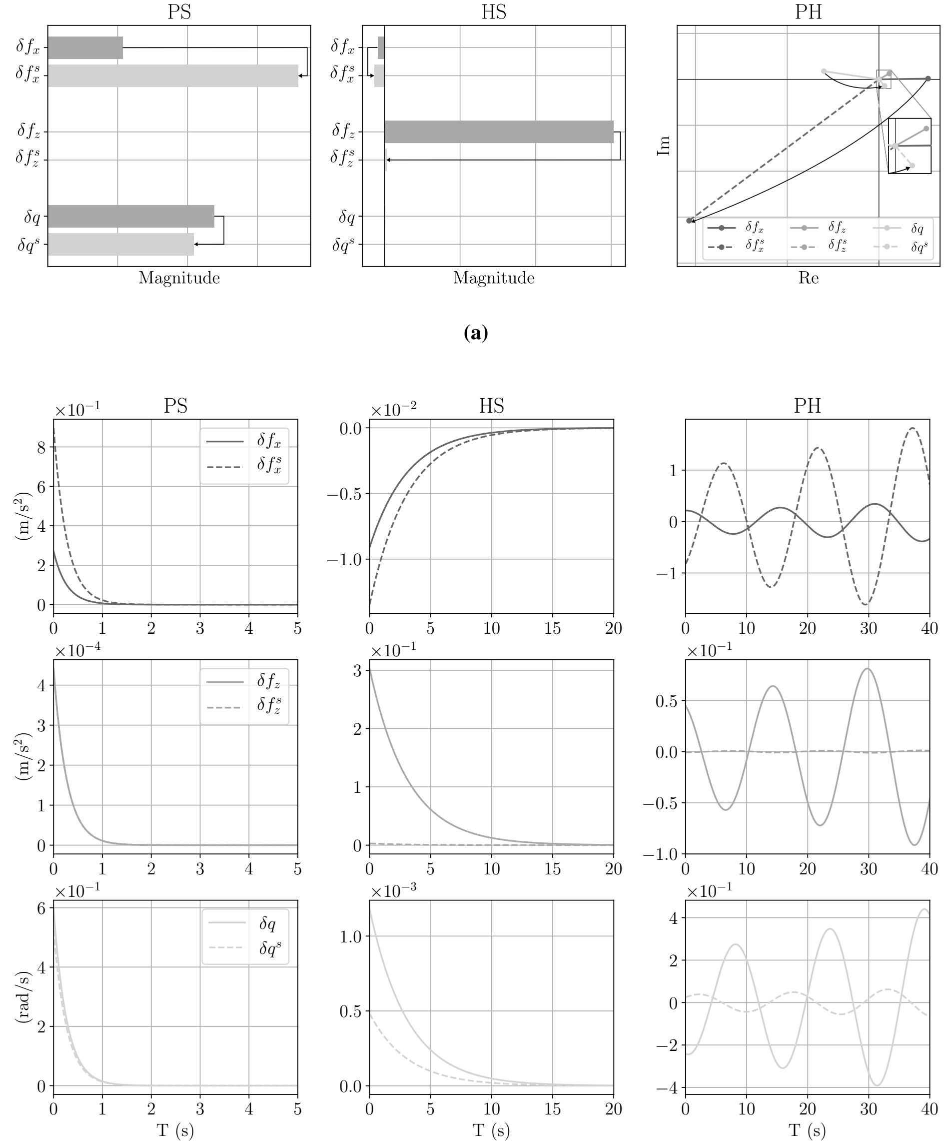

(a)

(b)

Figure 5.5: **(a)** MCA-induced modal distortion of human-perceived quantities in a three-dof linear model of the Bo-105 in hover and **(b)** corresponding modal time responses.

5.5.2. EFFECT OF CWA PITCH BREAK FREQUENCY

In Chapter 3, an interesting relation was exposed between variations in the break frequency of the high-pass filter in the CWA pitch channel and the resulting response of the specific force reproduced in surge. In order to investigate whether the same effect is observed when EMD is applied, ω_{3_q} as listed in Figure 3.1 is increased and the resulting modal distortion portraits are examined. The results are shown in Figure 5.6 for values of ω_{3_q} ranging from 0.8 (baseline) up to 6.0 rad/s, respectively. For reference, time-domain modal responses corresponding to Figures 5.6b–5.6d have also been included in Appendix C.

From Figure 5.6, the most significant effect of increasing ω_{3_q} appears in the MCA-induced distortion of the phugoid mode. For the baseline value of 0.8 rad/s (see Figure 5.6a), a strong amplification of the simulated specific force in surge could be distinguished with substantial phase *lag*. This is also evident from the time responses shown in Figure 5.5b. As ω_{3_q} is *increased*, it can be seen that the MCA-induced amplification as well as the phase lag of δf_x^s *diminish*. For values of ω_{3_q} in excess of 3.0 rad/s, the amplification of the simulated specific force in surge becomes *attenuation*. The effect on the simulated pitch rate in the phugoid mode is also discernable, where it can be seen that as ω_{3_q} is increased, δq^s also diminishes in amplitude. The effect on the phase of δq^s, however, is more substantial. Namely as ω_{3_q} is increased from 0.8 to 6.0 rad/s, the phase *lag* with respect to δq is reduced from 180° to 90°. In effect, the contributions of δf_x^s and δq^s remaining in the phugoid mode are largely a consequence of the applied *tilt coordination* in the CWA.

From the EMD analysis discussed thus far, it appears that constraining the rotational vehicle dofs in the MCA is beneficial for reproducing the low-frequency phugoid mode in helicopters. This result is in agreement with the findings from the (tailored) OMCT analysis in Chapter 3 (see Figure 3.13). In EMD, however, the consequence of larger values for ω_{3_q} become apparent from the MCA-induced distortion of the pitch subsidence mode. Namely, as ω_{3_q} is increased *up to* the approximate value of the frequency of the mode under consideration (i.e., 3.3 rad/s), it is seen from Figure 5.6 that the effect is rather limited and even results in a mild *amplification* of δq^s (see Figures 5.6b and 5.6c). However, as ω_{3_q} is increased beyond 3.0 rad/s, δq^s is found to strongly diminish in amplitude with respect to δq (see Figure 5.6d). At the same time, the amplification of δf_x^s with respect to δf_x also becomes smaller. Interestingly, however, the contribution of δf_x^s does remain more than twice as large compared to δf_x even for $\omega_{3_q} = 6.0$ rad/s. A final observation from Figure 5.6 is that the effect of ω_{3_q} on the MCA-induced distortion of the heave subsidence is negligible. This is expected, because the heave dof was assumed *uncoupled* from the other simulator dofs in the linearization of the CWA (see, e.g., Figure 5.4). Summarizing, the presented EMD analysis clearly reveals the effect of couplings between the different simulator dofs, particularly surge and pitch, and highlights the role of the various filter break frequencies in relation to the simulated vehicle dynamics.

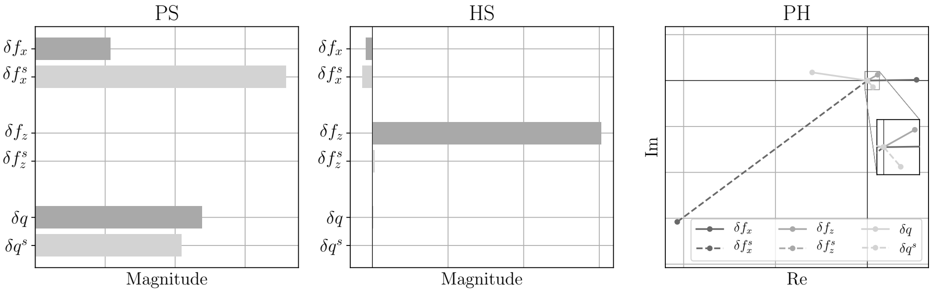

(a) ω_{3_q} = 0.8 rad/s

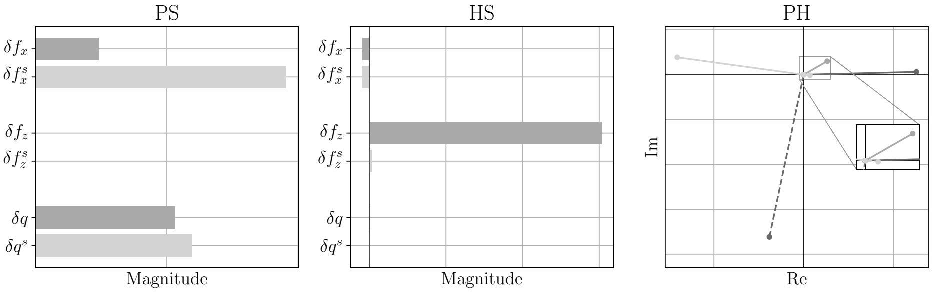

(b) ω_{3_q} = 1.5 rad/s

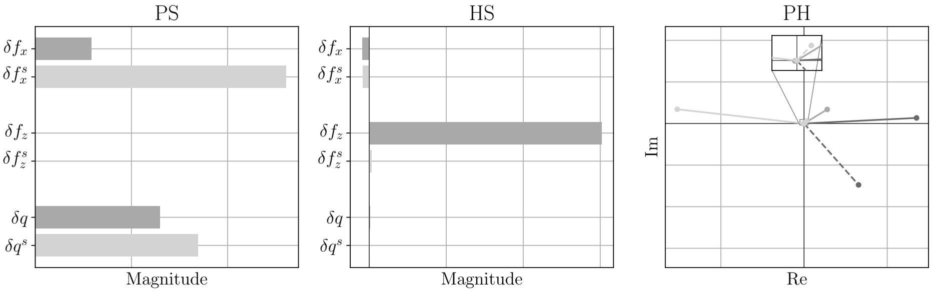

(c) ω_{3_q} = 3.0 rad/s

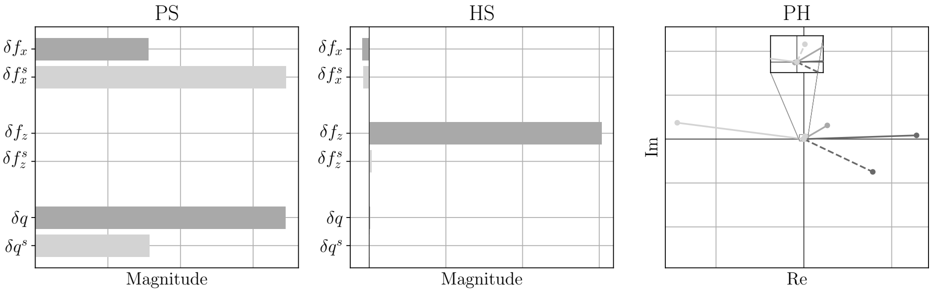

(d) ω_{3_q} = 6.0 rad/s

Figure 5.6: MCA-induced modal distortion with increasing ω_{3_q}.

5.6. CONCLUSION

This chapter has outlined the theoretical foundation of the new Eigenmode distortion (EMD) methodology. To exemplify the new method, a case study was presented. The analysis showed that the EMD method is capable of revealing many intricate interactions between the vehicle and Motion Cueing Algorithm (MCA) dynamics. Compared to existing tools like the Objective Motion Cueing Test (OMCT) studied in Chapter 3, the analytical foundation of EMD allows for a more systematic, model-based, analysis of contemporary MCAs (e.g., the Classical Washout Algorithm).

Nonetheless, like OMCT, EMD represents MCA-induced motion distortion in a rather abstract and, barring *relative* dimensions between human-perceived quantities, essentially *dimensionless* domain. While abstraction is necessary to permit the systematic analysis that the EMD method offers, it also means that the severity of certain motion distortions cannot be judged directly from the perspective of the *human operator*, i.e., including its *perceptual limitations*. In the next chapter of this thesis, the practical utility of the EMD method is therefore evaluated using several *pilot-in-the-loop* experiments.

6

USING EIGENMODE DISTORTION IN MOTION CUEING FIDELITY ASSESSMENT

In Chapter 5, Eigenmode distortion (EMD) was introduced as a new methodology for the quantitative analysis of motion cueing fidelity. To assess the practical utility of the method three pilot-in-the-loop experiments were conducted on two different simulators: the SIMONA Research Simulator (SRS) and the Desorientation Demonstrator Amst (Desdemona). In each of these experiments, a different task (or Mission Task Element) was executed, where the offered motion cues were varied in accordance with an EMD-based analysis. This chapter describes the methodology underlying these experiments and presents the obtained results.

First, the methodology is discussed in Section 6.2. This section outlines the characteristics of the simulator used, the controlled variables, hypotheses, independent variables and, finally, dependent measures. Conditions and results specific to each individual experiment are subsequently presented in Section 6.3. Finally, Section 6.4 discusses the results in view of the formulated hypotheses and Section 6.5 concludes the chapter.

6.1. GOAL

Within Eigenmode distortion (EMD), the vehicle's dynamic response is decomposed along *decoupled* coordinates known as the vehicle's *eigenmodes*. Helicopter dynamics are often analysed in terms of these modes [Padfield, 2007], as they contain crucial information about the vehicle's stability and dynamic response properties. EMD further assumes that the eigenmodes are perceived by the pilot as *characteristic* responses of the system. As shown in Chapter 5, the dynamics of the Motion Cueing Algorithm (MCA) *distort* these modes through a combination of scaling and filtering. The primary goal of the present chapter is to demonstrate the practical utility of EMD in motion cueing fidelity assessment.

The adopted approach is exploratory at its core, where EMD is used as a quantitative, "guiding", methodology to determine suitable motion cueing configurations for three typical helicopter tasks (or MTEs): a precision hover, lateral reposition and depart/abort [Anonymous, 2000]. In three separate experiments, these configurations are subsequently assessed *subjectively* by test pilots of the RNLAF. In addition, both attained task performance measures as well as the *modal excitation* of the used flight dynamics models are analyzed alongside subjective measures in relation to the evaluated motion cueing configurations.

6.2. METHODOLOGY

The experiments performed are labelled I, II and III for the precision hover, lateral reposition and depart/abort MTEs, respectively. The following sections describe the apparatus, controlled variables, independent variables, hypotheses and dependent measures pertaining to each of these three experiments.

6.2.1. APPARATUS

Experiments I and II were performed on the SIMONA Research Simulator (SRS), whereas experiment Experiment III was performed on the Desdemona simulator. Both platforms are shown in Figure 1.1 and were already discussed in Chapters 3 (see Section 3.4.1) and 4 (see Section 4.3).

6.2.2. CONTROLLED VARIABLES

Within the three individual experiments performed, two aspects were kept constant, namely: the *flight dynamics model*[1] and the *task*. These are discussed in the following paragraphs for each experiment.

Flight dynamics models All considered tasks were performed using the Draftsim (see Chapter 4) helicopter flight dynamics model developed in this dissertation. However, in Experiments I and II, a limited number of degrees-of-freedom were enabled. In Experiment I, the three *longitudinal* dofs (i.e., pitch, surge and heave) were considered. The type of model used in this experiment is the AH-64 Apache helicopter, *without* the SCAS. Figure 6.1 and Table 6.1 show the dynamic modes (in hover) as well as the associated stability and control derivatives, respectively, as computed from this model. From the figure, the

---

[1] In a part of Experiment II, the flight dynamics model *is* considered as an independent variable.

characteristic pitch and heave subsidences (i.e., PS and HS) as well as the phugoid (PH) can be distinguished.

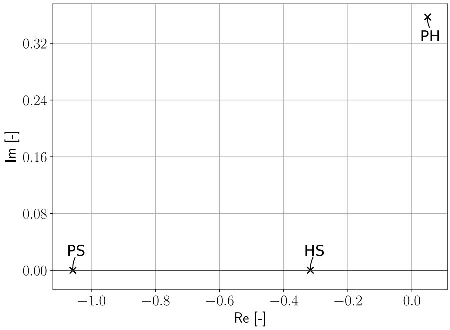

Figure 6.1: AH-64 modes in hover.

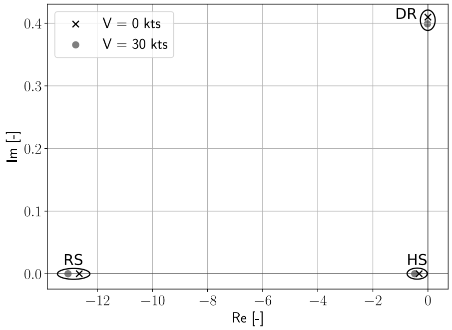

Figure 6.2: Bo-105 modes in hover and 30 kts sideward flight.

Table 6.1: AH-64 model derivatives in hover.

Stability derivatives		*Control derivatives*	
X_u	-0.034	X_{δ_0}	0.025
X_w	0.023	X_{δ_s}	0.053
X_q	0.27	Z_{δ_0}	-0.30
Z_u	0.022	Z_{δ_s}	$4.6\cdot10^{-3}$
Z_w	-0.31	M_{δ_0}	$-4.1\cdot10^{-4}$
Z_q	0.024	M_{δ_s}	-0.033
M_u	0.014		
M_w	$7.8\cdot10^{-4}$		
M_q	-0.27		

Table 6.2: Bo-105 model derivatives in hover and 30 kts sideward flight.

Stability derivatives			*Control derivatives*		
	0 kts	*30 kts*		*0 kts*	*30 kts*
Y_v	-0.023	-0.085	Y_{δ_0}	0.0	$6.1\cdot10^{-3}$
Y_w	0.0	$-6.7\cdot10^{-3}$	Y_{δ_c}	0.029	0.029
Y_p	-0.43	-0.56	Z_{δ_0}	-0.25	-0.24
Z_v	0.0	-0.19	Z_{δ_c}	0.0	0.029
Z_w	-0.32	-0.55	L_{δ_0}	0.0	-0.067
Z_p	0.0	-0.28	L_{δ_c}	0.45	0.45
L_v	-0.22	-0.21			
L_w	0.0	-0.065			
L_p	-12.6	-12.9			

In Experiment II, the three *lateral* dofs (i.e., roll, sway and heave) were enabled. Instead of the AH-64 Apache, however, the Bo-105 model was used in this experiment. This was done for two reasons. First, it demonstrates the applicability of EMD as a *universal* tool, independent of a specific helicopter type. Second, the choice for the Bo-105, with its hingeless rotor system, allows for an interesting analysis on the effect of more advanced *rotor dynamics* in relation to motion cueing fidelity. Figure 6.2 and Table 6.2 show the dynamic modes (in hover and 30 kts sideward flight) as well as the associated stability and control derivatives, respectively, as computed from this model. From the figure, the characteristic roll and heave subsidences (i.e., RS and HS) as well as the Dutch roll (DR) can be distinguished.

Finally, in Experiment III, a *six* dof model of the AH-64, *with* SCAS (but without attitude feedback, see Appendix A.9.1), will be considered. The application of this model aims to demonstrate the utility of EMD in more *realistic* applications. Do note that, even though a six dof *coupled* model is used to execute the depart/abort MTE under consideration, the *EMD* analysis remains constrained to the *decoupled* (primarily longitudinal) degrees-of-freedom. The reason for this is twofold. First, at present, the EMD method, while derived for the *coupled* six rigid-body dofs case (see Chapter 5), has been implemented only for the *decoupled* longitudinal and lateral helicopter dofs. Second, performing the analysis with these simplified, decoupled degree-of-freedom models could also provide a measure of the extent to which such models are representative in motion cueing fidelity assessment.

Tasks In each of the three experiments performed, a different Mission Task Element was evaluated. These MTEs are the *precision hover* (experiment I), the *lateral reposition* (experiment II) and the *depart/abort* (experiment III).

(a) Front view

(b) Side view

Figure 6.3: Impression of the precision hover MTE as seen from the SRS visuals.

In the precision hover MTE, the helicopter degrees-of-freedom were constrained to the *longitudinal motion only*. A description of the MTE was already given in Section 4.3.2. Of the stipulated requirements in ADS-33E [Anonymous, 2000] only those pertaining to the longitudinal (±3/±6 ft desired/adequate) and vertical (±2/±4 ft desired/adequate) dofs were enforced. To further simplify the analysis, the “transition phase” in the original maneuvre was omitted and the vehicle was already initialized in hover. The participants were instructed to keep the helicopter in a stable hover for the duration of 30 seconds. Also, in order to ensure sufficient (external) excitation during the task, moderate turbulence was incorporated. This turbulence was based on the Dryden spectra [Chalk et al., 1969] and tuned such to be comparable to the disturbances experienced by a light (fixed-wing) aircraft approach (see Appendix A.9.2 for details). Finally, the turbulence only affected the longitudinal and vertical vehicle degree-of-freedom. Figure 6.3 shows an impression of the task setup as seen from the visual system of the SRS.

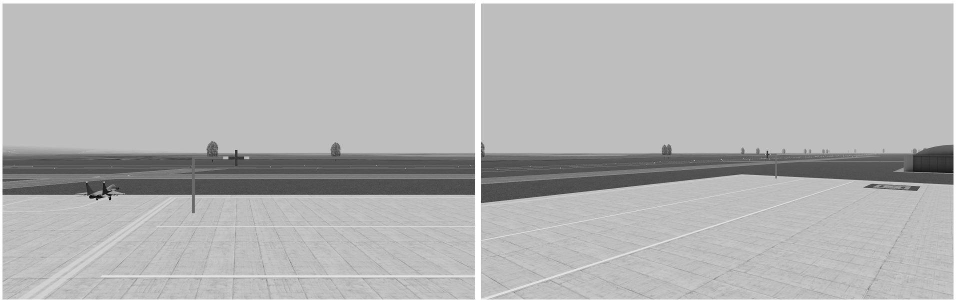

(a) Front view **(b)** Side view

Figure 6.4: Impression of the lateral reposition MTE as seen from the SRS visuals.

In the lateral reposition MTE, the helicopter degrees-of-freedom were constrained to *lateral motion only*, *including* vertical displacement (heave) and *excluding* yaw. A description of this MTE was also already given in Section 4.3.2. Of all the criteria pertaining to this MTE, only the maximum lateral velocity (35 kts) to be attained and the allowed lateral position offset from the intended point (±10 ft) were enforced. Thus, no time constraints or other (positional) accuracy requirements were considered. In Figure 6.4, an impression is shown of the task as seen from the visual system of the SRS.

In the depart/abort MTE considered, all six degrees-of-freedom of the helicopter were active. Again, a description of the task and the corresponding requirements from ADS-33E are included in Section 4.3.2. In this MTE, in analogy to the lateral reposition described in the previous paragraph, the maximum velocity (35 kts) and longitudinal position offset from the intended end point (±20 ft) were enforced. Time constraints and criteria on allowed lateral and altitude deviations were not considered. However, the participants were not permitted to overshoot the intended end point (as stipulated in ADS-33E) and the maximum pitch attitude was set at ±20 degrees. Figure 4.11 in Chapter 4 shows an impression of the task setup as seen in the VR-world of the Desdemona simulator.

6.2.3. INDEPENDENT VARIABLES

The primary independent variable of interest in each of the experiments is *motion*. Thus, in principle only parameters that pertain to the MCA are varied between individual experimental conditions. In experiment II, however, the effect of an alteration in the *flight dynamics model* was also investigated. This alteration pertains to the dynamics of the main rotor which, in the baseline flight dynamics model, are assumed *quasi-steady*. In the altered model also considered, the flapping dynamics of the rotor blades are added (see Appendix A.7.3).

The MCA configurations are selected using EMD analyses specific for the flight dynamics models and tasks under consideration. For this reason, a detailed discussion of the motion cueing conditions used in each experiment is postponed until Section 6.3. Nonetheless, the general rationale behind the different conditions is the same. Namely, because *a-priori* it is not known which vehicle *modes* are “dominant” in the tasks to be performed, it is opted to devise motion cueing configurations, based on EMD analyses, such to preserve individual dynamic modes (or components thereof) in the various flight dynamics models used. Also, each experiment incorporates a reference condition *without* simulator motion.

Between experiments I and II on the one hand and experiment III on the other, the *simulator* in which the tasks are performed is also different. Namely, the experiments I and II are executed on the SRS, whereas experiment III is performed on the Desdemona simulator. The primary difference between the two platforms, in these experiments, pertains less to the motion system, but rather to the *visual* system used. In Desdemona, use is made of Virtual Reality (VR), whereas in the SRS the collimated visuals are *projected* on a screen with a 180° field of view. The VR visuals can be argued to be more immersive and may therefore cause subjects to "reweight" visual and vestibular cues according to their reliability [Fetsch et al., 2009]. While this effect is not explicitly considered in this dissertation, it could substantially affect the experimental results. Therefore, a direct comparison of "fidelity" *between* the two simulators is not the intended focus of the present thesis.

6.2.4. HYPOTHESES

Prior to the execution of the experiments, a number of hypotheses were formulated. These are outlined in the following paragraphs for each individual experiment.

Experiment I: precision hover

① Position error decreases with all motion-*on* configurations as opposed to the *no*-motion condition. However, longitudinal position error is expected to be smallest in the motion condition aimed at cueing the pitch subsidence modes. Vertical position error, on the other hand, is expected to be smallest in the condition aimed at cueing the heave subsidence.

② It is hypothesised that motion cues in a specific vehicle mode are used to *subdue* participation of that particular mode in the vehicle's response. Hence, the overall participation of cued modes in the aircraft response will be less than that of modes that are not cued. This hypothesis is the primary result of a preliminary experiment performed on the SRS [Miletović et al., 2018].

③ The cued modes most valued by pilots are the pitch and heave subsidences, which is to become apparent through more favourable pilot ratings for the corresponding motion cueing configurations. In contrast, motion aimed at cueing the phugoid mode is expected to be valued least by pilots. This is because the phugoid is a mode that develops rather slowly and, therefore, motion cues in this mode are expected to provide less useful feedback to pilots in the precision hover MTE, which requires a control strategy with relatively high frequency, small amplitude inputs.

Experiment II: lateral reposition

④ Pilots will exhibit less over/undershoot in the vicinity of the target locations for conditions *with* motion in comparison to the *no*-motion condition. More specifically, motion aimed at cueing the roll subsidence mode is hypothesized to result in less oscillations around the target locations. Also, motion aimed at more accurately cueing the lower frequency Dutch roll mode is hypothesized to benefit the perception of lateral *velocity*, which could result in a lesser variance of the peak velocity reached during the task.

⑤ Overall, it is hypothesized that pilots will favour the condition aimed at cueing the roll subsidence mode rather than the condition aimed at cueing the Dutch roll mode. The reason behind this hypothesis is that pilots are assumed to be most actively controlling the aircraft in the "stabilization" phase of the lateral reposition MTE, in the vicinity of the target locations. Here, motion cues in the faster roll subsidence mode are expected to be of more use. By extension, the participation of the roll subsidence mode in the aircraft response close to hover is also expected to be less when motion aimed at cueing this mode is offered (see Hypothesis ③).

⑥ When blade flapping dynamics are incorporated in the flight dynamics model, pilots are hypothesized to notice a difference in the simulated flight environment *only* in the motion condition aimed at cueing the roll subsidence mode. A description pilots could use is that the model *with* flapping dynamics feels more "wobbly". This sensation is explained by the oscillatory roll/flap mode appearing in the altered flight dynamics model, replacing the non-oscillatory roll subsidence mode in the baseline model.

Experiment III: depart/abort

⑦ Introducing *time-varying* changes in the MCA, aimed at cueing the pitch subsidence in hover and the phugoid in forward flight is hypothesized to result in more favourable overall pilot ratings in comparison to motion cueing configurations where either *one* of these two individual modes are cued. This is because the fast rotational cues in the pitch subsidence are expected to benefit the stabilization of the aircraft in hover. In contrast, the more long-term motion cues in the Dutch roll are expected to be beneficial to pilots during acceleration and deceleration from/to forward flight.

6.2.5. DEPENDENT MEASURES

In order to evaluate the stipulated hypotheses, a number of dependent measures are gathered in the experiments. The primary dependent measure is the Motion Fidelity Rating (MFR) scale [Hodge et al., 2015a] (shown in Figure 2.2), aimed at subjectively evaluating the perceived fidelity of the physical motion cues simulated. This rating scale assumes that the "usefulness" of motion cues in relation to attained task performance is a measure of fidelity. While the extent to which this assumption is accurate can be debated, it does provide an intuitive framework against which the *relative* value of strongly differing motion cueing configurations can be evaluated (see also Chapter 2).

Two hypotheses, namely ① and ④, depend upon measures of task *performance*. In case of the precision hover MTE in experiment I, performance is measured in terms of position error. A convenient measure of position error that is used as a result in experiment I is the *Root-Mean-Square (RMS)* of the error between the aircraft position and the target hover position. For the lateral position MTE in experiment II, performance is measured in terms of over/undershoot at the target location as well as the peak velocity reached. These measures can be conveniently studied using *maneuvre phase portraits*.

In relation to EMD, the last dependent measure of interest is the *Mode Participation Factor (MPF)*, introduced in Chapter 5. This metric is used primarily in experiments I and II to study the influence of the various motion cueing configurations on the *modal excitation* of the flight dynamics models. From Section 5.1.1, the (measured) linear system state can be transformed to modal coordinates using:

$$\bar{r}(t) = W^{-1}\delta\bar{x}(t)$$

where W is the *modal matrix* and $\delta\bar{x}$ is the *perturbed* system state obtained from:

$$\delta\bar{x}(t) = \bar{x}(t) - \bar{x}_e(t) \tag{6.1}$$

In this equation, $\bar{x}_e(t)$ is the *equilibrium* state that corresponds to the "nearest" *linearized* model at time t. The individual MPFs, then, are defined as:

$$m_{\square} = \int_0^T |r_i(t)|\, dt \qquad \forall \qquad i \in (1, n) \tag{6.2}$$

where $\square$ is a placeholder for the abbreviated *label* of the i-th *mode* and T is the duration of the time interval of interest.

6.2.6. PARTICIPANTS AND PROCEDURES

In Experiments I and II, five test pilots of the RNLAF participated, three of which, all AH-64 Apache pilots, also participated in Experiment III. Prior to the experiments, the participants received a written briefing containing background information, the task descriptions and the experiment procedures (see Appendix E for an example of such a briefing). These briefings also included a copy of the MFR scale, such that participants could familiarize themselves with the evaluation framework and terminology used. In each experiment, pilots were explicitly informed of the fact that *only* motion would be varied between the various experimental conditions. The exception is a part of experiment II, where a change in the flight dynamics model was also introduced, which was also communicated to the participants.

Each experiment commenced with a brief (approximately 15 minutes) *training* phase, meant to familiarize the pilots with the flight dynamics model, task and simulation environment. During this training phase, the participants were also exposed to each of experimental conditions. After training, the actual experiment commenced, where care was taken to ensure that each participant performed the various conditions (and their repetitions) in a different order (i.e., according to a *within-subjects* Latin square experiment design). An example design is shown in Table 6.3, where each cell represents an evaluation of a motion cueing configuration (in this case labelled APM, AHM, PHM and NM). Up to three repetitions (or, runs) of the task within each of the shown conditions were allowed before the participants were asked to award an MFR rating. Note that pilots were requested to provide a rating for every condition evaluated, including conditions without motion (NM).

Table 6.3: Example of within-subjects Latin square experiment design used.

Subj.	Conditions											
1	PHM	NM	APM	AHM	APM	AHM	PHM	NM	AHM	PHM	NM	APM
2	APM	NM	AHM	PHM	NM	PHM	APM	AHM	AHM	APM	PHM	NM
3	NM	APM	AHM	PHM	PHM	NM	APM	AHM	AHM	PHM	NM	APM
4	PHM	APM	NM	AHM	APM	PHM	AHM	NM	NM	AHM	APM	PHM
5	APM	NM	PHM	AHM	PHM	AHM	APM	NM	AHM	APM	NM	PHM

6.3. RESULTS

The following sections present the specific motion cueing conditions selected as well as the results, in terms task performance, mode participation and awarded MFRs for each of the three experiments conducted.

6.3.1. EXPERIMENT I: PRECISION HOVER

Motion cueing conditions From Figure 6.1, the three-dof longitudinal model used in this experiment has three modes: the pitch subsidence (PS), heave subsidence (HS) and phugoid (PH). The corresponding motion cueing conditions devised are therefore labelled Aperiodic Pitch Motion (APM), Aperiodic Heave Motion (AHM) and Phugoid Motion (PHM), respectively. Table 6.4 lists the values of the individual parameters in every motion configuration. Figure 6.5 shows the MCA-induced modal distortion corresponding to each configuration as obtained from an EMD-analysis.

Table 6.4: CWA motion parameters used per condition in Experiment I.

APM		AHM		PHM		
K_x	0.5	K_x	-	K_x	0.8	-
ω_{1_x}	0.88	ω_{1_x}	-	ω_{1_x}	1.0	rad/s
K_z	0.8	K_z	0.9	K_z	-	-
ω_{1_z}	0.8	ω_{1_z}	0.6	ω_{1_z}	-	rad/s
K_q	1.0	K_q	-	K_q	0.8	-
ω_{3_q}	0.0	ω_{3_q}	-	ω_{3_q}	0.5	rad/s

Figure 6.5a shows the modal distortion induced by condition APM as predicted by an EMD analysis. It can be seen that this mode is reproduced almost one-to-one in the simulator. This is achieved primarily by nulling ω_{3_q} and by finding an appropriate balance in K_x and ω_{1_x} such to limit the resulting distortion in δf_x^s. It can also be seen that the consequence of these settings is a significant distortion of both the phugoid and the heave subsidence modes. To prevent the violation of motion limits in heave, a moderate value for both the gain and break frequency of the high-pass heave filter were required. However, as can be seen from Figure 6.5a, this did not substantially affect the magnitude of δf_z^s in the pitch subsidence mode.

Figure 6.5b shows the modal distortion induced by condition AHM as predicted by an EMD analysis. Compared to the PS mode, δf_z is much more dominant in the HS mode over the other perception states. Thus, it seems reasonable to disable the surge and pitch channels of the CWA. Due to the limited motion space of hexapod motion simulators in heave, it was also required to select a moderate value for ω_{1_z}. This resulted in a strongly diminished amplitude of δf_z^s with respect to δf_z, which was compensated by selecting a

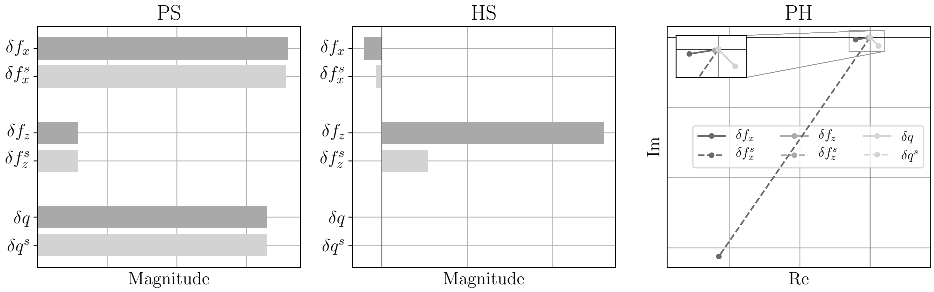

(a) Aperiodic Pitch Motion (APM)

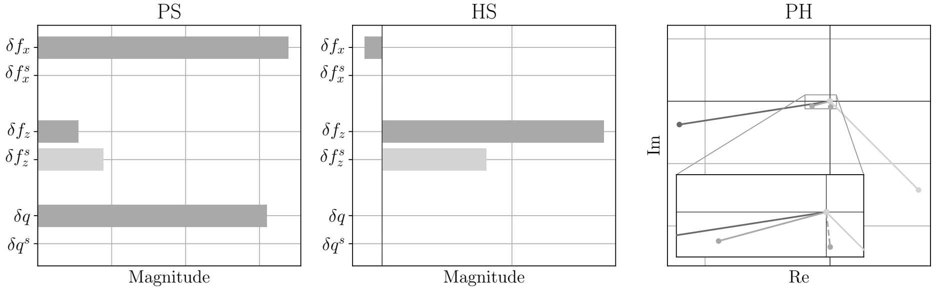

(b) Aperiodic Heave Motion (AHM)

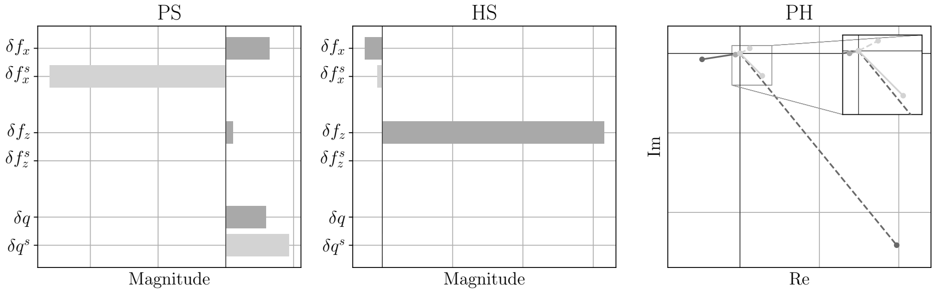

(c) Phugoid Motion (PHM)

Figure 6.5: EMD motion cueing configurations evaluated in experiment I.

slightly larger motion gain of 0.9. It can be seen from the figure that approximately half of the original contribution of δf_z in the heave subsidence mode is preserved.

Figure 6.5c shows the modal distortion induced by condition PHM. In hover, the phase difference between δf_x and the δq, the dominant contributors to this mode, is approximately ninety degrees. To preserve the phugoid mode shape, it is desired to not only match the magnitudes of the perceived states as closely as possible, but also their *relative* phases. At the same time, the phase differences of individual perception states with respect to the original vehicle mode shapes should be kept to a minimum, as this difference is effectively the mismatch between the *visual* and *inertial* motion cues. Figure 6.5c presents a possible (non-optimal) balance between these different requirements. It can be seen that the phase difference between δf_x^s and δq^s remains approximately ninety degrees. In terms of the magnitudes, it can be seen that δq^s is substantially attenuated with respect to δq, while δf_x^s is strongly amplified. By far the most critical parameters that influence the magnitude of δf_x^s were found to be K_q and ω_{3_q}, as also exemplified in Chapter 5. A larger value for ω_{3_q} results in a reduced amplification of the δf_x^s, at the cost of a greater distortion in phase and magnitude of δq^s (and the phase of δf_x^s). Similarly, reducing K_q also reduces the magnitude of δf_x^s, even more so than K_x. However, this comes at the cost of attenuation of δq^s. A third possibility to mitigate the amplification of δf_x^s in the phugoid mode is the utilization of tilt-coordination through ω_{2_x}. This, however, this mechanism is more suitable in tasks that involve *sustained* translational motion and was therefore not applied for the precision hover MTE considered in this experiment. As can be seen from Figure 6.5c, because of the seemingly strong false cue in δf_x^s, the pitch subsidence mode is also greatly distorted. Finally, because δf_z does not substantially contribute to the phugoid mode in hover, the heave channel of the CWA was disabled.

Performance Figure 6.6 shows a box plot of the RMS in feet, denoted by σ, of the longitudinal and vertical position error per experimental condition. The median and spread visible in this figure was derived from the *combined* simulation data of all five participants.

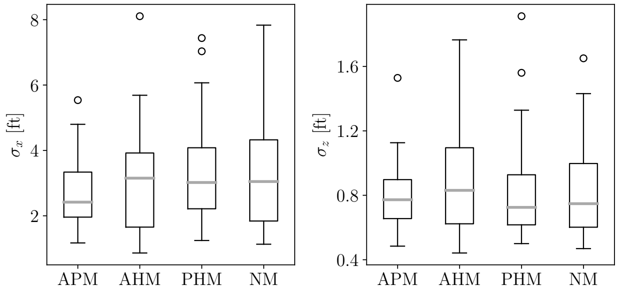

Figure 6.6: RMS of longitudinal and vertical position errors per condition in Experiment I.

In general, it can be seen from the figure that vertical position RMSs are substantially smaller in magnitude than longitudinal position RMSs. Also, the spread within and across conditions in the longitudinal position RMSs is larger than the spread in the vertical position

RMSs. This suggests that maintaining altitude is easier than maintaining longitudinal position, which is explained in part by the vehicle dynamics (i.e. unstable phugoid), but also by the available visual cues. Namely, the hover board provides direct visual feedback regarding altitude, whereas longitudinal position is discernible only from inspection of the relative orientation of the pylons on the right (see Figure 6.3).

For the horizontal position RMS (i.e., σ_x), it can be seen that both the median and the spread appear to be smaller in condition APM as compared to the other conditions. This is an indication that pitch motion cues, overall, contribute to maintaining longitudinal position more precisely in hover. It is also interesting to observe that the spread in σ_x for the condition with no motion (i.e., NM) is slightly larger as compared to the other conditions. The median of σ_x, however, does not differ substantially between conditions AHM, PHM and NM). In contrast, there appears to be no substantial difference in the median of σ_z between conditions. Interestingly, the condition with the most motion cues in heave (i.e., AHM) does exhibit a slightly larger median and more spread in the results as compared to the other conditions.

Based on these results, it appears that Hypothesis ① is partly confirmed, in that the condition aimed at cueing the PS mode is indeed the condition with the least median and spread in σ_x. However, there is no substantial difference in both σ_x and σ_z between the other conditions evaluated, which includes the no motion condition. Thus, it is not necessarily the case that motion cues contribute to a reduction of position error. In fact, their is some evidence of the contrary in σ_z, where in case of condition AHM a slightly larger median and spread were observed.

Mode Participation Factors Figure 6.7 shows a box plot of the obtained MPFs per condition and vehicle mode. These were also obtained from the *combined* data of all five participants. As explained in Section 5.1.1 and evidenced by Equation (6.2), the MPF is a measure of the contribution of each vehicle mode in the overall dynamics response.

From the figure, it can be seen that the absolute values and spreads of the MPFs of each mode across experimental conditions vary substantially . Interestingly however, when considering the *median* MPFs, the *relative* contribution of each mode remains remarkably constant across conditions. The PH mode, however, appears to dominate the vehicle response in *all* conditions evaluated, followed by the PS and HS modes, respectively. Also, the *absolute* values of the MPFs corresponding to the PH and PS modes appear larger in both conditions AHM and NM (with AHM being the larger still) in comparison to conditions APM and PHM. This indicates that the excitation of the PH and PS modes is *stronger* when pitch and surge motion cues are *absent*. Interestingly, it is also observed that this apparently stronger excitation of the PH and PS modes in condition AHM does not necessarily result in a larger longitudinal position error RMS, as also seen from Figure 6.6. The latter becomes particularly evident when comparing σ_x for conditions AHM and PHM. Finally, it is pointed out that the median and spread of the participation of the PH and PS modes are smaller in condition APM in comparison to condition PHM. In contrast, the excitation of the HS mode across conditions does not seem to differ substantially.

In accordance with Hypothesis ② and the preliminary results from Miletović et al. [2018], it thus appears that the presence of *pitch* motion cues indeed *subdues* the participation of the PS mode, but also the PH mode. However, the same does not seem to apply to surge and heave motion cues in relation to the PH and HS modes, respectively.

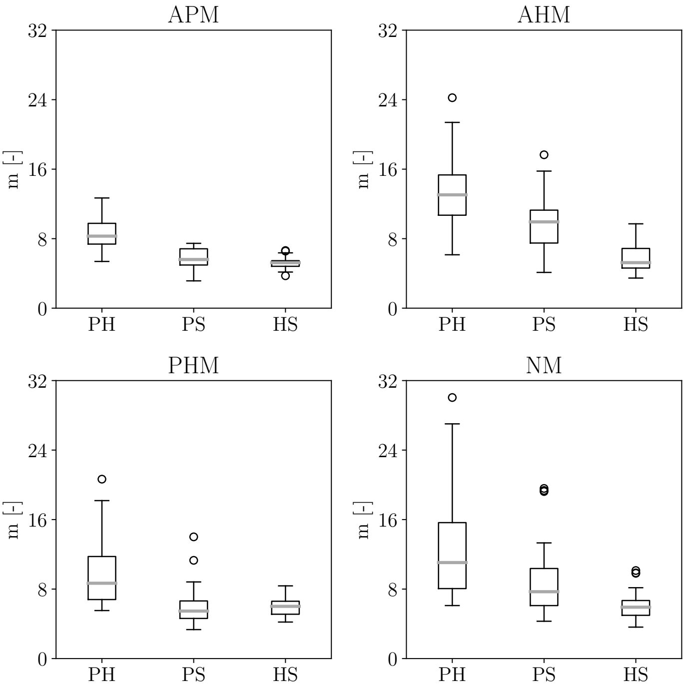

Figure 6.7: MPF's per condition in Experiment I.

Motion Fidelity Ratings Figure 6.8 shows the MFRs awarded by the participants for each condition evaluated. Because MFRs constitute *cardinal* data, the individual ratings and their counts are shown, as is the median.

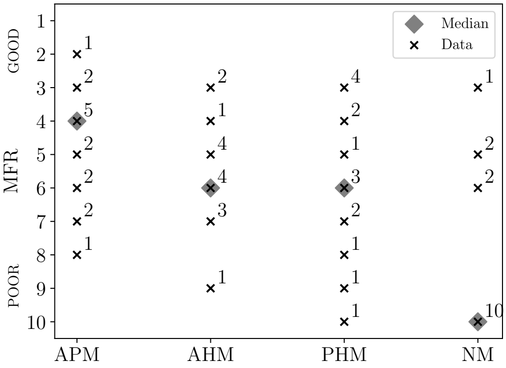

Figure 6.8: MFR's awarded per condition in Experiment I.

From the figure, it is seen that, based on overall median MFRs, condition APM is most favoured by the participants with a median rating of 4. Conditions AHM and PHM are equally rated at a median of 6, whereas the condition with no motion (NM) was correctly identified as such in the vast majority of cases (i.e., MFR of 10). However, it also becomes apparent that the spread in the results corresponding to the conditions *with* motion cues is substantial. This is particularly true for condition PHM, where an MFR rating of 3 was awarded four times. This makes it the condition that is most favoured in terms of best rating count. However, an MFR rating of 6 was awarded three times in conjunction with five even worse ratings, including one MFR rating of 10, signifying no motion cues at all were perceived. This is above all a testimony of the uncertainty and ambiguity involved in the subjective appreciation of motion cues in flight simulation (see also Chapter 2).

Nonetheless, Hypothesis ③ is partly confirmed, in that the participants do appear to value the (pitch) motion cues in the PS mode most for the precision MTE considered. The same does not apply to motion cues in the HS mode, however. Also, motion cues in the PH mode are not necessarily less valued than motion cues in the HS mode, or the PS mode (in terms of best MFR rating count).

6.3.2. EXPERIMENT II: LATERAL REPOSITION

The sidestep and/or lateral reposition tasks have been studied before in the domain of helicopter flight simulation by, e.g., Schroeder et al. [1997], Wiskemann et al. [2014] and Hodge et al. [2015b]. These studies hint at a delicate trade-off between matching motion cues in roll versus minimizing the accompanying false motion cues in sway that arise from the limited lateral motion travel of most motion-base flight simulators. In the experiment reported here, the view is adopted that a lateral reposition in a helicopter comprises two distinct phases, namely (1) a relatively fast and large attitude change and (2) a subsequent acceleration/deceleration to a constant speed/hover. From the perspective of *modes*, the former is enabled by the vehicle's fast rotational mode, i.e., the roll subsidence (RS), whereas the latter arises from excitation of the (much) lower-frequency Dutch roll mode (DR). Thus, for the lateral position MTE under consideration, it is argued that the roll rate contribution in the RS mode should be preserved in phase (1) and, conversely, the sway specific force contribution in the DR mode should be preserved for phase (2). The next paragraph describes the separate motion cueing conditions selected to evaluate these two cases. Motion cues in heave are not considered further. Nonetheless, the heave dof in the flight dynamics model remained active, such that pilots retained intuitive control over the collective and, thus, altitude (e.g., including the effect of translational lift).

Table 6.5: CWA motion parameters used in Experiment II.

ARM		DRM		
K_y	-	K_y	0.9	-
ω_{1_y}	-	ω_{1_y}	1.0	rad/s
ω_{2_y}	-	ω_{2_y}	1.0	rad/s
K_p	0.8	K_p	0.2	-
ω_{3_p}	0.3	ω_{3_p}	1.2	rad/s

Motion cueing conditions In order to preserve the contribution of δp^s with respect to δp in the RS mode, it was opted to fully utilize the motion space of the SRS in the roll axis. This was accomplished by using a combination of both scaling and high-pass filtering (washout). The motion parameters used for this condition, termed Aperiodic Roll Motion (ARM), are listed in Table 6.5. The resulting MCA-induced distortion of both the RS and DR modes is depicted in Figure 6.9 for both hover and a (constant) lateral speed of 30 kts. In the RS mode, it can be seen that the contribution of the roll rate is preserved at the cost of distortion, primarily in the *sign* of δf_y^s with respect to δf_y. This change in sign is a result of the accrued roll angle (i.e., "leans" [Schroeder et al., 1997]) during the time scale of the RS mode ($1/L_p \approx 0.08$ s), which otherwise would be cancelled by the force generated due to the rotor "flap-back" as captured by the stability derivative Y_p. This apparent "false cue", however, is over-ridden by the distortion of δf_y^s in the much longer-term DR mode, as can also be seen from Figure 6.9.

The second motion condition evaluated, termed Dutch Roll Motion (DRM), is therefore devised to strongly reduce this apparent distortion of δf_y^s in the DR mode. The corresponding motion parameters are also listed in Table 6.5. The most effective strategies were found to be reducing the roll gain (K_p) and increasing the break-frequency of the high-pass filter in the roll axis (ω_{3_p}). To further improve the representation of the δf_y^s with respect to δf_y, tilt-coordination (through ω_{2_x}) was applied in conjunction with high-pass filtering of δf_y (through ω_{1_x}). The resulting MCA-induced distortion of the RS and DR modes is depicted in Figure 6.9 for both hover and a (constant) lateral speed of 30 kts. From the figure, it can be seen that this configuration results in a strong attenuation of δp^s in both the RS and DR modes, while the amplitude of δf_y^s is well preserved in both modes. Also, in the DR mode, it can be seen that δf_y^s *lags* with respect to δf_y. with a phase of slightly less than 80° (in hover) and 47° at 30 kts lateral speed. This phase lag could be reduced further by substantially increasing the value for ω_{2_x}. For example, increasing ω_{2_x} up to 2 rad/s reduced the phase lag to 63° in hover and to 27° at 30 kts lateral speed, at the cost of a slight attenuation of both δf_y^s in the DR mode and δp^s in the RS mode. However, these improvements were found to be small when compared to the improvement already attained by changing ω_{2_x} up to ~1 rad/s from 0. Thus, a further "optimization" of this particular configuration was not undertaken.

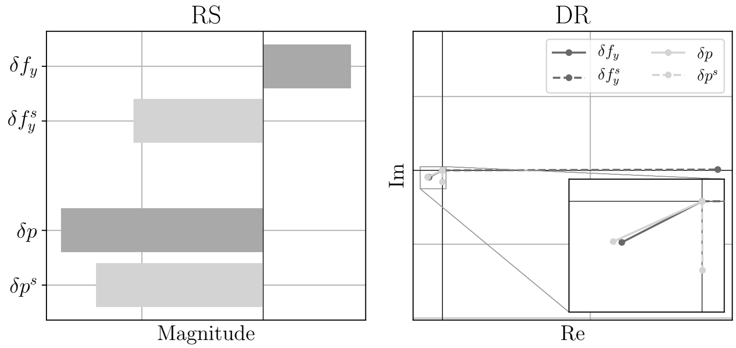

(a) Hover

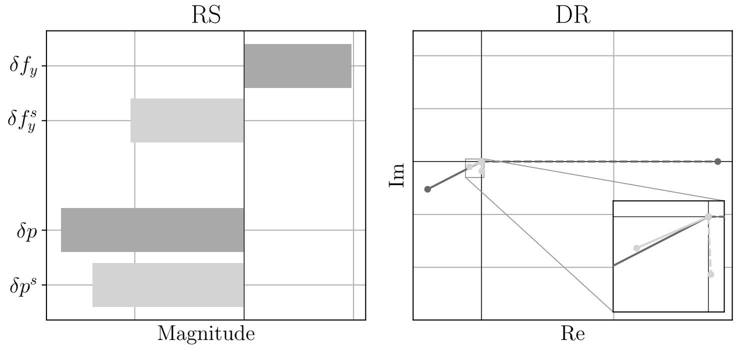

(b) 30 kts

Figure 6.9: MCA-induced modal distortion of Aperiodic Roll Motion (ARM) motion cueing configuration in hover (a) and at 30 kts lateral speed (b).

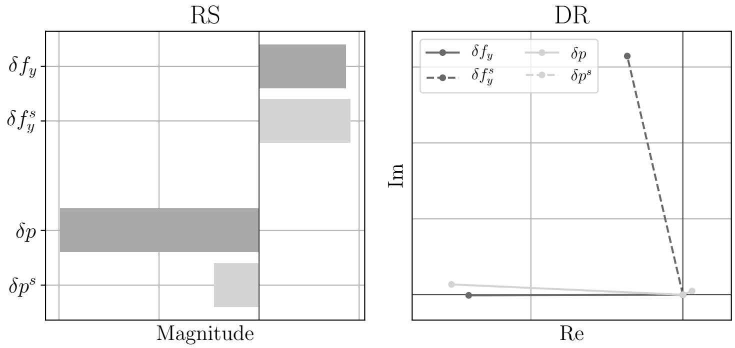

(a) Hover

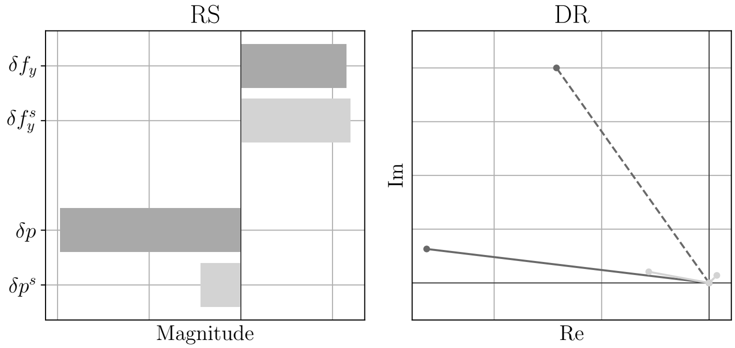

(b) 30 kts

Figure 6.10: MCA-induced modal distortion of Dutch Roll Motion (DRM) motion cueing configuration in hover (a) and at 30 kts lateral speed (b).

A note on motion limits Before discussing the experiment results, it is noted that that in 19 out of 30 recorded runs for condition ARM, soft motion limits of the simulator were reached, meaning the motion control software intervened to "brake" the actuators in order to prevent violation of excursion limits. In the majority of these runs (11), this occured only once and the "braking" cues experienced by the participants lasted less than 0.1 s with a magnitude of less than one 1 m/s^2. In 8 runs, motion limiting was more severe, occuring multiple times during a run and/or with a larger corresponding magnitude of braking cues. Figure 6.11 shows an example of both cases, with the visible sharp "peaks" in the plots denoting the motion limits. In the paragraphs to follow, the 8 runs with "severe" motion limiting are excluded from the analyses of task performance and MPFs. They are not, however, explicitly excluded in the discussion of the MFRs, because pilot comments associated with these ratings could also reveal other deficiencies than motion limits in support of the awarded ratings.

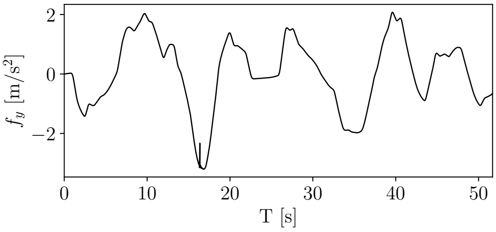

(a) "Minor" soft limit (included).

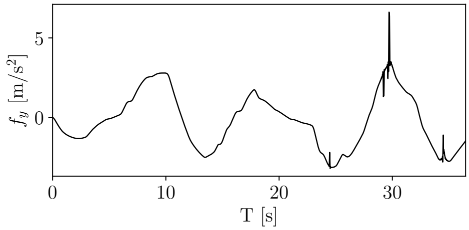

(b) "Major" soft limits (excluded).

Figure 6.11: Typical examples of encountered motion limiting in the recorded simulation data.

Task performance For the lateral reposition MTE, the peak velocity reached as well as the recorded over- and undershoots in the vicinity of the target locations were examined as measures of task performance. An appreciation of these quantities can be obtained from the aggragated *maneuvre phase portraits* depicted in Figure 6.12 for each experimental condition. The grey demarcations in the figure around 0 and 400 ft denote the regions of ± 10 ft from the target locations.

From Figure 6.12, a number of interesting observations can be made. In condition ARM, it appears that the peak velocities reached are generally lower than in conditions DRM and NM, where the peak velocities tend to be in excess of 30-35 kts more often. Despite this, condition ARM does not exhibit less under- and overshoot in the vicinity of the target locations. In contrast, condition NM does appear to exhibit a substantial *increase* in peak velocities reached. Here, however, it seems *less* under- and overshoots have occured in comparison to either of the two conditions *with* motion. In condition DRM, the spread of peak velocities between 30-35 kts appears somewhat lower. This is confirmed by the boxplot of peak velocities per condition shown in Figure 6.13. From the figure, it can be seen that the median of the peak velocities in condition DRM is slightly less than 35 kts and that its spread around this value is smaller than the spread of peak velocities in the other

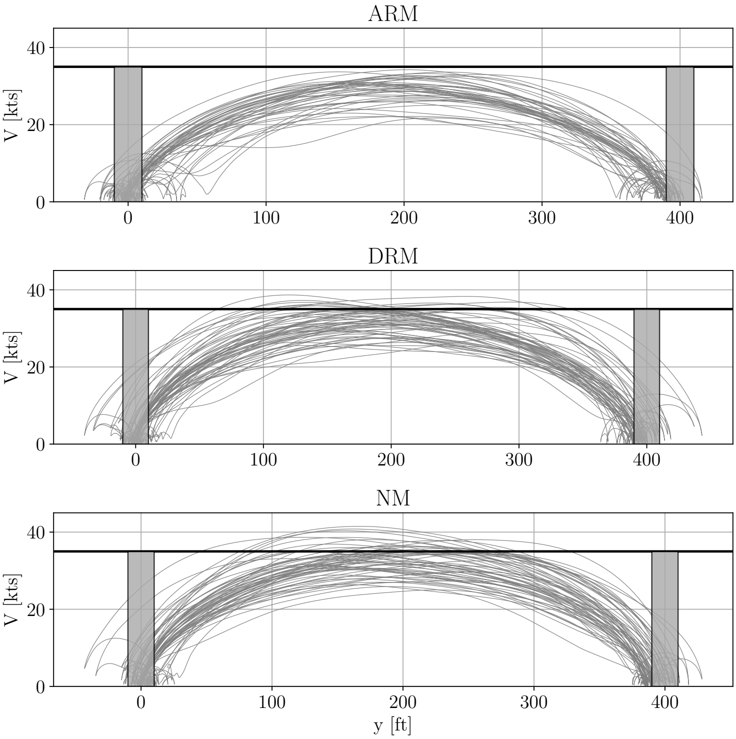

Figure 6.12: Aggragated maneuvre phase portraits for lateral reposition MTE in experiment II.

two conditions. It can also be seen that the median of peak velocities in condition ARM is substantially lower as compared to the two conditions and that it is skewed more towards lower velocities. The latter is clear evidence of pilots adapting their control strategy in relation to available motion cues (e.g., to avoid motion limits).

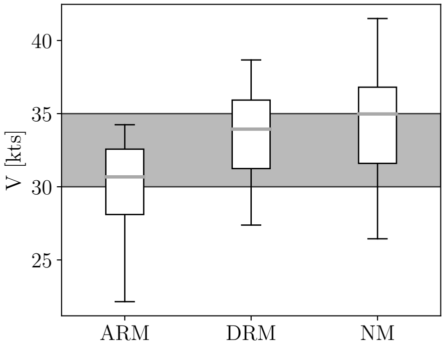

Figure 6.13: Boxplot of peak velocities in lateral reposition MTE in experiment II.

Summarizing the results in regard to hypothesis ④, it does not appear that motion cues aimed solely at representing the RS mode (or DR mode) help pilots to limit under- and overshoots in the vicinity of the target locations. In fact, the contrary seems true in comparison to condition NM. There is, however, some evidence that condition DRM is beneficial in terms of the accuracy of the attained peak velocity when compared to conditions ARM and NM. Thus, hypothesis ④ is partly confirmed.

Mode Participation Factors Unlike in experiment I, where the linearized vehicle dynamics could be assumed constant for the calculation of MPFs, here the vehicle dynamics *change* as a function of lateral airspeed (see also Table 6.2 and Figure 6.2). Thus, in order to compute the MPFs, the linear model used in Section 6.2.5 and Equations (6.1) and (6.2) was "updated" as a function of speed in steps of 5 kts. An example result of normalized mode participation of the RS and DR modes as a function of time (i.e., the integrand in Equation (6.2)) for each of the evaluated motion cueing configurations is shown in Figure 6.14. Also shown in the figure for reference is the normalized airspeed as a function of time (V).

Several interesting observations can be made from the figure about the relative excitation of the RS and DR modes during the lateral reposition MTE. Upon initiating the maneuvre, it can be seen that the participation of the RS mode momentarily increases as the roll angle is accrued, but drops thereafter. Subsequently, it can be seen that participation of the DR mode *increases* as the helicopter accelerates or decelerates. Around the peak velocity, when the helicopter again undergoes a large change in attitude, participation of the DR mode drops in favour of the RS mode. These trends are the same across the three conditions evaluated. Finally, close to hover, when during stabilization, the normalized participation of the RS mode seems to generally exceed that of the DR mode.

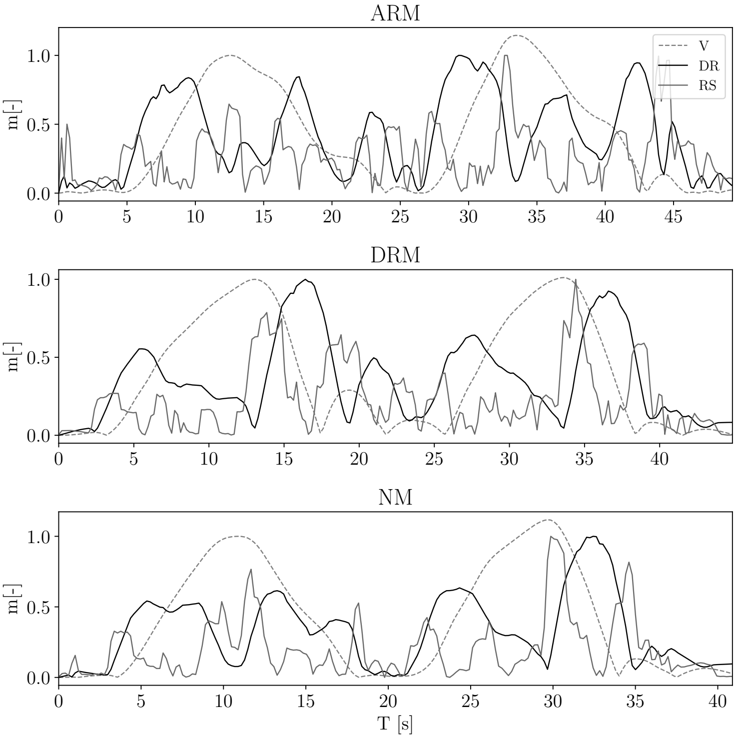

Figure 6.14: Example of normalized time responses of mode participation in each condition of experiment II.

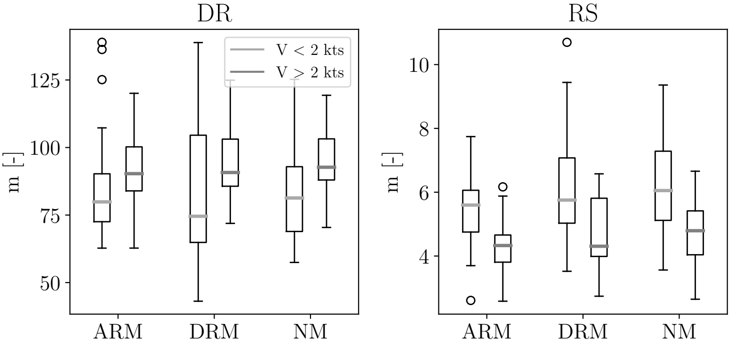

Figure 6.15: Boxplot of MPFs per condition of experiment II for speeds below and above 2 kts.

Figure 6.15 shows a boxplot of the MPFs modes as oomputed from Equation (6.2). A distinction is made between MPFs for speeds below and above 2 kts. It can be seen that in terms of the median value, the MPF of the DR mode is in excess of an order of magnitude larger than that of the RS mode. Interestingly, it also appears that participation of the DR mode *increases* for V> 2 kts, while participation of the RS mode is relatively *larger* for V< 2 kts. These trends appear to be similar across the three conditions evaluated and correspond to the trends also observed in the time traces shown in Figure 6.14. The MPF of the DR mode in condition DRM does exhibit a slightly lower median and a substantially larger spread than the other conditions. Also, median MPFs corresponding to the NM condition, overall, are slightly larger than the two conditions with motion, which is consistent with the results from experiment I (see Section 6.3.1). There appears to be no substantial difference in the MPF of the RS mode between conditions ARM and DRM.

Based on the latter result, motion cues in condition ARM *do not* necessarily result in a smaller MPF of the RS mode as compared to the condition with less motion cues in the roll axis (i.e., condition DRM). Thus, the element of Hypothesis ② that pertains to a reduced MPFs of the RS mode in condition ARM close to hover is rejected.

Motion Fidelity Ratings The last result of Experiment II to be discussed are the MFRs awarded by the five participants. These are depicted in Figure 6.16. From the figure, it is evident that condition ARM is rated substantially worse in comparison to DRM. In order to further explore the reasons behind this, corresponding comments for condition ARM were reviewed in more detail. These comments are summarized in Table 6.6 for each subject and per individual repetition of condition ARM in the experiment.

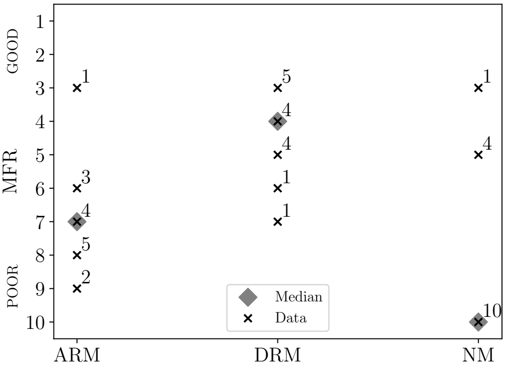

Figure 6.16: MFR's awarded per condition in Experiment II.

From the table, it can be appreciated that onset cues in the roll axis were perceived as too strong, or "overevident", by the majority of the subjects. Two of the participants (4 and 5) explicitly mentioned that the control strategy had to be adapted in comparison to the other conditions in order to avoid motion limits. However, this was less apparent from the comments of the other subjects, who complained more about perceived latencies and spurious cues in the motion, particularly during the deceleration to hover phase of the maneuvre. From Table 6.6, it can be seen that this was often described as "roll cues in the opposite direction" or "deceleration cues after levelling off".

To quantify this effect, Figure 6.17 compares representative time traces of the measured measured specific force and roll rate (f_y^s and p^s) in the simulator to f_y and p as computed from the flight dynamics model. This figure clearly depicts the problem of the spurious

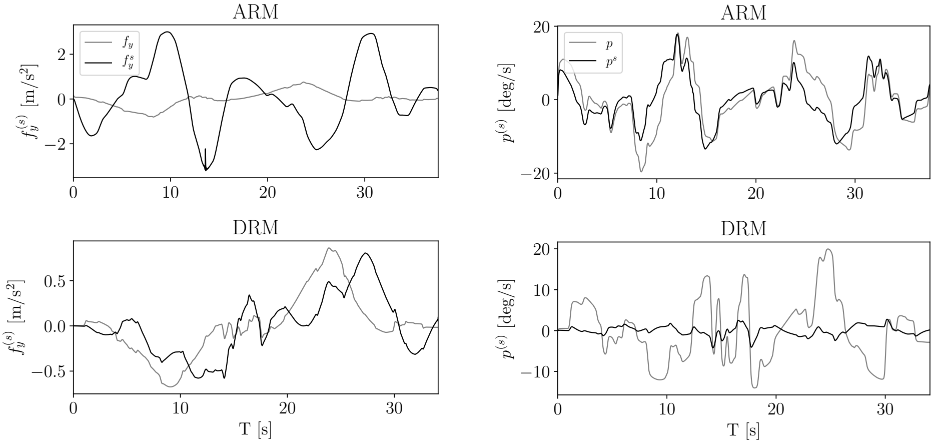

(a) f_y^s versus f_y

(b) p^s versus p

Figure 6.17: Time traces of sway specific force (a) and roll rate (b) in the simulator compared to flight dynamics model for conditions ARM and DRM.

"deceleration cues" perceived by the participants in the apparently opposing direction of motion. These namely correspond to the peaks in f_y^s visible in Figure 6.17a in the vicinity of 15 s (maneuvre from left to right) and 30 s (maneuvre from right to left). It can be seen that the flight dynamics model around these instants already predicts $f_y \approx 0$, corresponding to a level attitude (i.e., $\phi \approx 0$). The simulator, however, due to a combination of scaling and high-pass filtering of p^s, is still producing a specific force that is in line with a *"remnant" of the roll angle accrued during the deceleration to hover*. From Figure 6.17, it can also be seen that condition DRM largely mitigates these false cues in the sway specific force, at the cost of some lag in the signal and a poorly matching roll rate with respect to the flight dynamics model. These results fully correspond to the EMD-based predictions outlined in one of the previous paragraphs.

Summarizing, from the MFRs in Figure 6.16, it appears that in the lateral reposition MTE under consideration, the participants weight spurious sway specific force cues as more detrimental to motion cueing fidelity in comparison to more accurate roll cues. Thus, hypothesis ② is rejected. This does not mean, however, that condition DRM was not criticised. For example, it was often characterized as being "benign" or "subtle", or more generally as lacking cues in the roll axis. Interestingly, in this condition, the participants also complained more often about the lack of motion cues in *heave*. Finally, it is interesting to observe that, in 5 out of 15 cases, the NM condition was characterized as a condition *with* motion cues and the corresponding ratings awarded were generally better than the MFRs corresponding to condition ARM.

Table 6.6: Overview of pilot comments corresponding to condition ARM in experiment II.

	Repetition 1	*Repetition 2*	*Repetition 3*
Subject 1	Changed control strategy after first run; detrimental to performance; **latency (L) perceivable after deceleration**; acceleration phase of maneuvre matches.	Keeping altitude, initial roll and deceleration ok; **when levelling off, roll attitude annoying deceleration cues perceivable**; distracting.	*Motion cues “wings level” far too obvious*; disorienting/distracting. Initial roll and acceleration ok; **“wings level” feels like decelerating too hard**.
Subject 2	**Initial roll too strong**; heave not perceivable; deceleration in motion correct; vertical axis non-existent; distracting, out of proportion; motion rumble during initial roll.	Special but uncomfortable; initial roll too obvious; motion system perceivable; acceleration cues not perceivable; **during deceleration, sensation of roll cues in te opposite direction**; negative value; motion cues present that are not visible (mismatch with visuals).	Initial roll not good; digital; very little [motion, auth.] in vertical axis; difficult to maintain altitude; **too much motion in roll during deceleration**; not helpful for stabilizing, but not distracting.
Subject 3	Very choppy in lateral direction; little confidence; altitude control normal.	Obvious latency in axes; heave not ok; **sensation of roll in opposite direction during deceleration to hover**; L (latency), M (mismatch) and N (noise);	Obvious that motion cues must be ignored; heave ok; lateral/roll choppy; roll overdone w.r.t. visual; O (onset), **S (spurious cues)**, motion noise (N) with larger roll inputs.
Subject 4	Easier to assess velocity during transition [from hover to acceleration, auth.]; **roll axis too dominant during stabilisation; adapted strategy second run to avoid motion limits.**	Previous one [ARM, auth.] more heave, this one more roll, really overdone; less helpful for velocity perception; **overevident during stabilisation**; **annoying because too strong;** still useful but visual cues more dominant; uncomfortable.	Roll too evident; objectionable deficiencies; some heave cues also present.
Subject 5	Stopped giving inputs second run during stabilisation; roll dominant; missing heave cues; not sure if helpful; **more pleasant without roll**; **tried to avoid motion limits**; no harmonisation between roll and heave; helpful during transition [from hover to accel, auth.]; visuals dominant.	With adapted strategy, latency in motion less perceivable; much more pleasant in roll; bank angle during deceleration and transition representative, as is rate; more “present” than condition before [DRM, auth.].	**Far too dominant in roll and really need adaptation of control strategy to motion system [limits, auth.]**.

Intermezzo: the effect of dynamic blade flap To conclude experiment II and to highlight another possible application of EMD, the method was applied to an assessment of the effect of extended main rotor dynamics on motion cueing fidelity. To this end, the three-dof Bo-105 model introduced in Section 6.2 was extended to include *dynamic blade flap*, as outlined in Appendix A.8.2. The result of this is illustrated in Figure 6.18. It can be seen that, as expected [Curtiss, 1986], for the Bo-105 helicopter with its relatively stiff *hingeless* rotor system, the roll subsidence (RS) mode is replaced by an *oscillatory roll (OR)* mode. The low-frequency Dutch roll (DR) mode, however, is barely affected. Figure 6.18 also shows pulse responses of the model to a lateral cyclic input for a case with and without dynamic blade flap.

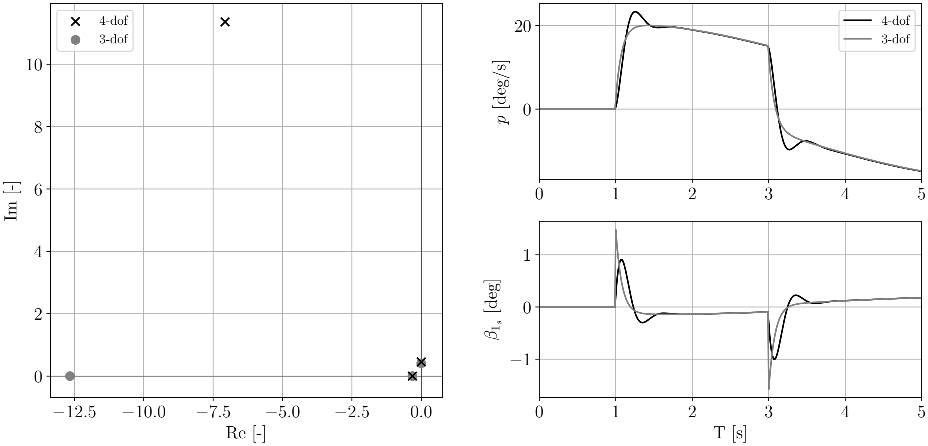

(**a**) Modes (**b**) Roll/lateral flap response

Figure 6.18: Effect of lateral dynamic flap on modes (a) and roll/lateral flap response (b) of the Bo-105 helicopter model.

Contrary to other tools, EMD enables a *quantitative* study of the effect of these added dynamics from the perspective of motion cueing fidelity, because the coupled vehicle-MCA system central to EMD and given by Equation (5.11) can be easily adapted. The details regarding this adaptation are included in Appendix C and won't be addressed here in full.

The end result of an EMD analysis applied to the model with dynamic blade flap is shown in Figure 6.19. This figure illustrates the modal distortion imposed by the motion cueing configurations ARM and DRM (see Table 6.5) on the extended model in hover. Compared to Figures 6.9 and 6.10, the most significant changes become apparent in the distortion of the OR mode. In the three-dof case, it was seen that the contribution of δf_y in RS underwent a change in *sign* as well as a slight *amplification*. In the new OR mode (see Figure 6.19a), it can be seen that the phase relation between δp and δf_y in OR is slightly *less* than 180° and that the effect of the CWA dynamics is to "bend" δf_y^s towards δp^s by approximately 90° with, in addition, a slight amplification as also seen in Figure 6.9. Furthermore, δp^s undergoes a very minor phase lead with respect to δp and its amplitude is attenuated to approximately the same extent as δp^s in the RS mode (see Figure 6.9).

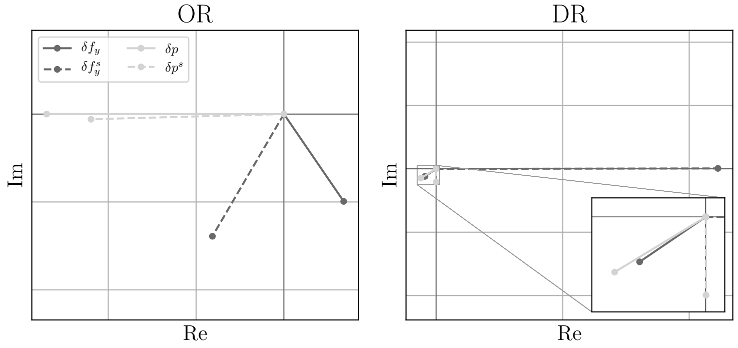

(a) Aperiodic Roll Motion (ARM)

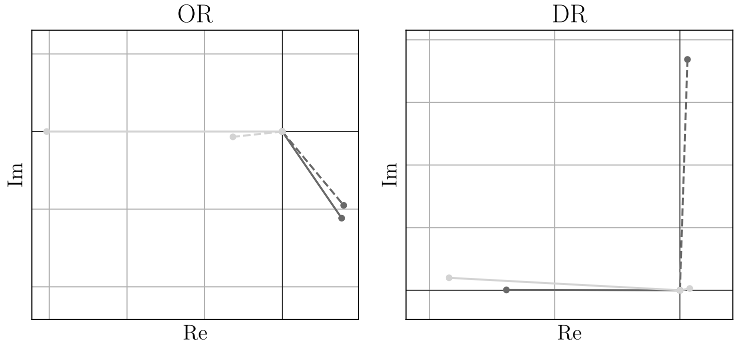

(b) Dutch Roll Motion (DRM)

Figure 6.19: MCA-induced modal distortion of motion cueing configurations ARM (a) and DRM (b) for Bo-105 flight dynamics model with lateral flapping dynamics (in hover).

Because condition ARM is aimed at preserving the contribution of δp^s in the faster roll mode of the vehicle, it seems that the addition of dynamic blade flap does not mandate a change in the motion parameters in to further improve the representation of the OR mode in the four-dof model. A similar reasoning applies to the modal distortion imposed by condition DRM (see Figure 6.19a) where, compared to Figure 6.10, it can also be seen that δf_y^s is preserved well in both the OR and DR modes at the cost of substantial distortion in δp^s. The contribution of δf_y^s in the DR mode of the four-dof model, however, does seem to undergo a slightly larger phase lag as compared to the three-dof model, but remains close to approximately 90° with respect to δf_y. This is explained by the slightly higher natural frequency of DR mode in the four-dof model, which results in a larger phase lag that is imposed by the low-pass filter in Channel 2 of the CWA.

To establish whether the added dynamic blade flap is noticeable during pilot-in-the-loop flight, a brief experiment was performed. To this end, both the three- and four-dof models were combined with each of the evaluated motion cueing configurations (i.e., ARM, DRM and NM). The resulting matrix of conditions per participant is shown in Table 6.7. In each condition, two trials of the lateral position MTE were performed. The first trial was always flown with the three-dof model (i.e., *without* dynamic blade flap). In each condition labelled "ON", the four-dof model was selected for the second trial, whereas in conditions labelled "OFF" the same (i.e., three-dof model) was also used for the second trial. After the second trial, the participants were simply asked whether or not changes in the vehicle dynamics were perceived. The comments per pilot and evaluated model-motion cueing combination are summarized in Table 6.8.

Table 6.7: Experiment matrix for the evaluation of the noticeability of lateral dynamic blade flap.

Subj.	Conditions					
1	NM (ON)	ARM (ON)	DRM (ON)	DRM (OFF)	NM (OFF)	ARM (OFF)
2	DRM (OFF)	NM (OFF)	ARM (OFF)	ARM (ON)	DRM (ON)	NM (ON)
3	ARM (ON)	NM (ON)	DRM (ON)	DRM (OFF)	ARM (OFF)	NM (OFF)
4	ARM (OFF)	DRM (OFF)	NM (OFF)	DRM (ON)	NM (ON)	ARM (ON)
5	DRM (ON)	ARM (ON)	NM (ON)	NM (OFF)	DRM (OFF)	ARM (OFF)

In Hypothesis ⑥ of Section 6.2 it was stated that pilots would notice the more oscillatory response in roll in condition ARM and that this response could be described as more "wobbly". The results from Table 6.8, however, do not suggest that the participants consistently noticed a change in the vehicle dynamics in conditions where dynamic flap was enabled between the two trials. Subjects 1 and 5 did comment on subtle changes in the roll axis in condition "ARM (ON)," but provided similar comments pertaining to changes in the roll axis in conditions where the model was *not* changed between the first and second trial. Interestingly, Subject 3 in condition "DRM (ON)", did mention that the model felt more "oscillatory", which could be consistent with the addition of dynamic blade flap. Overall, however, most subjects emphasized that perceived changes were subtle and difficult to qualify. Moreover, the comments in Table 6.8, especially those that pertain to aspects of the model that were unaffacted by the addition of dynamic blade flap (e.g., lateral acceleration/deceleration and control gearing), are most likely the result of changes in the applied control strategy between the first and second trials. It is concluded that the addition of lateral dynamic blade flap, while substantially affecting the vehicle response in the fast roll mode, is not evident to pilots during dynamic maneuvering flight, regardless of the motion cueing configuration applied.

6.3.3. Experiment III: depart/abort

The results from the two previous experiments described in this chapter suggest that pilot value motion (rotational) cues in the faster vehicle modes for tasks that involve precision maneuvering flight. This, however, does not appear to be true for tasks that involve more dynamic maneuvering flight, such as the lateral reposition MTE addressed in Section 6.3.2. Here, it was found that mitigating false specific force cues, which appear in the vehicle's slower rotational modes due to the absence of physical translational motion in the simulator, is more valued by pilots. This purpose of the third experiment is to determine whether a "best of both worlds" condition exists, with an application to the depart/abort MTE executed in the Desdemona simulator (see Section 2.2.1). This experiment is furthermore performed using

Table 6.8: Overview of pilot comments corresponding to evaluation of noticeability of lateral dynamic blade flap.

	ARM		*DRM*		*NM*	
FLAP	ON	OFF	ON	OFF	ON	OFF
Subject 1	Roll bit more accentuated	Maybe slightly more roll rate second time; difficult, little difference				Motion slightly stronger (roll acceleration); not sure, very similar
Subject 2	Almost no difference; more motion in heave; roll no change	Second time less roll overshoot during deceleration	Little difference; more initial roll towards right	Difficult; initial roll maybe better perceivable		
Subject 3		Better in lateral axis; less motion latency	More oscillatory; input less smooth and choppy; overcontrol	Not very significant; heave axis first run easier; no much different in lateral axis	Lateral response maybe bit slower; very subtle	Subtle difference in heave; no difference lateral axis
Subject 4	Subtle difference in gearing/control response	Lateral acceleration/deceleration better second run; roll not significantly different	Control response maybe little different	Lateral control response/gearing seems different, better; as if smaller inputs are necessary	Mayble little more damping in roll; no evident difference	
Subject 5	First more easy to control in roll angle (attitude command); not very dominant			Second run rate command, first attitude command; onset no difference		Second run roll rate seemed less, like attitude command;

a model of the AH-64 helicopter, with an angular rate feedback loop (see Appendix A.9.1) to represent the effect of the SCAS[2]. In the following paragraphs, the characteristics of the motion cueing conditions evaluated during the experiment are outlined first, after which the results in terms of awarded MFRs are discussed.

Motion cueing conditions In this experiment, three motion cueing configurations (and a condition without motion) are evaluated. Two conditions are chosen with a rationale that is similar to that adopted in experiment II. Namely, one condition, termed Direct Pitch Filter (DPF), aims to reproduce the rotational cues in the faster pitch subsidence (PS) mode, whereas a second condition, termed Coordinating Pitch Filter (CPF), aims to reproduce the specific force cues in the slower phugoid (PH) mode. The third motion cueing configuration evaluated, termed Adaptive Pitch Filter (APF), is a presumed “best of both world” solution. It combines the characteristics of the DPF configuration below 5 kts airspeed (hover) and the characteristics of the CPF configuration above 10 kts airspeed (forward flight). These speeds are chosen somewhat arbitrarily, but are assumed to be representative of the transition from hovering to forward flight. Table 6.9 lists the CWA motion cueing parameters corresponding to each condition. Note that, during the experiment, heave motion cues were also present in all conditions (except the NM condition) and also contained a Desdemona proprietary component to simulate rotor vibrations. Also, Channel 1 of the CWA (translational motion in surge) was disabled. This was done because, in the Desdemona simulator, translational motion in surge can only be simulated using the linear track, or by offsetting the cabin from the central yaw axis. The former solution exhibits a characteristic “turn-around bump”, which is especially bothersome close to hovering flight. The second solution, involving the central yaw axis, comes at the cost of auxilliary motion cues in yaw, which is also undesirable especially because these cues are “off-axis” in the depart-abort task under consideration[3]. Finally, because the experiment was performed with a six-dof model of the AH-64, the motion cueing settings for the pitch and (low-pass) surge dofs of the simulator listed in Table 6.9 were simply copied to the roll and sway channels of the CWA, respectively. The three evaluated configurations are discussed in more detail in the next paragraphs.

Table 6.9: CWA motion parameters used per condition in Experiment III.

DPF		CPF		APF		
K_x	0.8	K_x	0.8	K_x	0.8	-
$\omega 1_x$	-	$\omega 1_x$	-	$\omega 1_x$	-	rad/s
$\omega 2_x$	0.8	$\omega 2_x$	0.8	$\omega 2_x$	0.8	rad/s
K_z	0.8	K_z	0.8	K_z	0.8	-
$\omega 1_z$	2.0	$\omega 1_z$	2.0	$\omega 1_z$	2.0	rad/s
K_q	0.8	K_q	0.0	K_q	0.8 – 0.0	-
$\omega 3_q$	0.2	$\omega 3_q$	0.2	$\omega 3_q$	0.2	rad/s

---

[2] Appendix C discusses how the effect of a SCAS can be included in EMD.

[3] Both solutions were evaluated during the development of the experiment and were deemed unsatisfactory

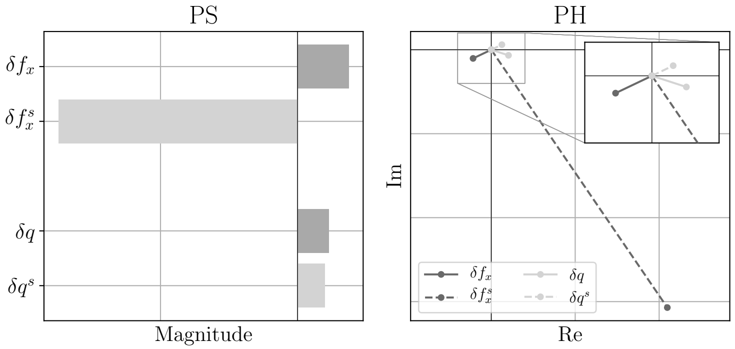

(a) Direct Pitch Filter (DPF)

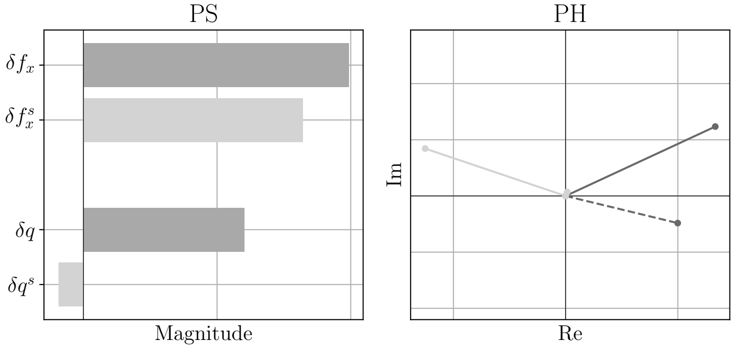

(b) Coordinating Pitch Filter (CPF)

Figure 6.20: MCA-induced modal distortion of motion cueing configurations DPF (a) and CPF (b) for (augmented) AH-64 flight dynamics model in hover.

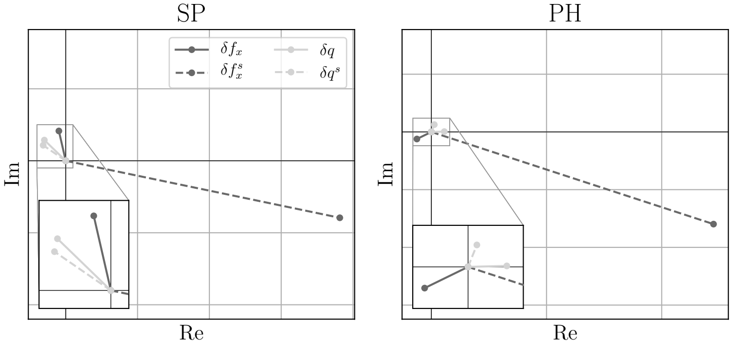

(a) Direct Pitch Filter (DPF)

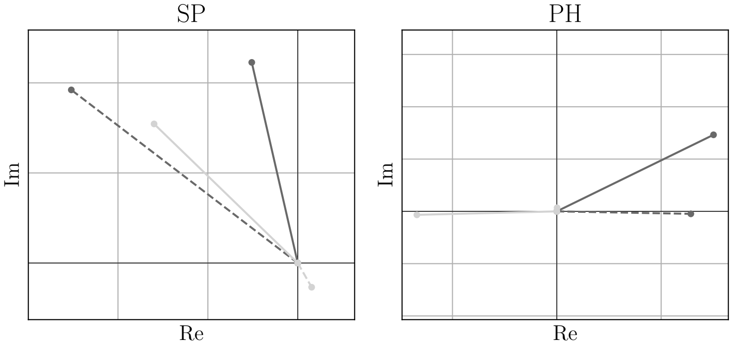

(b) Coordinating Pitch Filter (CPF)

Figure 6.21: MCA-induced modal distortion of motion cueing configurations DPF (a) and CPF (b) for (augmented) AH-64 flight dynamics model at 35 kts.

The MCA-induced distortion of configuration DPF is depicted in Figure 6.20a for hover and in Figure 6.21a for 35 kts forward flight. Note that in forward flight, for the AH-64, the pitch and heave subsidences combine to produce a short period (SP) mode. It can be seen that in both cases, the contribution of δq^s with respect to δq is well preserved. As expected, this comes at the cost of a strong distortion of δf_x^s with respect to δf_x in the PH mode, but also in the PS and SP modes in forward flight. The latter is explained by the complete lack of translational motion cues in surge. Note that, in contrast to conventional hexapod-based motion platforms, the Desdemona simulator has an essentially unlimited range of motion in roll, pitch and yaw. Thus, the high-pass filters in the rotational channels of the CWA are, strictly speaking, not necessary. However, completely disabling washout in pitch for the depart/abort task under consideration, has the undesirable effect that the pitch angles accrued during the maneuvre are essentially transmitted one-to-one. In the absence of translational motion cues in the simulator, this would lead to even stronger false cues in the surge specific force (i.e., the well-known "leans") than those depicted in Figure 6.20a and Figure 6.21a. To mitigate this effect, a small value for ω_{3_q} was set to ensure that the larger pitch attitudes attained upon acceleration and deceleration to/from hover are slowly washed out by the CWA.

The MCA-induced distortion of configuration CPF is depicted in Figure 6.20b for hover and in Figure 6.21b for 35 kts forward flight. From the listed CWA settings in Table 6.9, it can be seen that this configuration is essentially the same as DPF, with only the pitch motion gain (K_q) set to zero. By effectively disabling pitch motion cues other than those arising from the application of tilt-coordination in Channel 2, the amplification in the longitudinal specific force in the PS (hover) and SP (forward flight) modes as well the PH mode are reduced to a great exent as compared to the DPF configuration. The consequence thereof is apparent in δq^s, which is strongly attenuated and appears 180° out of phase with respect to δq in the PS (hover) and SP (forward flight) modes.

From the two preceeding paragraphs, it has become apparent that it is possible, using EMD, to craft motion cueing solutions that either portray short(er)-term rotational cues well or long(er)-term translational (specific force) cues well. Both, however, apparently come at the cost of substantial distortion of motion cues in other modes. Hence, configuration APF combines conditions APF and CPF by linearly reducing K_q from a value of 0.8 to zero as a function of airspeed between 5 and 10 kts. To illustrate the differences between the three different motion cueing configurations evaluated, Figure 6.22 shows, for each configuration, representative time-domain responses of $f_x^{(s)}$ and $q^{(s)}$ as recorded during the experiment. The corresponding velocity profiles are also shown for reference as dashed lines in the figure. This figure clearly reveals the substantial differences between the configurations that have also become appararent from the EMD analyses in the previous paragraphs. In condition DPF, q^s is seen to match q quite well, at the cost of substantial false cues in f_x^s, appearing particularly during acceleration/deceleration to/from hover as well as near the peak velocity. In condition CPF, it is seen that the general trend of f_x^s is in line with f_x, but higher-frequency components in f_x are not captured. Of the three conditions evaluated, however, CPF best matches f_x. q^s in condition CPF also appears out of phase with q by 180° and is strongly attenuated in amplitude. Finally, condition APF indeed appears to be a combination of configurations DPF and CPF, in the sense that false cues in f_x^s remain present in (near) hovering flight (i.e., for $V < 5$ kts). This is true particularly during acceleration from and in the final phase of the deceleration to hover. However, these cues are largely absent during forward flight near the manoeuvre peak velocity. In contrast, the pitch rate matches well close to hover, but is close to zero for airspeeds above 10 kts.

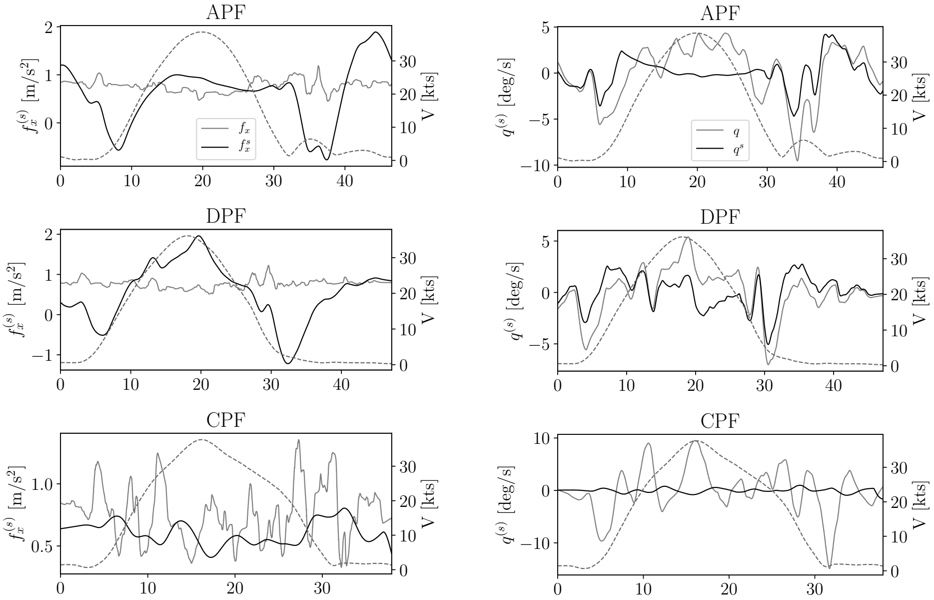

(a) f_y^s versus f_y

(b) p^s versus p

Figure 6.22: Time traces of surge specific force (a) and pitch rate (b) in the simulator compared to flight dynamics model for motion conditions.

Motion Fidelity Ratings The main results of the experiment are the MFRs awarded by the pilots for each of the evaluated motion cueing configurations (including NM). These are shown in Figure 6.23, which depicts both the counts as well as the medians of the ratings. Note that, instead of the expected 9 ratings per condition (i.e., one for each subject and every repetition of each condition), only 8 are present. This is because one of the three participants only completed two of the three repetitions of each condition during the experiment.

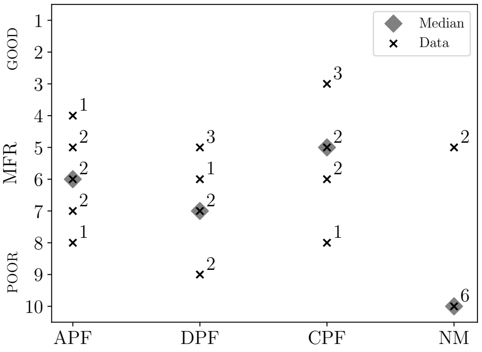

Figure 6.23: MFR's awarded per condition in Experiment III.

Recall that in Section 6.2, hypothesis ⑦, it was expressed that pilots would appreciate condition APF more than either conditions DPF or CPF. From the results in Figure 6.23, this *does not* appear to be the case. Namely, the best rated condition is condition CPF, both in terms of the median as well as the overall best rating awarded (and its count). Condition APF appears to be only marginally better received than condition DPF, which was rated worst by the participants. To understand the underlying reasons for these results, pilot comments associated with the ratings were also reviewed.

For condition DPF, it became apparent from the comments that the motion cues, in general, were perceived as too strong by the participants during each repetition. Also, each participant commented on a delay of "deceleration cues" with respect to the visuals, which often led to overcompensation and a perceived degradation of task performance. This characteristic is similar to the one found for condition ARM in Experiment II (see Section 6.3.2) and, therefore, not surprising. Interestingly however, while somewhat less frequent (4 out of 8 repetitions) and more apparent for larger changes in pitch attitude, the participants raised similar objections in condition APF. While condition CPF is received best by the participants in terms of the MFRs, it is most difficult to characterize. For example, one subject noted that motion cues in pitch and in the longitudinal direction were barely perceivable, while heave cues and vibrations were clearly present. Another subject characterized attitude changes in this condition as "overdone" in one repetition and acceleration/deceleration as "less present" in another repetition. A different participant characterized the pitch cues in CPF as "choppy" in one repetition and as being "ok" in another. Thus it is difficult to determine exactly which aspect of condition CPF lead to its overall most favourable ratings.

It is also interesting to notice that the MFRs seem to improve with *diminishing presence* of motion cues. This cannot be generalized to the condition *without* motion, however, as the MFR scale does not accommodate the evaluation of this condition (i.e., the evaluation is aborted when no motion is perceived and an MFR of 10 is automatically assigned). Nonetheless, in two repetitions of NM motion *was* perceived and relatively favourable ratings of 5 were awarded. Additionally, one participant commented that the task was easiest to execute without motion. Combined, this at least suggests that the NM condition is not necessarily worse than the conditions *with* motion and, therefore, it can be argued to remove the implied distinction between motion and no-motion in terms of perceived fidelity from the MFR scale.

The apparent trend towards improved MFRs with *less* motion is not new. For example, Wentink et al. [2009] and Correia Grácio et al. [2013] have also documented a preference towards a less than *one-to-one* motion amplitude with respect to available visual cues. However, this was attributed more to shortcomings in the *visual* cues rather than inertial motion cues. That is, a lower quality visual scene in the simulated environment cause subjects to underestimate their self-velocity [Correia Grácio et al., 2013], leading to an overestimation of inertial motion. In the presence of immersive VR-enabled visuals, however, an alternative argument can be made that *better* visual cues (i.e., increased field-of-view, more peripheral vision, etc.) cause subjects to "reweigh" the importance of inertial motion cues more in favour of visual cues [Fetsch et al., 2009]. A further discussion on this topic is beyond the scope of the present thesis, but is worthy of attention in future work.

6.4. DISCUSSION

The goal of the three experiments discussed in this chapter was to demonstrate the utility of EMD for motion cueing fidelity assessment in helicopter flight simulation. The format of choice was to use EMD as a guiding tool in the selection of appropriate motion cueing configurations for three typical helicopter MTEs. The relative merit of these configurations was subsequently assessed in individual pilot-in-the-loop experiments performed on the SRS and Desdemona with test pilots of the RNLAF.

Experiment I considered the precision hover MTE, performed using a three-dof longitudinal model of the AH-64 helicopter on the SRS. Three motion configurations were devised using EMD such to preserve either the pitch subsidence (PS), heave subsidence (HS) or phugoid (PH) modes. It was found that both the longitudinal position error RMS as well as the participation of the PS mode in the vehicle's response decreased in the condition aimed at cueing the PS mode. This condition was also the one that, on the overall, was most valued (in terms of MFRs) by the participants. In contrast, isolated motion cues in heave, aimed at preserving the HS mode, were not found to result in improved vertical position RMS or a reduced participation of the HS mode in the vehicle's response. Also, the condition aimed at cueing the HS mode, on the overall, received equal MFRs as the condition aimed at better cueing the PH mode. These results suggest that, for tasks that involve high precision manual control, motion cues in the "faster" rotational vehicle mode are more beneficial in comparison to "slower" translational motion cues.

Experiment II considered the lateral reposition MTE, performed using a three-dof lateral model of the Bo-105 helicopter on the SRS. This application was meant to illustrate the applicability of EMD for analyses involving more dynamic manoeuvering flight, where the linearized vehicle dynamics can no longer be assumed time-invariant. It was shown that the Mode Participation Factor (MPF), as well as the EMD analysis itself could be extended through the application of a Linear Parameter Varying (LPV) vehicle model. The experiment subsequently performed was aimed at investigating the relative (perceived) value of motion cues in the characteristic roll subsidence (RS) and Dutch roll (DR) vehicle modes. Motion cues in the RS mode were chosen such to best preserve the contribution of the roll rate, whereas those in the DR mode were aimed at an improved representation of the lateral (sway) specific force. Contrary to the a-priori stipulated hypothesis it was found that, in this task, the presence of motion cues did not necessarily contribute to enhanced performance in terms of over- and undershoot near the maneuver end points. Motion cues in the RS mode furthermore resulted in a substantial reduction of attained peak velocities, whereas motion cues in the DR mode resulted in a lesser spread of peak velocities (particularly above 35 kts) compared to a condition without motion. In terms of awarded MFRs, motion cues in the RS mode were rated substantially worse than motion cues in the DR mode. This was often attributed by participants to apparently latent "deceleration cues" during stabilization to hover directly after deceleration. The presence of these false cues was predicted in the EMD analysis and also became apparent from the recorded simulation data. Thus, contrary to the result in Experiment I, motion cues in the faster rotational vehicle mode are not necessarily more beneficial in tasks that involve dynamic maneuvering flight. In fact, mitigating false motion cues in the sway specific force of the low-frequency DR mode, on the overall, is more valued by participants.

As part of Experiment II, the utility of EMD was also demonstrated in a study on the effect of dynamic blade flap in the context of motion cueing fidelity. To this end, the three-dof Bo-105 helicopter model was extended with lateral dynamic blade flap to effectively produce a four-dof model. This new model, in which the RS mode is replaced by an oscillatory roll (OR) mode, was subsequently coupled to the linearized CWA dynamics using the method described in Chapter 5. An EMD analysis applied to the resulting coupled model revealed only minor differences in the modal distortion of the four-dof model in comparison to the original three-dof model. Thus, the addition of dynamic blade flap did not mandate changes in the parameters of the CWA. In order to investigate whether the added rotor dynamics are noticeable in flight, a small experiment was conducted on the SRS. Here, participants performed the lateral position task with both the three- and four-dof models in each of the evaluated motion cueing configurations (i.e., ARM, DRM and NM). For each of the resulting six vehicle model-motion combinations, the participants were asked whether a change in the vehicle dynamics was perceived. Results suggest that this is not the case, because none of the participants managed to consistently identify both the presence and nature of the changed vehicle dynamics.

Finally, the goal of Experiment III was to determine whether a "best of both worlds" combination exists beteen matching rotational motion cues near hover and mitigating false specific force cues during more dynamic maneuvering flight. To this end, an experiment involving the depart/abort MTE using a *SCAS augmented*, six-dof model of the AH-64 on the Desdemona simulator was performed. In this experiment, three different motion cueing configurations were evaluated. Two conditions were chosen using a similar rationale as the one adopted in Experiment II for the lateral reposition MTE. The third condition, however, combined the characteristics of these two configurations by adjusting the pitch motion gain (K_q) as a function of airspeed during the transitition from hover to forward flight. It was hypothesized that pilots would rate this third condition more favourably in comparison to the other two. The obtained experimental results, however, suggest that this condition is only marginally better received than the condition in which no effort was undertaken at all to mitigate false cues in the surge specific force. The condition most valued was the one in which *only* tilt-coordination was applied to track the general trend of the surge specific force experienced during the maneuvre. While this is the condition with the least false cues in the specific force, it is also the condition were the distortion of pitch motion cues is largest. These results seemed difficult to characterize, but the general trend in median MFRs suggests that *less motion* results in *better* ratings. While this result cannot be generalized to a condition *without* motion (because it is not measured by the MFR scale), the combined experiment results do suggest that the no-motion condition is not necessarily worse than the evaluated conditions *with* motion. A possible explanation could lie in the combination of inertial motion cues with immersive VR visuals, which could lead pilots to "reweigh" visual and vestibular cues according to their reliability [Fetsch et al., 2009].

6.5. CONCLUSION

This chapter described three experiments in which EMD was used as a guiding methodology for the selection of different motion cueing configurations applied to two different helicopter types (i.e., the AH-64 and Bo-105) in three typical helicopter MTEs (i.e., the precision hover, lateral reposition and depart/abort). These configurations were subsequently assessed "in-the-loop" by test pilots of the RNLAF. The experiments yielded, for the individual tasks considered, valuable knowledge on the relative merit of motion cues aimed at preserving the various vehicle modes. The capability of the EMD method to *predict* motion cueing fidelity remains questionable, however, as the obtained results in terms of subjective pilot ratings were not generally in line with the stipulated hypotheses. This is not necessarily attributed to limitations inherent in the EMD method, but is rather a general limitation of tools that aim to assess the fidelity of "isolated" elements in the simulated flight environment (see also Chapter 2). For example, the presence of stronger or more immersive visual cues in relation to motion cues (or vice versa) could lead to a different appreciation of "motion cueing fidelity".

Finally, this chapter also demonstrated more advanced considerations in relation to the EMD method, such as the incorporation of extended (rotor) dynamics or stability augmentation in EMD. Collectively, these applications highlight the generality and versatility of the EMD method in motion cueing fidelity assessment applied to helicopter flight simulation.

7

CONCLUSION

Helicopter flight simulators, or Flight Simulation Training Devices (FSTDs), play an increasingly important roles in pilot training and certification. These devices aim to reproduce the various *cues* (e.g., instrument readings, outside visuals, haptics, physical motion, etc.) available to pilots in actual flight as accurately as possible. To ensure that safety standards are met to a satisfactory degree, regulatory institutions around the world have formulated requirements on the necessary accuracy, or *fidelity*, that pertain to the many individual (sub)systems inherent in FSTDs. While detailed and predominantly *quantitative* requirements are prescribed on individual FSTD systems like, e.g., the mathematical flight model or the outside visuals, fidelity requirements on the physical motion to be reproduced are still primarily *qualitative*, i.e., based on subjective evaluation by experienced pilots.

Over the years, there have been some developments towards more quantitative approaches for the assessment of *motion fidelity*, the most recent and notable of which is perhaps the Objective Motion Cueing Test (OMCT). The OMCT constructs Frequency Response Functions (FRFs) of the complete Motion Cueing System (MCS) (i.e., both hard- and software), thereby characterizing its *linear* input-output behaviour. This approach, however, considers the MCS (and its degrees-of-freedom) in isolation and foregoes the effect of the vehicle dynamics, captured by the *mathematical flight model*, which acts as a *pre-filter* on the MCS inputs. In fact, based on a literature study (see Chapter 1), there currently exists no *quantitative* approach to capture the *combined* effect of the vehicle dynamics and the MCS. Therefore, in cooperation with TU Delft and Desdemona B.V.[1], the aim of this dissertation was formulated as:

> *Develop a* ***unifying tool*** *to quantify* ***motion cueing fidelity*** *in helicopter flight simulation and evaluate its suitability in* ***realistic*** *applications.*

This objective subsequently led to the definition of three research questions that have been addressed in the various chapters of this thesis. In the following paragraphs, answers to these research question are formulated based on the reported findings.

---

[1] Desdemona B.V. is the company that exploits the Desorientation Demonstrator Amst (Desdemona) simulator situated in Soesterberg, The Netherlands.

① **How to model the interaction between the helicopter dynamics and the MCS?**

This dissertation proposed two different approaches to capture the interaction between the simulated vehicle and MCS dynamics. The first is an extension of the OMCT, with altered input signals based on task- and vehicle-specific frequency-domain spectra derived from time traces of human-perceived quantities (i.e., specific forces and angular rates) as experienced during basic helicopter maneuvering flight.

A second and more general method, independent of specific vehicle dynamics and task, was also developed in this dissertation. This method is named Eigenmode distortion (EMD), where *linearized* models of the vehicle and the MCA are coupled *algebraically*. The application of *modal analysis* to the resulting coupled system was found to reveal the Motion Cueing Algorithm (MCA)-induced *distortion* of the vehicle's dynamic modes in terms of human-perceived quantities. EMD allows for quantitative and interactive analysis of the MCA characteristics from the perspective of the simulated vehicle dynamics.

A particular advantage of EMD, in comparison to existing tools such as OMCT, is that it also exposes the relative relation (and distortion) *between* the different human-perceived quantities in each of the vehicle's dynamic modes. Moreover, the notion of the *Mode Participation Factor (MPF)*, in turn, allows for the identification of dynamic modes that dominate the vehicle response in specific tasks, which may serve as an objective guide in tuning MCAs based on EMD.

② **What aspects of helicopter dynamics can the MCS feasibly reproduce?**

Based on the novel EMD methodology developed in this dissertation, several studies were carried out regarding the effect of the MCA on the simulated vehicle dynamics, covering multiple types of conventional helicopters. In this dissertation, the AH-64 and the Bo-105 were considered in hovering, longitudinal as well as lateral manoeuvering flight. A particularly interesting finding pertains to the role of a helicopter's relatively fast rotational modes (pitch and roll subsidence) in relation to its slower rotational/translational modes (phugoid and Dutch roll).

Namely, it was found that the contribution of the angular rates in the pitch and roll subsidence modes can be reproduced accurately by the MCA, even on Stewart platform (hexapod) based motion simulators. This, however, was also found to result in a strong distortion (in both phase and magnitude) of specific force cues in the phugoid and Dutch roll modes, because translational motion had to be strongly attenuated in the MCA in order to satisfy workspace constraints. In contrast, to feasibly reproduce the contribution of specific forces appearing in the slower phugoid and Dutch roll modes *without* translational motion, it was found that rotational motion cues had to be strongly attentuated, in favour of *tilt-coordination*, in the MCA.

Finally, this dissertation also demonstrated the utility of EMD in evaluating the effect of *added vehicle dynamics* by incorporating dynamic blade flap in the helicopter flight dynamics model. While these specific dynamics were found to be inconsequential in relation to *motion cueing*, the analysis demonstrated the versatility of EMD and inspires its use for applications involving other (aspects of) helicopter dynamics.

③ What aspects of helicopter dynamics cued by the MCS are most valued by pilots?

In order to evaluate the suitability of EMD in practice, several pilot-in-the-loop experiments were performed in this dissertation. In preparation of these experiments, a study on the utility of evaluation tools was conducted (see Chapter 2). In the domain of aeronautical flight simulation, evaluation of simulation fidelity is predominantly based on *subjective* metrics, involving pilot experience and opinion. This study exemplified that, based on these metrics alone, it is difficult to separate the influence of individual subsystems (more specifically, the mathematical flight model) on simulation fidelity from the perspective of the pilot. The remaining experiments in this thesis thus focused primarily on variations in *motion cueing*, in the absence of variations in other simulator subsystems.

In these experiments, EMD was used to obtain suitable configurations of the CWA such to preserve the various modes associated with conventional helicopter dynamics. These configurations were subsequently evaluated with multiple test pilots in three typical helicopter Mission Task Elements (MTEs), namely: the *precision hover*, the *lateral reposition* and, finally, the *take-off/abort*. In conjunction with subjective metrics and task performance metrics, MPFs of the dynamic vehicle modes were also computed and studied. An interesting result from this analysis is that motion cueing aimed at reproducing a certain mode seems to *reduce* the participation of that particular mode in the vehicle response. Also, task performance was found to vary substantially across the different motion cueing configurations evaluated.

In terms of the evaluated motion cueing configurations most valued by pilots *subjectively*, the overall results were less conclusive. For tasks involving precise manoeuvering flight (e.g., hovering), it seems that motion cues in the rotational subsidence modes are more valued than motion cues aimed at representing the longer-term rotational modes (e.g., phugoid and Dutch roll). For tasks that are more dynamic, involving rapid and large changes in the vehicle attitude, the overall experiment results suggest that the opposite is true. In an experiment conducted on the Desdemona simulator, a potential "best-of-both-worlds" MCA configuration was also evaluated, where the pitch motion gain was reduced with forward flight speed. This, however, did not yield a measurable improvement over a condition in which *only* tilt-coordination was active. A possible explanation for this could be the combination of physical motion cues with immersive VR visuals used in the Desdemona simulator during the experiment, which could lead pilots to "reweigh" the importance of visual and vestibular cues.

These results are a testimony of the fact that, in helicopter flight simulation, motion cueing fidelity is highly task-specific and, therefore, no single "optimum" can be formulated based on the results in this dissertation. Nonetheless, EMD combined with the notion of MPFs constitutes a quantitative, model-based framework to guide simulation engineers in estabilishing suitable trade-offs in MCAs for a wide variety of vehicle types and tasks.

Reflecting back on the main goal of this dissertation, it can be concluded that a novel and *unifying* tool has been delivered to *quantify* motion cueing fidelity *from the perspective of the simulated vehicle dynamics*. This tool is found in the EMD methodology, which quantifies the *distortion* of the simulated vehicle's dynamic modes due to the MCAs inherent in all moving-base flight simulators. The method is unifying because, unlike existing tools, it explicitly models the *coupled* dynamics of *both* the vehicle *and* the MCA. Also, the method itself is *task-agnostic*, i.e., it does not require knowledge that pertains to the execution of the simulated task (e.g., recorded time traces). However, the notion of task-specific MPFs in conjunction with EMD can serve as a valuable guide to determine suitable tuning strategies for practical and *realistic* applications. The latter was also demonstrated as part of this dissertation in a series of experiments, involving different tasks, simulators and multiple experienced test pilots.

Many future improvements and extensions to EMD can be suggested. First, while EMD was derived for the six (rigid-body) helicopter and MCA degrees-of-freedom, it has only been applied to *decoupled* longitudinal and lateral motion. An EMD analysis and experimental application to tasks that involves helicopter motion in six degrees-of-freedom would be of interest. Second, despite the fact that MPFs bridge the gap between the somewhat abstract *modal* domain and the time domain, assigning a relative *importance* to individual modes for EMD-based motion cueing fidelity analyses remains troublesome. This dissertation has merely illustrated the utility of MPFs in relation to a small number of typical helicopter MTEs and MCA configurations. Formally exploiting task-specific MPFs as, e.g., weighing factors in EMD-based optimization schemes, could yield improved MCA configurations for specific tasks. Third, while the current dissertation has applied EMD to different *conventional* helicopter types (i.e., the Bo-105 and AH-64), applications to other rotorcraft configurations (e.g., tandem-, tilt-rotor, etc.), fixed-wing aircraft [2] and other vehicles of interst in moving-base flight simulation are strongly encouraged. Finally, the extension of EMD with human operator perception and control models is of geat interest. This would effectively "close the loop" and potentially enable a fully *quantitative* analysis and validation of motion cueing fidelity.

---

[2] EMD was recently applied in an experimental study on motion cueing for the Cessna Citation II aircraft on the SIMONA Research Simulator (SRS) [Stoev et al., 2019].

APPENDICES

A

DEVELOPMENT OF A HELICOPTER FLIGHT DYNAMICS MODEL

This appendix describes the technical background of the Draftsim model, which is used in this thesis for all experiments and analyses performed. It is aimed at predicting helicopter flight characteristics in basic maneuvering flight. *Furthermore, it strives to be most suitable for applications where* high performance *(i.e., fast) and* real-time *(i.e., pilot-in-the-loop) execution are desired. The model is implemented directly in the C++ programming language, leveraging the capabilities of the Eigen matrix template library [Jacob and Guennebaud, 2018]. For off-line simulations, a wrapper was developed using Cython [Behnel et al., 2018] and Eigency [Boomsma, 2018]. This extension allows the model to be executed in a user-friendly Python programming environment while still maintaining high performance and avoiding duplicate implementations.*

The derivation of the flight dynamics model described in this appendix starts with an overview of the different helicopter subsystems. The forces and moments acting on each subsystem are subsequently derived and the rigid body equations of motion are then presented. Finally, a description of several reduced dof models used throughout the thesis is given.

A.1. Overview and main assumptions

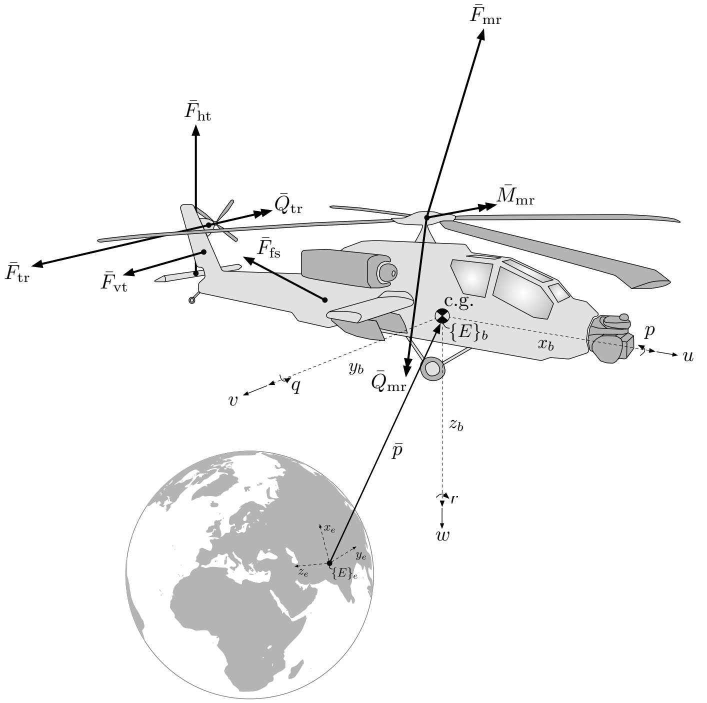

Figure A.1: Free body diagram of a helicopter in flight (vehicle wireframe based on 3D-render by [Sabates, 2016]).

Figure A.1 shows a schematic of a helicopter with six degrees-of-freedom (dofs). Three translational (u, v, w) and three rotational (p, q, r) dofs are shown. These dofs are defined with respect to the *body* frame, $\{E\}_b$, fixed to the center of gravity (c.g.) of the helicopter. The body frame, in turn, is defined with respect to the *flat-earth* frame, $\{E\}_e$, fixed to an arbitrary location on Earth. The location of the helicopter c.g. (and the origin of frame $\{E\}_b$) is furthermore given by the position vector $\bar{p}$. The orientation of frame $\{E\}_b$ with respect to $\{E\}_e$ is defined according to the Euler-Bryant angle convention:

$$\{E\}_b = T_{be}(\phi, \theta, \psi)\,\{E\}_e \tag{A.1}$$

Here, T_{be} is the transformation matrix from $\{E\}_e$ to $\{E\}_b$. The angles ψ, θ and ϕ are known as the yaw (heading), pitch and roll angles, respectively. T_{be} is defined as:

$$T_{be}(\psi, \theta, \phi) = \begin{bmatrix} \cos(\theta)\cos(\psi) & \cos(\theta)\sin(\psi) & -\sin(\theta) \\ \sin(\phi)\sin(\theta)\cos(\psi) - \cos(\phi)\sin(\psi) & \sin(\phi)\sin(\theta)\sin(\psi) + \cos(\phi)\cos(\psi) & \sin(\phi)\cos(\theta) \\ \cos(\phi)\sin(\theta)\cos(\psi) + \sin(\phi)\sin(\psi) & \cos(\phi)\sin(\theta)\sin(\psi) - \sin(\phi)\cos(\psi) & \cos(\phi)\cos(\theta) \end{bmatrix} \tag{A.2}$$

for which it also holds that $T_{eb} = T_{be}^{T}$. Illustrated in Figure A.1 are the various helicopter subsystems and their corresponding forces and moments. It can be seen that the main rotor generates both a force, $\bar{F}_{\mathrm{mr}}$, and a pair of moments, $\bar{M}_{\mathrm{mr}}$ and $\bar{Q}_{\mathrm{mr}}$. $\bar{F}_{\mathrm{mr}}$ is the resultant of the rotor thrust and in-plane forces (i.e., the so-called H- and S-forces), while $\bar{M}_{\mathrm{mr}}$ captures the contribution of the in-plane rotor moments, $\bar{Q}_{\mathrm{mr}}$ is the main rotor (reaction) torque. The tail rotor generates a force, $\bar{F}_{\mathrm{tr}}$, behind the c.g. such to counteract the main rotor torque. Similarly to the main rotor, the tail rotor generates a torque, $\bar{Q}_{\mathrm{tr}}$. In forward flight, the horizontal and vertical tailplane also generate forces, denoted by $\bar{F}_{\mathrm{ht}}$ and $\bar{F}_{\mathrm{vt}}$, respectively. Finally, the fuselage itself generates an aerodynamic (drag) force, $\bar{F}_{\mathrm{fs}}$, and a moment, $\bar{M}_{\mathrm{fs}}$.

Because Draftsim is aimed at predicting helicopter flight dynamics primarily in basic maneuvering flight, several simplifying assumptions are made throughout the derivation of the model. While these will be stipulated in detail in the sections to follow, the most significant assumptions are listed here for quick reference:

- The main rotor blades are assumed to be rigid, with all flexibility concentrated at the hub in the form of an eccentric flapping hinge.
- The main rotor blade flapping dynamics are principally assumed to be *quasi-steady*, which means that a blade's flapping response is treated as *instantaneous* due to a change in blade pitch or local flow conditions. This assumption will be relaxed in Appendix A.2.6, where the case of dynamic flapping is treated.
- The main rotor blade lead-lag and torsional dynamics are neglected.
- The main and tail rotor rotational speeds are assumed to be constant. This is a reasonable assumption for all but the most extraordinary flight conditions (e.g., autorotation).
- Blade aerodynamics are assumed to be *linear* and (dynamic) stall effects are neglected.
- The tail rotor blade flapping dynamics and built-in pitch-flap coupling are neglected. This means that the tail rotor generates an *instantaneous* thrust force in response to a change in tail rotor blade pitch.
- Terms in the various rotor equations to be developed that are $\ll \mu^2$, where μ is the rotor *advance ratio*, are neglected. According to Padfield [2007], this incurs an error of less than 10% in the rotor's (flapping) response.

In summary, the Draftsim model has only *six* rigid body dofs, with all its subsystems shown in Figure A.1 generating *quasi-steady* forces and moments at the helicopter's c.g.. The detailed contribution of each of these subsystems is treated in the subsequent sections.

A.2. MAIN ROTOR

The lifting capacity of any conventional helicopter is provided by one or multiple rotors. The operating principle of a rotor is as follows. The engine delivers a torque to the rotor, which causes the blades to spin at a certain angular velocity, Ω_{mr}. The angular velocity of the rotor is a design parameter and is usually kept constant by the rotor governor within a small margin of error. Without loss of generality, this thesis also assumes a *counter-clockwise* rotation of the main rotor as viewed from above. As a consequence of the angular velocity, the blades trace a circular trajectory in space and are therefore subjected to a relative velocity with respect to the surrounding air. This causes the blades to exert a force on the surrounding air, thereby accelerating the air "downstream" of the rotor. By virtue of Newton's third law, a reaction force, which constitutes the rotor thrust, is developed in the opposite direction. Both the magnitude and direction of the thrust force can be controlled by varying the pitch of the rotor blades. The enabling mechanism for this ability to control thrust magnitude and direction is the blade flapping motion. Because of its central role in helicopter flight mechanics, the blade flapping motion is discussed first. The derivation of the rotor thrust and in-plane forces are outlined thereafter, followed by the derivation of the rotor torque and in-plane moments.

A.2.1. BLADE FLAPPING MOTION

Figure A.2 illustrates a single blade's flapping motion. Several definitions become apparent from this figure. First and foremost, a number of reference frames are defined. The transformations between these various frames follow the Euler-Bryant angle convention given by Equation (A.2). $\{E\}_h$ is the *hub* frame, the origin of which is attached to the rotor hub, located at some distance $\bar{r}_h$ of the c.g., and the axes of which are aligned with the body axes of the helicopter (i.e., frame $\{E\}_b$). $\{E\}_s$ is the *shaft* frame, the origin of which coincides with frame $\{E\}_h$, but is tilted (typically forward and built-in) such that the z_s-axis is parallel to the rotor shaft:

$$\{E\}_s = T_{sh}(0, -\gamma_s, 0)\,\{E\}_h \tag{A.3}$$

$\{E\}_w$ is the *relative wind* frame, the origin of which also coincides with that of frames $\{E\}_s$ and $\{E\}_h$. The x_w-axis, however, is aligned with the azimuthal direction of the relative velocity vector, V_∞, in the shaft plane:

$$\{E\}_w = T_{ws}(\psi_w, 0, 0)\,\{E\}_s \tag{A.4}$$

The final reference frame that is defined is $\{E\}_\beta$, the origin of which is attached to the blade root with the x_β-axis parallel to the blade. The blade root, in general, is eccentric to the shaft by a distance eR, where R is the blade length and e is a fraction of R. The orientation of $\{E\}_\beta$ depends on both the azimuthal location of the blade, ψ (not to be confused with the *heading*!), as well as the *flapping angle*, β:

$$\{E\}_\beta = T_{\beta w}(\psi, \beta)\,\{E\}_w \tag{A.5}$$

where:

$$T_{\beta w}(\psi, \beta) = T_{\beta 1}(0, -\beta, 0)\,T_{1w}(-\psi, 0, 0) \tag{A.6}$$

The origin of frame $\{E\}_1$ coincides with that of frame $\{E\}_w$, but its orientation is equal to that of frame $\{E\}_\beta$ for $\beta = 0$. Hence, both $\{E\}_1$ and $\{E\}_\beta$ are *rotating* reference frames. Also note that the azimuthal location of the blade is defined with respect to the negative z_w-axis, as shown in Figure A.2 for the special case when $\psi = 90°$.

The blade dofs also become apparent from Figure A.2. The hub frame is subjected to the body angular rates, p, q and r. In the relative wind frame, these rates are decomposed

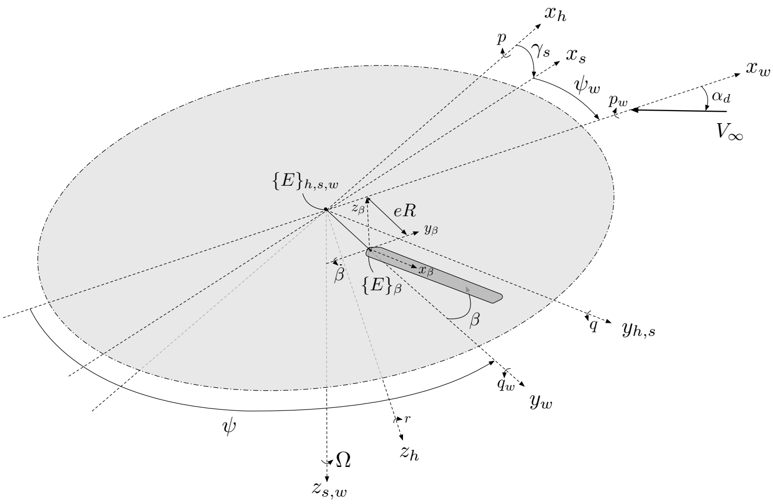

Figure A.2: Schematic of a blade's flapping motion.

into a roll rate, p_w, and a pitch rate, q_w. The yaw rate in the wind frame is ignored, because it is assumed that its magnitude is negligible in relation to the rotor angular velocity, Ω. The rotor angular velocity is defined in the shaft frame, along the negative z_s-axis. Also note that even though *all* frames are subjected to the body angular rates, *only* frame $\{E\}_\beta$, which is fixed to the blade root, is subjected to the rotor angular velocity. The blade, and hence frame $\{E\}_\beta$, is also subjected to the flapping rate, $\dot{\beta}$, defined along the negative y_β-axis. In the following paragraphs, the main rotor equations of interest will be derived with respect to the relative wind frame. The advantage of using this frame, as opposed to the hub or shaft frame, is that there are only two translational velocity components (horizontal and vertical). This simplifies the development of the equations.

Formulation of the flapping equation The first step in the development of the main rotor forces and moments is the derivation of the differential equation that describes a blade's flapping motion. The flapping motion is described relative to frame $\{E\}_\beta$. The time rate of change of angular momentum, $\bar{h}$, relative to this point is given by Euler's equation [Bramwell et al., 2001]:

$$\dot{\bar{h}} = \bar{T} - m_b\, \bar{r}_g \times \bar{a}_0 \tag{A.7}$$

where m_b is the total blade mass, $\bar{r}_g$ is the position of the blade's c.g., $\bar{T}$ is the external moment and $\bar{a}_0$ is the translational acceleration of the origin of frame $\{E\}_\beta$. $\bar{h}$ can be expressed as:

$$\bar{h} = J\,\bar{\omega}$$

where J is the moment of inertia of the blade with respect to the axes of frame $\{E\}_\beta$ and $\bar{\omega}$ is the angular velocity of the blade expressed in frame $\{E\}_\beta$. The time derivative of $\bar{h}$, noting that it is defined in a *rotating* frame of reference, is given by:

$$\dot{\bar{h}} = J\,\dot{\bar{\omega}} + \bar{\omega} \times J\bar{\omega} \tag{A.8}$$

Substitution of Equation (A.8) into Equation (A.7) leads to the following vector equation that describes the angular motion of the blade:

$$J\,\dot{\bar{\omega}} + \bar{\omega} \times J\bar{\omega} = \bar{T} - m_b\,\bar{r}_g \times \bar{a}_0 \tag{A.9}$$

The angular velocity of the blade can subsequently be written as:

$$\begin{aligned} \bar{\omega} &= \begin{bmatrix} p_w & q_w & -\Omega \end{bmatrix} \{E\}_w + \begin{bmatrix} 0 & -\dot{\beta} & 0 \end{bmatrix} \{E\}_\beta \\ &= \left(\begin{bmatrix} p_w & q_w & -\Omega \end{bmatrix} T_{w\beta}(\psi,\beta) + \begin{bmatrix} 0 & -\dot{\beta} & 0 \end{bmatrix} \right) \{E\}_\beta = \bar{\omega}_\beta \{E\}_\beta \end{aligned} \tag{A.10}$$

where $T_{w\beta}(\psi,\beta) = T^T_{\beta w}(\psi,\beta)$ and $T^T_{\beta w}(\psi,\beta)$ is given by Equation (A.6). To obtain angular acceleration, the derivative of Equation (A.10) with respect to time must be evaluated. Invoking the product rule yields:

$$\dot{\bar{\omega}} = \dot{\bar{\omega}}_\beta \{E\}_\beta + \bar{\omega}_\beta \{\dot{E}\}_\beta = \dot{\bar{\omega}}_\beta \{E\}_\beta + \bar{\omega}_\beta\, \Omega_\times(\bar{\omega}_\beta) \{E\}_\beta = \dot{\bar{\omega}}_\beta \{E\}_\beta \tag{A.11}$$

where $\Omega_\times(\bar{\omega}_\beta)$ is the skew-symmetric rotation operator. The position of the origin of frame $\{E\}_\beta$ can be expressed in terms of the intermediate frame $\{E\}_1$ (appearing in Equation (A.6)) as:

$$\bar{r}_0 = \begin{bmatrix} eR & 0 & 0 \end{bmatrix} \{E\}_1 \tag{A.12}$$

Double differentiation with respect to time of Equation (A.12) yields the *inertial* acceleration of the flapping hinge:

$$\begin{aligned} \bar{a}_0 &= \begin{bmatrix} eR & 0 & 0 \end{bmatrix} \left(\Omega_\times(\dot{\bar{\omega}}_1) + \Omega^2_\times(\bar{\omega}_1) \right) \{E\}_1 \\ &= \begin{bmatrix} eR & 0 & 0 \end{bmatrix} \left(\Omega_\times(\dot{\bar{\omega}}_1) + \Omega^2_\times(\bar{\omega}_1) \right) T_{1\beta}(0,\beta,0) \{E\}_\beta \end{aligned} \tag{A.13}$$

where $\bar{\omega}_1$ contains the angular velocity components of frame $\{E\}_1$, expressed in the same frame:

$$\bar{\omega}_1 = \begin{bmatrix} p_w & q_w & -\Omega \end{bmatrix} T_{w1}(\psi,0,0) \tag{A.14}$$

In Equation (A.13), $T_{1\beta}(0,\beta,0) = T^T_{\beta 1}(0,-\beta,0)$ (see Equation (A.6)). Similarly, in Equation (A.14), $T_{w1}(\psi,0,0) = T^T_{w1}(-\psi,0,0)$. Finally, let x_g denote the fraction of R to the blade's c.g, and let A, B and C denote the principal moments of inertia of the blade with respect to frame $\{E\}_\beta$. Then, invoking the classical approximation that the helicopter blade is symmetric, it follows:

$$\bar{r}_g = \begin{bmatrix} x_g R & 0 & 0 \end{bmatrix} \{E\}_\beta \quad \text{and} \quad J = \begin{bmatrix} A & 0 & 0 \\ 0 & B & 0 \\ 0 & 0 & C \end{bmatrix} \tag{A.15}$$

Substitution of Equations (A.10), (A.11), (A.13) and (A.15) into Equation (A.9) yields the three angular equations of motion of the blade about the axes of frame $\{E\}_\beta$. The final expressions are unwieldy and won't be listed here in full. For the flapping equation, the second Euler equation, describing the motion of the blade about the (negative) y_β-axis, is of special interest. The following assumptions are made to further simplify the flapping equation:

Assumption A.2.1 (Flapping equation simplifications (I))

- *The angular rates of the helicopter body are small and develop slowly in relation to the rotor's angular velocity. This means that terms containing higher order products of* p_w *and* q_w *(i.e.,* p_w^2, q_w^2, $p_w q_w$, *etc.) are assumed* $\ll \mu^2$ *and therefore neglected. Also, terms containing* $\dot{p}_w$ *and* $\dot{q}_w$ *are neglected.*
- *The flapping angle,* β, *is assumed to be small. This means that trigonometric terms involving* β *can be approximated by* $\sin\beta \approx \beta$ *and* $\cos\beta \approx 1$. *Also, terms containing higher products of* β *are ignored.*
- *The angular velocity of the rotor is constant, such that* $\dot{\Omega} = 0$.
- *The blade thickness is assumed to be negligible compared to its chord and length. As a consequence, the principal moment of inertia about the* z_β*-axis can be written as* $C = A + B$.
- *A new quantity, defined as* $\epsilon = \dfrac{x_g m_b e R^2}{I_\beta}$, *is introduced. Note that, for clarity sake, the notation* I_β *is adopted for* B *from this point onwards to denote the flap moment of inertia. Also, the external (aerodynamic) moment about the negative* y_β*-axis is denoted by* M_a.

The first two assumptions strongly reduce the complexity of the resulting flapping equation, at the cost of some accuracy for high-speed and dynamic flight. Such applications are not within the scope of this thesis and are therefore not accommodated in Draftsim. Adopting the stipulated assumptions leads to the final result:

$$\ddot{\beta} + \Omega^2(1+\epsilon)\beta = \frac{M_a}{I_\beta} + 2\Omega(1+\epsilon)\left(p_w \cos\psi - q_w \sin\psi\right) \tag{A.16}$$

which governs the blade flapping dynamics. The second term on the left hand side of Equation (A.16) contains the squared of the flapping frequency. In fact, the quantity $\sqrt{1+\epsilon}$ is the *normalized (first) flapping frequency*, which is larger than 1 for $\epsilon > 0$. This explains why the phase difference between pitch and flap is typically less than 90 degrees for rotor systems (e.g., articulated or hingeless) where $e > 0$. The forcing terms on the right hand side of Equation (A.16) consist of the aerodynamic flapping moment and the blade response due to hub rotations. The expression for the aerodynamic flapping moment will be developed in the following paragraphs. This will introduce terms that capture the blade response due to, e.g., collective and cyclic control inputs, but also *aerodynamic damping*.

Blade element forces To obtain expressions for the forces and moments acting on the main rotor as a whole, the forces acting on a single blade over a single rotation must be evaluated. To this end, consider a blade element as depicted in Figure A.3.

The relative velocity, V, is composed of the contributions of the shaft rotation, the motion of the helicopter body and the rotor downwash. To capture these separate contributions, it is convenient to define the components of velocity *tangential* and *perpendicular* to the blade:

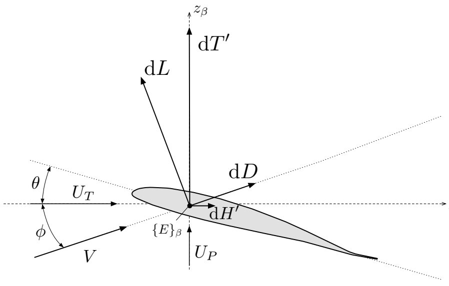

Figure A.3: Schematic of the forces acting on a blade element.

$$U_T = V\cos\phi \quad \text{and} \quad U_P = V\sin\phi \tag{A.17}$$

The component of velocity in the *radial* direction of the blade is assumed to be small and is therefore ignored. U_T and U_P can subsequently be obtained by considering a blade element at a distance xR along the x_β-axis. The position of the blade element can be expressed as:

$$\bar{r} = \begin{bmatrix} eR & 0 & 0 \end{bmatrix} \{E\}_1 + \begin{bmatrix} xR & 0 & 0 \end{bmatrix} \{E\}_\beta \tag{A.18}$$

Differentiation of Equation (A.18) with respect to time yields:

$$\begin{aligned} \dot{\bar{r}} = \bar{V}_r &= \begin{bmatrix} eR & 0 & 0 \end{bmatrix} \{\dot{E}\}_1 + \begin{bmatrix} xR & 0 & 0 \end{bmatrix} \{\dot{E}\}_\beta \\ &= \left(\begin{bmatrix} eR & 0 & 0 \end{bmatrix} \Omega_\times(\bar{\omega}_1) T_{1\beta}(\beta) + \begin{bmatrix} xR & 0 & 0 \end{bmatrix} \Omega_\times(\bar{\omega}_\beta) \right) \{E\}_\beta \end{aligned} \tag{A.19}$$

where $\bar{\omega}_1$ is given by Equation (A.14) and $\bar{\omega}_\beta$ is defined in Equation (A.10). Evaluating Equation (A.19) yields the velocity components of the blade element expressed in terms of reference frame $\{E\}_\beta$. In addition to the existing assumptions adopted in the derivation of the flapping equation, the following is noted:

- The relative air velocity induced by the rotor, v_i, is assumed to be in a direction perpendicular to the rotor shaft:

$$\begin{aligned} \bar{V}_i &= \begin{bmatrix} 0 & 0 & v_i \end{bmatrix} \{E\}_w \\ &= \begin{bmatrix} 0 & 0 & v_i \end{bmatrix} T_{w\beta}(\psi, \beta) \{E\}_\beta \end{aligned} \tag{A.20}$$

- The velocity of the air relative to the rotor disc, V_∞ (see Figure A.2), can be expressed as:

$$\begin{aligned}\bar{V}_\infty &= \begin{bmatrix}-V_\infty\cos\alpha_c & 0 & -V_\infty\sin\alpha_c\end{bmatrix}\{E\}_w \\ &= \begin{bmatrix}-V_\infty\cos\alpha_c & 0 & -V_\infty\sin\alpha_c\end{bmatrix} T_{w\beta}(\psi,\beta)\,\{E\}_\beta\end{aligned} \tag{A.21}$$

Note that V_∞ also includes the rotor hub velocity induced by the angular velocity of the helicopter body.

- For the evaluation of the blade element velocity, it is assumed that the effect of blade eccentricity can be neglected, that is, $e \ll 1$.

Combining Equations (A.19)–(A.21) and noting that the positive directions of *relative* airspeed U_T and U_P are defined along the negative y_β-axis en positive z_β-axis, respectively, the following expressions are finally obtained:

$$U_T = xR\left[\beta\left(p_w\cos\psi - q_w\sin\psi\right) + \Omega\right] + V_\infty\cos\alpha_c\sin\psi \tag{A.22}$$

$$U_P = xR\left(p_w\sin\psi + q_w\cos\psi - \dot{\beta}\right) - V_\infty\beta\cos\alpha_c\cos\psi + V_\infty\sin\alpha_c - v_i \tag{A.23}$$

Referring back to Figure A.3, it can be seen that a blade element generates a lift force, dL, perpendicular to V and a drag force, dD, parallel to V. These forces can be expressed as:

$$\begin{aligned}\mathrm{d}L &= \frac{1}{2}\rho V^2 c_l c = \frac{1}{2}\rho(U_T^2 + U_P^2)c_l c \\ \mathrm{d}D &= \frac{1}{2}\rho V^2 c_d c = \frac{1}{2}\rho(U_T^2 + U_P^2)c_d c\end{aligned} \tag{A.24}$$

Before evaluating these forces in terms of U_T and U_P, the following assumptions are made:

- $U_T \gg U_P$, such that ϕ is small and therefore $\phi \approx \tan\phi = \sin\phi$ as well as $\cos\phi \approx 1$. Moreover, $U_T^2 + U_P^2 \approx U_T^2$.
- The airfoil aerodynamics are linear, i.e., $c_l = a\alpha$ and $c_d = \delta$ and constant along the blade. In addition, the blade chord, c, is also assumed constant along the blade.

As a consequence, it can be found that:

$$\begin{aligned}\mathrm{d}L = \frac{1}{2}\rho U_T^2\left(\theta + \phi\right)ac &= \frac{1}{2}\rho U_T^2\left(\theta + \frac{U_P}{U_T}\right)ac \\ &= \frac{1}{2}\rho\left(U_T^2\theta + U_T U_P\right)ac\end{aligned} \tag{A.25}$$

and:

$$\mathrm{d}D = \frac{1}{2}\rho U_T^2\delta c \tag{A.26}$$

To obtain the contribution of the blade element to the thrust and drag generated by the rotor disc as a whole, the lift and drag must be expressed in terms of $\mathrm{d}T'$ and $\mathrm{d}H'$ (see Figure A.3). Performing this step with the assumptions in mind, the following expressions are obtained:

$$\mathrm{d}T' = \mathrm{d}L \tag{A.27}$$

$$\mathrm{d}H' = \mathrm{d}D\cos\phi - \mathrm{d}L\sin\phi = \mathrm{d}D - \mathrm{d}L\left(\frac{U_P}{U_T}\right) \tag{A.28}$$

From Equation (A.16), it becomes apparent that the blade's flapping motion is governed by the aerodynamic flapping moment M_a about the negative y_β-axis. M_a can be obtained by integration of each blade element's contribution to the moment around the flapping hinge. Let x again denote the location of a blade element along the x_β-axis expressed as a fraction of R, then, using Equations (A.25) and (A.27):

$$\begin{aligned} M_a &= R\int_0^1 x\mathrm{d}T'\,\mathrm{d}x = R\int_0^1 x\mathrm{d}L\,\mathrm{d}x \\ &= \frac{1}{2}\rho acR\int_0^1 x\left(U_T^2\theta + U_T U_P\right)\mathrm{d}x \end{aligned} \tag{A.29}$$

Note that in the last step, the simplifying assumption has been made that the blade chord and local airfoil aerodynamics are constant along the blade. The local tangential and perpendicular velocity (see Equations (A.22) and (A.23)) as well as the blade pitch, however, do vary both along the blade span and also depend on the blade's azimuthal location, ψ. The blade's local pitch angle can be expressed as:

$$\theta = \theta_0 - \theta_{1_c}\cos\psi - \theta_{1_s}\sin\psi + \theta_{tw}x \tag{A.30}$$

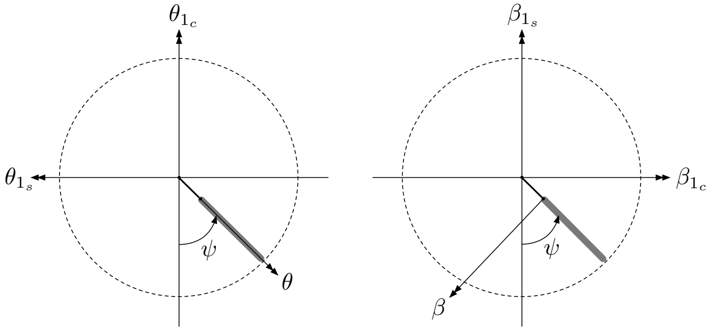

Figure A.4: Sign conventions adopted for the cyclic pitch and flapping angle components.

Here, θ_0 is the collective pitch, which is constant both along the blade as well as the azimuthal location of the blade. θ_{1_c} and θ_{1_s} are the *lateral* and *longitudinal cyclic* pitch, respectively. These contributions depend on the azimuthal location of the blade, resulting in a *periodically* forced blade flapping motion. The sign convention adopted for the cyclic pitch angles is illustrated left in Figure A.4. It can be seen that *forward* longitudinal cyclic and *left* lateral cyclic are positive, respectively. Finally, θ_{tw} is the blade twist, the contribution of which varies linearly along the blade span.

Forced flapping response Before a solution to the flapping equation, Equation (A.16), can be formulated using the newly acquired insights, the following two assumptions are adopted. Subsequent substitution of Equation (A.39) into Equation (A.16) and dividing both sides by Ω^2 yields:

$$\beta'' + (1+\epsilon)\beta = \frac{M_a}{\Omega^2 I_\beta} + 2(1+\epsilon)\left(\bar{p}\cos\psi - \bar{q}\sin\psi\right) \tag{A.31}$$

where $\bar{p}$ and $\bar{q}$ are the *non-dimensional* rates:

$$\bar{p} = \frac{p_w}{\Omega} \qquad \text{and} \qquad \bar{q} = \frac{q_w}{\Omega} \tag{A.32}$$

Additional non-dimensional quantities are defined as:

$$\mu = \frac{V_\infty \cos\alpha_c}{\Omega R}, \mu_z = \frac{V_\infty \sin\alpha_c}{\Omega R}, \lambda = \frac{v_i}{\Omega R} \quad \text{and} \quad \gamma = \frac{\rho a c R^4}{I_\beta} \tag{A.33}$$

where γ is the so-called blade *Lock number*, expressing the ratio of aerodynamic versus inertial contributions to the blade's flapping response. The non-dimensional induced velocity is assumed to be of the form [Bramwell et al., 2001; Glauert, 1926]:

$$\lambda = \lambda_0 \left(1 + Kx\cos\psi\right) \tag{A.34}$$

This expression approximates the non-uniformity of the induced velocity along the longitudinal direction of the rotor disc (i.e., along the x_w-axis) by a linear gradient with a slope given by K. The term in Equation (A.31) involving the aerodynamic flapping moment given by Equation (A.29) can, after substitution of Equations (A.22), (A.23), (A.30), (A.34) and (A.39) and evaluating the integral, be expressed as:

$$\frac{M_a}{\Omega^2 I_\beta} = f\left(\beta, \beta', \mu, \mu_z, \lambda_0, \bar{p}, \bar{q}, \theta_0, \theta_{1_c}, \theta_{1_s}, \theta_{tw}, \psi\right) \tag{A.35}$$

The complete expression is unwieldy and won't be listed here in full. It suffices to note that the result is periodic in ψ. Furthermore, terms that contain products of β' constitute *aerodynamic damping* introduced through the flapping moment. Other forcing terms depend on the local flow conditions (μ, μ_z, λ_0, $\bar{q}$ and $\bar{p}$), blade geometry (θ_{tw}) and control inputs (θ_0, θ_{1_c} and θ_{1_s}).

Assumption A.2.2 (Flapping equation simplifications (II))

- *Because the blade is forced* periodically, *the flapping response of the blade is also assumed to be periodic in* ψ. *That is, a solution in terms of a Fourier series can be formulated:*

  $$\beta = \beta_0 - \beta_{1_c} \cos\psi - \beta_{1_s} \sin\psi - \beta_{2_c} \cos 2\psi - \beta_{2_s} \sin 2\psi \; - \; \ldots \tag{A.36}$$

  It can be shown that the coefficients in Equation (A.36) *corresponding to higher-than-one order harmonics significantly diminish in magnitude [Stewart, 1953]. Therefore, a solution in terms of first-order harmonics suffices:*

  $$\beta = \beta(t, \psi) = \beta_0(t) - \beta_{1_c}(t) \cos\psi - \beta_{1_s}(t) \sin\psi \tag{A.37}$$

  The flapping response in the form of Equation (A.37) *can be intuitively interpreted as rotor disc* coning *and* tilt. *The latter is illustrated right in Figure A.4. It can be seen that* β_{1_c} *represents longitudinal disc tilt, defined positive* backward, *while* β_{1_s} *represents lateral disc tilt, defined positive* left.

- *The flapping angle is a function of both time and blade azimuth as can be seen from Equation* (A.37). *However, it can be shown that the flapping response is significantly more rapid than that of the helicopter as a whole [Padfield, 2007]. Therefore, for most flight mechanics purposes,* time scale separation *applies and the flapping response can be assumed* quasi-steady. *That is:*

  $$\beta = \beta(\psi) = \beta_0 - \beta_{1_c} \cos\psi - \beta_{1_s} \sin\psi \tag{A.38}$$

  It then becomes convenient to define derivatives of β *not with respect to time, but with respect to* ψ. *This can be accomplished by:*

  $$\begin{aligned} \dot{\beta} &= \dot{\beta}\frac{\Omega}{\Omega} = \Omega\frac{d\beta}{dt}\frac{dt}{d\psi} = \Omega\frac{d\beta}{d\psi} = \Omega\beta' \\ \ddot{\beta} &= \ddot{\beta}\frac{\Omega^2}{\Omega^2} = \Omega^2\frac{d^2\beta}{dt^2}\left(\frac{dt}{d\psi}\right)^2 = \Omega^2\frac{d^2\beta}{d\psi^2} = \Omega^2\beta'' \end{aligned} \tag{A.39}$$

Assumption A.2.3 (Flapping equation simplifications (III))

- *Higher harmonics in ψ that appear in the flapping equation as a result of products of β, θ and the components of helicopter body rotation are ignored. This is because, from Equation* (A.38)*, the flapping response is only a function of the first harmonic in ψ.*
- *The flapping coefficients (β_0, β_{1_c} and β_{1_s}) are assumed to be small. Consequently, terms containing products of these quantities with an order higher than* two *are assumed $\ll \mu^2$ and are therefore neglected.*
- *The helicopter body angular rates are assumed to be small. Consequently, terms containing orders of $\bar{p}$ and $\bar{q}$ that are higher than* one *are assumed $\ll \mu^2$ and are therefore neglected. Terms containing products of $\bar{p}$ and $\bar{q}$ together with the flapping coefficients are also ignored.*

Combining Equations (A.31) and (A.35) together with the assumed solution of the form given by Equation (A.38), yields an equation that can be used to solve for the flapping coefficients β_0, β_{1_c} and β_{1_s}. A closed-form solution can be obtained by adopting the Assumption A.2.3. The disc coning angle is consequently found to be:

$$\beta_0 = \frac{\gamma}{(1+\epsilon)}\left(\frac{1}{8}\left(1+\mu^2\right)\theta_0 + \frac{1}{2}\left(\frac{1}{5}+\frac{1}{6}\mu^2\right)\theta_{tw} + \frac{1}{6}\left(\mu_z - \lambda_0\right) + \frac{1}{12}\mu\bar{p} - \frac{1}{6}\mu\theta_{1_s}\right) \tag{A.40}$$

while the longitudinal and lateral disc tilt angles can be obtained from the solution of:

$$\begin{bmatrix} 1 & -\frac{8\epsilon}{\gamma(1-\frac{\mu^2}{2})} \\ \frac{8\epsilon}{\gamma(1+\frac{\mu^2}{2})} & 1 \end{bmatrix} \begin{bmatrix} \beta_{1_c} \\ \beta_{1_s} \end{bmatrix} = \begin{bmatrix} \frac{1}{1-\frac{\mu^2}{2}}\left(2\mu(\mu_z-\lambda_0) + \frac{8}{3}\mu\theta_0 + 2\mu\theta_{tw} + \bar{p} - \frac{16(1+\epsilon)}{\gamma}\bar{q} - \theta_{1_s}\left(1+\frac{3}{2}\mu^2\right)\right) \\ \theta_{1_c} + \frac{1}{1+\frac{\mu^2}{2}}\left(\frac{4}{3}\mu\beta_0 + K\lambda_0 - \bar{q} - \frac{16(1+\epsilon)}{\gamma}\bar{p}\right) \end{bmatrix} \tag{A.41}$$

A.2.2. THRUST AND IN-PLANE FORCES

The forces generated by the main rotor blades can be decomposed into three elements. The largest contribution stems from the thrust, T, which acts along the negative z_w-axis. The other components are the so-called H-force and S-force, acting in the plane of the rotor disc along the negative x_w- and y_w-axis, respectively. To obtain expressions for these forces, consider the forces acting on a blade element as depicted in Figure A.3. In addition, consider the forces acting on a blade element that appear from top and side views of the blade as shown in Figure A.5.

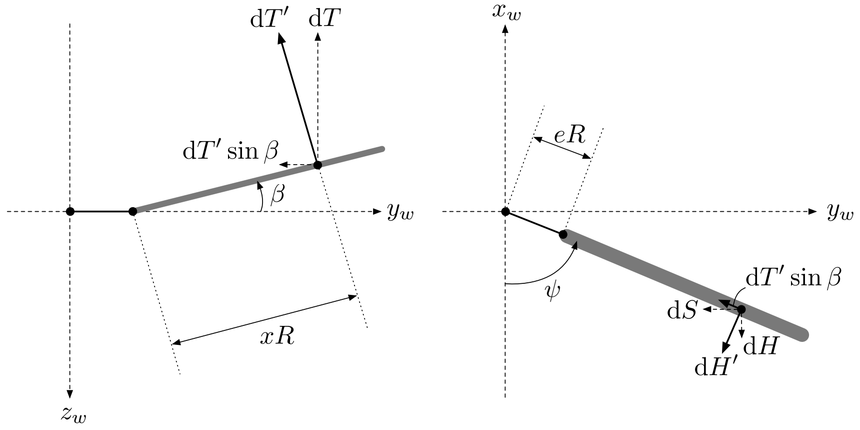

Figure A.5: Schematic of a blade element's contribution to the rotor thrust and in-plane forces.

Noting that β is assumed to be small, from the schematic, it then follows that:

$$\mathrm{d}T = \mathrm{d}T' = \mathrm{d}L$$

where $\mathrm{d}L$ is given by Equation (A.25). To obtain an expression for the total rotor thrust, the contribution of each blade element is averaged over a single rotation and the separate blade element contributions are subsequently integrated over the blade span. For a rotor with b blades, the result can be written as:

$$T = \frac{b}{2\pi}\int_0^{2\pi}\int_0^{1} \mathrm{d}L\, dx d\psi = \frac{b}{4\pi}\rho a c\int_0^{2\pi}\int_0^{1}\left(U_T^2\theta + U_T U_P\right) dx d\psi \tag{A.42}$$

Taking note of the assumptions stipulated in the derivation of a blade's forced flapping response, Equation (A.42) can be combined with Equations (A.22), (A.23) and (A.30) to obtain a solution for the total rotor thrust. In non-dimensional form, the result is:

$$C_T = \frac{T}{\rho(\Omega R)^2\pi R^2} = \frac{\sigma a}{24}\left(\theta_0\left(4 + 6\mu^2\right) + 3\mu\bar{p} + 6\left(\mu_z - \lambda_0\right) + 3\theta_{tw}\left(1 + \mu^2\right) - 6\mu\theta_{1_s}\right) \tag{A.43}$$

Here, a new quantity, σ, was introduced. σ is the rotor *solidity* defined as:

$$\sigma = \frac{bc}{R\pi}$$

and expresses the ratio of blade area versus rotor disc area. To obtain the in-plane forces, a similar procedure is applied. First, the contribution of a single blade element to the H-force is written as (see Equations (A.27) and (A.28) as well as Figure A.3):

$$\mathrm{d}H = \mathrm{d}D \sin\psi - \mathrm{d}L\left(\phi\sin\psi + \beta\cos\psi\right) \tag{A.44}$$

The first term in this equation captures the *profile* drag, while the second term constitutes the *induced* drag. Substitution of Equations (A.25) and (A.26) into Equation (A.44) and evaluating the integral, an expression can be found for the H-force. Applying the same assumptions stipulated in the derivation of forced flapping response, the result in non-dimensional form is:

$$
\begin{aligned}
C_h = \frac{H}{\rho(\Omega R)^2 \pi R^2} = \frac{\sigma \delta \mu}{4} + \frac{\sigma a}{96} (&3K\mu\lambda_0\theta_{1_c} - 3K\mu\beta_{1_s}\lambda_0 + 24\mu_z\mu\theta_0 + 12\mu_z\mu\theta_{tw} - \\
&8K\beta_0\lambda_0 - 9\mu\bar{p}\theta_{1_s} - 3\mu\bar{q}\theta_{1_c} - 12\mu\beta_0^2 - 12\mu\beta_{1_c}^2 + 12\mu\beta_{1_c}\theta_{1_s} - 24\mu\lambda_0\theta_0 - \\
&12\mu\lambda_0\theta_{tw} + 24\mu_z\bar{p} - 36\mu_z\beta_{1_c} - 12\mu_z\theta_{1_s} - 24\bar{p}\lambda_0 + 8\bar{p}\theta_0 + 6\bar{p}\theta_{tw} + 8\beta_0\beta_{1_s} - \\
&8\beta_0\theta_{1_c} + 36\beta_{1_c}\lambda_0 - 16\beta_{1_c}\theta_0 - 12\beta_{1_c}\theta_{tw} + 12\lambda_0\theta_{1_s})
\end{aligned}
\tag{A.45}
$$

In the same way, the S-force can be derived by first writing the contribution of a single blade element as (see Figure A.4):

$$
\mathrm{d}S = \mathrm{d}D \cos\psi + \mathrm{d}L\,(\beta \sin\psi - \phi\cos\psi) \tag{A.46}
$$

Consequently, the following result in non-dimensional is obtained:

$$
\begin{aligned}
C_s = \frac{S}{\rho(\Omega R)^2 \pi R^2} = \frac{\sigma a}{96} (&21K\mu\beta_{1_c}\lambda_0 - 3K\lambda_0\theta_{1_s}\mu + 48\beta_0\mu^2\beta_{1_c} - 24\beta_0\mu^2\theta_{1_s} - \\
&24\mu^2\beta_{1_s}\theta_0 - 12\mu^2\beta_{1_s}\theta_{tw} + 24K\mu_z\lambda_0 - 24K\lambda_0^2 + 8K\theta_0\lambda_0 + 6K\lambda_0\theta_{tw} + \\
&72\beta_0\mu\mu_z - 72\beta_0\mu\lambda_0 + 36\beta_0\theta_0\mu + 24\beta_0\mu\theta_{tw} + 3\mu\bar{p}\theta_{1_c} + 3\mu\bar{q}\theta_{1_s} - \\
&12\mu\beta_{1_c}\beta_{1_s} + 12\mu\beta_{1_c}\theta_{1_c} + 24\mu\beta_{1_s}\theta_{1_s} - 8\beta_0\beta_{1_c} - 8\beta_0\theta_{1_s} - 24\mu_z\bar{q} - \\
&12\mu_z\theta_{1_c} + 36\mu_z\beta_{1_s} + 24\bar{q}\lambda_0 - 8\bar{q}\theta_0 - 6\bar{q}\theta_{tw} + 36\beta_{1_s}\lambda_0 - 16\theta_0\beta_{1_s} - \\
&12\beta_{1_s}\theta_{tw} - 12\lambda_0\theta_{1_c})
\end{aligned}
\tag{A.47}
$$

A.2.3. INDUCED VELOCITY

The uniform (or *mean*) induced velocity, λ_0, defined in Equation (A.34) appears as a variable in Equations (A.41), (A.43), (A.45) and (A.47). It can be shown that the mean induced velocity can be expressed using *Glauert's* equation [Glauert, 1926]:

$$
v_{i_0} = \frac{T}{2\rho\pi R^2 V} \tag{A.48}
$$

where T is the rotor thrust and V is the *total* relative airspeed with respect to the rotor. A general proof of the validity of this equation does not exist. It is accepted, however, because it reduces to the momentum equation in hovering flight and at higher speeds is equivalent to the induced velocity of an elliptically loaded wing [Bramwell et al., 2001]. Moreover, its accuracy was demonstrated using experiments [Bramwell, 1974]. In forward flight, the total relative airspeed can be written as (see Figure A.2) [Glauert, 1926]:

$$
V = \sqrt{(V\cos\alpha_d)^2 + (V\sin\alpha_d - v_{i_0})^2} \tag{A.49}
$$

Substitution of Equation (A.49) into Equation (A.48) and dividing both sides of Equation (A.48) by $(\Omega R)^2$, yields an alternative expression for C_T:

$$C_T = 2\lambda_0\sqrt{\mu_z^2 + (\mu_z - \lambda_0)^2} \tag{A.50}$$

Equation (A.50) can, together with Equation (A.43), be used to solve for both λ_0 and C_T consecutively. This can be accomplished using, e.g., a numerical method such as Newton-Raphson.

A.2.4. TORQUE

The torque transferred by the power plant to the rotor shaft is required to overcome the in-plane drag force produced by each blade element (i.e., $\mathrm{d}H'$ in Figure A.3). Therefore, the elemental torque around the rotor shaft can, using Equation (A.28), be written as:

$$\mathrm{d}Q = xR\,\mathrm{d}H' = xR\left(\mathrm{d}D - \mathrm{d}L\left(\frac{U_P}{U_T}\right)\right) \tag{A.51}$$

Two contributions to the rotor torque can be distinguished. The first term in Equation (A.51) is the torque due to profile drag and the second term is the torque due to induced drag. The first term, denoted by $\mathrm{d}Q_p$ can be obtained using the familiar procedure with which expressions for C_T, C_h and C_s were obtained. That is, first Equations (A.22) and (A.26) are substituted for $\mathrm{d}D$ in Equation (A.51). Subsequently, the result is integrated along the blade, averaged over a single rotation and multiplied by the number of blades:

$$Q_p = \frac{b}{2\pi}\int_0^{2\pi}\int_0^1 xR\,\mathrm{d}D\,\mathrm{d}x\mathrm{d}\psi = \frac{bR}{4\pi}\rho\delta c\int_0^{2\pi}\int_0^1 x\,U_T^2\,\mathrm{d}x\mathrm{d}\psi$$

Evaluating the integral and applying the same assumptions and definitions outlined in the derivations of the rotor thrust and in-plane forces (see Equations (A.43), (A.45) and (A.47)), the following contribution of the profile drag to the rotor's torque coefficient is obtained:

$$C_{q_p} = \frac{Q_p}{\rho(\Omega R)^2\pi R^3} = \frac{\delta\sigma(\mu^2+1)}{8} \tag{A.52}$$

The contribution of induced drag to the rotor torque can be obtained in a similar way. However, an alternative and more algebraically convenient approach can be applied. This approach is outlined in [Bramwell et al., 2001] and won't be repeated here for the sake brevity. The end result, however, is that the torque due to induced drag can be written as a function of the in-plane H-force coefficient and the thrust coefficient as [Bramwell et al., 2001]:

$$C_{q_i} = \frac{\delta\sigma\mu^2}{4} - \mu C_h - (\mu_z - \lambda_0)C_T \tag{A.53}$$

Consequently, the rotor's total torque coefficient becomes:

$$C_q = C_{q_p} + C_{q_i} = \frac{\delta\sigma(1+3\mu^2)}{8} - \mu C_h - (\mu_z - \lambda_0)C_T \tag{A.54}$$

The terms involving C_T and C_h represent the work done by the rotor to produce the resultant thrust force in the direction of the relative airflow with respect to the rotor. The term involving δ is the torque required to overcome the overall profile drag. In the derivation of Equation (A.53), the contribution of the span-wise component of flow along the blades was not taken into account. This results in an underestimation of the profile drag, which can be corrected for by increasing the factor of 3 multiplying μ^2 in Equation (A.54) to finally obtain [Stepniewski, 1973]:

$$C_q = C_{q_p} + C_{q_i} = \frac{\delta\sigma(1 + 4.7\mu^2)}{8} - \mu C_h - (\mu_z - \lambda_0)C_T \tag{A.55}$$

A.2.5. IN-PLANE MOMENTS

Other than a torque about the shaft axis, the rotor also produces a set of moments in the plane of the rotor disc. These moments are the result of blade eccentricity and provide *stiffness* to the rotor. Figure A.6 depicts the mechanism by which the in-plane moments are generated.

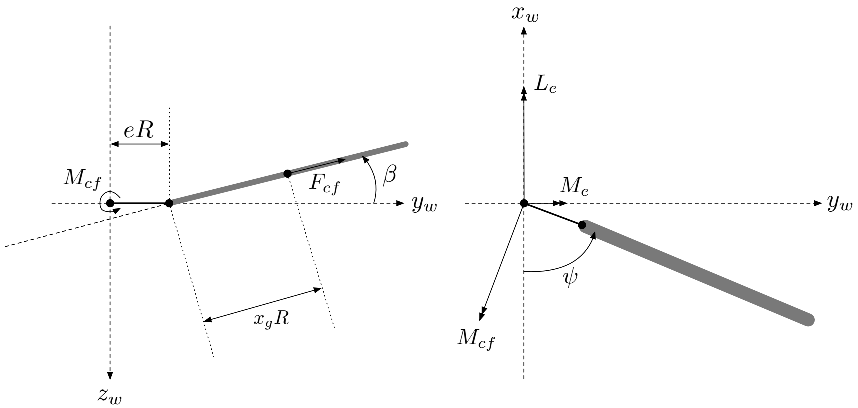

Figure A.6: Schematic of the centrifugal force and moment acting upon a blade (left) and the decompositions in the wind frame (right).

It can be seen that a centrifugal force acts upon the blade in the blade's centre of gravity. The magnitude of this force, under the assumptions that both e and β are small, can be expressed as:

$$F_{cf} = m_b \Omega^2 x_g R$$

Consequently, for small β, the centrifugal moment about a line perpendicular to the shaft axis is found to be (see Figure A.6, left):

$$M_{cf} = eRF_{cf} \sin\beta \approx x_g m_b e(\Omega R)^2 \beta \tag{A.56}$$

In the wind frame, the centrifugal moment can be decomposed in a roll and pitch moment (see Figure A.6, right). The *mean* values for these in-plane moments averaged over a blade's single rotation can be written as:

$$M_e = -\frac{1}{2\pi}\int_0^{2\pi} M_{cf}\cos\psi\,\mathrm{d}\psi \qquad \text{and} \qquad L_e = -\frac{1}{2\pi}\int_0^{2\pi} M_{cf}\sin\psi\,\mathrm{d}\psi \tag{A.57}$$

Substitution of Equation (A.38) into Equation (A.56), combining the result with Equation (A.57), evaluating the integrals and multiplying by the number of blades, yields the following expressions for the in-plane moments in terms of the disc tilt angles:

$$M_e = \frac{1}{2}bx_g m_b e(\Omega R)^2\beta_{1_c} \qquad \text{and} \qquad L_e = \frac{1}{2}bx_g m_b e(\Omega R)^2\beta_{1_s} \tag{A.58}$$

A.2.6. DYNAMIC BLADE FLAP

In the development of Equations (A.40) and (A.41), it was assumed that blade flapping occurred in a *quasi-steady* fashion. That is, the effect of time derivatives of the flapping coefficients β_0, β_{1_c} and β_{1_s} was neglected. In Chapter 6 of this thesis, however, an investigation is presented on the effect of higher-order blade dynamics in relation to simulator motion cueing. As such, an optional extension to Draftsim was developed that includes dynamic blade flapping. The goal of this extension is to capture the rotor's *regressing flap mode*, which for certain types of rotor systems can result in substantially different dynamic response types [Curtiss, 1986].

The derivations of the dynamic flapping equations starts with a reconsideration of Equations (A.37)–(A.39). In these equations, β was assumed periodic in ψ only. Consequently, the time derivatives $\dot{\beta}$ and $\ddot{\beta}$ could be written as a products of the rotor angular velocity and the change of β with ψ. Starting from Equation (A.37), it possible to re-express $\dot{\beta}$ and $\ddot{\beta}$ in terms of the flapping coefficients:

$$\begin{aligned}
\frac{\dot{\beta}}{\Omega} &= \beta' = \beta_0' - \beta_{1_c}'\cos\psi - \beta_{1_s}'\sin\psi + \beta_{1_c}\sin\psi - \beta 1_s\cos\psi \\
\frac{\ddot{\beta}}{\Omega^2} &= \beta'' = \beta_0'' - \beta_{1_c}''\cos\psi - \beta_{1_s}''\sin\psi + 2\beta_{1_c}'\sin\psi - 2\beta_{1_s}'\cos\psi + \beta_{1_c}\cos\psi + \beta_{1_s}\sin\psi
\end{aligned} \tag{A.59}$$

where the *prime* (′) notation is used to signify *dimensionless* derivatives. The expressions in Equation (A.59) can subsequently be substituted in Equation (A.31), the non-dimensional flapping equation, and Equation (A.35), the non-dimensional flapping moment. After applying Assumption A.2.3, the flapping equation can be solved to produce an end result in the form:

$$\bar{\beta}'' + C_{\mathrm{nr}}\bar{\beta}' + D_{\mathrm{nr}}\bar{\beta} = F_{\mathrm{nr}}, \quad \text{where} \quad \bar{\beta} = \begin{bmatrix}\beta_0 & \beta_{1_c} & \beta_{1_s}\end{bmatrix}\{E\}_w \tag{A.60}$$

where:

$$
\begin{aligned}
C_{\mathrm{nr}} &= \frac{\gamma}{8}\begin{bmatrix} 1 & 0 & -\frac{2\mu}{3} \\ 0 & 1 & \frac{16}{\gamma} \\ -\frac{4\mu}{3} & -\frac{16}{\gamma} & 1 \end{bmatrix}, \qquad D_{\mathrm{nr}} = \frac{\gamma}{8}\begin{bmatrix} \frac{8(1+\epsilon)}{\gamma} & 0 & 0 \\ -\frac{4\mu}{3} & \frac{8\epsilon}{\gamma} & 1+\frac{1}{2}\mu^2 \\ 0 & \frac{1}{2}\mu^2-1 & \frac{8\epsilon}{\gamma} \end{bmatrix} \\
F_{\mathrm{nr}} &= \frac{\gamma}{8}\begin{bmatrix} \theta_0(1+\mu^2)+\theta_{tw}(\frac{4}{5}+\frac{2}{3}\mu^2)-\frac{4\mu}{3}\theta_{1_s}+\frac{2\mu}{3}\bar{p}+\frac{4}{3}(\mu_z-\lambda_0) \\ -\frac{16(1+\epsilon)}{\gamma}\bar{p}+\theta_{1_c}(1+\frac{1}{2}\mu^2)-\bar{q}+K\lambda_0 \\ \frac{16(1+\epsilon)}{\gamma}\bar{q}+\theta_{1_s}(1+\frac{3}{2}\mu^2)-2\mu(\mu_z-\lambda_0)-2\mu(\frac{4}{3}\theta_0+\theta_{tw})-\bar{p} \end{bmatrix}
\end{aligned}
\tag{A.61}
$$

Equation (A.61) represents the *forced flapping response* of a rotor expressed in a non-rotating frame of reference. Extending Draftsim with this equation effectively yields a *nine* degree-of-freedom model, giving rise to additional *advancing* and *regressing* flap modes in conjunction to the vehicle's rigid body modes. To capture the regressing flap mode only, Equation (A.61) can be further simplified by dropping the second-order derivatives of the flapping coefficients as well as the dynamic equation for the coning angle, β_0. The resulting expression is:

$$
\begin{aligned}
&\begin{bmatrix} 1 & \frac{16}{\gamma} \\ -\frac{16}{\gamma} & 1 \end{bmatrix}\begin{bmatrix} \beta'_{1_c} \\ \beta'_{1_s} \end{bmatrix} + \begin{bmatrix} \frac{8\epsilon}{\gamma} & 1+\frac{1}{2}\mu^2 \\ \frac{1}{2}\mu^2-1 & \frac{8\epsilon}{\gamma} \end{bmatrix}\begin{bmatrix} \beta_{1_c} \\ \beta_{1_s} \end{bmatrix} = \\
&\qquad \begin{bmatrix} -\frac{16(1+\epsilon)}{\gamma}\bar{p}+\theta_{1_c}(1+\frac{1}{2}\mu^2-\bar{q}+K\lambda_0+\frac{4\mu}{3}\beta_0 \\ \frac{16(1+\epsilon)}{\gamma}\bar{q}+\theta_{1_s}(1+\frac{3}{2}\mu^2)-2\mu(\mu_z-\lambda_0)-2\mu(\frac{4}{3}\theta_0+\theta_{tw})-\bar{p} \end{bmatrix}
\end{aligned}
\tag{A.62}
$$

Note that while the dynamics of the coning angle are neglected, its steady-state value computed from Equation (A.40) still affects the coupled dynamics of β_{1_c} and β_{1_s} as seen from the right-hand side of Equation (A.62). Also, it can be seen that the vehicle states (through μ, μ_z and q) affect the dynamic flap derivatives (*body-flap* coupling). In reality, the dynamic flap derivatives themselves will also *directly* affect the main rotor forces (*flap-body* coupling). This would entail that the expressions for the rotor thrust and in-plane forces (see Equations (A.43), (A.45) and (A.47)) need to be re-derived using the new equation for β' in Equation (A.59).To capture the regressing flap mode and its interaction with the vehicle rigid-body modes, however, this second step is not necessary and therefore omitted.

A.2.7. MISCELLANEOUS CONSIDERATIONS

To arrive at the final expressions presented for the various forces and moments acting on the main rotor, a number of simplifying assumptions had to be made. Amongst these assumptions are two that deserve special attention, namely the correction factor for non-uniformity of the rotor inflow and the value for the blade profile drag coefficient. Detailed expressions for these quantities were not specified in the preceding discussion and will therefore be outlined in the first two of the following paragraphs. Thereafter, the effect of introducing an additional assumption, namely that of blade mass uniformity, is presented.

Correction for non-uniform inflow In the derivation of the flapping coefficients, given by Equations (A.40) and (A.41), an induced velocity distribution of the form given by Equation (A.34) was assumed. Equation (A.34) was proposed by Glauert in recognition of the fact that an upwash in the flow exists at the leading edge of the rotor disc, while an increase in induced velocity can be observed towards the trailing edge. Bramwell et al. [2001] proposes a value for K that is slightly greater than one, citing a typical value of 1.2.

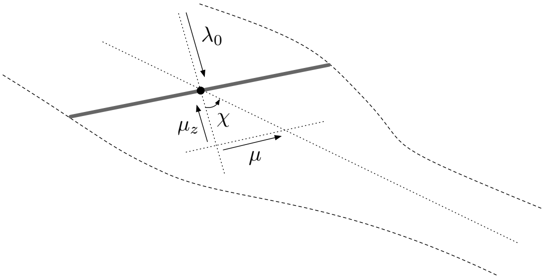

Figure A.7: Schematic of rotor wake angle.

A more sophisticated proposition for K follows from a theoretical consideration of the rotor wake [Coleman et al., 1947]. A solution for K in closed form could not be obtained from this analysis, but the longitudinal distribution of induced velocity was found to be approximately linear over the majority of the rotor diameter [Bramwell et al., 2001]. In addition, it was found that the slope of the induced velocity distribution is related to the *wake angle*, χ. Consequently, a value for K equal to $\tan\left(\frac{\chi}{2}\right)$ is proposed [Bramwell et al., 2001]. The wake angle can be expressed as (see Figure A.7):

$$\chi = \tan^{-1}\left(\frac{\mu}{\lambda_0 - \mu_z}\right) \tag{A.63}$$

Profile drag coefficient The blade profile drag coefficient (δ) appears in the expressions for the H-force coefficient (Equation (A.45)) and the rotor torque coefficient (Equation (A.55)). In the derivation of these expressions, δ was assumed to be a constant. In reality, this is not the case and δ will depend on the local blade element profile and angle of attack, Mach number and Reynolds number [Johnson, 1994]. Nonetheless, a mean value for δ is often used and can provide a reasonable approximation [Bramwell et al., 2001; Padfield, 2007]. A more refined approach [Johnson, 1994], was proposed by Bailey [1941]. Bailey derived an empirical approximation for δ in the form of a polar that is a function of the *mean blade incidence*:

$$\delta = a_0 + a_1\alpha_m + a_2\alpha_m^2 \tag{A.64}$$

The mean blade incidence can be derived from the mean lift coefficient which, in turn, is found in terms of the rotor thrust by integrating the thrust produced by each blade element along the blade span [Bramwell et al., 2001; Johnson, 1994]:

$$T = b\int_0^1 \mathrm{d}L\,\mathrm{d}x = b\int_0^1 \frac{1}{2}\rho(\Omega x R)^2 C_{l_m} c\,\mathrm{d}x = \frac{b}{6}\rho(\Omega R)^2 c C_{l_m} \tag{A.65}$$

Subsequently dividing both sides of Equation (A.65) by the rotor disk area and recalling the definition of the rotor solidity in Appendix A.2.2:

$$C_{l_m} = \frac{6T}{\rho(\Omega R)^2 \pi R^2 \sigma} = \frac{6C_T}{\sigma} \tag{A.66}$$

The mean lift coefficient is then used to finally obtain an expression for the mean incidence angle of the blades by combining Equation (A.66) with the expression for the local lift coefficient:

$$a\alpha_m = C_{l_m} = \frac{6C_T}{\sigma} \qquad \text{or} \qquad \alpha_m = \frac{6C_T}{\sigma a} \tag{A.67}$$

The coefficients a_0, a_1 and a_2 appearing in Equation (A.64) depend on the blade section (airfoil) aerodynamic characteristics. For the NACA 23012 airfoil at Re = $2 \cdot 10^6$, Bailey [1941] proposed the values of $a_0 = 0.0087$, $a_1 = -0.021$ and $a_2 = 0.4$. This result is accurate in the working range of the blade incidence, up to the stall limit at approximately 11°. As demonstrated by Johnson [1994], the coefficients vary slightly for other types of airfoils. With little assumed loss of accuracy, the coefficients are nonetheless kept constant in the model for the sake of simplicity.

Blade mass uniformity In the derivation of the flapping equation given by Equation (A.16), no particular assumptions regarding the blade geometry and composition were made (with the exception that the blade can be approximated by a flat plat). By further stipulating that the blade mass is distributed evenly along the blade, an expression for the mass moment of inertia around the flapping hinge, I_β, can be found. Noting that the normalized distance from the flapping hinge to the blade's center of gravity becomes $x_g = \frac{1}{2}(1-e)$, I_β can be expressed as:

$$I_\beta = \frac{1}{12} m_b \left((1-e)R\right)^2 + m_b \left(\frac{1}{2}(1-e)R\right)^2 = \frac{1}{3} m_b (1-e)^2 R^2 \tag{A.68}$$

Consequently, a simplified expression for ϵ appearing in Equation (A.16) can be defined in terms of only the flapping hinge eccentricity:

$$\epsilon = \frac{\frac{1}{2}(1-e) m_b e R^2}{\frac{1}{3} m_b (1-e)^2 R^2} = \frac{3e}{2(1-e)} \tag{A.69}$$

Another implication of a uniform blade mass distribution is that the expressions for the in-plane moments due to flapping hinge eccentricity (Equation (A.58)) can be simplified by assuming $x_g \approx \frac{1}{2}$ (for small e):

$$M_e = \frac{1}{4} b m_b e (\Omega R)^2 \beta_{1_c} \qquad \text{and} \qquad L_e = \frac{1}{4} b m_b e (\Omega R)^2 \beta_{1_s} \tag{A.70}$$

Cyclic control mixing Because of the equivalent eccentricity (or stiffness) of the rotor hub, the phase shift between applied cyclic pitch and flap is typically less than ninety degrees for articulated and hingeless rotors [Padfield, 2007]. Thus, longitudinal and lateral cyclic inputs (θ_{1_s} or θ_{1_c}) applied at the blades will result in coupled roll and pitch responses. To somewhat alleviate this response coupling, cyclic *control mixing* can be applied. In this case, the cyclic pitch angles applied at the blade are written as a combination of the cyclic pitch angles commanded by the pilot [Padfield, 2007]:

$$\begin{bmatrix}\theta_{1_c}\\ \theta_{1_s}\end{bmatrix} = \begin{bmatrix}\cos\psi_{\text{mx}} & -\sin\psi_{\text{mx}}\\ \sin\psi_{\text{mx}} & \cos\psi_{\text{mx}}\end{bmatrix}\begin{bmatrix}\theta'_{1_c}\\ \theta'_{1_s}\end{bmatrix} \tag{A.71}$$

where ψ_{mx} is the *mixing angle*. Note that, while the mixing angle is kept constant for simplicity sake, the amount of response coupling experienced varies with the flight condition and velocity.

A.3. TAIL ROTOR

Referring back to Figure A.1, it can be seen that the tail rotor is situated some distance behind the c.g. of the helicopter and that it generates a sideways directed force. This force produces a moment about the c.g. of the helicopter such to counteract the main rotor torque. The tail rotor also produces a torque. The treatment of the tail rotor is analogous to the treatment of the main rotor with a few simplifying assumptions:

- Only collective pitch inputs are applied to the tail rotor blades, i.e., the tail rotor swash-plate is unable to tilt.
- No pitch-flap coupling is taken into account. As such, tail rotor blade pitch is only influenced by the pilot-commanded collective pitch and not by blade flapping (i.e., rotor disc coning and tilt).
- Tail rotor in-plane forces are neglected. That is, it assumed that the H-force and S-force acting on the tail rotor are negligible in magnitude.
- In contrast to the main rotor, the rotation of the helicopter body is assumed to *only* influence the relative airspeed perceived by the tail rotor as a whole. In other words, body rotation is assumed to not influence the incidence angle of the individual blades.
- Tail rotor blade twist *is* taken into account.

Given these assumptions, it becomes evident that the tail rotor produces a single thrust force directed towards the positive y_b-axis as well as a torque that acts about the negative y_b-axis. Also, the consideration of tail rotor blade flapping becomes superfluous. As a consequence, Equation (A.43) can be used to write the tail rotor thrust coefficient as:

$$C_T = \frac{T}{\rho(\Omega R)^2\pi R^2} = \frac{\sigma a}{24}\left(\theta_0\left(4+6\mu^2\right)+6\left(\mu_z-\lambda_0\right)+3\theta_{tw}\left(1+\mu^2\right)\right) \tag{A.72}$$

Note that all rotor-specific quantities (e.g., solidity, lift curve slope, etc.) appearing in Equation (A.72) now pertain to the *tail rotor*. For the sake of notational convenience, no additional symbols have been introduced. Also, the relative (induced) velocity components are non-dimensionalised with the tail rotor radius and angular velocity. Finally, note that the non-dimensional velocity components μ and μ_z also include translational components induced by the rotation of the helicopter body. Similarly, the tail rotor torque coefficient, from Equation (A.55), is found to be:

$$C_q = \frac{\delta\sigma(1+3\mu^2)}{8} - (\mu_z - \lambda_0)C_T \tag{A.73}$$

A.4. FUSELAGE

From Figure A.1 it becomes apparent that the fuselage produces an aerodynamic drag force as well as an aerodynamic moment. In contrast to fixed-wing aircraft, the fuselage of a helicopter is responsible for a large proportion of the total parasitic drag, of which the rotor hub is the largest contributor (approximately 25-50%) [Johnson, 1994]. The drag force can be approximated by using the notion of an *equivalent flat plate* area. f_{fs}, such that the magnitude of the aerodynamic drag force can be expressed:

$$F_{\text{fs}} = \frac{1}{2}\rho V^2 f_{\text{fs}} \tag{A.74}$$

where V is the resultant velocity of helicopter. Note that the effect of rotor downwash on the resultant velocity is neglected. The equivalent flat plate area, f_{fs}, is typically estimated from empirical data (see, e.g., [Johnson, 1994], but can also be obtained from wind tunnel tests with representative (full-)scale models.

Because of the shape of a typical helicopter fuselage, side and bottom areas are substantially larger than the frontal area. For this reason, it is convenient to decompose Equation (A.74) into individual components along the individual body axes of the vehicle:

$$F_{\text{fs}}^x = \frac{1}{2}\rho u V f_{\text{fs}}^x, \qquad F_{\text{fs}}^y = \frac{1}{2}\rho v V f_{\text{fs}}^y \qquad \text{and} \qquad F_{\text{fs}}^z = \frac{1}{2}\rho w V f_{\text{fs}}^z \tag{A.75}$$

where f_{fs}^x, f_{fs}^y and f_{fs}^z are the equivalent flat plate drag areas as viewed from the front, side and bottom of the vehicle, respectively. Often, however, only the frontal equivalent flat plate drag area is available. In that case, values for f_{fs}^y and f_{fs}^z can be approximated from the ratio of the *physical* areas of the side and bottom of the vehicle with respect to the frontal area.

In Draftsim, the center of pressure of the fuselage drag force is assumed to coincide with the c.g. of the helicopter. The fuselage drag force vector acts opposite to the direction of motion and can therefore be expressed as:

$$\bar{F}_{\text{fs}} = -\begin{bmatrix} F_{\text{fs}}^x & F_{\text{fs}}^y & F_{\text{fs}}^z \end{bmatrix} \{E\}_b \tag{A.76}$$

where α_{fs} and β_{fs} are the fuselage angle of attack and angle of sideslip, respectively. The aerodynamic moment produced by the fuselage can be decomposed into two dominant components, a pitching and yawing moment, M_{fs} and N_{fs}, respectively. Values for these components can be obtained using data from wind tunnel tests (see, e.g., [Padfield, 2007]) or from empirical approximations. One such an empirical approximation that is adopted in Draftsim is proposed in [Marinescu and Anghel, 1992] and applied in [Pavel, 2001]. The expressions are given by:

$$M_{\text{fs}} = \rho V^2 K_{\text{fs}} V_{\text{fs}_m} \alpha_{\text{fs}} \qquad \text{and} \qquad N_{\text{fs}} = \rho V^2 K_{\text{fs}} V_{\text{fs}_n} \beta_{\text{fs}} \tag{A.77}$$

where α_{fs} and β_{fs} are fuselage angle of attack and sideslip, respectively, calculated from:

$$\alpha_{\text{fs}} = \sin^{-1}\left(\frac{w}{V}\right) \qquad \text{and} \qquad \beta_{\text{fs}} = \sin^{-1}\left(\frac{v}{V}\right) \tag{A.78}$$

in non-hovering flight. In Equation (A.78), K_{fs} is a correction factor, the value of which is determined by the geometry of the fuselage as can be seen from Figure A.8.

The quantities V_{fs_m} and V_{fs_n} are equivalent volumes that are determined by the geometry of the helicopter, assuming circular sections, using the following expressions [Marinescu and Anghel, 1992]:

$$V_{\text{fs}_m} = \frac{\pi}{4}\int_0^{l_{\text{fs}}} d^2(x)\,\mathrm{d}x \qquad \text{and} \qquad V_{\text{fs}_n} = \frac{\pi}{4}\int_0^{l_{\text{fs}}} h^2(x)\,\mathrm{d}x \tag{A.79}$$

In this equation, $d(x)$ and $h(x)$ are the *width* and *height*, respectively, of the fuselage at an arbitrary section x. The fuselage aerodynamic moment vector then becomes:

$$\bar{M}_{\text{fs}} = \begin{bmatrix} 0 & M_{\text{fs}} & N_{\text{fs}} \end{bmatrix} \{E\}_b \tag{A.80}$$

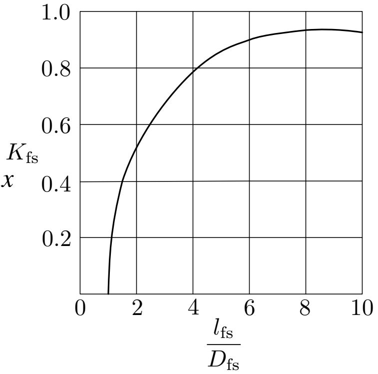

Figure A.8: Determination of correction factor K_{fs} [Marinescu and Anghel, 1992].

A.5. EMPENNAGE

The empennage comprises the horizontal and vertical tailplane of the helicopter. These surfaces provide stability at higher speeds and are therefore also modeled in Draftsim. In contrast to fixed wing aircraft, rotorcraft have a versatile manoeuvering capability which included both vertical and lateral flight. As a consequence, the empennage is generally susceptible to a large range of angle of attacks. Up to approximately 20 to 30 degrees of angle of attack, the forces acting on the surfaces can be assumed to be governed by simple linear aerodynamics [Padfield, 2007]. Beyond that value, stall occurs and the forces produced by the empennage diminish drastically. While physically modeling the stall behaviour of the surfaces is beyond the scope of this thesis, the effect can be incorporated in a more rudimentary fashion. To this end, a transition region is assumed between 20 and 30 degrees of angle of attack. In this region, the *lift* force produced by the surface smoothly drops to zero and a *drag* force is produced instead. Summarizing, a total force coefficient can be defined as:

$$C_{f_\square} = -\left(c_{l_\square}\cos\alpha_\square + c_{d_\square}\sin\alpha_\square\right) \tag{A.81}$$

where the negative sign ensures the correct direction of the force perpendicular to the surface and □ is a placeholder for the type of surface (i.e., 'ht' for the horizontal tailplane and 'vt' for the vertical tailplane). Note that the force acting parallel to the surface is neglected. The angles of attack are obtained from:

$$\alpha_{\text{ht}} = \sin^{-1}\left(\frac{w}{V_{\text{ht}}}\right) \qquad \text{and} \qquad \alpha_{\text{vt}} = \sin^{-1}\left(\frac{v}{V_{\text{vt}}}\right) \tag{A.82}$$

where $V_\square$ is the relative airspeed at the respective surface. Note that these speeds include contributions due to the rotation of the helicopter body. The effect of main rotor downwash, however, is neglected. The values of the lift and drag coefficients subsequently depend on the angle of attack:

$$c_{l_\square} = \begin{cases} a_\square \alpha_\square & 0^\circ \leq \alpha_\square \leq 20^\circ \\ a_\square \alpha_\square \rightarrow 0 & 20^\circ < \alpha_\square \leq 30^\circ \\ 0 & \alpha_\square > 30^\circ \end{cases} \qquad \text{and} \qquad c_{d_\square} = \begin{cases} 0 & \alpha_\square \leq 20^\circ \\ c_{d_0} & \alpha_\square > 20^\circ \end{cases} \tag{A.83}$$

where $a_\square$ are the lift curve slopes in the linear region and c_{d_0} is the drag coefficient of a flat plate orientated perpendicular to the airflow (assumed equal to 1.28). In effect, the empennage forces $F_\square$ are expressed as:

$$F_\square = \frac{1}{2}\rho V_\square^2 C_{f_\square} S_\square \tag{A.84}$$

where $S_\square$ denotes the surface area of the respective surface.

A.6. EQUATIONS OF MOTION

The forces and moments acting on each of the subsystems covered in the preceding sections contribute to the overall motion of the helicopter. The helicopter motion is described with respect to an inertial frame of reference. For the purposes of this thesis, any Earth-fixed frame is considered to be an inertial frame. In Figure A.1, such a frame is denoted by $\{E\}_e$. As expressed in Equation (A.1), the orientation of the aircraft-fixed body frame $\{E\}_b$ with respect to frame $\{E\}_e$ is a function of attitude. Therefore, to describe the motion of the helicopter, equations are needed to capture the variations of helicopter position and attitude in time.

To this end, it is convenient to define a *state* vector that contains the position ($\bar{p}$), attitude ($\bar{\Phi}$), velocity in the body frame ($\bar{V}$) and angular rate ($\bar{\omega}$) of the helicopter:

$$\bar{x} = \begin{bmatrix} \bar{p} & \bar{\Phi} & \bar{V} & \bar{\omega} \end{bmatrix}^T \tag{A.85}$$

In addition, it is convenient to define the *input* vector to the flight mechanics model as:

$$\bar{u} = \begin{bmatrix} \theta_0 & \theta_{1_s} & \theta_{1_c} & \theta_{0_{\text{tr}}} \end{bmatrix}^T \tag{A.86}$$

Here, the subscript tr is added to signify tail rotor collective pitch. The time derivative of the state vector describes the evolution of the motion of the helicopter in time. The time derivatives of position and attitude follow from basic kinematics as:

$$\dot{\bar{p}} = T_{eb}(\psi, \theta, \phi)\, \bar{V} \qquad \text{and} \qquad \dot{\bar{\Phi}} = \begin{bmatrix} 1 & \sin\phi \tan\theta & \cos\phi \tan\theta \\ 0 & \cos\phi & -\sin\phi \\ 0 & \frac{\sin\phi}{\cos\theta} & \frac{\cos\phi}{\cos\theta} \end{bmatrix} \bar{\omega} \tag{A.87}$$

The time derivatives of velocity and angular rates can be obtained, under the assumption that the helicopter is a rigid body, from Newton's and Euler's equations. For translational acceleration, the application of Newton's law yields:

$$\dot{\bar{V}} = \frac{\bar{F}_{\text{cg}}(\bar{x},\bar{u})}{m} + T_{be}(\psi,\theta,\phi)\,\bar{G} - \bar{\omega}\times\bar{V} \tag{A.88}$$

In this equation, $\bar{F}_{\text{cg}}$ is the sum of all force vectors acting on the helicopter, which depends on the state as well as the input, and $\bar{G}$ is the gravitational acceleration vector defined in frame $\{E\}_e$. For rotational acceleration, a similar application of Euler's equations yields:

$$\dot{\bar{\omega}} = J^{-1}\left(\bar{M}_{\text{cg}}(\bar{x},\bar{u}) - \bar{\omega}\times J\bar{\omega}\right) \tag{A.89}$$

with $\bar{M}_{\text{cg}}$ defined as the state and input dependent sum of all moments acting in the aircraft's c.g. and J denoting the inertia tensor of the aircraft. The inertia tensor contains the mass moments of inertia with respect to the aircraft's c.g. For helicopters, which are typically symmetrical with respect to the body xz-plane, the inertia tensor simplifies to:

$$J = \begin{bmatrix} I_{xx} & 0 & -I_{xz} \\ 0 & I_{yy} & 0 \\ -I_{xz} & 0 & I_{xx} \end{bmatrix} \tag{A.90}$$

where I_{xx}, I_{yy} and I_{zz} are the roll, pitch and yaw moments of inertia, respectively, and I_{xz} is the roll-yaw product of inertia.

A.7. Reduced degree-of-freedom (dof) models

Throughout the thesis, models with reduced degrees-of-freedom are extensively used. This section describes how these reduced models are obtained from the full, six dof, model described in the preceding sections of this appendix. A distinction is made between models that approximate the longitudinal and lateral vehicle dynamics, respectively. In addition, extending these reduced models to incorporate dynamic flap is discussed.

A.7.1. Three dof longitudinal

The active dofs in this model are surge, heave and pitch. The model is thus inactive in sway, roll and yaw. The necessary simplifications in each of the vehicle's subsystems are outlined in the following paragraphs.

Main rotor The assumed quasi-steady dynamics of the main rotor are fully described by Equations (A.40), (A.41), (A.43), (A.45), (A.47), (A.50), (A.55) and (A.58). In the longitudinal case, the direction of the airflow relative to the rotor is constrained such that $\psi_w = 0$, i.e., frames $\{E\}_s$ and $\{E\}_w$ coincide. Terms in listed the equations that include off-axis quantities (i.e., $\bar{p}$, θ_{1_c} and β_{1_s}) can be dropped. The airspeed relative to the rotor, V_∞, used in the definitions of μ and μ_z in Equation (A.33), includes only components due to u, w and q. The S-force given by Equation (A.47), the rotor torque described by Equation (A.55) and the lateral in-plane moment, L_e, defined in Equation (A.57) can all be omitted. Finally, the built-in shaft tilt, γ_s, is accounted for using T_{sh} from Equation (A.3). This is necessary both to express the components of V_∞ with respect to the shaft plane ($\{E\}_s$), as well as to express the rotor thrust, H-force and longitudinal in-plane moment in the vehicle's body frame ($\{E\}_b$).

Tail rotor The tail rotor force is omitted from the longitudinal model as it affects only the vehicle's sway and yaw dofs, both of which are inactive.

Fuselage The fuselage longitudinal and vertical drag forces, F^x_{fs} and ,F^z_{fs}, specified in Equation (A.75) and pitch moment, M_{fs}, defined in Equation (A.77), are both included in the longitudinal model. The lateral drag force and fuselage yaw moment are omitted.

Empennage The vertical force generated by the horizontal tailplane, F_{ht}, defined in Equation (A.84) is included in the model. The resulting moment around the center of gravity is also present. The lateral force and yaw moment generated by the vertical tailplane are omitted.

Equations of motion In the longitudinal three dof model, the active vehicle states are u, w, θ and q. As such, the rigid-body equations of motion defined in Equations (A.88) and (A.89) can be simplified to:

$$\dot{u} = \frac{F^x_{\mathrm{cg}}}{m} - g\sin\theta - qw, \quad \dot{w} = \frac{F^z_{\mathrm{cg}}}{m} + g\cos\theta + qu, \quad \dot{\theta} = q, \quad \dot{q} = \frac{M^y_{\mathrm{cg}}}{I_{yy}} \tag{A.91}$$

with the additional kinematic equations simplifying to:

$$\dot{x} = u\cos\theta + w\sin\theta \qquad \text{and} \qquad \dot{w} = -u\sin\theta + w\cos\theta \tag{A.92}$$

A.7.2. THREE DOF LATERAL

The active dofs in this model are sway, heave and roll. The model is thus inactive in surge, pitch and yaw. The necessary simplifications in each of the vehicle's subsystems are outlined in the following paragraphs.

Main rotor The main rotor in the lateral model is essentially identical to the one in the longitudinal model described in the previous section. The main difference is that, in the lateral case, the airflow relative to the rotor is constrained to $\psi_w = \pm 90°$. This means that V_∞ is affected only by v, w and p. In addition, from the perspective of the main rotor, the vehicle's *positive* pitch rate in the longitudinal model is equivalent to a *negative* roll rate in the lateral model, i.e., $\bar{q} = -\bar{p}$. Similarly, the longitudinal cyclic input θ_{1_s} is equivalent to θ_{1_c} and occurrences of β_{1_c} in the rotor force and moment equations become $-\beta_{1_s}$. Finally, in the lateral model, built-in shaft tilt is omitted.

Tail rotor Because the yaw dof is also inactive in the lateral model used in Chapter 6 of this thesis, the tail rotor has no utility and is therefore omitted. This also entails that there is no *sideforce* due to the tail rotor thrust and ensures symmetry between left and right sideward flight.

Fuselage The fuselage lateral and vertical drag forces, F^y_{fs} and ,F^z_{fs}, defined in Equation (A.75) are included in the lateral model. The longitudinal drag force and fuselage yaw moment are omitted.

Empennage The lateral force generated by the vertical tailplane, F_{vt}, defined in Equation (A.84), is included in the model. In the lateral model, the yaw moment around the center of gravity is omitted. The vertical force and pitch moment generated by the horizontal tailplane are also omitted.

Equations of motion In the lateral three dof model, the active vehicle states are v, w, ϕ and p. As such, the rigid-body equations of motion defined in Equations (A.88) and (A.89) can be simplified to:

$$\dot{v} = \frac{F^y_{\text{cg}}}{m} + g\sin\phi - pw, \quad \dot{w} = \frac{F^z_{\text{cg}}}{m} + g\cos\phi + pv, \quad \dot{\phi} = p, \quad \dot{p} = \frac{M^x_{\text{cg}}}{I_{xx}} \tag{A.93}$$

with the additional kinematic equations simplifying to:

$$\dot{y} = v\cos\phi - w\sin\phi \qquad \text{and} \qquad \dot{w} = v\sin\phi + w\cos\phi \tag{A.94}$$

A.7.3. INCORPORATING DYNAMIC FLAP

In Appendix A.2.6, the equations for dynamic blade flap were developed for the six dof model. The result, Equation (A.62), captures the regressing flap mode of the main rotor. In Chapter 6, the effect of this dynamic mode on the three dof lateral dynamics of the Bo-105 helicopter is investigated. Hence, the simplified main rotor model used in the reduced dof models presented in this section was extended to include the effect of dynamic blade flap. To this end, Equation (A.62) is further simplified by *only* including the equation for $\dot{\beta}_{1_c}$ (second row in Equation (A.62)) and omitting off-axis terms (i.e., $\bar{p}$ and β_{1_s} and β'_{1_s}):

$$\beta'_{1_c} = \frac{\dot{\beta}_{1_c}}{\Omega} = \frac{\gamma}{16}\left(-\theta_{1_s}(1+\frac{3}{2}\mu^2) + 2\mu(\mu_z - \lambda_0) + 2\mu(\frac{4}{3}\theta_0 + \theta_{tw}) + \beta_{1_c}(\frac{1}{2}\mu^2 - 1)\right) - (1+\epsilon)\bar{q} \tag{A.95}$$

Note that the derivative β'_{1_c} appearing in the first row of Equation (A.62) is a *damping* term that affects the off-axis response (through β'_{1_s}) of the rotor and is therefore inconsequential in the reduced dof models.

A.8. LINEAR MODELS

This appendix thus far has presented only *non-linear* models suitable for the analysis and prediction of helicopter dynamics in basic maneuvering flight. Throughout the thesis, however, *linear* models are extensively relied upon for, e.g., the detailed analysis of helicopter dynamics through *modal analysis* in Chapter 4 and in the novel *eigenmode distortion* methodology proposed in Chapter 5. This section will outline the applied linearization of the non-linear models, which includes both the rigid-body dynamics as well as the dynamic flap response.

A.8.1. LINEARIZATION OF THE RIGID BODY DYNAMICS

The rigid-body dynamics of the helicopter are captured in the translational and rotational equations of motion, see Equation (A.87) and Equation (A.89), respectively. Starting from these expressions, the following paragraphs will outline the necessary steps to obtain linear models for both the six dof as well as the reduced dof cases.

Six dof linear model In the six dof case, expressions for the translational body acceleration $\dot{u}$, $\dot{v}$ and $\dot{w}$ can be obtained from the evaluation of Equation (A.87). For example, the *longitudinal* body acceleration can be written as:

$$\dot{u} = \frac{F_{\mathrm{cg}^x}}{m} - g\sin\theta + rv - qw \tag{A.96}$$

This quantity can be linearized using the process of analytical *perturbation*, where each (non-constant) parameter that appears in the expression is written as the sum of a reference value, often termed *equilibrium*, and a small perturbation term. For the expression in Equation (A.96), this results in:

$$\dot{u}_e + \delta\dot{u} = \frac{F^x_{\mathrm{cg}_e} + \delta F^x_{\mathrm{cg}}}{m} - g\sin\left(\theta_e + \delta\theta\right) + (r_e + \delta r)(v_e + \delta v) - (q_e + \delta q)(w_e + \delta w) \tag{A.97}$$

where quantities subscripted with e denote the equilibria and the quantities preceded by δ constitute the perturbation terms. It is important to note that the equilibria are *constants* in the linear model. The next step in the linearization is to evaluate the right hand side of Equation (A.97). To this end, products of the quantities within brackets are expanded and the trigonometric relation:

$$\sin\left(\theta_e + \delta\theta\right) = \sin\theta_e\cos\delta\theta + \cos\theta_e\sin\delta\theta$$

is used to produce:

$$\begin{aligned}\dot{u}_e + \delta\dot{u} = {} & \frac{F^x_{\mathrm{cg}_e} + \delta F^x_{\mathrm{cg}}}{m} - g(\sin\theta_e\cos\delta\theta + \cos\theta_e\sin\delta\theta) + \\ & r_e v_e + r_e\delta v + \delta r v_e + \delta r\delta v - q_e w_e - q_e\delta w - \delta q w_e - \delta q\delta w\end{aligned} \tag{A.98}$$

This equation can be simplified by applying a number of assumptions. First, the non-linear model is assumed to be linearized from an *equilibrium* condition. In that case, $\dot{u}_e = 0$ and all terms on the right hand side that *only* contain equilibria (i.e. terms subscripted with e) will cancel each other out. Furthermore, because the perturbation terms are assumed to be small, $\cos\delta\theta \approx 1$ and $\sin\delta\theta \approx \delta\theta$. Moreover, products of perturbation terms can be neglected. The resulting expression describes the dynamics of $\delta\dot{u}$:

$$\delta\dot{u} = \frac{\delta F^x_{\mathrm{cg}}}{m} - g\cos\theta_e\delta\theta + v_e\delta r - w_e\delta q + r_e\delta v - q_e\delta w \tag{A.99}$$

It can be seen from Equation (A.99) that $\delta\dot{u}$ is linear in the perturbed vehicle states, but also depends on the *perturbed force* along the body x-axis. It is common to approximate the perturbed force as the *linear* sum of its partial derivatives with respect to the vehicle states and control inputs, multiplied by perturbed vehicle states and control inputs:

$$\begin{aligned}\frac{\delta F^x_{\text{cg}}}{m} &= \frac{\partial X}{\partial u}\delta u + \frac{\partial X}{\partial v}\delta v + \frac{\partial X}{\partial w}\delta w + \frac{\partial X}{\partial p}\delta p + \frac{\partial X}{\partial q}\delta q + \frac{\partial X}{\partial r}\delta r + \\ &\quad \frac{\partial X}{\partial \theta_0}\delta\theta_0 + \frac{\partial X}{\partial \theta_{1_c}}\delta\theta_{1_c} + \frac{\partial X}{\partial \theta_{1_s}}\delta\theta_{1_s} + \frac{\partial X}{\partial \theta_{0_{tr}}}\delta\theta_{0_{tr}} \\ &= X_u\delta u + X_v\delta v + X_w\delta w + X_p\delta p + X_q\delta q + \\ &\quad X_r\delta r + X_{\theta_0}\delta\theta_0 + X_{\theta_{1_c}}\delta\theta_{1_c} + X_{\theta_{1_s}}\delta\theta_{1_s} + X_{\theta_{0_{tr}}}\delta\theta_{0_{tr}}\end{aligned} \tag{A.100}$$

In Equation (A.100), X denotes the longitudinal force normalized by the vehicle mass, m. Also, partial derivatives of X with respect to the vehicle Euler angles ϕ, θ and ψ are zero (i.e., the force is independent of the vehicle attitude). Substitution of Equation (A.100) into Equation (A.99) finally yields:

$$\begin{aligned}\delta\dot{u} &= X_u\delta u + (X_v + r_e)\delta v + (X_w - q_e)\delta w - g\cos\theta_e\delta\theta + X_p\delta p + (X_q - w_e)\delta q + \\ &\quad (X_r + v_e)\delta r + X_{\theta_0}\delta\theta_0 + X_{\theta_{1_c}}\delta\theta_{1_c} + X_{\theta_{1_s}}\delta\theta_{1_s} + X_{\theta_{0_{tr}}}\delta\theta_{0_{tr}},\end{aligned} \tag{A.101}$$

from which it is seen that $\delta\dot{u}$ is fully linear. In an analogous fashion, equations for $\delta\dot{v}$ and $\delta\dot{w}$ can also be derived as:

$$\begin{aligned}\delta\dot{v} &= (Y_u - r_e)\delta u + Y_v\delta v + (Y_w + p_e)\delta w + g\cos\theta_e\cos\phi_e\,\delta\phi - g\sin\theta_e\sin\phi_e\,\delta\theta + \\ &\quad (Y_p + w_e)\delta p + Y_q\delta q + (Y_r - u_e)\delta r + Y_{\theta_0}\delta\theta_0 + Y_{\theta_{1_c}}\delta\theta_{1_c} + Y_{\theta_{1_s}}\delta\theta_{1_s} + Y_{\theta_{0_{tr}}}\delta\theta_{0_{tr}}\end{aligned} \tag{A.102}$$

and:

$$\begin{aligned}\delta\dot{w} &= (Z_u + q_e)\delta u + (Z_v - p_e)\delta v + Z_w\delta w - g\cos\theta_e\sin\phi_e\,\delta\phi - g\sin\theta_e\cos\phi_e\,\delta\theta + \\ &\quad (Z_p - v_e)\delta p + (Z_q + u_e)\delta q + Z_r\delta r + Z_{\theta_0}\delta\theta_0 + Z_{\theta_{1_c}}\delta\theta_{1_c} + Z_{\theta_{1_s}}\delta\theta_{1_s} + Z_{\theta_{0_{tr}}}\delta\theta_{0_{tr}},\end{aligned} \tag{A.103}$$

respectively. In Equations (A.101) and (A.103), Y and Z denote the lateral and vertical body forces normalized with the vehicle mass, m.

The rotational equations of motion can be linearized in an equivalent fashion starting with Equation (A.89). As can be seen from this equation, this also requires the inversion of the inertia tensor, J, given by Equation (A.90). Performing the inversion and evaluating the equation, it is obtained, for example, for the roll acceleration:

$$\dot{p} = \frac{I_{zz}}{I_{xx}I_{zz} - I_{xz}^2}M^x_{\text{cg}} + \frac{I_{xz}}{I_{xx}I_{zz} - I_{xz}^2}M^z_{\text{cg}} + \frac{I_{yy}I_{zz} - I_{zz}^2 - I_{xz}^2}{I_{xx}I_{zz} - I_{xz}^2}rq + \frac{I_{xz}(I_{xx} - I_{yy} + I_{zz})}{I_{xx}I_{zz} - I_{xz}^2}pq \tag{A.104}$$

Before perturbing Equation (A.104) analytically and linearizing the moments as was also done for the case of the translational accelerations, a number of convenience definitions are given, namely:

$$k_1 := \frac{I_{xz}(I_{xx} - I_{yy} + I_{zz})}{I_{xx}I_{zz} - I_{xz}^2} \qquad \text{and} \qquad k_2 := \frac{I_{yy}I_{zz} - I_{zz}^2 - I_{xz}^2}{I_{xx}I_{zz} - I_{xz}^2}, \tag{A.105}$$

as well as:

$$L_\square := \frac{I_{zz}}{I_{xx}I_{zz} - I_{xz}^2}\frac{\partial M_{\text{cg}}^x}{\partial \square} + \frac{I_{xz}}{I_{xx}I_{zz} - I_{xz}^2}\frac{\partial M_{\text{cg}}^z}{\partial \square}, \tag{A.106}$$

where $\square$ is used as a placeholder to signify partial derivatives of the moments with respect to the vehicle states and control inputs and L is the *normalized* roll moment around the body x-axis. Thus, analytically perturbing Equation (A.104) around an equilibrium condition, e, linearizing the roll and yaw moments in accordance with Equation (A.100), and using the definitions in Equations (A.105) and (A.106), the *linear* roll acceleration is obtained:

$$\begin{aligned}\delta\dot{p} = {} & L_u\delta u + L_v\delta v + L_w\delta w + (L_p + k_1 q_e)\delta p + (L_q + k_1 p_e + k_2 r_e)\delta q + (L_r + k_2 q_e)\delta r + \\ & L_{\theta_0}\delta\theta_0 + L_{\theta_{1_c}}\delta\theta_{1_c} + L_{\theta_{1_s}}\delta\theta_{1_s} + L_{\theta_{0_{tr}}}\delta\theta_{0_{tr}}\end{aligned} \tag{A.107}$$

In an analogous fashion, linear expressions for $\delta\dot{q}$ and $\delta\dot{r}$ can also be obtained. To this end, a number of additional convenience definitions are given:

$$k_3 := \frac{I_{xx}^2 - I_{xx}I_{yy} + I_{xz}^2}{I_{xx}I_{zz} - I_{xz}^2}, \quad k_4 := \frac{I_{zz} - I_{xx}}{I_{yy}} \quad \text{and} \quad k_5 := \frac{I_{xz}}{I_{yy}} \tag{A.108}$$

as well as:

$$M_\square := \frac{1}{I_{yy}}\frac{\partial M_{\text{cg}}^y}{\partial \square} \tag{A.109}$$

$$N_\square := \frac{I_{xx}}{I_{xx}I_{zz} - I_{xz}^2}\frac{\partial M_{\text{cg}}^z}{\partial \square} + \frac{I_{xz}}{I_{xx}I_{zz} - I_{xz}^2}\frac{\partial M_{\text{cg}}^x}{\partial \square}, \tag{A.110}$$

where $\square$ again signifies partial derivatives with respect to the vehicle states and control inputs and where M and N are the *normalized* pitch and yaw moments, respectively. Perturbing the pitch and yaw equations of motion, linearizing the roll and yaw moments, and using the definitions in Equations (A.108)–(A.110), it is obtained:

$$\begin{aligned}\delta\dot{q} = {} & M_u\delta u + M_v\delta v + M_w\delta w + (M_p + k_4 r_e - 2k_5 p_e)\delta p + M_q\delta q + (M_r + k_4 p_e + 2k_5 r_e)\delta r + \\ & M_{\theta_0}\delta\theta_0 + M_{\theta_{1_c}}\delta\theta_{1_c} + M_{\theta_{1_s}}\delta\theta_{1_s} + M_{\theta_{0_{tr}}}\delta\theta_{0_{tr}}\end{aligned} \tag{A.111}$$

and:

$$
\begin{aligned}
\delta\dot{r} = {} & N_u\delta u + N_v\delta v + N_w\delta w + (N_p + k_3 q_e)\delta p + (N_q + k_3 p_e - k_1 r_e)\delta q + (N_r - k_1 q_e)\delta r + \\
& N_{\theta_0}\delta\theta_0 + N_{\theta_{1_c}}\delta\theta_{1_c} + N_{\theta_{1_s}}\delta\theta_{1_s} + N_{\theta_{0_{tr}}}\delta\theta_{0_{tr}}
\end{aligned}
\tag{A.112}
$$

The partial derivatives of X, Y, Z, L, M and N with respect to the vehicle states and control inputs appearing in Equations (A.101)–(A.103) and Equations (A.107), (A.111) and (A.112) are typically referred to as the *stability* and *control* derivatives, respectively. Values for these derivatives can be obtained analytically or numerically from a non-linear vehicle model or derived from flight test data. In this thesis, it has been opted for simplicity sake to numerically compute the stability and control derivatives from the non-linear model. This has been done using the method of *central finite differences* [Olver, 2014].

To complete the linear model of the six dof vehicle dynamics, it is necessary to develop two more expressions, namely for $\delta\dot{\phi}$ and $\delta\dot{\theta}$, that appear in Equations (A.101)–(A.103). These can be obtained from the kinematic relation given in Equation (A.87). For example, the roll angle rate, $\dot{\phi}$, is a function of the angular rates expressed in the vehicle body frame:

$$
\dot{\phi} = p + q\ \sin\phi\tan\theta + r\ \cos\phi\tan\theta
$$

This equation is most conveniently linearized by evaluating its first-order Tailor series expansion around an equilibrium point, e, where the derivative $\dot{\phi}_e = 0$. In this way, the perturbed roll angle derivative can be written as:

$$
\delta\dot{\phi} = \left.\frac{\partial\dot{\phi}}{\partial p}\right|_e \delta p + \left.\frac{\partial\dot{\phi}}{\partial q}\right|_e \delta q + \left.\frac{\partial\dot{\phi}}{\partial r}\right|_e \delta r + \left.\frac{\partial\dot{\phi}}{\partial\phi}\right|_e \delta\phi + \left.\frac{\partial\dot{\phi}}{\partial\theta}\right|_e \delta\theta
\tag{A.113}
$$

where the notation $|_e$ is used to signify that the partial derivative is evaluated in the equilibrium state. Developing the partial derivates in Equation (A.113) and subsequently substituting the equilibrium state, it is obtained:

$$
\begin{aligned}
\delta\dot{\phi} = {} & \delta p + \sin\phi_e\tan\theta_e\,\delta q + \cos\phi_e\tan\theta_e\,\delta r + (q_e\cos\phi_e - r_e\sin\phi_e)\tan\theta_e\,\delta\phi + \\
& (q_e\sin\phi_e + r_e\cos\phi_e)\sec^2\theta_e\,\delta\theta
\end{aligned}
\tag{A.114}
$$

where $\sec^2\theta_e = 1/\cos^2\theta_e$. In a similar fashion, an expression for $\delta\dot{\theta}$ can also be obtained from its non-linear equivalent given by Equation (A.87):

$$
\delta\dot{\theta} = -(q_e\sin\phi_e + r_e\cos\phi_e)\ \delta\phi + \cos\phi_e\,\delta q - \sin\phi_e\,\delta r
\tag{A.115}
$$

Equations (A.114) and (A.115) complete the collection of equations necessary to capture the linear rigid-body dynamics. Note that an expression for the linearized heading angle derivative, $\dot{\psi}$, is not necessary because the vehicle dynamics are independent of ψ.

The linear system of equations given by Equations (A.101)–(A.103), Equations (A.107), (A.111) and (A.112) and Equations (A.114) and (A.115) can finally be formulated in *state-space* form:

$$
\delta\dot{\bar{x}} = A\,\delta\bar{x} + B\,\delta\bar{u},
\tag{A.116}
$$

where the *system* (A) and *input* (B) matrices are defined as:

$$A = \begin{bmatrix} X_u & X_v + r_e & X_w - q_e & 0 & -g\cos\theta_e & X_p & X_q - w_e & X_r + v_e \\ Y_v - r_e & Y_v & Y_w + p_e & g\cos\theta_e \times \cos\phi_e & -g\sin\theta_e \times \sin\phi_e & Y_p + w_e & Y_q & Y_r - u_e \\ Z_u + q_e & Z_v - p_e & Z_w & -g\cos\theta_e \times \sin\phi_e & -g\sin\theta_e \times \cos\phi_e & Z_p - v_e & Z_q + u_e & Z_r \\ 0 & 0 & 0 & (q_e\cos\phi_e - r_e\sin\phi_e) \times \tan\theta_e & (q_e\sin\phi_e + r_e\cos\phi_e) \times \sec^2\theta_e & 1 & \sin\phi\tan\theta_e & \cos\phi_e\tan\theta_e \\ 0 & 0 & 0 & -(q_e\sin\phi_e + r_e\cos\phi_e) & 0 & 0 & \cos\phi_e & -\sin\phi_e \\ L_u & L_v & L_w & 0 & 0 & L_p + k_1 q_e & L_q + k_1 p_e + k_2 r_e & L_r + k_2 q_e \\ M_u & M_v & M_w & 0 & 0 & M_p + k_4 r_e - 2k_5 p_e & M_q & M_r + k_4 p_e + 2k_5 r_e \\ N_u & N_v & N_w & 0 & 0 & N_p + k_3 q_e & N_q + k_3 p_e - k_1 r_e & N_r - k_1 q_e \end{bmatrix}$$

$$B = \begin{bmatrix} X_{\theta_0} & X_{\theta_{1_c}} & X_{\theta_{1_s}} & X_{\theta_{0_{tr}}} \\ Y_{\theta_0} & Y_{\theta_{1_c}} & Y_{\theta_{1_s}} & Y_{\theta_{0_{tr}}} \\ Z_{\theta_0} & Z_{\theta_{1_c}} & Z_{\theta_{1_s}} & Z_{\theta_{0_{tr}}} \\ 0 & 0 & 0 & 0 \\ 0 & 0 & 0 & 0 \\ L_{\theta_0} & L_{\theta_{1_c}} & L_{\theta_{1_s}} & L_{\theta_{0_{tr}}} \\ M_{\theta_0} & M_{\theta_{1_c}} & M_{\theta_{1_s}} & M_{\theta_{0_{tr}}} \\ N_{\theta_0} & N_{\theta_{1_c}} & N_{\theta_{1_s}} & N_{\theta_{0_{tr}}} \end{bmatrix} \tag{A.117}$$

and where the corresponding perturbed state and input vectors are:

$$\delta\bar{x} = \begin{bmatrix} \delta u & \delta v & \delta w & \delta\phi & \delta\theta & \delta p & \delta q & \delta r \end{bmatrix}^T, \qquad \delta\bar{u} = \begin{bmatrix} \delta\theta_0 & \delta\theta_{1_c} & \delta\theta_{1_s} & \delta\theta_{0_{tr}} \end{bmatrix}^T \tag{A.118}$$

Note that the definitions in Equation (A.117) comply with those found elsewhere, e.g., [Duke et al., 1988; Padfield, 2007].

Reduced dof linear models The reduced dof models described in Appendix A.7 are also linearized. These linear models can be obtained directly from the six dof linear model described by Equations (A.116)–(A.118).

For the three dof *longitudinal* model, the states δv, $\delta\phi$, δp and δr are eliminated from the perturbed state vector and ϕ_e, p_e and r_e are set to zero. Also, $\delta\theta_{1_c}$ and $\delta\theta_{0_{tr}}$ are eliminated from the perturbed input vector. The system and input matrices in Equation (A.116) then simplify to:

$$A = \begin{bmatrix} X_u & X_w - q_e & -g\cos\theta_e & X_q - w_e \\ Z_u + q_e & Z_w & -g\sin\theta_e & Z_q + u_e \\ 0 & 0 & 0 & 1 \\ M_u & M_w & 0 & M_q \end{bmatrix}, \qquad B = \begin{bmatrix} X_{\theta_0} & X_{\theta_{1_s}} \\ Z_{\theta_0} & Z_{\theta_{1_s}} \\ 0 & 0 \\ M_{\theta_0} & M_{\theta_{1_s}} \end{bmatrix} \tag{A.119}$$

with:

$$\delta\bar{x} = \begin{bmatrix} \delta u & \delta w & \delta\theta & \delta q \end{bmatrix}^T, \qquad \delta\bar{u} = \begin{bmatrix} \delta\theta_0 & \delta\theta_{1_s} \end{bmatrix}^T \tag{A.120}$$

For the three dof *lateral* model, the states δu, $\delta\theta$, δq and δr are eliminated from the perturbed state vector and θ_e, q_e and r_e are set to zero. Also, $\delta\theta_{1_s}$ and $\delta\theta_{0_{tr}}$ are eliminated from the perturbed input vector. The system and input matrices in Equation (A.116) then simplify to:

$$A = \begin{bmatrix} Y_v & Y_w + p_e & g\cos\phi_e & Y_p + w_e \\ Z_v - p_e & Z_w & -g\sin\phi_e & Z_p - v_e \\ 0 & 0 & 0 & 1 \\ L_v & L_w & 0 & L_p \end{bmatrix}, \qquad B = \begin{bmatrix} Y_{\theta_0} & Y_{\theta_{1_c}} \\ Z_{\theta_0} & Z_{\theta_{1_c}} \\ 0 & 0 \\ L_{\theta_0} & L_{\theta_{1_c}} \end{bmatrix} \tag{A.121}$$

with:

$$\delta\bar{x} = \begin{bmatrix} \delta v & \delta w & \delta\phi & \delta p \end{bmatrix}^T, \qquad \delta\bar{u} = \begin{bmatrix} \delta\theta_0 & \delta\theta_{1_c} \end{bmatrix}^T \tag{A.122}$$

A.8.2. LINEARIZATION OF THE DYNAMIC FLAP RESPONSE

In Chapter 6, an extended linear model of the three dof lateral dynamics of the Bo-105 helicopter is analyzed. This model includes the linearized effect of lateral dynamic flap and extends the linearized rigid-body dynamics described by Equations (A.121) and (A.122).

To incorporate the linearized blade flap dynamics, first the non-linear expression for the *longitudinal* dynamic flap given by Equation (A.95) is considered. An equivalent expression for the dynamic flap response in the reduced dof *lateral* model can be obtained by the following variable substitutions. These follow from the adopted sign conventions (see Figure A.4): $\beta_{1_c} = -\beta_{1_s}$, $\bar{p} = -\bar{q}$ and $\theta_{1_c} = \theta_{1_s}$. The resulting expression becomes:

$$\dot{\beta}_{1_s} = \frac{\Omega\gamma}{16}\left(\theta_{1_c}(1 + \frac{3}{2}\mu^2) - 2\mu(\mu_z - \lambda_0) - 2\mu(\frac{4}{3}\theta_0 + \theta_{tw}) + \beta_{1_s}(\frac{1}{2}\mu^2 - 1)\right) - (1+\epsilon)p \tag{A.123}$$

Before this expression can be linearized, it is necessary to expand the non-dimensional velocities μ, μ_z and λ_0. For the lateral case, the in-plane velocity at the hub is equal to $v + ph_{mr}$, where h_{mr} is the vertical distance of the main rotor from the vehicle c.g. The vertical velocity at the rotor hub is simply w, since shaft tilt is neglected in the lateral model. Hence:

$$\mu = \frac{v + h_{mr}p}{\Omega R}, \quad \mu_z = \frac{w}{\Omega R}, \quad \text{and} \quad \lambda_0 = \frac{v_0}{\Omega R}$$

Substituting these relations into Equation (A.123), one obtains:

$$\begin{aligned} \dot{\beta}_{1_s} = \frac{\Omega\gamma}{16}\Bigg(\theta_{1_c}\left(1 + \frac{3}{2}\left(\frac{v + h_{mr}p}{\Omega R}\right)^2\right) - 2\left(\frac{v + h_{mr}p}{\Omega R}\right)\left(\frac{w}{\Omega R} - \frac{v_0}{\Omega R}\right) - \\ 2\left(\frac{v + h_{mr}p}{\Omega R}\right)\left(\frac{4}{3}\theta_0 + \theta_{tw}\right) + \beta_{1_s}\left(\frac{1}{2}\left(\frac{v + h_{mr}p}{\Omega R}\right)^2 - 1\right)\Bigg) - (1+\epsilon)p \end{aligned} \tag{A.124}$$

This equation can be linearized around an equilibrium state, e, with the perturbed state vector as given in Equation (A.122). Thus, an expression for the perturbed lateral flap angle derivative can be defined:

$$
\begin{aligned}
\delta\dot{\beta}_{1_s} &:= B_v\delta v + B_w\delta w + B_p\delta p + B_{\beta_{1_s}}\delta\beta_{1_s} + B_{\theta_0}\delta\theta_0 + B_{\theta_{1_c}}\delta\theta_{1_c} \\
&= \left.\frac{\partial\dot{\beta}_{1_s}}{\partial v}\right|_e \delta v + \left.\frac{\partial\dot{\beta}_{1_s}}{\partial w}\right|_e \delta w + \left.\frac{\partial\dot{\beta}_{1_s}}{\partial p}\right|_e \delta p + \left.\frac{\partial\dot{\beta}_{1_s}}{\partial\beta_{1_s}}\right|_e \delta\beta_{1_s} + \left.\frac{\partial\dot{\beta}_{1_s}}{\partial\theta_0}\right|_e \delta\theta_0 \left.\frac{\partial\dot{\beta}_{1_s}}{\partial\theta_{1_c}}\right|_e \delta\theta_{1_c}
\end{aligned}
\tag{A.125}
$$

Subsequently evaluating the partial derivatives, it is obtained:

$$
\begin{aligned}
B_v &= -\frac{\gamma\left(\Omega R(6\theta_{tw} + 8\theta_{0_e}) - 3\beta_{1_{se}}(v_e + h_{mr}p_e) - 9\theta_{1_{ce}}(v_e + h_{mr}p_e) + 6(w_e - w_{0_e})\right)}{48\Omega R^2} \\
B_w &= -\frac{\gamma(v_e + h_{mr}p_e)}{8\Omega R^2} \\
B_p &= \frac{\gamma h_{mr}}{8R}\left(-\frac{(w_e - w_{0_e})}{\Omega R} - \left(\frac{4}{3}\theta_{0_e} + \theta_{tw}\right) + \frac{3\theta_{1_{ce}}(v_e + h_{mr}p_e)}{2\Omega R} + \frac{\beta_{1_{se}}(v_e + h_{mr}p_e)}{2\Omega R}\right) - \\
&\quad (1 + \epsilon) \\
B_{\beta_{1_s}} &= -\frac{\Omega\gamma}{16} + \frac{\gamma(v_e + h_{mr}p_e)^2}{32\Omega R^2} \\
B_{\theta_0} &= -\frac{\gamma(v_e + h_{mr}p_e)}{6R} \\
B_{\theta_{1_c}} &= \frac{\Omega\gamma}{16} + \frac{3\gamma(v_e + h_{mr}p_e)^2}{32\Omega R^2},
\end{aligned}
\tag{A.126}
$$

where the subscript e again denotes the values of the vehicle states and control inputs in the equilibrium condition. In order to augment the linearized flap angle dynamics to the three dof lateral rigid-body dynamics, it is also necessary to evaluate a number of additional stability derivates. These are the change of the (normalized) lateral and vertical forces as well as the roll moment with respect to the perturbed lateral flap angle. These extra stability derivatives are denoted by $X_{\beta_{1_s}}$, $Y_{\beta_{1_s}}$ and $L_{\beta_{1_s}}$, respectively, and are obtained numerically from the non-linear model like the other stability derivatives. In conclusion, the *four* dof lateral model can finally be defined as:

$$
A = \begin{bmatrix}
Y_v & Y_w + p_e & g\cos\phi_e & Y_p + w_e & Y_{\beta_{1_s}} \\
Z_v - p_e & Z_w & -g\sin\phi_e & Z_p - v_e & Z_{\beta_{1_s}} \\
0 & 0 & 0 & 1 & 0 \\
L_v & L_w & 0 & L_p & L_{\beta_{1_s}} \\
B_v & B_w & 0 & B_p & B_{\beta_{1_s}}
\end{bmatrix}, \qquad
B = \begin{bmatrix}
Y_{\theta_0} & Y_{\theta_{1_c}} \\
Z_{\theta_0} & Z_{\theta_{1_c}} \\
0 & 0 \\
L_{\theta_0} & L_{\theta_{1_c}} \\
B_{\theta_0} & B_{\theta_{1_c}}
\end{bmatrix},
\tag{A.127}
$$

with:

$$
\delta\bar{x} = \begin{bmatrix}\delta v & \delta w & \delta\phi & \delta p & \delta\beta_{1_s}\end{bmatrix}^T, \qquad \delta\bar{u} = \begin{bmatrix}\delta\theta_0 & \delta\theta_{1_c}\end{bmatrix}^T
\tag{A.128}
$$

and where $B_{\square}$ are defined as in Equation (A.126).

A.9. OTHER COMPONENTS

Two other components that are used in this dissertation have also been implemented, but are not necessarily part of the core flight dynamics model. These are a model of a Stability and Control Augmentation System (SCAS) and a turbulence model for external excitation.

A.9.1. SIMPLIFIED STABILITY AND CONTROL AUGMENTATION SYSTEM

In general, a SCAS of a helicopter can be very complex, consisting of many control loops to enable *rate damping* in its most basic form, but also advanced functionality such as *attitude* and *altitude* hold. The SCAS can also be used to *tailor* the vehicle's dynamic response, ranging from a simple *rate command* system, to *attitude command* and *translational rate command*. In this thesis, it is exemplified how the effect of a SCAS can be incorporated in a more simple form, e.g., for rudimentary HQs analysis, but also as part of EMD. The general form of such a SCAS (or, more correctly, Stability Augmentation System (SAS)) is illustrated in Figure A.9.

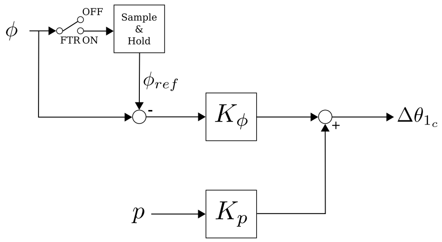

Figure A.9: Example schematic of the simple SCAS implemented in Draftsim.

This figure shows a control loop (for the roll axis) that can be generalized to all rotational vehicle dofs. First, the vehicle's rotational rates (i.e., p, q and r) are measured and multiplied by a gain, thereby capturing the effect of *rate feedback*. In Draftsim, the unit of this gain is $\%\,s/$rad. In conjunction, a separate loop measures the vehicle attitude (i.e., ϕ, θ or ψ), from which a constant (reference signal) is subtracted before the result is multiplied by a gain, thereby providing an *attitude feedback* mechanism. In Draftsim, the unit of this gain is $\%/rad$. The purpose of attitude feedback is to capture the effect of additional stability mechanism, often present in the form of (limited authority) attitude hold modes. The subtracted reference signal represents the *desired* attitude to be maintained. During manoeuvering flight, substantial attitude changes are necessary, thus the attitude feedback loop is *disabled* when the Force Trim Release (FTR) switch is enabled. The FTR switch is often located on the cyclic control stick. In the control scheme shown, the FTR also resamples the attitude reference used. The sum of the rate and attitude feedback channels are subsequently added directly to the pilot commanded inputs (i.e., in terms of % deflection of the control input).

The major advantage of the simplified control scheme in Figure A.9 is that its effect is straightforward to capture in *linear* form, without the necessity to include extra states. Instead, a *feedback gain* matrix is defined such that:

$$\bar{u}_{\text{sas}} = K\,\bar{x} \tag{A.129}$$

where $\bar{x}$ is the (measured) vehicle state. With a (linear) state vector and input as defined in Equation (A.118), the matrix K can be written as:

$$K = \begin{bmatrix} 0 & 0 & 0 & 0 & 0 & 0 & 0 & 0 \\ 0 & 0 & 0 & K_\phi & 0 & K_p & 0 & 0 \\ 0 & 0 & 0 & 0 & K_\theta & 0 & K_q & 0 \\ 0 & 0 & 0 & 0 & 0 & 0 & 0 & K_r \end{bmatrix} \tag{A.130}$$

Here, the first row contains zeros because no augmentation is present on the *collective* control. In addition, K_ψ has been omitted, as it is not a state in Equation (A.118). The effect of the SCAS can now be analysed using a vast number of tools available from linear control system design, including but not limited to the *pole placement* and *root-locus* methods. This is accomplished simply using the definition of the *augmented system* matrix (to replace the system matrix given by Equation (A.117)) as:

$$A_{\text{sas}} = A - B\,K \tag{A.131}$$

A.9.2. TURBULENCE MODEL

In actual flight, helicopters are perturbed by atmospheric turbulence. Particularly at low speed, close or in hover, pilot compensation for turbulence is often necessary. During an experiment conducted in Chapter 6 of this thesis, where a precision hover task was simulated, turbulence was added in order to make the task more representative and challenging. Although dedicated turbulence models for helicopters exist in literature (e.g.,[Dahl and Faulkner, 1978]), it was opted to implement a more simple model based on the Dryden turbulence spectra [Chalk et al., 1969], derived for fixed-wing aircraft. In fact, the transfer functions documented on the Mathworks website were implemented in Draftsim [MathWorks, 2017]. As a further simplification, it was also opted to only implement turbulence along the horizontal (i.e., u) and vertical (i.e., w) axes of the vehicle's body frame.

The Dryden turbulence spectra are obtained by passing band-limited white noise through so-called *forming filters*. These forming filters vary depending on the longitudinal, lateral and vertical dofs of the vehicle. For the longitudinal and vertical dof, the forming filters are defined as:

$$H_u(s) = \sigma_u \sqrt{\frac{2L_u}{\pi V}} \frac{1}{1 + \frac{L_u}{V}s} \quad \text{and} \quad H_w(s) = \sigma_w \sqrt{\frac{L_w}{\pi V}} \frac{1 + \frac{\sqrt{3}L_w}{V}s}{1 + \frac{L_w}{V}s} \tag{A.132}$$

In this equation, L_u and L_w are the *turbulence scale lengths*, $sigma_u$ and $sigma_w$ are the *turbulence intensities* and V is the aircraft (reference) speed. For low altitudes (below 1000 ft), these quantities can be obtained from the following relations [Chalk et al., 1969]:

$$L_u = \frac{h}{(0.177 + 8.23 \cdot 10^{-4}h)^{1.2}} \quad \text{and} \quad L_w = h \tag{A.133}$$

with h defined as the altitude in *feet*, and:

$$\sigma_u = \frac{\sigma_w}{(0.177 + 8.23 \cdot 10^{-4}h)^{0.4}} \quad \text{and} \quad \sigma_w = 0.1W_{20} \tag{A.134}$$

In Equation (A.134), W_{20} represents the wind speed at an altitude of 20 ft, with common values of 15 knots for light, 30 knots for moderate and 45 knots for severe turbulence, respectively [MathWorks, 2017]. The parameters in Equations (A.133) and (A.134) were chosen such to be representative of a light aircraft in moderate turbulence (i.e., W_{20} = 30 knots) at an airspeed of 120 knots and at an altitude of 500 ft. The turbulence velocity components are computed in real-time, and the result are added to the vehicle's body u and w components *before* evaluating the forces and moments, equations of motion and invoking the solver.

B

AH-64 DYNAMIC STABILITY ANALYSIS AND VERIFICATION

Like the Bo-105 helicopter used in Chapter 4 of this thesis, the AH-64 was also linearized in order to study its flight dynamics in more detail. The analysis focuses on stability derivatives and characteristic dynamics modes in hover, although some predicted trends with increasing airspeed were also compute. To this end, the stability derivatives corresponding to the AH-64 in hover were computed using Draftsim and compared to public reference data. This reference data contain stability derivatives in hover derived both from actual flight (from Schroeder et al. [1991]) as well as using Boeing's proprietary Flyrt model (from Hossein Mansur [1995]).

B.1. STABILITY DERIVATIVES

The computed stability derivatives are shown side-by-side in Table B.1. Note that the Flyrt and experimental data shown in this table correspond to an *unaugmented* helicopter (that is, the so-called DASE, Digital Automatic Stabilization Equipment, in the AH-64 was turned off). A number of interesting insights can be gained from Table B.1.

First, notice that the middle column corresponding to the flight test data contains many zeros. These are mostly cross-axis derivatives that were, according to Hossein Mansur [1995], eliminated during the determination of the model structure. As a consequence, it appears the estimated stability derivatives from the experimental data pertain to a mostly *uncoupled* model. When comparing the non-zero entries to values predicted by Flyrt and Draftsim, both similarities and discrepancies emerge. For example, some derivatives such as X_u, Z_w and M_q match quite well in terms of both sign and order of magnitude.

Others, however, such as X_p, Y_v, Y_p and L_q show great differences in magnitude and/or sign as compared to the flight test data. In some cases, the values predicted by Draftsim and Flyrt match remarkably well, see, e.g., X_p, Y_v and N_v, while differing substantially when compared to the experimental data. In others, however, the two models also show great discrepancies when compared to one another. A notable example is Y_p, where the Draftsim prediction is different by more than an order of magnitude. While Flyrt is also a factor of two off when compared to the experimental data in this case, in other cases (e.g., N_p and N_r) Flyrt matches the experimental data well while Draftsim appears to be a factor of 2-3 off. There are also cases where Flyrt exhibits somewhat peculiar results. For example, X_q and Z_r in case of Flyrt are quite significant in magnitude, while the corresponding values in Draftsim are orders of magnitude smaller. Moreover, these derivatives are eliminated in the experimental data.

A final interesting observation is that, as compared to both the experimental data and Flyrt, Draftsim exhibits stronger inter-axis coupling. This is evident primarily from the values of the moment derivatives L_p, L_q, M_q and M_p. In Draftsim, the contribution of the on-axis derivatives (i.e. M_q and L_p) is smaller than the off-axis derivatives (i.e., M_p and L_q). This result does not match with the flight data or the derivatives predicted by Flyrt, for which in both cases the on-axis derivatives are larger in magnitude than the off-axis derivatives.

Table B.1: AH-64 stability derivatives in hover compared with reference data. Flyrt and experimental data from Hossein Mansur [1995] and Schroeder et al. [1991], respectively.

Derivative	Flyrt	Flight	Draftsim	Units
X_u	-0.0332	-0.02	-0.0198	1/s
X_v	0.0121	0	-0.0135	
X_w	0.0279	0	0.0248	
X_p	-0.441	0.685	-0.523	m/s rad
X_q	3.023	0	0.0698	
X_r	-0.0322	0	-0.0454	
Y_u	-0.00833	0	0.0150	1/s
Y_v	-0.0502	-0.279	-0.0318	
Y_w	-0.0174	0	-0.00512	
Y_p	-2.938	-1.56	-0.104	m/s rad

Table B.1: AH-64 stability derivatives in hover compared with reference data. Flyrt and experimental data from Hossein Mansur [1995] and Schroeder et al. [1991], respectively (cont.).

Derivative	Flyrt	Flight	Draftsim	Units
Y_q	-1.203	0	-0.529	
Y_r	0.4704	0	0.117	
Z_u	0.0045	0	0.0227	1/s
Z_v	-0.0039	0	-0.0135	
Z_w	-0.2921	-0.122	-0.315	
Z_p	-0.2241	0	-0.0771	m/s rad
Z_q	0.1199	0	0.00748	
Z_r	2.171	0	0.00644	
L_u	-0.0069	0	0.0735	rad/s m
L_v	-0.0171	-0.00425	-0.0737	
L_w	-0.0115	0	0.00544	
L_p	-2.424	-1.828	-1.268	1/s
L_q	-0.960	1.04	-1.665	
L_r	-0.078	0	0.0235	
M_u	-0.0037	0.000844	0.00976	rad/s m
M_v	-0.0014	0.00710	0.0121	
M_w	-0.0006	-0.00514	0.000376	
M_p	0.0875	-0.227	0.276	1/s
M_q	-0.552	-0.419	-0.206	
M_r	0.0116	-0.09	0.0239	
N_u	-0.0018	0	0.00902	rad/s m
N_v	0.0066	0.00301	0.00674	
N_w	-0.0007	0	0.00475	
N_p	-0.338	-0.309	-0.125	1/s
N_q	-0.111	0	-0.213	
N_r	-0.318	-0.270	-0.138	

B.2. DYNAMIC MODES

It is of interest to investigate the *impact* of these discrepancies on the predicted characteristics of the vehicle's *dynamic modes*. To this end, the stability derivatives listed in Table B.1 are used to construct corresponding linear system matrices (see App. B). Note that, in this process, the vehicle's state in trim, mass and inertial properties are also necessary. While these are known exactly for Draftsim, they are not all known in case of the experimental data and Flyrt. To resolve this issue, the trim, mass and inertial properties corresponding to Draftsim were simply used in the contruction of the system matrices for the experimental data and Flyrt as well. While this may not be fully accurate, it is assumed that the effect of (minor) mismatches in trim, mass and inertial properties between the different data sets is negligible. The resulting eigenvalues, together with a characterization of the corresponding vehicle modes, are shown in Figure B.1. This figure also shows Draftsim trends with increasing airspeed (up to 60 knots).

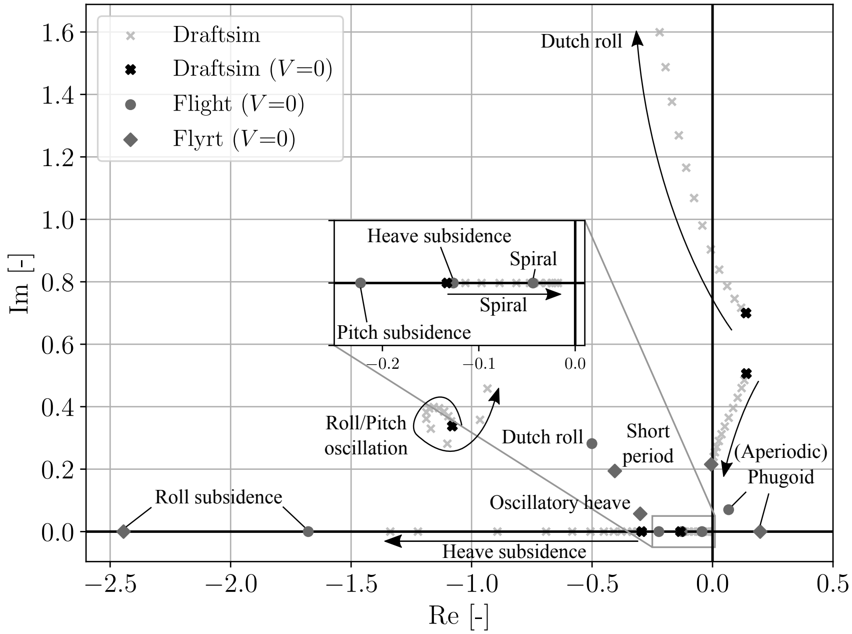

Figure B.1: AH-64 eigenvalues compared with reference data.

From this figure, it becomes apparent that the discrepancies between the stability derivatives that emerge from Table B.1 also result in vastly different modes. Based on this figure, it appears that both Draftsim and Flyrt fail to accurately describe the dynamic properties of the AH-64 in hover. In hover, the experimental data dictates that the AH-64 exhibits the classic rotorcraft modes, i.e., the phugoid, pitch/heave/roll subsidences and Dutch roll. While Draftsim also predicts the phugoid, Dutch roll and heave subsidence modes, the roll and pitch subsidence are replaced by a combined and oscillatory roll/pitch mode. The latter mode is a common occurence for rotorcraft with an articulated rotor at low speed. An example is the Puma helicopter described in Padfield [2007], which also happens to be similar to the AH-64 in terms of mass and size. The fact that the oscillatory roll/pitch mode is absent in the experimental data could be a consequence of the explicit elimination of the many (cross-)derivatives.

Regardless of differences in the *type* of mode (i.e., oscillatory vs. non-oscillatory), the other classic modes predicted by Draftsim also do not match well with the experimental data in terms of stability, frequency and/or time constant. For example, while the phugoid mode predicted by Draftsim is unstable, its frequency in hover is a lot higher than dictated by the experimental data. The same can be noted about the time constants of the spiral and heave subsidence modes, which appear to be significantly lower. Furthermore, the Dutch roll, an oscillatory mode, is predicted to be unstable while the experimental data dictates a stable mode at somewhat lower frequency and with improved damping. An unstable Dutch roll, however, is also seen in the Puma helicopter at lower airspeeds and is therefore not uncommon for rotorcraft with an articulated rotor [Padfield, 2007]. At higher airspeeds, the classic modes predicted by Draftsim develop in a similar fashion as already seen for the Bo-105 helicopter in Figure 4.4. Most notably, the Dutch roll increases in frequency and crosses over to the stable region of the complex plane, while the phugoid also approaches the imaginary axis. However, the roll/pitch oscillation and heave subsidence persists at higher airspeeds and do not evolve into non-oscillatory roll subsidence and short period modes, as described in [Padfield, 2007] for the Puma helicopter.

The discussion in the previous paragraphs is a testimony of the level of uncertainty in helicopter flight dynamics models and the apparent impact thereof on the predicted vehicle dynamics. Apparently, these can differ substantially between different descriptions of the same aircraft in the same condition. A possible explanation for the discrepancies found in the specific case of the AH-64 could be the presence of system dynamics not modelled in Draftsim and/or Flyrt, e.g., actuators or the BUCS. Nonetheless, an important contributing factor can also be found in the many differing assumptions underlying models of different origins. For example, the experimental data was obtained under the assumption that the longitudinal and lateral vehicle dynamics are uncoupled, while first principles models like Flyrt and Draftsim are derived under a different set of physical (and often non-physical) assumptions.

B.3. MODE SHAPES

The apparent discrepancies between Flyrt and the flight data, on the other hand, are more difficult to characterize. While the Flyrt modes appear closer in vicinity to the modes corresponding to the experimental data, their type is rather unconventional. While, like Draftsim, three oscillatory modes and two non-oscillatory modes are present, their *shapes* differ significantly. To illustrate this, Table B.2 shows the Flyrt eigenvalues together with the magnitudes of the individual states in each of the corresponding eigenvectors. For illustrative purposes, an identical table is also included for Draftsim and the flight data in Tables B.3 and B.4, respectively. The magnitudes listed in these tables are a measure of the contribution of each model state in the corresponding mode and, therefore, provide insight about the mode *shape*.

Table B.2: Magnitude of states in each eigenvector per eigenvalue in case of Flyrt (in hover, from Hossein Mansur [1995]).

Eigenvalue	u	v	w	ϕ	θ	p	q	r
-2.4	0.094	0.93	0.013	0.13	0.0051	0.33	0.014	0.048
0.20	0.99	0.11	0.031	0.0023	0.025	0.00016	0.0048	0.0038
-0.0056+0.22i	0.18	0.97	0.13	0.023	0.0041	0.0066	0.0018	0.024
-0.41+0.19i	0.95	0.26	0.19	0.011	0.037	0.0048	0.016	0.0064
-0.30+0.057i	0.32	0.29	0.90	0.0091	0.0077	0.0019	0.0033	0.027

Table B.3: Magnitude of states in each eigenvector per eigenvalue in case of Draftsim (in hover).

Eigenvalue	u	v	w	ϕ	θ	p	q	r
-1.1+0.32i	0.43	0.88	0.099	0.098	0.042	0.11	0.046	0.013
0.14+0.68i	0.16	0,98	0.045	0.070	0.013	0.049	0.0090	0.016
0.14+0.51i	0.62	0.78	0.062	0.043	0.034	0.024	0.017	0.019
-0.32	0.047	0.049	1.0	0.0022	0.0041	0.0015	0.00025	0.027
-0.13	0.75	0.42	0.10	0.010	0.0096	0.039	0.018	0.49

Table B.4: Magnitude of states in each eigenvector per eigenvalue in case of flight reference data (in hover, from Schroeder et al. [1991]).

Eigenvalue	u	v	w	ϕ	θ	p	q	r
-1.7	0.18	0.96	0.017	0.11	0.019	0.18	0.030	0.037
-0.50+0.28i	0.63	0.77	0.041	0.026	0.035	0.014	0.02	0.013
0.067+0.070i	0.99	0.12	0.037	0.0045	0.011	0.00045	0.0011	0.0011
-0.22	0.90	0.40	0.14	0.0014	0.018	0.0052	0.0064	0.059
-0.044	0.98	0.17	0.045	0.0041	0.0024	0.00041	0.0	0.0028
-0.13	0.63	0.44	0.64	0.0066	0.0067	0.0019	0.0014	0.013

From Table B.2, it becomes evident that Flyrt exhibits one unstable and non-oscillatory mode, where the dominant states appear to be u, θ and, to a lesser extent, q. This division of dominant states is typical for the phugoid mode (see Tab. 5). Hence, the naming "aperiodic phugoid" indicated in Figure B.1 for this mode predicted by Flyrt. There is a mode located almost on the imaginary axis, where the dominant states appear to be v, ϕ, p and r. This is a characteristic of the Dutch roll mode. The remaining modes appear to be an oscillatory motion dominated by heave, where the dominant states are w and r, a short period with dominant states u and q and a non-oscillatory roll subsidence dominated by v and p.

B.4. CONCLUSION

As shown, predictions from basic models of rotorcraft flight dynamics can differ considerably for identical aircraft in the same flight conditions. This holds true for models derived directly from flight test data, where critical assumptions are made in the identification process, as well as first principles models like Flyrt and Draftsim, where simplifying physical (and often non-physical) assumptions are necessary in the model development process. When such models are subsequently applied for design and development of rotorcraft and related systems, or more closely related to the topic of this thesis, for flight simulation purposes, such model limitations are important to keep in mind.

C

THE EIGENMODE DISTORTION METHOD: COMPLETE MATRICES

Chapter 5 of this thesis presented the theory underlying the novel Eigenmode distortion (EMD) method developed in this dissertation. The main idea behind EMD is to couple linear *models of the vehicle and Motion Cueing Algorithm (MCA) dynamics, after which a modal coordinate transformation can be applied to reveal the* distortion *of vehicle modes due to the MCA. However, for the sake of brevity, many (full) equations were omitted from Chapter 5. These equations are included in this appendix.*

C.1. COUPLED VEHICLE-MCA DYNAMICS

Recall Equation (5.11), the definition of a prospective coupled model to describe the *linear* vehicle and MCA dynamics:

$$
\begin{aligned}
\delta\dot{\bar{x}}^c &= \begin{bmatrix} A^p & 0 \\ A^{pm} & A^m \end{bmatrix} \begin{bmatrix} \delta\bar{x}^p \\ \delta\bar{x}^m \end{bmatrix} + \begin{bmatrix} B^p \\ B^m \end{bmatrix} \delta\bar{u}^p = A^c \delta\bar{x}^c + B^c \delta\bar{u}^p \\
\delta\bar{y}^c &= \begin{bmatrix} C^p & 0 \\ C^{pm} & C^m \end{bmatrix} \begin{bmatrix} \delta\bar{x}^p \\ \delta\bar{x}^m \end{bmatrix} + \begin{bmatrix} D^p \\ D^m \end{bmatrix} \delta\bar{u}^p = C^c \delta\bar{x}^c + D^c \delta\bar{u}^p
\end{aligned}
$$

with (see Equations (5.56) and (5.57)):

$$
\begin{aligned}
\delta\bar{x}^p &= \begin{bmatrix} \delta u & \delta v & \delta w & \delta\phi & \delta\theta & \delta p & \delta q & \delta r \end{bmatrix}^T \\
\delta\bar{u}^p &= \begin{bmatrix} \delta\theta_0 & \delta\theta_{1_c} & \delta\theta_{1_s} & \delta\theta_{0_{tr}} \end{bmatrix}^T \\
\delta\bar{y}^p &= \begin{bmatrix} \delta f_x & \delta f_y & \delta f_z & \delta p & \delta q & \delta r \end{bmatrix}^T
\end{aligned}
$$

and (see Equations (5.53) and (5.54)):

$$
\begin{aligned}
\delta\bar{x}^m &= \begin{bmatrix} \bar{q}_{1_x}^T & \bar{q}_{1_y}^T & \bar{q}_{1_z}^T & \bar{q}_{2_x}^T & \bar{q}_{2_y}^T & \bar{q}_{3_p}^T & \bar{q}_{3_q}^T & \bar{q}_{3_r}^T & (\bar{\Phi}^s)^T \end{bmatrix}^T \\
\delta\bar{y}^m &= \begin{bmatrix} \delta f_x^s & \delta f_y^s & \delta f_z^s & \delta p^s & \delta q^s & \delta r^s \end{bmatrix}^T
\end{aligned}
$$

Chapter 5 elaborated on the role and derivation of each parameter and (sub)matrix appearing in these equations. All matrices superscripted with p pertain to the *vehicle* dynamics and, for applications described in this thesis, apply solely to helicopters. Appendix A.8 already presented expressions for A^p and B^p corresponding to the six degrees-of-freedom as well separate lateral and longitudinal degree-of-freedom models (see Appendix A, Equations (A.117), (A.119) and (A.121)). However, C^p and D^p will be addressed here, as these extract the *human-perceived quantities* contained in these models. The matrices superscripted with m pertain to the *MCA* dynamics, while matrices superscripted pm are the *coupling* terms. Each of these listed matrices will be described in more detail in the following sections.

C.2. MATRICES C^p AND D^p

Equation (A.117) governs the linear helicopters dynamics, but it does not excplicity contain all human-perceived quantities of interest. This is only true for the angular rates (i.e., δp, δq and δr), which appear directly in the defined vehicle state vector $\delta\bar{x}^p$ (see Equation (A.118)). The specific forces (i.e., δf_x, δf_y and δf_z) can be obtained from Equation (5.59). Thus, to obtain the output vector $\delta\bar{y}^p$, C^p and D^p can be defined:

$$C^p = \begin{bmatrix} X_u & X_v & X_w & 0 & 0 & X_p & X_q & X_r \\ Y_u & Y_v & Y_w & 0 & 0 & Y_p & Y_q & Y_r \\ Z_u & Z_v & Z_w & 0 & 0 & Z_p & Z_q & Z_r \\ 0 & 0 & 0 & 0 & 0 & 1 & 0 & 0 \\ 0 & 0 & 0 & 0 & 0 & 0 & 1 & 0 \\ 0 & 0 & 0 & 0 & 0 & 0 & 0 & 1 \end{bmatrix}, \quad D^p = \begin{bmatrix} X_{\delta_0} & X_{\delta_{1_c}} & X_{\delta_{1_s}} & X_{\delta_{0_{tr}}} \\ Y_{\delta_0} & Y_{\delta_{1_c}} & Y_{\delta_{1_s}} & Y_{\delta_{0_{tr}}} \\ Z_{\delta_0} & Z_{\delta_{1_c}} & Z_{\delta_{1_s}} & Z_{\delta_{0_{tr}}} \\ 0 & 0 & 0 & 0 \\ 0 & 0 & 0 & 0 \\ 0 & 0 & 0 & 0 \end{bmatrix} \tag{C.1}$$

C.3. MATRICES A^m AND C^m

The matrix A^m governs the *internal* dynamics of the CWA and is defined in relation to the motion state vector $\delta\bar{x}^m$. Given the dynamics of the various filters contained in the CWA (see Equations (5.34), (5.35), (5.38), (5.50) and (5.52)), A^m can be defined as:

$$A^m = \left[\begin{array}{ccc|cc|ccc|c} A_{1_x} & 0 & 0 & 0 & 0 & 0 & 0 & 0 & \begin{array}{ccc} 0 & 0 & 0 \\ 0 & -g & 0 \end{array} \\ 0 & A_{1_y} & 0 & 0 & 0 & 0 & 0 & 0 & \begin{array}{ccc} 0 & 0 & 0 \\ g & 0 & 0 \end{array} \\ 0 & 0 & A_{1_z} & 0 & 0 & 0 & 0 & 0 & 0 \\ \hline 0 & 0 & 0 & A_{2_x} & 0 & 0 & 0 & 0 & 0 \\ 0 & 0 & 0 & 0 & A_{2_y} & 0 & 0 & 0 & 0 \\ \hline 0 & 0 & 0 & 0 & 0 & A_{3_p} & 0 & 0 & 0 \\ 0 & 0 & 0 & 0 & 0 & 0 & A_{3_q} & 0 & 0 \\ 0 & 0 & 0 & 0 & 0 & 0 & 0 & A_{3_r} & 0 \\ \hline 0 & 0 & 0 & 0 & 0 \quad -1/g & C_{3_p} & 0 & 0 & 0 \\ 0 & 0 & 0 & 0 \quad 1/g & 0 & 0 & C_{3_q} & 0 & 0 \\ 0 & 0 & 0 & 0 & 0 \quad 0 & 0 & 0 & C_{3_r} & 0 \end{array}\right] \tag{C.2}$$

Note that, without loss of generality, this formulation assumes *second-order* low- and high-pass filters are used in the CWA as also outlined in Chapter 5. Thus, $A_{1_\square}$, $A_{2_\square}$ and $A_{3_\square}$ are 2×2 matrices, whereas $C_{3_\square}$ are 1×2. For clarity, the rows and columns corresponding to the different CWA elements have been delineated. The entries at the top of the fourth delineated column containing the gravitational acceleration represent the terms $-g\delta\theta^s$ and $g\phi^s$, respectively, appearing in Equation (5.35). In addition, the entries at the bottom of the second delineated column represent the terms $-\delta\dot{f}_y^s/g$ and $\delta\dot{f}_x^s/g$, respectively, appearing in Equation (5.52).

The matrix C^m extracts the contribution of the elements in $\delta\bar{x}^m$ (i.e., the CWA state) to the CWA-filtered specific forces and rotational rates. As a result, C^m can be written as:

$$C^m = \left[\begin{array}{ccc|cc|ccc|c}
C_{1_x} & 0 & 0 & 0 & 0 & & \cdots & & 0 \\
0 & C_{1_y} & 0 & 0 & 0 & & \cdots & & 0 \\
0 & 0 & C_{1_z} & 0 & 0 & & \cdots & & 0 \\
\hline
0 & 0 & 0 & 0 & 0 \quad -1/g & C_{3_p} & 0 & 0 & 0 \\
0 & 0 & 0 & 0 \quad 1/g & 0 & 0 & C_{3_q} & 0 & 0 \\
0 & 0 & 0 & 0 & 0 & 0 & 0 & C_{3_r} & 0
\end{array}\right] \tag{C.3}$$

Note that $C_{1_\square}$, like $C_{3_\square}$, are also 1×2 matrices.

C.4. MATRICES A^{pm} AND B^m

The matrices A^{pm} and B^m define the inputs to the linearized CWA, which are the vehicle specific forces and rotational rates, scaled by the motion gains $K_\square$. For *second-order* filters, A^{pm} can be written as:

$$A^{pm} = \left[\begin{array}{cccccccc}
0 & 0 & 0 & 0 & 0 & 0 & 0 & 0 \\
K_xX_u & K_xX_v & K_xX_w & 0 & 0 & K_xX_p & K_xX_q & K_xX_r \\
0 & 0 & 0 & 0 & 0 & 0 & 0 & 0 \\
K_yY_u & K_yY_v & K_yY_w & 0 & 0 & K_yY_p & K_yY_q & K_yY_r \\
0 & 0 & 0 & 0 & 0 & 0 & 0 & 0 \\
K_zZ_u & K_zZ_v & K_zZ_w & 0 & 0 & K_zZ_p & K_zZ_q & K_zZ_r \\
\hline
0 & 0 & 0 & 0 & 0 & 0 & 0 & 0 \\
K_xX_u & K_xX_v & K_xX_w & 0 & 0 & K_xX_p & K_xX_q & K_xX_r \\
0 & 0 & 0 & 0 & 0 & 0 & 0 & 0 \\
K_yY_u & K_yY_v & K_yY_w & 0 & 0 & K_yY_p & K_yY_q & K_yY_r \\
\hline
0 & 0 & 0 & 0 & 0 & 0 & 0 & 0 \\
0 & 0 & 0 & 0 & 0 & K_p & 0 & 0 \\
0 & 0 & 0 & 0 & 0 & 0 & 0 & 0 \\
0 & 0 & 0 & 0 & 0 & 0 & K_q & 0 \\
0 & 0 & 0 & 0 & 0 & 0 & 0 & 0 \\
0 & 0 & 0 & 0 & 0 & 0 & 0 & K_r \\
\hline
0 & 0 & 0 & 0 & 0 & K_p & 0 & 0 \\
0 & 0 & 0 & 0 & 0 & 0 & K_q & 0 \\
0 & 0 & 0 & 0 & 0 & 0 & 0 & K_r
\end{array}\right] \tag{C.4}$$

whereas B^m is:

$$B^m = \left[\begin{array}{cccc}
0 & 0 & 0 & 0 \\
K_x X_{\delta_0} & K_x X_{\delta_{1_c}} & K_x X_{\delta_{1_s}} & K_x X_{\delta_{0_{tr}}} \\
0 & 0 & 0 & 0 \\
K_y Y_{\delta_0} & K_y Y_{\delta_{1_c}} & K_y Y_{\delta_{1_s}} & K_y Y_{\delta_{0_{tr}}} \\
0 & 0 & 0 & 0 \\
K_z Z_{\delta_0} & K_z Z_{\delta_{1_c}} & K_z Z_{\delta_{1_s}} & K_z Z_{\delta_{0_{tr}}} \\
\hline
B_{2_x} K_x X_{\delta_0} & B_{2_x} K_x X_{\delta_{1_c}} & B_{2_x} K_x X_{\delta_{1_s}} & B_{2_x} K_x X_{\delta_{0_{tr}}} \\
B_{2_y} K_y Y_{\delta_0} & B_{2_y} K_y Y_{\delta_{1_c}} & B_{2_y} K_y Y_{\delta_{1_s}} & B_{2_y} K_y Y_{\delta_{0_{tr}}} \\
\hline
0 & 0 & 0 & 0 \\
\vdots & \vdots & \vdots & \vdots \\
0 & 0 & 0 & 0 \\
\hline
0 & 0 & 0 & 0 \\
0 & 0 & 0 & 0 \\
0 & 0 & 0 & 0
\end{array}\right] \tag{C.5}$$

Note that, in Equation (C.5), B_{2_x} and B_{2_y} are 1 × 2 vectors according to the definition in Equation (5.38).

C.5. MATRICES C^{pm} AND D^m

The matrices C^{pm} and D^m complete the formulation of the coupled vehicle and CWA dynamics in linear form. They represent the contribution of the *vehicle* state to both the unfiltered and CWA-filtered specific forces and rotational rates in $\delta\bar{y}^p$ and $\delta\bar{y}^m$, respectively. These matrices follow directly from C^p and D^p in Equation (C.1):

$$C^{pm} = \begin{bmatrix} K_x & 0 & 0 & 0 & 0 & 0 \\ 0 & K_y & 0 & 0 & 0 & 0 \\ 0 & 0 & K_z & 0 & 0 & 0 \\ 0 & 0 & 0 & K_p & 0 & 0 \\ 0 & 0 & 0 & 0 & K_q & 0 \\ 0 & 0 & 0 & 0 & 0 & K_r \end{bmatrix} \cdot C^p, \quad D^m = \begin{bmatrix} K_x & 0 & 0 & 0 & 0 & 0 \\ 0 & K_y & 0 & 0 & 0 & 0 \\ 0 & 0 & K_z & 0 & 0 & 0 \\ 0 & 0 & 0 & 0 & 0 & 0 \\ 0 & 0 & 0 & 0 & 0 & 0 \\ 0 & 0 & 0 & 0 & 0 & 0 \end{bmatrix} \cdot D^p \tag{C.6}$$

C.6. THE EFFECT OF CHANGES IN THE VEHICLE DYNAMICS

Chapter 6 in this dissertation considered the effect of changes in the vehicle dynamics in relation to motion cueing using the EMD method. To enable these analyses, several changes to the matrices presented in the preceding sections are necessary.

Additional states Changes to the vehicle dynamics become apparent first and foremost through changes in the matrix A^p. This was already shown in Appendix A.8.2, where the rotor flapping dynamics were linearized and augmented to the linearized rigid-body dynamics. From this derivation, it became apparent that the augmented model contains extra states (i.e., the flapping angles) in order to capture the flapping dynamics, which additionally introduced extra derivatives (i.e., $B_\square$ in Equation (A.126)). Moreover, as a result of the extra flapping angle states, additional stability derivatives were necessary to fully describe the perturbed forces and moments on the vehicle. To summarize, both the A and B matrices as well as the vehicle state definitions had to be adapted to accommodate for the addition of flapping dynamics (see Equations (A.122) and (A.127)).

From the perspective of the EMD method, the addition of extra states in the vehicle dynamics becomes apparent through both the A^p and B^p matrices. The definition of C^p in Equation (C.1) is also affected, as it will require the incorporation of derivatives of X, Y and Z with respect to the new states in order to complete the description of the perturbed specific forces. Moreover, because the perturbed specific forces are direct inputs to the linearized CWA dynamics, the coupling matrices A^{pm} and C^{pm} need to adapted likewise.

Stability augmentation Another common element added to the vehicle dynamics that was addressed in this dissertation is the Stability and Control Augmentation System (SCAS) (see Appendix A.9.1). The effect of a simple SCAS, consisting of a set of feedback gains on rotational rates and attitudes, can be captured using a modified system matrix according to (see Equation (A.131)):

$$A - B\,K$$

with B and K as given by Equation (A.117) and Equation (A.130), respectively. The feedback gain matrix K multiplies the vehicle state vector directly and, therefore, can be seen as an element that introduces *damping* to the system through the input matrix B.

From the perspective of the EMD method, the SCAS therefore primarily affects the definition of A^p, which is replaced by the expression Equation (A.131). However, the definitions of the perturbed specific forces in the outputs of the vehicle model (and, thus, the inputs to linearized CWA dynamics) are also affected. For example, stability derivatives pertaining to a feedback state, say δq, are replaced with:

$$X'_q = X_q - X_{\delta_s} K_q, \quad Y'_q = Y_q - Y_{\delta_s} K_q, \quad Z'_q = Z_q - Z_{\delta_s} K_q \tag{C.7}$$

and likewise for the derivatives with respect to δp and δr. In addition, new terms with respect to $\delta\phi$ and $\delta\theta$ enter the expressions when the gains K_ϕ and K_θ are non-zero. These are of the form:

$$\begin{aligned} -Y_{\delta_s} K_\theta\,\delta\theta, &\quad -X_{\delta_s} K_\theta\,\delta\theta, \quad -Z_{\delta_s} Z_\theta\,\delta\theta \\ Y_{\delta_c} K_\phi\,\delta\phi, &\quad -X_{\delta_c} K_\phi\,\delta\phi, \quad -Z_{\delta_c} Z_\phi\,\delta\phi \end{aligned} \tag{C.8}$$

Thus, the matrices C^p, A^{pm} and C^{pm} need to be changed in order to incorporate Equations (C.7) and (C.8).

D

PILOT COMMENTS ACCOMPANYING SFR AND MFR SCALE RATINGS IN CHAPTER 2

This appendix contains a summary of the pilot comments corresponding to the SFR and MFR ratings presented in Chapter 2 of this thesis.

Subject 1 The subject noted during b30s that overshoot bothered him and that it felt worse in conditions d60s, noting it felt “more like sitting in a rocking chair”. During d60s, the pilot also indicated he noticed no adaption of control strategy between conditions, even though the ratings between the conditions differ. b60s was described as “feeling a little better” than d60s. During condition d30s, the pilot noted that in reality, a less aggressive strategy would be adopted and that it would be easier to level off towards the end of the maneuver. This is somewhat consistent with this subject’s comments during condition b30s.

In condition d30m, the subject commented that motion felt better than prior condition d30s and that the “g-force” felt better; the pilot still noted motion seemed to “lag” too much. He also emphasized the importance of timing control inputs to mitigate overshoot as much as possible. During conditions b60m and d60m, the pilot provided the indication “R” in conjunction to the MFR rating, indicating the motion deficiency “return to neutral”. During condition b60m, the pilot commented that motion seemed to level out slower than in reality.

Subject 2 During the training trials with the baseline condition, the subject noted that motion seemed to lead visuals and that the lateral velocity of the helicopter diminished too fast after levelling out. In a later training trial, however, this pilot noted that lateral motion seemed to “continue” while being confident that the helicopter was stable. The subject attributed this peculiarity to the tail rotor. During condition b30s, the pilot remarked on the high workload required in levelling out the helicopter, noting in particular the “high inertia” and the need for a “jerky” deceleration to hover. During condition b60s, the pilot again noted that the velocity built up was lost too quickly after levelling out. During condition d30s, the pilot remarked that it felt like he was “flying a different helicopter every time”. The pilot noted that d30s, however, seemed to react more promptly to cyclic inputs and was therefore easier to control and level out towards the end of the maneuver. During d60s, the pilot noted that motion felt exaggerated and distracting, but otherwise “pleasant” to fly. The awarded SFR ratings in favour of degraded rotorcraft dynamics with baseline motion therefore seem consistent with the provided comments, in that the pilot preferred the more agile rotorcraft dynamics in condition d30s.

The subject furthermore perceived motion in condition b30m to be too strong, but still realistic. In addition, the subject noted fidelity diminished for a more aggressive control strategy and seemed to improve when a less aggressive strategy was adopted. During condition b60m, the pilot commented on a “noticeable Coriolis effect” and noted he was “actively ignoring motion”. In addition, the pilot noted motion seemed to “tilt” too much, noting exaggerated “leans” and provided the indicator “M” (for mismatch cues). Condition d30m was deemed “realistic” by the pilot, except toward the end of the maneuver where motion seemed to “overshoot“ in the “wrong direction”. The “flight model”, however, felt “pleasant”. Here, it clearly appears that a change in rotorcraft dynamics was perceived by the pilot as a change in motion. During condition d60m, the pilot noted that motion seemed to “overcompensate” and “overshoot”. Indicators “M” (for mismatch cues) and “O” (for onset cues) were provided as well, with the additional comment that motion seemed to “lag” and “overshoot”.

Subject 3 During training sessions, the subject noted that the helicopter lost lateral velocity too quickly as compared to the real helicopter. During condition b30s, the pilot noted that adequate performance could be attained with more trials, but provided a rating of 10 because adequate performance could not be achieved on the basis of the four opportunities given. During condition d30s, the pilot noted that control inputs had to be given “more in advance” and that “anticipation for overshoot” (i.e., lead) was required. Similar comments were given during condition b60s, where the pilot also noted that the applied task strategy bared resemblance to what would be required in a Huey (Bell UH-1) helicopter. During condition d60s, the pilot remarked that the experience was “significantly” different from the real helicopter and that, in hindsight, the pilot would “maybe” improve the rating awarded in the previous condition (b60s) from a value of 7 to a value of 6.

During condition b30m, the pilot noted motion matched “reasonably well”, but during levelling out of bank the pilot commented on mismatch (“out of phase”) in motion. Condition d30m felt notably different to the pilot, again resembling the Huey helicopter and noting that more anticipation was required due to an apparent “lag” in inputs. The pilot therefore provided indicator “L” in conjunction with motion rating, indicating latency. Condition b60m was received by the pilot with the comment that it would “be a good one for PIO”, although a significant adaptation in control strategy was “not necessary”. The pilot also noticed that motion “continued somewhat longer”, but did contribute to the “overall feeling”. The indicator “L”, signifying latency, was again provided. During condition d60m, the pilot seemed to notice that motion moved in an opposite direction to control inputs. The pilot also expressed doubt in providing indicators “R” and/or “M” (for return to neutral and mismatch cues). In this condition, the pilot also noted that motion seemed “50% useful and 50% distracting”. Initial cues to control inputs seemed “OK”, but during levelling out a significant mismatch was perceivable.

Subject 4 During training sessions, the pilot remarked that the helicopter seemed “supersensitive” and seemed to act “opposite to inertia”, meaning it was much more sensitive at low movement rates than at high movement rates. Baseline condition b30s was complimented with having “by far the best correlation with actual helicopter” and that the response to controls seems “on the spot”, adding that “if training in the sim, best transfer [to real helicopter] would be obtained”. With degrading dynamics (condition d30s), the pilot noted that a minimal adaptation of control strategy was required, but that motion appeared to be “exaggerated” and that “from pressure on body” it seems like “flying faster than previous condition” (d30m) and that motion “feels like going faster than it looks”. Here, it again seems that a pure change of rotorcraft dynamics is perceived by a subject as a degradation of motion fidelity. In condition b60s, the pilot noted that “in between crosses” the experience felt “very similar” and that the motion also “feels realistic”. However, upon approaching the cross, the pilot noted that motion felt “very deceiving” and that the response to controls “seems exaggerated”. The lower rating was therefore attributed to the motion and it was added that an adaptation of control strategy was noticeable from the first trial to the second trial. Degradation of both rotorcraft dynamics and motion in condition d60s resulted in the pilot noticing a “big difference with this one”, elaborating that “proprioceptive cues upon bank” seemed “bigger than what appears from visuals”. Also, for the “same” bank angle, motion seemed to “feel stronger” than visuals. However, the pilot added that this observation may have been due to “pre-conditioning in earlier experimental conditions”.

During condition b30m, the pilot noted that the sensation [of motion] “matched visual very well” and that it ”overall felt very normal”. The subject also added that “others conditions felt very simulator-like, this one felt more like the real thing”. During condition d30m, the pilot only mentioned that motion “felt close to real flight”. During condition b60m, the pilot noted that “overwhelming majority felt normal”, but “close to hover at banks, motion feels exaggerated”. Finally, during condition d60m, the pilot noted that it felt “very real”, with the “caveat” being that “motion and sim” feels too responsive upon initiating maneuver, adding it “happens too fast”. However, the “visual with motion” felt “very good” in this condition.

E

EXPERIMENT BRIEFING EXAMPLE

TUDelft

DESDEMONA
motion simulation for your proficiency

De rol van beweging in helikoptersimulatoren

Briefing voor piloten

Introductie

Dit experiment wordt uitgevoerd als onderdeel van een onderzoeksproject georganiseerd door de Technische Universiteit Delft in samenwerking met Desdemona B.V. te Soesterberg. Het onderzoek heeft als doel om meer kennis te vergaren over de rol van beweging in helikoptersimulatoren. Hiermee draagt het bij aan het verbeteren van gesimuleerde vliegomgevingen ten behoeve van toekomstige opleidingen en cursussen voor (militaire) piloten.

In dit specifieke experiment, zullen twee vliegtaken aan bod komen, waarbij de gesimuleerde beweging zal worden gevarieerd om steeds andere aspecten van de helikopterdynamika te benadrukken. Ook zal de invloed van de helikopterdynamika zelf worden onderzocht. Het experiment wordt uitgevoerd op de SIMONA onderzoekssimulator in Delft.

Opzet

Het experiment bestaat uit drie afzonderlijke delen. In deel I staat de *precisie hover* taak centraal (zie figuur 1). Het is de bedoeling om in deel I vier verschillende bewegingscondities te evalueren, waarbij het vliegmodel tussen de condities onveranderd blijft. Deze evaluatie vindt plaats op basis van een waarderingsschaal (zie figuur 3), namelijk de zogeheten *Motion Fidelity Rating (MFR)* schaal. Deze schaal meet de mate waarin de gesimuleerde beweging bijdraagt tot het behalen van de gespecificeerde taakprestaties (zie kop “taakomschrijving”). Het vliegmodel waarmee in deel I wordt gevlogen is gebaseerd op de AH-64 Apache helikopter, waarbij alléén de *longitudinale* bewegingsvrijheden actief zijn.

In deel II staat de *laterale reposition* taak (zie figuur 2) over een afstand van ca. 400 voet centraal. In deel II is het, net als in deel I, de bedoeling om verschillende bewegingscondities te evalueren op basis van de MFR schaal, waarbij tussen de condities wederom het vliegmodel onveranderd blijft. In tegenstelling tot deel I, zullen in deel II maar drie bewegingscondities aan bod komen. Ook is het vliegmodel in deel II gebaseerd op de BO-105 helikopter, waarbij alléén de *laterale* bewegingsvrijheden actief zijn.

In deel III staat tot slot het vliegmodel zelf centraal. Zowel de taak als de bewegingscondities die aan bod zullen komen zijn identiek aan deel II. Ook is het vliegmodel nog steeds gebaseerd op de BO-105. Echter zal in deel III per bewegingsconditie worden onderzocht of veranderingen in het vliegmodel waarneembaar zijn.

Taakomschrijving

De vliegtaken die in dit experiment aan bod komen zijn de *precisie hover* en *laterale reposition* zoals beschreven in de Aeronautical Design Standaard, versie 33E (ADS-33E). Een impressie van deze taken is te zien in figuren 1 en 2. Een belangrijke opmerking in de precisie hover taak, is dat er al gestart wordt op de eindpositie (d.w.z., geen verplaatsing). Er is kunstmatige turbulentie toegevoegd om het model gedurende de taak te exciteren. De specificaties voor deze twee taken zijn als volgt:

- *Precisie hover*: de positie van de helikopter dient gedurende ca. 30 seconden binnen een toegestane afwijking van 3 voet longitudinaal en 2 voet verticaal (*gewenst*) òf tenminste binnen 6 voet longitudinaal en 4 voet verticaal (*adequaat)* gehouden te worden.

- *Laterale reposition*: verplaats de helicopter vanuit hover in één laterale vloeiende beweging over een afstand van 400 voet, waarbij een snelheid van circa 35 knopen dient te worden bereikt. Zowel het begin- als het eindpunt zijn gemarkeerd met kruizen (zie figuur 3). De helikopter dient binnen een toegestane afwijking van 10 voet van deze kruizen in een stabiele hover tot stilstand te worden gebracht.

Procedure

In deel I en deel II van het experiment zal worden gestart met een trainingsfase om te wennen aan de gesimuleerde vliegomgeving. Dit zal circa 10 minuten per deel in beslag nemen. Hierna zal direct worden gestart met het inhoudelijke experiment. Zoals vermeld onder de kop “opzet”, bestaan deel I en II van het experiment uit vier, respectievelijk drie, verschillende condities. Elk van deze condities zal *drie keer* in willekeurige volgorde worden herhaald. Binnen elke herhaling zijn *twee repetities* van de taak beoogd alvorens zal worden gevraagd om een *MFR rating*. Per geëvalueerde conditie levert dit uiteindelijk drie MFR ratings op.

In deel III van het experiment wordt de waarneembaarheid van veranderingen in het vliegmodel onderzocht. De taak en het (baseline) vliegmodel zijn hetzelfde als in deel II. Deel III bestaat ook uit drie verschillende condities, die ieder *twee keer* worden herhaald. Binnen elke herhaling wordt het vliegmodel vervolgens twee keer “back-to-back” gevlogen. Tussen deze repetities wordt er al dan niet een verandering aangebracht in het vliegmodel. Na de tweede repetitie zal telkens worden gevraagd om aan te geven of een verandering is waargenomen en, zo ja, in welke vorm deze zich tijdens de taak heeft gemanifesteerd.

Tussen ieder deel van het experiment is een rustpauze van ca. 15 minuten beoogd. Tevens zal de coordinator gedurende het experiment meermaals vragen naar de gesteldheid van de proefpersoon, op basis van de zogenaamde *misery scale* (MISC, zie figuur 4). Na het experiment zal er een korte debriefing plaatsvinden, die zowel jou als de coordinator in staat stelt om naar eventuele nadere feedback en/of toelichtingen te vragen. Het programma is samengevat in tabel 1.

Tabel 1

Onderdeel	Tijd (min.)
Briefing	10
Deel I - precisie hover (training)	10
Deel I - precisie hover (experiment)	50
Pauze	15
Deel II - laterale reposition (training)	10
Deel II - laterale reposition (experiment)	40
Pauze	15
Deel III - laterale reposition (model)	20
Debriefing	10
	ca. 3 uur

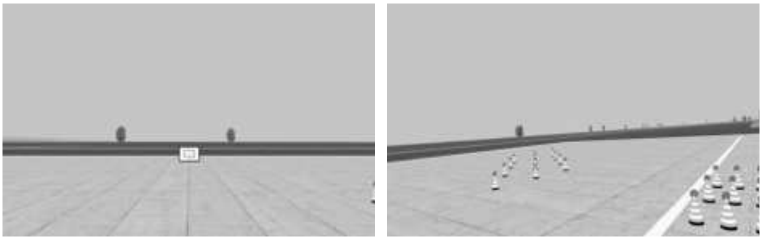

Figuur 1: opzet van de precisie hover taak.

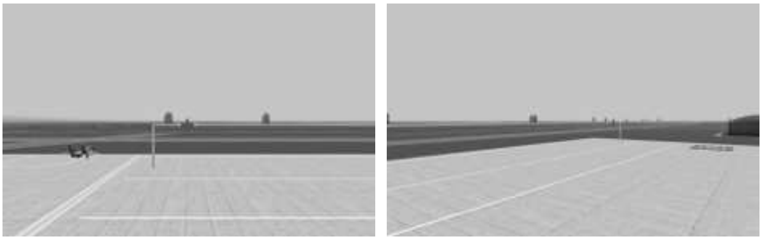

Figuur 2: opzet van de laterale reposition taak.

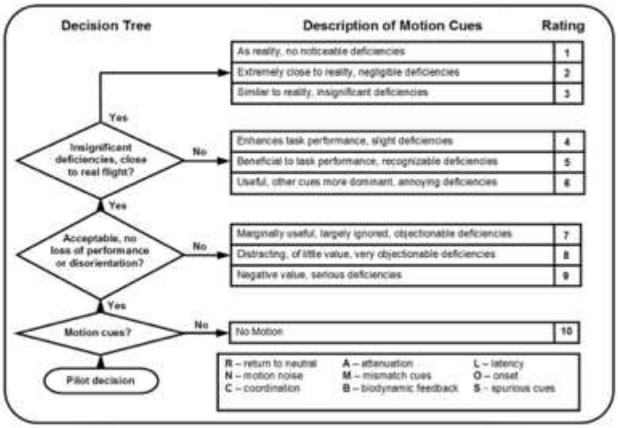

Figuur 3: de Motion Fidelity Rating (MFR) schaal.

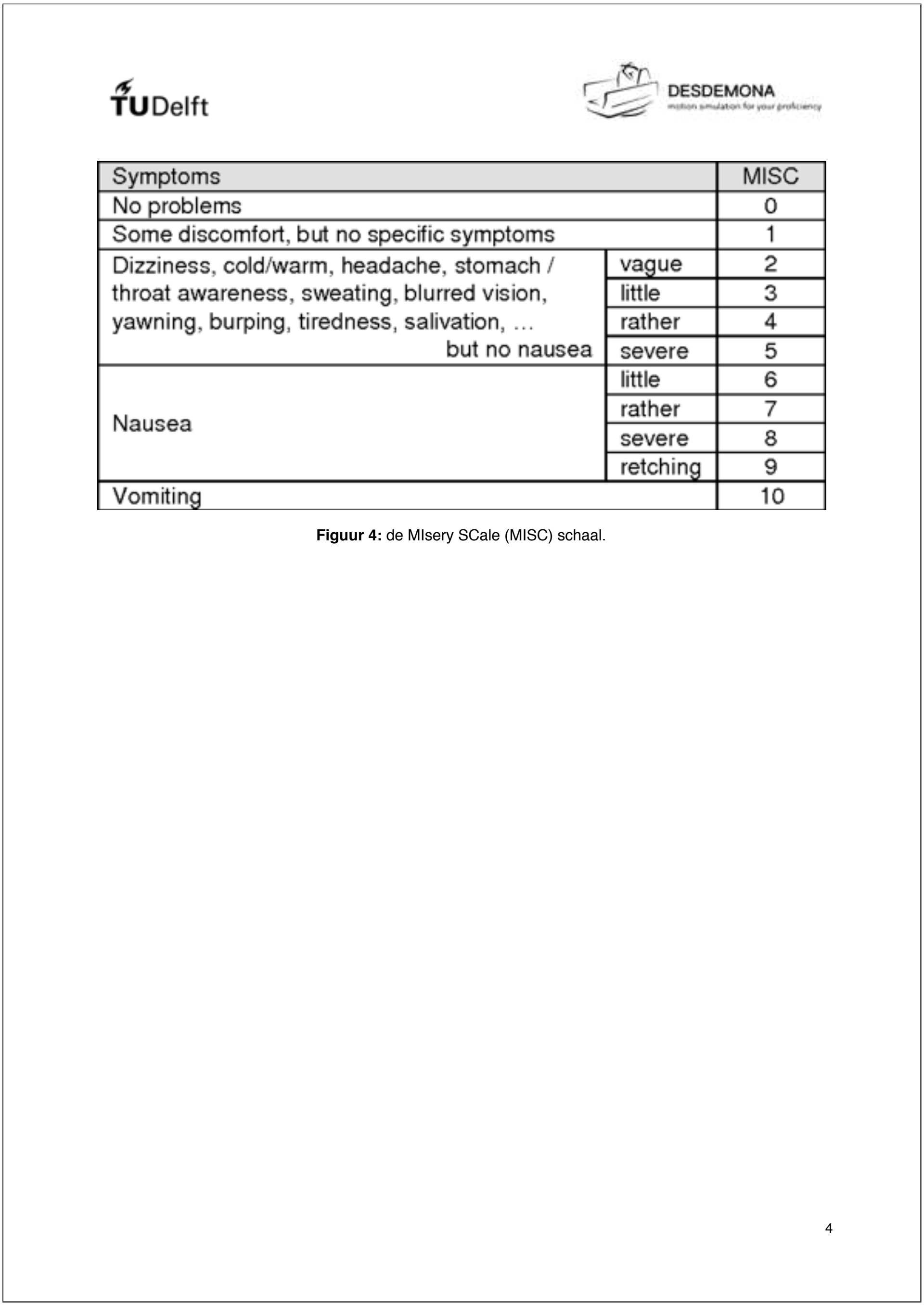

Symptoms		MISC
No problems		0
Some discomfort, but no specific symptoms		1
Dizziness, cold/warm, headache, stomach / throat awareness, sweating, blurred vision, yawning, burping, tiredness, salivation, … but no nausea	vague	2
	little	3
	rather	4
	severe	5
Nausea	little	6
	rather	7
	severe	8
	retching	9
Vomiting		10

Figuur 4: de MIsery SCale (MISC) schaal.

4

REFERENCES

Advani, S. K. and Hosman, R. J. A. W. (2006a). Revising Civil Simulator Standards – An Opportunity for Technological Pull. In *Proceedings of the AIAA Modeling and Simulation Technologies Conference and Exhibit, Keystone, CO, Aug. 21-24*, number AIAA-2006-6248.

Advani, S. K. and Hosman, R. J. A. W. (2006b). Towards Standardizing High-Fidelity Cost-Effective Motion Cueing in Flight Simulation. In *Proceedings of the Royal Aeronautical Society Flight Simulation Conference, London, UK, Nov. 7-8*.

Advani, S. K., Hosman, R. J. A. W., and Potter, M. (2007). Objective Motion Fidelity Qualification in Flight Training Simulators. In *AIAA Modeling and Simulation Technologies Conference and Exhibit, Hilton Head, South Carolina, Aug. 20-23*, number AIAA 2007-6802.

Anonymous (1980). Military Specification MIL-F-8785C, Flying Qualities of Piloted Airplanes. Technical report, United States Army.

Anonymous (2000). Aeronautical Design Standard-33E-PRF, Performance Specification, Handling Qualities Requirements for Military Rotorcraft. Technical report, US Army AMCOM, Redstone, Alabama, USA.

Anonymous (2002). Operator’s Manual for Helicopter, Attack, AH-64D, Longbow Apache. Technical report, Headquarters United States Army.

Anonymous (2009). ICAO 9625: Manual of Criteria for the Qualification of Flight Simulation Training Devices. Volume 1: Aeroplanes. Technical report, International Civil Aviation Authority. Third Edition.

Anonymous (2017). Global Commercial Helicopter Market 2017-2027. Technical report, Strategic Defence Intelligence.

Ashkenas, I. L. (1986). Collected Flight and Simulation Comparisons and Considerations. In *AGARD Conference Proceedings Number 408, Flight Simulation*, volume AGARD-CP-408, pages 26–1–26–34. Advisory Group for Aerospace Research and Development, North Atlantic Treaty Organization.

Augusto, B. D. C. and Loureiro, R. J. L. (2009). Motion Cueing in the Chalmers Driving Simulator: A Model Predictive Control Approach. Master’s thesis, Chalmers University of Technology.

Bailey, F. R. (1941). A Simplified Theoretical Method of Determining the Characteristics of a Lifting Rotor in Forward Flight. Technical Report 716, NACA.

Barfoot, T., Forbes, J. R., and Furgale, P. T. (2011). Pose Estimation Using Linearized Rotations and Quaternion Algebra. *Acta Astronautica*, 68(1):101 – 112.

Baseggio, M., Beghi, A., Bruschetta, M., Maran, F., and Minen, D. (2011). An MPC Approach to the Design of Motion Cueing Algorithms for Driving Simulators. In *Proceedings of the International IEEE Conference on Intelligent Transportation Systems, Washington DC, Oct. 5-7*.

Beard, S. D., Reardon, S. E., Tobias, E. L., and Aponso, B. L. (2012). Simulation System Optimization for Rotorcraft Research on the Vertical Motion Simulator. In *Proceedings of the AIAA Modeling and Simulation Technologies Conference, Minneapolis, MN, Aug. 13-16*, number AIAA-2012-4634.

Beard, S. D., Reardon, S. E., Tobias, E. L., and Aponso, B. L. (2013). Simulation System Fidelity Assessment at the Vertical Motion Simulator. In *Proceedings of the AHS 69th Annual Forum, Phoenix, AZ, May 21-23*.

Beghi, A., Bruschetta, M., Maran, F., and Minen, D. (2012). A Model-based Motion Cueing Strategy for Compact Driving Simulation Platforms. In *Proceedings of the Driving Simulation Conference, Paris, France, Sep. 6-7*.

Behnel, S., Bradshaw, R., Dalcin, L., Florisson, M., Makarov, V., and Seljebotn, D. S. (2018). Cython is an Optimising Static Compiler for both the Python Programming Language and the Extended Cython Programming Language. `www.cython.org`. Accessed: October 2018.

Bender, G. L., Diekmann, V. L., Ottomeyer, J. D., Picasso, B. D., and Higgins, L. B. (1981). Engineering Design Test 4 YAH Advanced Attack Helicopter. Technical report, United States Army Aviation Engineering Flight Activity, Edwards Air Force Base, CA.

Bender, G. L., Voss, J. S., Macmullin, R., and Adkins, J. M. (1984). First Article Preproduction tests of the AH64a Helicopter. Technical report, United States Army Aviation Engineering Flight Activity, Edwards Air Force Base, CA.

Benson, A. J. (1990). Sensory Functions and Limitations of the Vestibular System. In Warren, R. and Wertheim, A. H., editors, *Perception and Control of Self-Motion*, pages 145–170, Hillsdale, NJ, USA. Lawrence Erlbaum.

Bles, W. (1999). Coriolis Effects and Motion Sickness Modelling. *Brain Research Bulletin*, 47(5):543–549.

Bludau, J., Rauleder, J., Friedmann, L., and Hajek, M. (2017). Real-Time Simulation of Dynamic Inflow using Rotorcraft Flight Dynamics Coupled with a Lattice-Boltzmann Based Fluid Simulation. In *55th AIAA Aerospace Sciences Meeting, Grapevine, TX, Jan. 9-13*.

Boomsma, W. (2018). Eigency is a Cython Interface Between Numpy arrays and Matrix/Array Objects from the Eigen C++ Library. `www.github.com/wouterboomsma/eigency`. Accessed: October 2018.

Bramwell, A. R. S. (1974). Some Remarks on the Induced Velocity Field of a Lifting Rotor and on Glauert's Formula. In *Aeronautical Research Council Current Papers No. 1301*.

Bramwell, A. R. S., Done, G., and Balmford, D. (2001). *Bramwell's Helicopter Dynamics*. Butterworth-Heinemann.

Brunner (2019). CLS-P Cyclic, CLS-P Collective and CLS-P Rudder with Toe Brakes. `https://www.brunner-innovation.swiss/product/`. Accessed: February 2019.

Burki-Cohen, J., Booth, E. M., Soja, N. N., DiSario, R., Go, T., and Londridge, T. (2000). Simulator Fidelity - The Effect of Platform Motion. In *Proceedings of the Royal Aeronautical Society Conference on Flight Simulation - The Next Decade, London, UK, May 10*.

Carpenter, P. J. and Fridovich, B. (1953). Effect of Rapid-Pitch Increase on the Thrust and Induced-Velocity Response of a Full-Scale Helicopter Rotor. Technical Report TN-3044, NACA.

Chalk, C., Neal, T., Harris, T., Pritchard, F. E., and Woodcock, R. J. (1969). Background Information and User Guide for MIL-F–8785B(ASG): Military Specification-Flying Qualities of Piloted Airplanes. Technical Report AFWAL-TR-81-3109, Flight Dynamics Laboratory, Air Force Wright Aeronautical Libraries.

Chen, R. T. N. (1986). Influence of Dynamic Inflow on the Helicopter Vertical Response. Technical Report TM88327, NASA Ames Research Center, Ames Research Center, Moffet Field, CA.

Chen, R. T. N. (1989). A Survey of Nonuniform Inflow Models for Rotorcraft Flight Dynamics and Control Applications. Technical Report TM102219, National Aeronautics and Space Administration, Ames Research Center, Moffet Field, CA.

Chen, R. T. N., Lebacqz, V. J., Aiken, E. W., and Tischler, M. B. (1988). Helicopter Mathematical Models and Control Law Development for Handling Qualities Research. Technical Report 19880007259, NASA Ames Research Center, Ames Research Center, Moffet Field, CA.

Cleij, D., Venrooij, J., Pretto, P., Katliar, M., Bülthoff, H., Steffen, D., Hoffmeyer, F., and Schoener, H. (2017a). Comparison Between Filter- and Optimization-Based Motion Cueing Algorithms for Driving Simulation. *Transportation Research Part F: Traffic Psychology and Behaviour*, 61(2019):53–68.

Cleij, D., Venrooij, J., Pretto, P., Pool, D., Mulder, M., and Bülthoff, H. (2017b). Continuous Subjective Rating of Perceived Motion Incongruence during Driving Simulation. *IEEE Transactions on Human-Machine Systems*, 48(1):17–29.

Coleman, R. P., Feingold, A. M., and Stempin, C. W. (1947). Evaluation of the Induced Velocity Field of an Idealized Helicopter Rotor. Technical Report NACA-ARR-L5E10, NACA.

Conrad, B., Douvillier, J. G., and Schmidt, S. F. (1973). Washout Circuit Design for Multi-Degrees-Of-Freedom Moving Base Simulators. In *Proceedings of the AIAA Visual and Motion Simulation Conference, Palo Alto, CA, Sep. 10-12*, number AIAA-1973-929.

Cooper, G. E. and Harper, Jr., R. P. (1969). The Use of Pilot Rating in the Evaluation of Aircraft Handling Qualities. Technical Report NASA TN D-5153, National Aeronautics and Space Administration.

Correia Grácio, B. J., Valente Pais, A. R., van Paassen, M. M., Mulder, M., Kelly, L. C., and Houck, J. A. (2013). Optimal and Coherence Zone Comparison Within and Between Flight Simulators. *Journal of Aircraft*, 50(2):493–507.

Curtiss, H. C. (1986). Stability and Control Modelling. In *Proceedings of the 12th European Rotorcraft Forum, Garmisch-Partenkirchen, Germany, Sep. 22-25*.

Cyrus, M. L. (1977). Engineering and Geometric Constraints of a six Degrees of Freedom Synergistic Platform Motion System. Technical Report AFHRL-TR-77-5, Air Force Human Resources Laboratory, Williams Air Force Base, AZ.

Dagdelen, M., Reymond, G., Kemeny, A., Bordier, M., and Maïzi, N. (2004). MPC Based Motion Cueing Algorithm: Development and Application to the ULTIMATE Driving Simulator. In *Proceedings of the Driving Simulation Conference 2004 Europe, Paris, France, Sep.*, pages 221–233.

Dahl, H. J. and Faulkner, A. J. (1978). Helicopter Simulation in Atmospheric Turbulence. In *Proceedings of the Fourth European Rotorcraft and Powered Lift Aircraft Forum, Stresa, Italy, Sep. 13-15*.

Dalmeijer, W., Miletović, I., Stroosma, O., and Pavel, M. (2017). Extending the Objective Motion Cueing Test to Measure Rotorcraft Simulator Motion Characteristics. In *Proceedings of the AHS 73rd Annual Forum, Fort Worth, TX, May 9-11*, pages 1876–1891.

Dalmeijer, W. H. (2016). Extending the Objective Motion Cueing Test to Measure Rotorcraft Simulator Motion Characteristics. Master's thesis, Delft University of Technology.

Damveld, H. J. (2009). *A Cybernetic Approach to Assess the Longitudinal Handling Qualities of Aeroelastic Aircraft*. PhD thesis, Delft University of Technology, Faculty of Aerospace Engineering.

de Graaf, B., Bles, W., and Hosman, R. J. A. W. (2002). Desdemona: Advanced Disorientation Trainer and (Sustained-g) Flight Simulator. In *Proceedings of The First Swedish-American Workshop on Modeling and Simulation, Orlando, FL, Oct. 30-31*.

de Winter, J. C. F., Dodou, D., and Mulder, M. (2012). Training Effectiveness of Whole Body Flight Simulator Motion: A Comprehensive Meta-Analysis. *The International Journal of Aviation Psychology*, 22(2):164–183.

Desdemona B.V. (2019). DESDEMONA: Motion Simulation for Your Proficiency. `http://www.thedesdemona.com/`. Accessed: February 2019.

dos Santos Buinhas, L., Correia Grácio, B. J., Valente Pais, A. R., van Paassen, M. M., and Mulder, M. (2013). Modeling Coherence Zones in Flight Simulation During Yaw Motion. In *Proceedings of the AIAA Modeling and Simulation Technologies Conference, Boston, MA, Aug. 19-22*, number AIAA-2013-5223.

Duke, E. L., Antoniewicz, R. F., and Krambeer, K. D. (1988). Derivation and Definition of a Linear Aircraft Model. Technical Report NASA RP-1207, National Aeronautics and Space Administration.

EASA (2012a). Acceptable Means of Compliance and Guidance Material to Part Organisation Requirements for Aircrew (Part-ORA).

EASA (2012b). CS-FSTD (H) Helicopter Flight Simulation Training Devices.

Ellerbroek, J., Stroosma, O., Mulder, M., and van Paassen, M. M. (2008). Role Identification of Yaw and Sway Motion in Helicopter Yaw Control Tasks. *Journal of Aircraft*, 45(4):1275–1289.

FAA (2016). CFR-Part 60 Flight Simulation Training Device Initial an Continuing Qualification and Use.

Feenstra, P., Wentink, M., Grácio, B. C., and Bles, W. (2009). Effect of Simulator Motion Space on Realism in the Desdemona Simulator. In *Proceedings of the Driving Simulation Conference, Monaco, Feb. 4-6*, pages 133–144.

Fetsch, C. R., Turner, A. H., DeAngelis, G. C., and Angelaki, D. E. (2009). Dynamic reweighting of visual and vestibular cues during self-motion perception. *Journal of Neuroscience*, 29(49):15601–15612.

Gaonkar, G. H. and Peters, D. A. (1985). A Review of Dynamic Inflow and its Effect on Experimental Correlations. Technical Report CP-2400, NASA.

GARTEUR HC/AG 21 (2015). Rotorcraft Simulation Fidelity Assessment: Predicted and Perceived Measures of Fidelity. `http://www.garteur.org/Action%20Group%20posters/HC_AG-21%20Poster%20v160301.pdf`. Accessed: February 2019.

Glauert, H. (1926). A General Theory of the Autogyro. In *Aeronautical Research Council Reports & Memoranda*, volume 1111.

Gori, R., Pavel, M. D., and Gennaretti, M. (2015). Prediction and Simulator Verification of State-Space Rotor Modelling on Helicopter Manoeuvering Flight. In *Proceedings of the 41st European Rotorcraft Forum, Munich, Germany, Sep. 1-4*.

Gouverneur, B., Mulder, J. A., van Paassen, M. M., Stroosma, O., and Field, E. J. (2003). Optimisation of the SIMONA Research Simulator's Motion Filter Settings for Handling Qualities Experiments. In *Proceedings of the AIAA Modeling and Simulation Technologies Conference and Exhibit, Austin, Texas, Aug. 11-14*, number AIAA-2003-5679.

Grant, P. R. and Lee, P. T. S. (2007). Motion-Visual Phase-Error Detection in a Flight Simulator. *Journal of Aircraft*, 44(3):927–935.

Grant, P. R. and Schroeder, J. A. (2010). Modelling Pilot Control Behaviour for Flight Simulator Design and Assessment. In *Proceedings of the AIAA Guidance, Navigation, and Control Conference, Toronto, Canada, Aug. 2-5*, number AIAA-2010-8356.

Groen, E. L., Valenti Clari, M. S. V., and Hosman, R. J. A. W. (2001). Evaluation of Perceived Motion during a Simulated Takeoff Run. *Journal of Aircraft*, 38(4):600–606.

Gundry, A. J. (1976). Man and Motion Cues. In *Proceedings of the R.A.e.S. Symposium Theory and Practice in Flight Simulation, London, UK , Apr. 8*.

Harding, J., H Mansur, M., Tischler, M., J Moody, S., and C Mccann, R. (2007). Optimization and Piloted Simulation Results of the AH-64D Modern Control Laws. *Proceedings of the 63rd Forum of the American Helicopter Society, Virginia Beach, VA, May 1-3*.

Heerspink, H., Berkouwer, W., Stroosma, O., van Paassen, R., Mulder, M., and Mulder, B. (2005). Evaluation of Vestibular Thresholds for Motion Detection in the SIMONA Research Simulator. In *AIAA Modeling and Simulation Technologies Conference and Exhibit, San Fransisco, CA, Aug. 15-18*, number AIAA-2005-6502.

Heffley, R. K. (1982). A Pilot-in-the Loop Analysis of Several Kinds of Helicopter Acceleration-Deceleration Manoeuvers. In *Proceedings of a Specialists Meeting on Helicopter Handling Qualities*, number CP 2216. NASA.

Heffley, R. K., Clement, W. F., Ringland, R. F., F., J. W., Jex, H. R., McRuer, D. T., and Carter, V. E. (1981). Determination of Motion and Visual System Requirements for Flight Training Simulators. Technical Report 546, U. S. Army Institute for the Behavioral and Social Sciences.

Henn, V., Cohen, B., and Young, L. R. (1980). Visual-Vestibular Interaction in Motion Perception and the Generation of Nystagmus. *Neurosciences Research Program Bulletin*, 18(4):457–651.

Hess, R. A. (1990). Model for Human Use of Motion Cues in Vehicular Control. *Journal of Guidance, Control, and Dynamics*, 13(3):476–482.

Hess, R. A. (1997). Unified Theory for Aircraft Handling Qualities and Adverse Aircraft-Pilot Coupling. *Journal of Guidance, Control, and Dynamics*, 20(6):1141–1148.

Hess, R. A. and Malsbury, T. (1991). Closed-loop Assessment of Flight Simulator Fidelity. *Journal of Guidance, Control, and Dynamics*, 14(1):191–197.

Hess, R. A., Malsbury, T., and Atencio, Jr., A. (1993). Flight Simulator Fidelity Assessment in a Rotorcraft Lateral Translation Maneuver. *Journal of Guidance, Control, and Dynamics*, 16(1):79–85.

Hess, R. A. and Marchesi, F. (2009). Analytical Assessment of Flight Simulator Fidelity Using Pilot Models. *Journal of Guidance, Control, and Dynamics*, 32(3):760–770.

Hodge, S. J., Manso, S., and White, M. D. (2015a). Challenges in Roll-Sway Motion Cueing Fidelity: A View from Academia. In *Proceedings of the Conference on Challenges in Flight Simulation, London, UK, Jun. 9-10*. Flight Simulation Group, Royal Aeronautical Society.

Hodge, S. J., Perfect, P., Padfield, G. D., and White, M. D. (2015b). Optimising the Roll-Sway Motion Cues Available from a Short Stroke Hexapod Motion Platform. *The Aeronautical Journal*, 119(1211):23–44.

Hodge, S. J., Perfect, P. S., Padfield, G. D., and White, M. D. (2011). Optimising the Vestibular Cues Available from a Short Stroke Hexapod Motion Platform. In *67th Annual Forum of the American Helicopter Society, Virginia Beach, VA, May 3-5*.

Hosman, R. and Stassen, H. (1998). Pilot's Perception and Control of Aircraft Motions. In *7th IFAC Symposium on Analysis, Design and Evaluation of Man Machine Systems (MMS'98), Kyoto, Japan, Sep. 16-18*, volume 31, pages 311 – 316.

Hosman, R. J. A. W. (1996). *Pilot's Perception and Control of Aircraft Motions*. PhD thesis, Delft University of Technology, Faculty of Aerospace Engineering.

Hosman, R. J. A. W. and Advani, S. K. (2013). Are Criteria for Motion Cueing and Time Delays Possible? part 2. In *Proceedings of the AIAA Modeling and Technologies Conference, Boston, MA, Aug. 19-22*, number AIAA 2013-4833.

Hosman, R. J. A. W. and Advani, S. K. (2016). Design and Evaluation of the Objective Motion Cueing Test and Criterion. *The Aeronautical Journal*, 120(1227):873–891.

Hosman, R. J. A. W. and van der Steen, F. A. M. (1993). False Cue Detection Thresholds in Flight Simulation. In *Proceedings of the AIAA Flight Simulation Technologies Conference, Monterey, CA, Aug. 9-11*, number AIAA-1993-3578.

Hossein Mansur, M. (1995). Development and Validation of a Blade-Element Mathematical Model for the AH-64A Apache Helicopter. Technical Report NASA-TM-108863, NASA.

Jacob, B. and Guennebaud, G. (2018). Eigen is a C++ Template Library for Linear Algebra: Matrices, Vectors, Numerical Solvers, and Related Algorithms. `http://eigen.tuxfamily.org`. Accessed: October 2018.

Johnson, W. (1994). *Helicopter Theory*. Dover Publications Inc.

Jones, M. (2016). Optimizing the Fitness of Motion Cueing for Rotorcraft Flight Simulation. In *Proceedings of the AHS 72nd Annual Forum, West Palm Beach, FL, May 17-19*.

Jones, M. (2017a). A Method for Automatic Tuning of Flight Simulator Motion Platforms. *International Journal of Modeling, Simulation, and Scientific Computing*, 08(04):1743004.

Jones, M. (2017b). Motion Cueing Optimisation Applied to Rotorcraft Flight Simulation. *CEAS Aeronautical Journal*, 8(3):523–539.

Kelley, H. L. (1990). Aerodynamic Performance of a 0.27-Scale Model of an AH-64 Helicopter with Baseline and Alternate Rotor Blade Sets. Technical Report TM-4201, National Aeronautics and Space Administration.

Kerler, M., Hönle, J., and Kau, H. P. (2012). Modeling of Bo-105 Flight Dynamics for Research on Fuel Savings due to Single Engine Operation. In *Proceedings of the 38th European Rotorcraft Forum, Amsterdam, Sep. 4-7*.

Kunz, D. L. and Jones, H. E. (2001). Modeling and Simulation of the Apache Rotor System in CAMRAD II. In *AHS International Structures Specialists' Meeting, Williamsburge, VA, Oct. 30 – Nov. 1*.

Lele, A. (2013). Virtual Reality and Its Military Utility. *Journal of Ambient Intelligence and Humanized Computing*, 4(1):17–26.

Levison, W. H. (1981). Effects of Whole-Body Motion Simulation on Flight Skill Development. Technical Report 4645, Bolt Beranek and Newman, Inc.

Li, M. (2016). Effects of Helicopter Degree of Freedom and Motion Cues on Allowable Error Envelopes. Master's thesis, Delft University of Technology, Faculty of Aerospace Engineering.

Liu, G. P. and Patton, R. (1998). *Eigenstructure Assignment for Control System Design*. John Wiley & Sons, Inc., New York, NY, USA.

Low, E. and Garrard, W. L. (1993). Design of Flight Control Systems to Meet Rotorcraft Handling Qualities Specifications. *Journal of Guidance, Control, and Dynamics*, 16(1):69–78.

Lu, T. (2018). *Objective Evaluation of Human Manual Control Adaptation Boundaries using a Cybernetic Approach*. PhD thesis, Delft University of Technology, Faculty of Aerospace Engineering.

Manso, S., White, M. D., and Hodge, S. J. (2016). An Investigation of Task Specific Motion Cues for Rotorcraft Simulators. In *Proceedings of the AIAA Modeling and Simulation Technologies Conference, San Diego, CA, Jan. 4–8*, number AIAA 2016-2138.

Marinescu, A. and Anghel, V. (1992). *Helicopter Aerodynamics and Dynamics*. Academy Press.

MathWorks (2017). Dryden Wind Turbulence Model (Continuous). `https://nl.mathworks.com/help/aeroblks/drydenwindturbulencemodelcontinuous.html`. Accessed: September 2017.

McRuer, D. T. (1980). Human Dynamics in Man-Machine Systems. *Automatica*, 16(3):237–253.

McRuer, D. T., Graham, D., Krendel, E. S., and Reisener, W. J. (1965). Human Pilot Dynamics in Compensatory Systems, Theory Models and Experiments with Controlled Element and Forcing Function Variations. Technical Report AFFDL-TR-65-15, Air Force Flight Dynamics Laboratory, Wright-Patterson Air Force Base (OH).

McRuer, D. T. and Jex, H. R. (1967). A Review of Quasi-Linear Pilot Models. *IEEE Transactions on Human Factors in Electronics*, HFE-8(3):231–249.

Miletović, I., Pavel, M. D., Stroosma, O., Pool, D. M., van Paassen, M. M., Wentink, M., and Mulder, M. (2018). Eigenmode Distortion as a Novel Criterion for Motion Cueing Fidelity in Rotorcraft Flight Simulation. In *Proceedings of the 44th European Rotorcraft Forum, Delft, The Netherlands, Sep. 18–21*.

Mitchell, D. G., Hoh, R. H., Atencio, Jr., A., and Key, D. L. (1992). Ground-Based Simulation Evaluation of the Effects of Time Delays and Motion on Rotorcraft Handling Qualities. USAAVSCOM Technical Report 91-A-010, Aeroflightdynamics Directorate, U.S. Army Aviation Systems Command, Ames Research Center, Moffett Field, CA.

Mitchell, D. G., Hoh, R. H., He, C., and Strope, K. (2006). Determination of Maximum Unnoticeable Added Dynamics. In *Proceedings of the AIAA Atmospheric Flight Mechanics Conference and Exhibit, Keystone, CO, Aug. 21–24*, number AIAA-2006-6492.

Moore, B. (1976). On the Flexibility Offered by State feedback in Multivariable Systems Beyond Closed Loop Eigenvalue Assignment. *IEEE Transactions on Automatic Control*, 21(5):689–692.

Mulder, M., Pool, D. M., Abbink, D. A., Boer, E. R., Zaal, P. M. T., Drop, F. M., van der El, K., and van Paassen, M. M. (2018). Manual Control Cybernetics: State-of-the-Art and Current Trends. *IEEE Transactions on Human-Machine Systems*, 48(5):468–485.

Nieuwenhuizen, F. M. (2012). *Changes in Pilot Control Behaviour Across Stewart Platform Motion Systems*. PhD thesis, Delft University of Technology, Faculty of Aerospace Engineering.

Nieuwenhuizen, F. M., Zaal, P. M. T., Teufel, H. J., Mulder, M., and Bülthoff, H. H. (2009). The Effect of Simulator Motion on Pilot Control Behaviour for Agile and Inert Helicopter Dynamics. In *Proceedings of the 35th European Rotorcraft Forum, Hamburg, Germany, Sep. 22-25*.

Oculus (2019). Oculus Rift Overview. `https://www.oculus.com/rift`. Accessed: February 2019.

Ogata, K. (2001). *Modern Control Engineering*. Prentice Hall PTR, Upper Saddle River, NJ, USA, 4th edition.

Olver, P. J. (2014). *Introduction to Partial Differential Equations*. Undergraduate Texts in Mathematics. Springer International Publishing, 1st edition.

OpenSceneGraph (2019). The Openscenegraph Project Website. `http://www.openscenegraph.org/`. Accessed: December 2019.

Oppenheim, A. V. and Verghese, G. C. (2015). *Signals, System & Inference*. Pearson.

Ormistron, R. A. (1976). Application of Simplified Inflow Models to Rotorcraft Dynamic Analysis. *Journal of the American Helicopter Society*, 21(3):34–37.

Padfield, G. D. (2007). *Helicopter Flight Dynamics: The Theory and Application of Flying Qualities and Simulation Modelling*. Blackwell Publishing, 2nd edition.

Padfield, G. D. (2011). The Tau of Flight Control. *The Aeronautical Journal*, 115(1171):521–556.

Padfield, G. D., Charlton, M. T., Jones, J. P., and Bradley, R. (1994). Where Does The Workload Go When Pilots Attack Manoeuvres? An Analysis of Results from Flying Qualities Theory and Experiment. In *Proceedings of the 20th European Rotorcraft Forum, Amsterdam, The Netherlands, Oct. 4-7*.

Padfield, G. D., Lee, D. N., and Bradley, R. (2003). How do Helicopter Pilots Know When to Stop, Turn or Pull-Up (Developing Guidelines for Visual Aids). *Journal of the American Helicopter Society*, 48(2):108–119.

Padfield, G. D., McCallum, A. T., Haverdings, A., Dequin, A. M., Haddon, D., Kampa, K., Basset, P. M., and Von Grünhagen, W. (1996). Predicting Rotorcraft Flying Qualities Through Simulation Modelling: A Review of Key Results from GARTEUR AG-06. In *Proceedings of the 22nd European Rotorcraft Forum, Brighton, United Kingdom, Sep. 16-19*.

Padfield, G. D. and White, M. D. (2005). Measuring Simulation Fidelity Through an Adaptive Pilot Model. *Aerospace Science and Technology*, 9(5):400–408.

Parrish, R. V., Dieudonne, J. E., Bowles, R. L., and Martin, Jr., D. J. (1975). Coordinated Adaptive Washout for Motion Simulators. *Journal of Aircraft*, 12(1):44–50.

Pavel, M. D. (2001). *On The Necessary Degrees of Freedom for Helicopter and Wind Turbine Low-Frequency Modelling*. PhD thesis, Delft University of Technology, Faculty of Aerospace Engineering.

Pavel, M. D., Jump, M., Dang-Vu, B., Masarati, P., Gennaretti, M., Ionita, A., Zaichik, L., Smaili, H., Quaranta, G., Yilmaz, D., Jones, M., Serafini, J., and Malecki, J. (2013a). Adverse Rotorcraft Pilot Coupling - Past, Present and Future Challenges. *Progress in Aerospace Sciences*, 62(0):1 – 51.

Pavel, M. D., White, M. D., Padfield, G. D., Roth, G., Hamers, M., and Taghizad, A. (2013b). Validation of Mathematical Models for Helicopter Flight Simulators Current and Future Challenges. *The Aeronautical Journal*, 117(1190):343–388.

Penn, H. S. M. (2013). Investigating the Feasibility of Applying MUAD to Helicopter Simulator Model Validation. Master's thesis, Delft University of Technology.

Perfect, P., Timson, E., White, M. D., Padfield, G. D., Erdos, R., and Gubbels, A. W. (2014). A Rating Scale for the Subjective Assessment of Simulation Fidelity. *The Aeronautical Journal*, 118(1206):953–974.

Perfect, P., White, M. D., Padfield, G. D., and Gubbels, A. W. (2013). Rotorcraft Simulation Fidelity: New Methods for Quantification and Assessment. *The Aeronautical Journal*, 117(1189):235–282.

Peters, D. A. (2009). How Dynamic Inflow Survives in the Competitive World of Rotorcraft Aerodynamics. *Journal of the American Helicopter Society*, 54(1):011001.

Peters, D. A. and HaQuang, N. (1988). Dynamic Inflow for Practical Applications. *Journal of the American Helicopter Society*, 33(4):64–68.

Picasso, B. D., Downs, G. T., Buckanin, R. M., and Herbst, M. K. (1982). Airworthiness and Flight Characteristics Test pof YAH-64 Advanced Attack Helicopter, Prototype Qualification Test-Government, part 3 and Production Validation Test-Government for Handbook Verification. Technical report, United States Army Aviation Engineering Flight Activity, Edwards Air Force Base, CA.

Pitt, D. M. and Peters, D. A. (1981). Theoretical Prediction of Dynamic-Inflow Derivatives. *Vertica*, 5(1):21–34.

Pool, D. M. (2012). *Objective Evaluation of Flight Simulator Motion Cueing Fidelity Through a Cybernetic Approach*. PhD thesis, Delft University of Technology, Faculty of Aerospace Engineering.

Pool, D. M., Harder, G. A., and van Paassen, M. M. (2016). Effects of Simulator Motion Feedback on Training of Skill-Based Control Behavior. *Journal of Guidance, Control, and Dynamics*, 39(4):889–902.

Previc, F. H. and Ercoline, W. R. (2004). *Spatial Disorientation in Aviation*. American Institute of Aeronautics and Astronautics Inc.

Reardon, S. E. and Beard, S. D. (2015). Evaluation of Motion Tuning Methods on the Vertical Motion Simulator. In *Proceedings of the AHS 71st Annual Forum, Virginia Beach, VA, May 5-7*.

Reardon, S. E., Beard, S. D., and Aponso, B. L. (2014). Effects of Motion Filter Parameters on Simulation Fidelity Ratings. In *Proceedings of the AHS 70th Annual Forum, Montreal, Canada, May 20-22*.

Rehmann, A. J., Mitman, R. D., and Reynolds, M. C. (1995). A Handbook for Flight Simulation Fidelity Requirements for Human Factors Research. Technical Report DOT/FAA/CT-TN95/46, Crew System Ergonomics Information Center, Wright Patterson Airforce Base.

Reid, L. D. and Nahon, M. A. (1985). Flight Simulation Motion-Base Drive Algorithms. Part 1: Developing and Testing the Equations. Technical Report UTIAS 296, University of Toronto, Institute for Aerospace Studies.

Reid, L. D. and Nahon, M. A. (1986). Flight Simulation Motion-Base Drive Algorithms. Part 2: Selecting the System Parameters. Technical Report UTIAS 307, University of Toronto, Institute for Aerospace Studies.

Sabates, M. (2016). Image of 3D-render of the AH-64 helicopter. `http://imagineape.com/portfolios/3623/`. Accessed: October 2016.

Schroeder, J. A. (1999). Helicopter Flight Simulation Motion Platform Requirements. Technical Report TP-1999-208766, NASA, Moffett Field, CA.

Schroeder, J. A., Chung, W. W., and Laforce, S. (1997). Effects of Roll and Lateral Flight Simulation Motion Gains on a Sidestep Task. In *Proceedings of the American Helicopter Society 53rd Annual Forum, Virginia Beach, VA, Apr. 29 - May 1*.

Schroeder, J. A. and Grant, P. R. (2010). Pilot Behavioral Observations in Motion Flight Simulation. In Silvestro, M., editor, *Proceedings of the AIAA Guidance, Navigation, and Control Conference, Toronto, Canada, Aug. 2-5*, number AIAA-2010-8353.

Schroeder, J. A., Watson, D. C., Tischler, M. B., and Eshow, M. M. (1991). Identification and Simulation Evaluation of an AH-64A Helicopter Hover Math Model. In *AIAA Atmospheric Flight Mechanics Conference, New Orleans, LA, Aug. 12-14*, number AIAA 91-2877.

Seehof, C., Durak, U., and Duda, H. (2014). Objective Motion Cueing Test - Experiences of a New User. In *Proceedings of the AIAA Modeling and Simulation Technologies Conference, Atlanta, GA, Jun. 16-20*, number AIAA 2014-2205.

Serafini, J., Molica Colella, M., and Gennaretti, M. (2014). A Finite-State Aeroelastic Model for Rotorcraft-Pilot Coupling Analysis. *CEAS Aeronautical Journal*, 5(1):1–11.

Sinacori, J. B. (1977). The Determination of Some Requirements for a Helicopter Research Simulation Facility. Technical Report NASA-CR-152066, Systems Technology Inc.

Sivan, R., Ish-Shalom, J., and Huang, J.-K. (1982). An Optimal Control Approach to the Design of Moving Flight Simulators. *IEEE Transactions on Systems, Man, and Cybernetics*, SMC-12(6):818–827.

Sobel, K. and Shapiro, E. (1985). Eigenstructure Assignment for Design of Multimode Flight Control Systems. *IEEE Control Systems Magazine*, 5(2):9–15.

Stapleford, R. L., Peters, R. A., and Alex, F. R. (1969). Experiments and a Model for Pilot Dynamics with Visual and Motion Inputs. Technical Report NASA CR-1325, Systems Technology, Inc., Hawthorne, CA.

Stepniewski, W. Z. (1973). Basic Aerodynamics and Performance of the Helicopter. Technical Report AGARD-LS-63, Advisory Group for Aerospace Research & Development.

Steurs, M., Mulder, M., and van Paassen, M. M. (2004). A Cybernetic Approach to Assess Flight Simulator Fidelity. In *Proceedings of the AIAA Modelling and Simulation Technologies Conference and Exhibit, Providence, RI, Aug. 16-19*, number AIAA-2004-5442.

Stewart, D. (1965). A Platform with Six Degrees of Freedom. *Proceedings of the Institution of Mechanical Engineers*, 180(1):371–386.

Stewart, W. (1953). Higher harmonics of flapping on the helicopter rotor. Technical Report C.P. No. 121, Aeronautical Research Council.

Stoev, S., van Paassen, M. M., Stroosma, O., Miletović, I., and Mulder, M. (2019). Eigenmode Distortion Analysis for Motion Cueing Evaluation in Fixed-Wing Aircraft Simulators. In *Proceedings of the AIAA Modeling and Simulation Technologies Conference, San Diego, CA, Jan. 9-13*, number AIAA-2019-0179.

Strang, G. (2006). *Linear Algebra and its Applications*. Thomson, Brooks/Cole, Belmont, CA.

Stroosma, O., Van Paassen, M. M., and Mulder, M. (2003). Using The SIMONA Research Simulator For Human-Machine Interaction Research. In *AIAA Modeling and Simulation Technologies Conference and Exhibit, Austin, TX, Aug. 11-14*, number AIAA-2003-5525.

Stroosma, O., van Paassen, M. M., Mulder, M., Hosman, R. J. A. W., and Advani, S. K. (2013). Applying the Objective Motion Cueing Test to a Classical Washout Algorithm. In *Proceedings of the AIAA Modeling and Simulation Technologies Conference, Boston, MA, Aug. 19-22*, number AIAA-2013-4834.

Telban, R. J. and Cardullo, F. M. (2005). Motion Cueing Algorithm Development: Human-Centered Linear and Nonlinear Approaches. Technical Report NASA CR-2005-213747, National Aeronautics and Space Administration, Langley Research Center, Hampton, Virginia 23681-2199.

Telban, R. J., Cardullo, F. M., and Kelly, L. C. (2005). Motion Cueing Algorithm Development: Piloted Performance Testing of the Cueing Algorithms. Technical Report NASA CR-2005-213748, National Aeronautics and Space Administration, Langley Research Center, Hampton, Virginia 23681-2199.

Timson, E. (2013). *Flight Simulation Fidelity for Rotorcraft Design, Certification and Pilot Training*. PhD thesis, University of Liverpool.

Tischler, M. B. (1995). System Identification Methods for Aircraft Flight Control Development and Validation. Technical Report TM-110369, NASA.

Valente Pais, A. R. (2013). *Perception Coherence Zones in Vehicle Simulation*. PhD thesis, Delft University of Technology, Faculty of Aerospace Engineering.

van Biervliet, F. (2008). Lateral Manoeuvring Motion. In *RAeS Flight Simulation Group "Expanding Horizons: Technology Advances in Flight Simulation" Conference, Hilton Head, SC, Jun. 4-8*.

van der Steen, F. A. M. (1998). *Self-Motion Perception*. PhD thesis, Delft University of Technology, Faculty of Aerospace Engineering.

van der Steen, F. A. M. (2000). Measuring the Realism of Motion in Flight Simulators. In *Proceedings of the AIAA Modeling and Simulation Technologies Conference and Exhibit, Denver, CO, Jun. 5-9*, number AIAA-2000-4293.

van der Vaart, J. C. (1992). *Modelling of Perception and Action in Compensatory Manual Control Tasks*. PhD thesis, Delft University of Technology, Faculty of Aerospace Engineering.

Van Holten, T. and Melkert, J. (2002). Helicopter Performance, Stability and Control. Technical report, Delft University of Technology, Faculty of Aerospace Engineering.

Venrooij, J., Pretto, P., Katliar, M., Nooij, S., Nesti, A., Lächele, M., N de Winkel, K., and Cleij, D. (2015). Perception-Based Motion Cueing: Validation in Driving Simulation. In *Proceedings of the Driving Simulation Conference, Tübingen, Germany, Sep. 16-18*.

Wan, J. (2014). *Ornicopter Multidisciplinary Analyses and Conceptual Design*. PhD thesis, Delft University of Technology, Faculty of Aerospace Engineering.

Wentink, M., Bles, W., Hosman, R. J. A. W., and Mayrhofer, M. (2005). Design & Evaluation of Spherical Washout algorithm for Desdemona Simulator. In *Proceedings of the AIAA Modeling and Simulation Technologies Conference and Exhibit, San Francisco, CA, Aug. 15-18*, number AIAA-2005-6501.

Wentink, M., Correia Grácio, B. J., and Bles, W. (2009). Frequency Dependence of Allowable Differences in Visual and Vestibular Motion Cues in a Simulator. In *Proceedings of the AIAA Modeling and Simulation Technologies Conference and Exhibit, Chicago, IL, Aug. 10-13*, number AIAA-2009-6248.

Wiener, N. (1961). *Cybernetics: or Control and Communication in the Animal and the Machine*. The M.I.T. Press, Cambridge, Massachusetts, 2nd edition.

Wiskemann, C. M., Drop, F. M., Pool, D. M., van Paassen, M. M., Mulder, M., and Bülthoff, H. H. (2014). Subjective and Objective Metrics for the Evaluation of Motion Cueing Fidelity for a Roll-Lateral Reposition Maneuver. In *Proceedings of the AHS 70th Annual Forum, Montreal, Canada, May 20-22*.

Wonham, W. (1967). On Pole Assignment in Multi-Input Controllable Linear Systems. *IEEE Transactions on Automatic Control*, 12(6):660–665.

Wood, J. R. and Hodgkinson, J. (1980). Definition of Acceptable Levels of Mismatch for Equivalent Systems of Augmented CTOL Aircraft. Technical Report MDC A6792, McDonnel Douglas Corp.

Wu, W. (1997). Development of Cueing Algorithm for the Control of Simulator Motion Systems. Master's thesis, State University of New York at Binghamptom.

Wu, W. and Cardullo, F. M. (1997). Is There an Optimum Motion Cueing Algorithm? In *Proceedings of the AIAA Modeling and Simulation Technologies Conference and Exhibit, New Orleans, LA, Aug. 11-13*, number AIAA-1997-3506, pages 23–29.

Yilmaz, D. (2018). *Identification of Manual Control Behaviour to Assess Rotorcraft Handling Qualities*. PhD thesis, Delft University of Technology, Faculty of Aerospace Engineering.

Young, L. R. (1969). On Adaptive Manual Control. *Ergonomics*, 12(4):635–674.

Zaal, P. and Mobertz, X. (2017). Effects of Motion Cues on the Training of Multi-Axis Manual Control Skills. In *AIAA Modeling and Simulation Technologies Conference, Denver, CO, Jun. 5-9*, number AIAA 2017-3666.

Zaal, P., Schroeder, J., and Chung, W. (2017). Objective Motion Cueing Criteria Investigation Based on Three Flight Tasks. *The Aeronautical Journal*, 121(1236):163–190.

Zaal, P. M. T. (2011). *Pilot Control Behavior Discrepancies Between Real and Simulated Flight Caused by Limited Motion Stimuli*. PhD thesis, Delft University of Technology, Faculty of Aerospace Engineering.

Zaal, P. M. T. and Pool, D. M. (2014). Multimodal Pilot Behavior in Multi-Axis Tracking Tasks with Time-Varying Motion Cueing Gains. In *Proceedings of the AIAA Modeling and Simulation Technologies Conference, National Harbor, MD, Jan. 13-17*, number AIAA-2014-0810.

Zaal, P. M. T., Popovici, A., and Zavala, M. A. (2015a). Effects of False Tilt Cues on the Training of Manual Roll Control Skills. In *Proceedings of the AIAA Modeling and Simulation Technologies Conference, Kissimmee, FL, Jan. 5-9*, number AIAA-2015-0655.

Zaal, P. M. T., Schroeder, J. A., and Chung, W. W. Y. (2014). Transfer of Training on the Vertical Motion Simulator. In *Proceedings of the AIAA Modeling and Simulation Technologies Conference, Atlanta, GA, Jun. 16-20*, number AIAA-2014-2206.

Zaal, P. M. T., Schroeder, J. A., and Chung, W. W. Y. (2015b). Objective Motion Cueing Criteria Investigation Based on Three Flight Tasks. In *Proceedings of the RAeS Flight Simulation Conference, London, UK, Jun 9-10*. Royal Aeronautical Society.

ACKNOWLEDGEMENTS

The journey towards a Ph.D. degree is never completed alone, as many candidates before me will undoubtedly endorse. I am forever grateful to my promotors, Max and Marilena, for their continuous trust and support during this special, yet often difficult process. I am also grateful to Mark, Bernd and Martijn at Desdemona B.V., without whom this dissertation would not have existed. Thank you for the confidence and for all the support and opportunities you have provided over the years. I hope that in return I have been able to make a lasting contribution (and I hope many will follow for a long time to come...). The rest of my supervisory team at C&S also cannot be given enough praise. Olaf, your untamed enthusiasm, ideas, experience as well as your constant willingness to help have been more than instrumental to the foundations of this dissertation. I have often contemplated if it is not my own, but your name that should be on the cover of this thesis. Daan and René, I am equally fortunate as I am grateful to have been able to leverage your vast knowledge on topics ranging from many nitty-gritty mathematical details to the basics of running proper experiments. Finally, I would like to thank all the excellent pilots that have volunteered to participate in my experiments, with special regards to the people at "Commando Testvliegen" of the RNLAF. Your professionalism and skill have made a lasting impression.

On a somewhat lesser professional note, I would like to thank everybody that has made my Ph.D. experience enjoyable and memorable. This includes the countless friendly chats and discussions at the notorious C&S "coffee corner" on topics ranging from Trumpian politics to Clark's infamous and maximally-invasive experiment measurement methods. Of course, my fellow Ph.D. candidates in particular cannot remain unmentioned. In no particular order and with the risk of omitting names (sorry... you are hereby acknowledged!), thank you: Kasper, Kirk, Kimberly, Joaõ, Jaime, Jerom, Jelmer, Julia, Mario, Diana, Paolo, Daniel, Ezgi, Dirk, Rolf, Sophie, Deniz, Fede, Junzi, Emmanuel, Tao, Wei, Annemarie, Isabel, Ewoud, Sarah, Maarten, Shuo, Sihao, Yinghzi and Ye. Likewise, I hereby acknowledge Steffen, Joris, Maarten, Henk and Mitchell. You guys always made the long drive to Soesterberg worthwile.

Lastly, this dissertation certainly would not have been completed without the inexhaustible support from my family. I express the deepest gratitude to my dear wife. Your unconditional love and patience during the process of writing this thesis is equally worthy of the title that is its reward. Thank you, mom and stepdad, for your continuous encouragement and faith in my ambitions. To know I have your pride, regardless of my achievements, fills my heart with joy. To my beloved son, I hope one day you will be able to read this thesis and challenge its every word.

ABOUT THE AUTHOR

Ivan Miletović was born in Sarajevo, Former Republic of Yugoslavia, in 1990. He spent the first three years of his live growing up in a small mountain village by the name of Pogar, in the vicinity of the city Vareš. During the Bosnian War, he fled the country with his mother and settled in the Netherlands. At the age of 12, in his first year of high school, he met the love of his life, Jessie. Together with her and their young son, Milan, he lives near Rotterdam.

Ivan's academic career at TU Delft began in 2008, when he enrolled for the bachelor program at the faculty of Aerospace Engineering. He earned his B.Sc. degree *cum laude* in 2011, before enrolling for an M.Sc. degree at the Section of Control & Simulation (C&S). He completed an internship at Rheinmetall Defence Electronics (RDE) in Bremen, Germany, in 2012 and subsequently graduated *cum laude* on his thesis titled "*Optimal Reconstruction of Flight Simulator Motion Cues*" in 2014. This also earned him the honorary title of "*C&S Best Graduate*" of the academic year 2014/2015.

After earning his M.Sc. degree, Ivan briefly worked for RDE as a System Engineer before coming back to Delft in 2015 to pursue a Ph.D degree. He currently works as Senior Software Engineer at Desdemona B.V. and as Technical Software Consultant through his own company, Miletović Dynamics. He also remains actively involved as a Researcher at TU Delft on the work that has evolved from his dissertation.

Ivan enjoys spending off-time with his family and likes outdoor activities such as walking, running, skiing and hiking. In the quiet hours, you may find him tinkering with computers and software (mostly breaking stuff that isn't broken only to fix it again. . .), reading a book or playing the occassional video game.

LIST OF PUBLICATIONS

10. **I. Miletović**, M. D. Pavel, O. Stroosma, D. M. Pool, M. M. van Paassen, M. Wentink, M. Mulder, *Using Eigenmode Distortion for Motion Cueing Analysis on the Desdemona Simulator*, to be submitted.
9. **I. Miletović**, M. D. Pavel, O. Stroosma, D. M. Pool, M. M. van Paassen, M. Wentink, M. Mulder, *Using Eigenmode Distortion for Motion Cueing Analysis on the SIMONA Research Simulator*, to be submitted.
8. **I. Miletović**, M. D. Pavel, O. Stroosma, D. M. Pool, M. M. van Paassen, M. Wentink, M. Mulder, *Eigenmode Distortion: A New Perspective on Motion Cueing Fidelity in Flight Simulation*, to be submitted.
7. S. Stoev, O. Stroosma, M. M. van Paassen, **I. Miletović**, M. Mulder *Eigenmode Distortion Analysis for Motion Cueing Evaluation in Fixed-Wing Aircraft Simulators*, Proceedings of the AIAA Modeling and Simulation Technologies conference, San Diego (CA), 2019.
6. **I. Miletović**, M. D. Pavel, O. Stroosma, D. M. Pool, M. M. van Paassen, M. Wentink, M. Mulder, *Eigenmode Distortion as a Novel Criterion for Motion Cueing Fidelity in Rotorcraft Flight Simulation*, Proceedings of the 44th European Rotorcraft Forum, Delft, The Netherlands, 2018.
5. **I. Miletović**, D. M. Pool, O. Stroosma, M. D. Pavel, M. Wentink, M. Mulder, *The Use of Pilot Ratings in Rotorcraft Flight Simulation Fidelity Assessment*, Proceedings of the AHS 73d Annual Forum, Fort Worth (TX), 2017.
4. W. Dalmeijer, **I. Miletović**, O. Stroosma, M. D. Pavel, *Extending the Objective Motion Cueing Test to Measure Rotorcraft Simulator Motion Characteristics*, Proceedings of the AHS 73rd Annual Forum, Fort Worth (TX), 2017.
3. **I. Miletović**, D. M. Pool, O. Stroosma, M. M. van Paassen, Q. P. Chu, *Improved Stewart Platform State Estimation using Inertial and Actuator Position Measurements*, Control Engineering Practice, 2017 , 62 , 102-115.
2. R. Gori, M. Gennaretti, M. D. Pavel, O. Stroosma, **I. Miletović**, *Prediction and Simulator Verification of State-Space Rotor Modelling on Helicopter Manoeuvring Flight*, Proceedings of the 41st European Rotorcraft Forum, Munich, Germany, 2015.
1. **I. Miletović**, D. M. Pool, O. Stroosma, Q. P. Chu, M. M. van Paassen, *Using Iterated Extended Kalman Filtering for Estimation of Hexapod Flight Simulator Motion State*, Proceedings of the 11th PEGASUS-AIAA Student Conference, Salon de Provence, France, 2015.